Development of a Coaxial Circuit QED Architecture for Quantum Computing

Joseph Rahamim

Pembroke College, Oxford

A thesis submitted for the degree of

Doctor of Philosophy

Trinity 2019

Supervised by Dr. Peter Leek

Development of a Coaxial Circuit QED Architecture for Quantum Computing

Joseph Rahamim, Pembroke College, University of Oxford

Trinity Term 2019

Abstract of thesis submitted for the degree of Doctor of Philosophy

Superconducting circuit QED is a promising approach for building a quantum computer. In order to realise superconducting circuits at a sufficient scale for useful near-term applications, an architecture with an extensible design is required which implements good connectivity between qubits, and allows for selective readout and control of the qubits without introducing detrimental crosstalk or decoherence.

This thesis describes the development of a new coaxial circuit QED architecture that fulfils this requirement of extensibility by incorporating out-of-plane wiring into the sample holder. Single-qubit unit cells consisting of a transmon qubit and readout resonator with coaxial geometries are fabricated on opposing sides of a substrate, and selective control and readout of the qubits is achieved via a capacitance to coaxial wiring built into the device enclosure. Unit cells of qubit and resonator can be arranged in a 2D array without modification of the wiring scheme. A single-qubit unit cell of this architecture is used to implement dispersive circuit QED, and a full characterisation of the Hamiltonian is performed. The device is shown to have parameters comparable to those found in other approaches, such as a coupling between qubit-resonator of ≈ 100 MHz and a coherence time of order ≈ 10 μs. The extension of this scheme to 2D arrays of qubits is then presented, and realizations of two-qubits gates are demonstrated with fidelities all above 87% on a four qubit device. Further evaluations are performed on multi-qubit devices, including a characterisation of the drive isolation of the mode-matched drive ports, finding values in the range of 50 dB and 30 dB for measurement and control respectively. Similarly, the cross coupling between circuits is shown to have values $\approx 2\%$ of the coupling within a unit cell. The effective circuit temperatures are measured, finding typical values of ≈ 100 mK, and the techniques of spin-locking and T_2 spectroscopy are employed

to probe the noise environment. Finally the architecture is extended to incorporate frequency tuning of qubits with gradiometric SQUID loops by way of off-chip flux bias lines (FBLs). These lines are used to tune qubits with a signal isolation of $> 99\%$. Furthermore, the ability of these FBLs to dynamically control the qubit frequency is shown by demonstrating switching of the frequency on a nanosecond time-scale, and parametric driving over a frequency range of gigahertz.

To my grandfather Murad Dalah.

Contents

Chapter 1

Introduction

1.1 Quantum Computing

The realization of a quantum computer has become a global cross-disciplinary research effort, incorporating developments across physics, material science, engineering and computer science. A universal quantum computer [1] will be able to run a variety of algorithms to solve computational problems that are intractable for classical computers, no matter the processing power [2]. The core concept is to encode bits of information in physical systems that can have quantum states rather than classical, and to utilise phenomena in quantum mechanics such as state superposition and entanglement to perform computations that would be physically impossible for conventional computers.

The idea of using quantum systems to overcome limits of classical computation is widely attributed to Feynman [3]. This concept was made explicit when in 1985 David Deutsch proved that a classical computer cannot efficiently simulate such a quantum computer [4], highlighting the distinction between quantum and classical information. In 1992 the discovery of the Deutsch-Jozsa algorithm [5] demonstrated the first algorithm that a quantum computer could perform with exponentially fewer steps than any classical routine, and over years that followed increasingly many quantum algorithms were discovered that were more efficient than classical alternatives [6, 7]. However any physical implementation of a quantum bit (or qubit) is prone to errors which must be mitigated in order to efficiently run these algorithms. Conventional error correction schemes are not

a viable solution as they require measurement of the qubit state, and thus the quantum information would be lost due to the state collapse. Fortunately errors in quantum computational systems can be corrected with quantum error correction (QEC), first proposed by Peter Shor in 1996 [8]. Since then several correction schemes have been devised [9, 10], all combining multiple qubits with sufficiently low error rates to act as one fault-tolerant logical qubit.

Whilst the theoretical work continued, practical implementations of a quantum computer remained a challenge, and it wasn't until 1998 that a quantum algorithm was first demonstrated on a physical quantum computer, based on Nuclear Magnetic Resonance (NMR) [11]. Unfortunately quantum computing with NMR was shown to be an approach that would be increasingly difficult to scale for a variety of reasons [12]. However the motivation to realize such a computer did not dissatisfy, and since then several different physical systems have been explored. This list includes trapped ion systems [13], photonic waveguides in silicon [14], quantum dots [15], diamond nitrogen-vacancy centres [16, 17], optical lattices of neutral atoms [18], spins in silicon [19, 20], and the implementation used in this thesis, superconducting circuits [21].

Much progress has been made in the last twenty years in realising the foundations of a quantum computer. As of the time of writing, implementations with ion trap systems still have the best achievements in state preparation, readout, and gate fidelities [22, 23, 24]. Despite the relatively slow progress of scaling such systems due to the complexity of the technical challenges, there is still plenty of research on how to build larger scale systems with this approach [25]. More recently, superconducting circuits have emerged as another leading approach for building a large scale quantum computer. This implementation has attracted a large amount of research, both from academic laboratories and commercial enterprises [26, 27]. Two qubit gate operations with fidelities of $> 99\%$ have been demonstrated with various circuit designs and gate implementations [28, 29, 30], and a logical qubit with a longer lifetime time than its components has been demonstrated [31]. A variety of algorithms and simulations have been carried out on circuits of $10 - 20$ physical qubits [32, 33, 34], and devices of $49 - 128$ qubits are currently under development

[35, 36, 37, 38].

In this approach macroscopic circuits are cooled to cryogenic temperatures, and are used to engineer nonlinear quantised systems to be used as qubits [39]. The superposition of Cooper pair states necessary to achieve this was demonstrated in 1997 [40], and in 1999 these states were first coherently controlled in a qubit named the Cooper pair box [41]. An important advancement of this field was the development of circuit quantum electrodynamics (QED) [42, 43]. The interaction of light and quantum states of matter was first studied in the field of cavity QED, on atoms coupled to light confined in reflective cavities [44, 45]. This physics was applied to superconducting circuits by coupling qubits acting as artificial atoms to microwave resonators. This approach is advantageous as it shields the qubit from its environment and mitigates radiative losses that might otherwise lead to loss of quantum information. It also enables efficient readout of the qubit state without demolition of the classical information it contains [46, 47]. In general, superconducting circuits can be fabricated with pre-existing nanofabrication technologies used for conventional integrated circuits, and controlled with pre-existing microwave electronics developed for the radar and telecommunications industries. The versatility afforded by the ability to engineer specific quantum systems, and the ease of scaling afforded by the integrated circuit fabrication, are just two reasons why this implementation is one of the leading candidates for producing a large scale quantum computer.

1.2 Approaches to Scaling Circuits

Quantum computers will require a large number of qubits in order to run the many different algorithms possible [52]. This requirement comes not only from the necessary computational ability, but also in order to meet the demands of QEC, which requires several coupled physical qubits in order to form one robust logical qubit. The challenge of building large scale circuits to process quantum information is about more than simply increasing the number of qubits, as the degree of qubit connectivity and the level of errors during gate operations also place limits on the depth of gate sequences that can be performed [53]. With that in mind, there are currently many efforts being made to develop

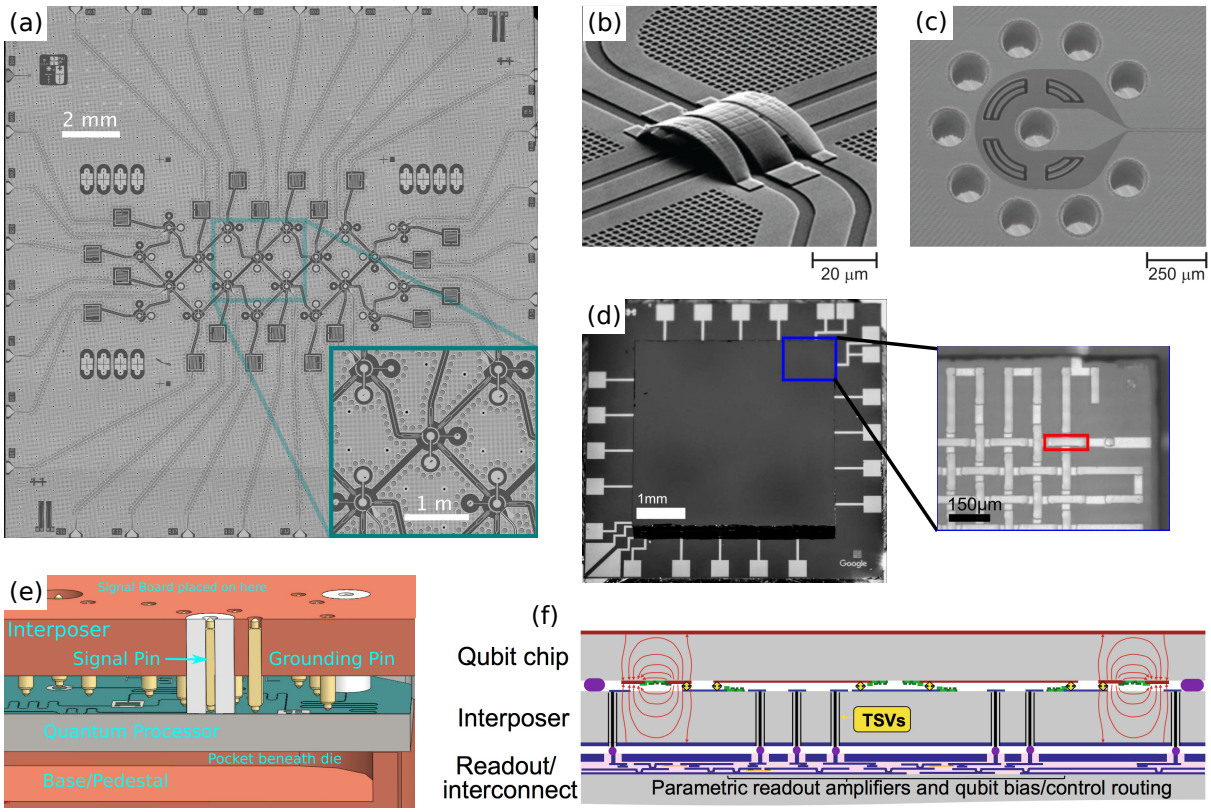

Figure 1.1: Current approaches to developing extensible circuit architectures, images are from the following works. (a): A 19 qubit device from Rigetti Computing, with through-silicon vias (TSVs) to suppress chip modes [32]. (b): Air bridges to bridge transmission lines and connect patches of ground plane developed at Delft [48]. (c): Coaxial TSVs to deliver microwave signals from the other side of the substrate developed at Delft [48]. (d): Developed at UCSB, two substrates are fixed together in a flip-chip layout with indium bump-bonds to electrically connect wiring from one chip to another [49]. The zoom-in is an infra-red image showing the connection of the two circuit layers. (e): Chip packaging developed at IBM and NIST, whereby signals are delivered out of the chip plane by pogo-pins [50]. (f): Flip-chip architecture that is being developed at Lincoln Labs, separating the circuit elements of qubits, wiring and readout into different chips, connected by indium bonds and TSVs [51].

circuit architectures that are extensible in design, without compromising on the ability to achieve low error rates and without limiting connectivity between circuits. There are a great deal of challenges to scaling that are being approached with several methods (see Fig. 1.1). Some of these approaches concern the experimental setup itself, such as devising efficient schemes for providing control signals [48], or evaluating the thermal load of the provision these control signals to circuits of hundreds of qubits [54]. However here we focus on measures taken to scale the device and its circuit design directly.

One problem of scaling devices arises simply from the increasing dimensions of the microwave enclosure in which the chips are mounted. These enclosures form cavities that can have electromagnetic modes with comparable frequencies to the operational frequencies of qubits. Coupling to such modes may introduce mechanisms for loss, and bring about undesired coupling between circuit elements. Approaches to tackling this issue include the use of metallised through-silicon vias (TSVs) to change the mode structure within the substrate [55], utilising spring-loaded contacts to alter the resonant modes in the vacuum gap between the chip and sample holder [56], and introducing a structured recess underneath the chip to similarly modify the microwave environment [50, 57]. Other than cavity modes, there can be spurious slotline modes in the patches of the ground plane on the surface of the chip that are separated by on-chip wiring. These must be electrically connected to prevent the formation of such modes by way of free-standing air bridges, which can also be used to thread transmission lines across one another [58, 48].

Another challenge in developing larger scale devices is the so called wiring problem. Simply put, conventional wiring of superconducting devices is achieved by wire-bonding to launches at the edges of the chips. This edge-connectivity becomes increasingly intractable as the device circuitry is scaled up to larger numbers of qubits. Consider a two-dimensional array of $N \times N$ qubits, the number of qubits that need a physical connection scale as N^2 however the number of available sites for bonds only scales as $\approx N$. With this in mind, many laboratories are investigating different approaches for wiring devices in an extensible manner. The common theme of all the different approaches is to provide vertical wiring elements for the chip that run perpendicular to the device plane. This 3D wiring enables

the mapping of the 2D plane of circuits to a 2D plane of connection sites in an extensible manner. One common method of achieving this involves the routing of control wiring from the back of the chip, through the substrate, and into to the circuit plane with metallised through-silicon vias (TSVs) [48, 55]. This allows the backside of the device to house most of the wiring elements, and can be wafer-bonded to a printed circuit board (PCB) to provide a means of connecting to the device. An alternative approach is to use spring-loaded microwave contacts or pogo-pins [59, 50] to directly connect to launch sites in the device plane. A third approach is to mount micromachined superconducting caps to the device that provide an electrical connection as well as provide isolation of the circuits [60]. There has also been work to connect a flipped silicon chip directly to a multi-layer PCB though mechanical contact with vias in the PCB circuitry [61]. Many groups are utilising indium bump-bonding to connect multiple circuit layers in a "flip-chip" layout [49, 51], which allows for different circuits, such as qubits and readout elements, to be separated into different layers. This brings the benefits of achieving higher circuit connectivity without crowding in the design plane, and also reduces the number of fabrication steps required to make each component chip, which is expected to reduce potential sources of loss. A general concern for any of these measures is to ensure that qubit lifetimes and coherence are not significantly impacted by the extra circuit fabrication processes such approaches entail.

1.3 The Coaxial Circuit QED Architecture

In this thesis we present the development of a new circuit QED architecture based on coaxial circuits with off-chip wiring as an alternative approach to realising extensible designs [62]. The circuit design is shown in Fig. 1.2, and consists of coaxial circuits patterned on opposite sides of the same chip, with qubit circuits on one side, coupled to LC circuits for readout on the other. They are controlled from coaxial drive ports orientated perpendicular to the chip plane and built into the sample packaging. These ports can be used for independent control and readout of the qubits.

By virtue of the out-of-plane readout and wiring elements, the architecture may be

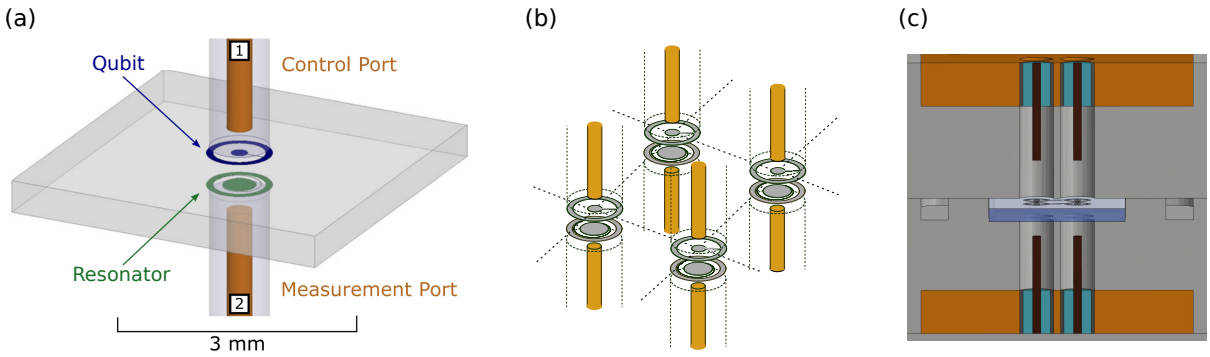

Figure 1.2: The coaxial circuit QED architecture. (a): CAD design of the single-qubit unit cell, with qubit and readout resonator on opposing sides of a chip, and control and measurement ports perpendicular to the chip plane. (b): Unit cells can be arranged in a 2D array without change to the wiring design. (c): CAD design of a four-qubit device inside the sample holder, with drive ports for individual qubit control and readout incorporated into the holder design.

extended to large 2D arrays of unit cells without any alteration to the wiring design. The double-sided structure and absence of wiring elements in the circuit design avoids crowding on the chip, hence reducing sources of microwave crosstalk between drive lines and circuits. Similarly the separation of qubit and readout circuits into two different planes allows qubit circuits to be connected to one another without constraints introduced by the presence of other circuit elements. Selective control and coupling is intrinsic to this architecture, due to the mode-matching of coaxial circuit elements to out-of-plane coaxial wiring. In addition, there is no reason for the level of crosstalk and cross couplings to get worse as the device is extended to larger arrays of qubits. The vertical wiring is implemented with only capacitive couplings, and is achieved without the need for bonds or TSVs that would otherwise necessitate further fabrication steps. The device itself requires only two lithography steps to fabricate, which is advantageous for realising devices with high qubit lifetimes as there are fewer opportunities to introduce sources of loss.

1.4 Overview of This Thesis

In the following chapters we expand on the development of this architecture and the demonstration of its viability as a platform for scaling superconducting circuits. In Chapter 2 we give an overview of the underlying theory that has been produced by the research

community over the years. In particular we focus on the dispersive regime of the Jaynes-Cummings Hamiltonian and its physical implementation with superconducting circuits, circuit QED. In Chapter 3 we detail the experimental setup used to control and measure devices, as well as provide details on the device sample holders and how the off-chip wiring is practically implemented. Chapter 4 focuses on the circuit design and nano-fabrication of the devices, and outlines considerations and optimisations implemented to improve qubit coherence and device yield. In Chapter 5 we present results from the first realization of a single-qubit unit cell of this architecture. We experimentally characterise the system Hamiltonian to show it is in the strong dispersive limit of the Jaynes-Cummings model, and demonstrate the qubit's coherence. In Chapter 6 we extend the architecture to circuits with multiple coupled qubits and demonstrate the viability of this approach by way of a full investigation of the drive port crosstalk, circuit cross-coupling, circuit temperatures and sources of qubit decoherence. The cross-resonance interaction [63, 64] is used to perform two-qubit gates on such devices, using a calibration scheme previously developed in this group as part of the work of [65]. Chapter 7 details an extension of this architecture to incorporate frequency tuning of qubits via off-chip flux bias lines. We measure the flux line crosstalk and demonstrate dynamic tuning and parametric driving of the qubit frequency using this approach. Finally in Chapter 8 we summarize our results and present an outlook for the continued development of this architecture.

Chapter 2

Theory of Superconducting Circuits

2.1 Fundamental concepts in Quantum Information

A qubit is defined as a quantum system that can only have two states, labelled $|0\rangle$ and $|1\rangle$. Being a quantum object it can exist in a superposition of those two states, as represented mathematically by the vector

$$|\psi\rangle = \alpha\,|0\rangle + \beta\,|1\rangle\,, \tag{2.1}$$

where α and β are complex numbers with the relation $|\alpha|^2 + |\beta|^2 = 1$. For convenience of notation and visualisation it is practical to rewrite $\alpha = \cos\left(\frac{\theta}{2}\right)e^{i\phi_\alpha}$ and $\beta = \sin\left(\frac{\theta}{2}\right)e^{i\phi_\beta}$ noting that the original relation is still satisfied, allowing the qubit state vector to be rewritten

$$|\psi\rangle = \cos\left(\frac{\theta}{2}\right)|0\rangle + e^{i\phi}\sin\left(\frac{\theta}{2}\right)|1\rangle\,, \tag{2.2}$$

where $\phi = \phi_\beta - \phi_\alpha$ and the global phase $-\phi_\alpha$ is ignored on the basis of having no physical relevance. This maps the qubit state to a point on a sphere, known as the Bloch sphere. The state on the Bloch sphere is then described by the Bloch vector $[\cos\left(\frac{\theta}{2}\right), e^{i\phi}\sin\left(\frac{\theta}{2}\right)]$ and an xyz axis is defined as in Fig. 2.1.

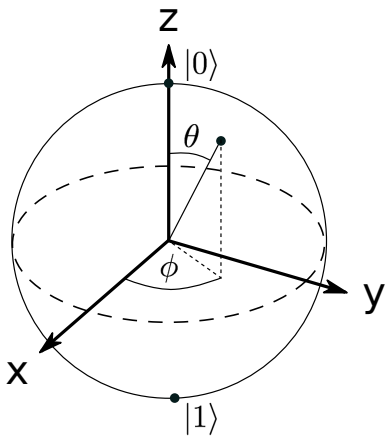

Figure 2.1: The Bloch sphere representation of the qubit state. The qubit wavefunction is mapped to a point of the surface of the sphere by rewriting it as $|\psi\rangle = \cos\left(\frac{\theta}{2}\right)|0\rangle + e^{i\phi}\sin\left(\frac{\theta}{2}\right)|1\rangle$. The state can be fully described by the coordinates θ and ϕ.

The probability for the qubit to be in the state $|0\rangle$ is given by $(1+\cos\theta)/2$, which is linearly related to the z-coordinate defined by $\cos\frac{\theta}{2}$. Assigning values of $z = 1$ for $|0\rangle$ and $z = -1$ for $|1\rangle$ allows us to define the operator

$$\hat{Z} = |0\rangle\langle 0| - |1\rangle\langle 1|\,, \tag{2.3}$$

such that $\langle\hat{Z}\rangle = z$. Similarly for the other two axes one can define operators

$$\hat{X} = |+X\rangle\langle +X| - |-X\rangle\langle -X|\,, \tag{2.4}$$

$$\hat{Y} = |+Y\rangle\langle +Y| - |-Y\rangle\langle -Y|\,, \tag{2.5}$$

where

$$|\pm X\rangle = \frac{1}{\sqrt{2}}\left(|0\rangle \pm |1\rangle\right), \tag{2.6}$$

$$|\pm Y\rangle = \frac{1}{\sqrt{2}}\left(|0\rangle \pm i\,|1\rangle\right). \tag{2.7}$$

with $\langle\hat{X}\rangle = x$ and $\langle\hat{Y}\rangle = y$. The three operators $\hat{X}$, $\hat{Y}$ and $\hat{Z}$ are called the Pauli operators and form a very convenient basis set for representing the dynamics of the qubit state on the Bloch sphere. Since the application of a Pauli operator corresponds to a rotation of π around the corresponding axis on the Bloch sphere, we can standardise the

notation of axis rotations to the axis of rotation and the angle applied, e.g. we write $\hat{X}_{+\frac{\pi}{2}}$ to denote a rotation of $+\frac{\pi}{2}$ around the x-axis. When describing rotations in a multi-qubit Hilbert space, e.g. a system with two qubits, we sometimes use the convenience notation $\hat{XX} = \hat{X}_1 \otimes \hat{X}_2$, with a similar style for the other qubit-specific Pauli operators. We have presented here only the minimum information needed to understand the the work in this thesis, however for those interested to learn more there are many excellent references on the subject such as [2].

2.2 Circuit QED and the Dispersive Limit

Many architectures for quantum information processing make use of the coupling between quantum states of matter and individual photons confined inside a cavity. This approach shields matter from its environment and mitigates radiative losses that might otherwise lead to loss of quantum information. The interaction of light and matter under such conditions was first studied using reflective cavities coupled to atoms [44, 45], and brought into existence the field of cavity quantum electrodynamics (QED). Following this, cavity QED was extended to include different physical implementations. From this work emerged circuit QED, an implementation of analogous physics between microwave photons and artificial atoms constructed from superconducting circuits. This system was first proposed and subsequently demonstrated in 2004 at Yale [42, 43].

In circuit QED a qubit is often implemented as a two-level system, and is coupled to a harmonic oscillator to act as the cavity and enable readout of the qubit state. The physics of such a coupled system is captured by the Jaynes-Cummings Hamiltonian [66]

$$H_{\mathrm{JC}}/\hbar = \omega_r(\hat{a}^\dagger\hat{a} + \frac{1}{2}) + \frac{\omega_a}{2}\hat{Z} + g(\hat{a}^\dagger\hat{\sigma}^- + \hat{a}\hat{\sigma}^+), \tag{2.8}$$

where ω_r, ω_a are the resonator and qubit frequencies respectively, $\hat{a}^\dagger$, $\hat{a}$ are the raising and lowering operators of the resonator, $\hat{\sigma}^+ = |0\rangle\langle 1|$, $\hat{\sigma}^- = |1\rangle\langle 0|$, and $\hat{Z}$ are the Pauli matrices as described in Sec. 2.1, and finally g is the interaction rate between qubit and resonator, also called the coupling. The first and second terms of Eq. (2.8) are the Hamiltonians of

the resonator (modelled as a harmonic oscillator) and qubit respectively, and the third term describes a dipole interaction where the qubit can absorb a quantum of energy from the resonator ($\hat{a}\hat{\sigma}^+$) or emit energy to the resonator ($\hat{a}^\dagger\hat{\sigma}^-$).

In addition to the physics described by Eq. (2.8), experimental demonstrations also have to consider the coupling of the system to the environment. This is captured by the decay rate of photons from the resonator to the environment κ, and the decay rate of an excitation in the qubit to the environment Γ_1. To use such a system for quantum logic we want to achieve many energy exchanges between the qubit and resonator before losing the excitations through decay, that is the strong coupling limit $g \gg \kappa, \Gamma_1$. The interaction between the qubit and resonator can be made dispersive by increasing the detuning $\Delta = \omega_a - \omega_r$, such that $g \ll \Delta$. This regime is called the dispersive limit. In this limit, making a unitary transformation to Eq. (2.8) and using perturbation theory to expand in powers of g/Δ to second order yields the dispersive Jaynes-Cummings Hamiltonian [66]

$$H_{\text{disp}}/\hbar = (\omega_r + \chi\hat{Z})\hat{a}^\dagger\hat{a} + \frac{1}{2}(\omega_a + \chi)\hat{Z}, \tag{2.9}$$

which can also be written as

$$H_{\text{disp}}/\hbar = \omega_r\hat{a}^\dagger\hat{a} + (\omega_a + 2\chi\hat{a}^\dagger\hat{a} + \chi)\hat{Z}, \tag{2.10}$$

where $\chi = g^2/\Delta$. χ is called the dispersive shift, and it's presence in the first term of Eq. (2.9) indicates that the dressed resonator frequency depends on the $\langle\hat{Z}\rangle$ value of the qubit. If the qubit is in the ground state the resonance will be found at $\tilde{\omega}_{r0} = \omega_r - \chi$, compared to the excited state at $\tilde{\omega}_{r1} = \omega_r + \chi$. This qubit-state dependent shift of the resonator frequency is the principle of dispersive readout, where $\langle\hat{Z}\rangle$ can be determined by probing whether the resonator frequency is $\tilde{\omega}_{r0}$ or $\tilde{\omega}_{r1}$. Dispersive readout is a quantum non-demolition measurement (QND) which means that it projects the state of the system into the one it measures, which is useful for implementing high fidelity measurement which in turn is vital for any quantum logic that requires feedback.

Eq. (2.8) can be diagonalised to get the eigenstates and corresponding energy levels

of the system. The energy levels are given by

$$E_{\pm,n} = \hbar \left(n\omega_r \pm \frac{1}{2}\sqrt{4ng^2 + \Delta^2} \right), \tag{2.11}$$

where n corresponds to the total number of excitations in the system including the qubit, and $\pm$ the higher and lower energy state of the nth excitation level. In the limit of small dispersive shifts $ng^2/\Delta \ < 1$, this expression can be linearised by Taylor-expanding the square root to give

$$E_{\pm,n} \approx \hbar \left(n\omega_r \pm \frac{1}{2}\left(\Delta + \frac{2ng^2}{\Delta} \right) \right). \tag{2.12}$$

If the number of photons is too large then this dispersive approximation breaks down and non-linear effects come into play. The critical photon number is the value of n such that the Taylor expansion diverges and is given by

$$n_{\text{crit}} = \frac{\Delta^2}{4g^2}. \tag{2.13}$$

To see how the dressed transition frequency of the qubit depends on the photon number in the resonator we take the difference between the energy of the qubit in the ground state $E_{-,n}$ and the excited state $E_{+,n+1}$ (accounting for the addition of the qubit excitation to the total number of excitations).

$$\tilde{\omega}_{a,n} = E_{+,n+1} - E_{-,n} = \hbar \left(\omega_a + (2n+1)\frac{g^2}{\Delta} \right). \tag{2.14}$$

Writing $n = \hat{a}^\dagger \hat{a}$ we recover the qubit dependent terms of Eq. (2.10). In order for this relation to hold it is important to ensure the number of photons in the resonator does not come close to n_{crit} (particularly relevant for experiments presented in Subsec. 6.2.1 and Subsec. 6.2.2).

2.3 Superconducting Circuits

Weakly driven circuits formed of superconducting material can demonstrate quantum mechanical behaviour [67]. Lumped element components such as inductors and capacitors, and distributed elements such as waveguides can be combined to define resonant circuits with frequencies in the microwave regime to interface with conventional RF electronics. The discovery of the Josephson junction [68] added another component to this list in the form of an inductor with non-linearity. The collective motion of Cooper pairs across this component can be used to create non-linear electronic circuits with quantised energy levels that act as qubits, as was done in [40, 41]. Coupling these qubits to harmonic resonant circuits led to the realisation of circuit QED in 2004 [42, 43].

In this section we present an overview of superconducting circuits with a focus on the circuit elements used to implement the coaxial circuit QED architecture in this thesis. Similar to other approaches [21], we form a circuit QED system with a lumped-element LC resonator for the harmonic oscillator, and a type of charge qubit known as the "transmon" [69] providing the basis for the two-level system. We give a brief overview of each of these components and how they are used to form a system with a comparable Hamiltonian to Eq. (2.8). We then consider how the introduction of SQUID loops enables the transition frequency of qubits to be tuned.

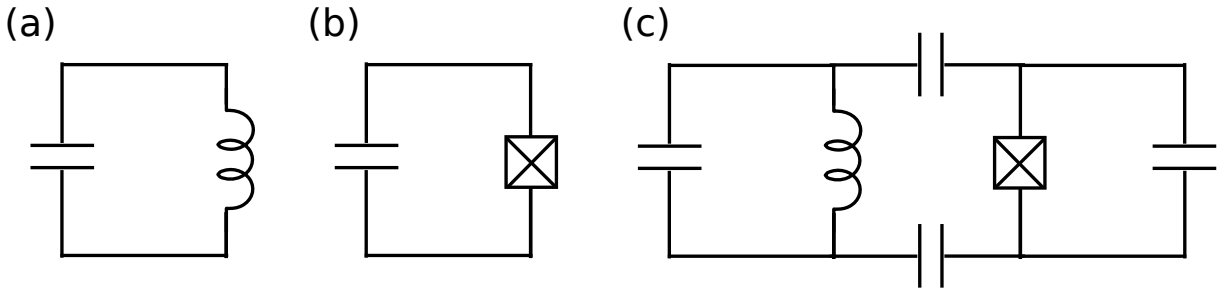

Figure 2.2: Circuit diagrams for the key components in this thesis. (a): A capacitor and inductor connected in parallel form the basis for an LC resonator, which acts as a harmonic oscillator. (b): A capacitor and Josephson junction connected in parallel form the basis of the Cooper-pair box. (c): The transmon and LC resonator are capacitively coupled.

2.3.1 The LC circuit

From the circuit quantisation [70] of the LC circuit shown in Fig. 2.2(a), one arrives at the following Hamiltonian,

$$H/\hbar = \frac{1}{\sqrt{LC}}\hat{a}^\dagger\hat{a}. \tag{2.15}$$

This is in the form of a harmonic oscillator with frequency $\omega_r = \frac{1}{\sqrt{LC}}$.

2.3.2 The Transmon

The transmon is an anharmonic resonator that is used to approximate a two-level system that can be used as the qubit. First demonstrated in [69], it has since become one of the most widely used implementations of a qubit in circuit QED, favoured for its relatively simple design and robustness to noise. We start by explaining the Cooper-pair box (CPB) [41], and we shall later see how the transmon is a special case of such a circuit. The circuit of a CPB is shown in Fig. 2.2(b) and is formed by replacing the inductor of an LC circuit with a Josephson junction [71, 72], which is a non-dissipative inductive element with non-linear behaviour. First discovered in 1962 [68], the quantum mechanical tunnelling of Cooper pairs across two superconducting leads separated by a thin insulating barrier, gives rise to non-linear effects. Specifically, the current and voltage across the junction are given by the DC and AC Josephson relations respectively,

$$I = I_c \sin(\phi),$$

$$\frac{d\phi}{dt} = \frac{2\pi V}{\Phi_0},$$

where I_c is the critical current (the maximal supercurrent the junction can support), ϕ is the potential difference across the junction and $\Phi_0 = h/(2q_e)$ is the flux quantum. These expression allow us to calculate the energy stored in the inductor,

$$U = -E_J \cos\left(2\pi\frac{\phi}{\Phi_0}\right), \tag{2.16}$$

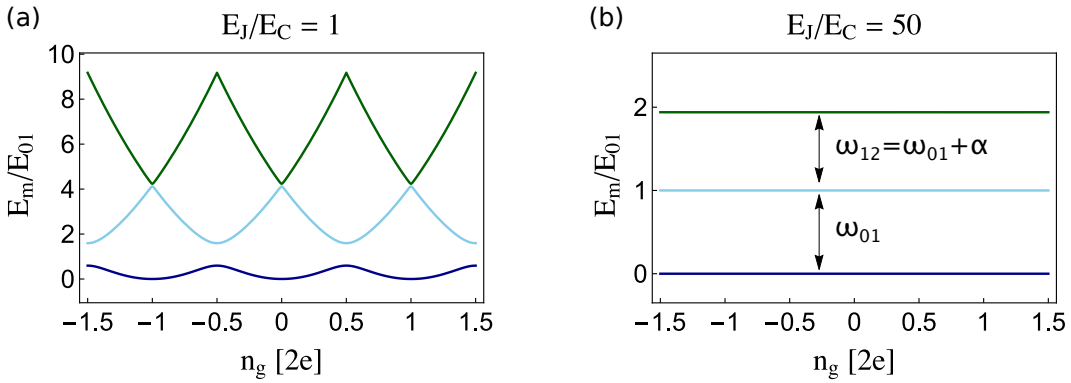

Figure 2.3: The first three energy levels of the Cooper-pair box as a function of the gate charge N_g. As the system moves into the transmon limit ($E_J \gg E_C$) the energy level spacing becomes increasingly insensitive to N_g.

where $E_J = \Phi_0 I_c/(2\pi)$ is the Josephson energy. The cosine dependence of ϕ is responsible for the non-linearity of the Josephson Junction inductance. With this expression, circuit quantization can be performed on the Cooper-pair box circuit [42] to arrive at the following Hamiltonian

$$H = 4E_C(\hat{N} - N_g)^2 - E_J \cos(\phi). \tag{2.17}$$

Here $E_C = q_e^2/2C$ is the charging energy, and is the energy of a single Cooper pair stored in the capacitor. We have also defined $\hat{N}$, which is the number of electrons across the capacitor. A gate charge N_g has been included so that we can inspect the effects of a constant applied offset voltage on the circuit. This Hamiltonian can be solved exactly [69] or using pertubative techniques [73] to find the energy levels of the system shown in Fig. 2.3. From this we can see that the energy level spacing, and thus the transition frequencies of the CPB, depend on the offset charge N_g. However as the ratio of E_J/E_C increases in value, the sensitivity to N_g decreases. A transmon is a CPB in the limit $E_J \gg E_C$ such that the energy levels are insensitive to charge fluctuations, and thus robust to a potential noise channel on the qubit frequency. The charge dispersion of the energy level n, is calculated for the transmon limit in [69] as

$$\epsilon_n = (-1)^n E_C \frac{2^{4n+5}}{n!}\sqrt{\frac{2}{\pi}}\left(\frac{E_J}{2E_C}\right)^{\frac{n}{2}+\frac{3}{4}} e^{-8\sqrt{E_J/E_C}}. \tag{2.18}$$

As one can see the charge dispersion is always larger for higher energy levels, and thus more significant for higher level transition frequencies. The form of the energy level diagram for a transmon is that of an anharmonic resonator. The energy level spacing decreases by a constant amount with each step, described by $E_{n+1,n} = E_{01} + n\alpha$ where α is the referred to as the anharmonicity, and has a negative sign. The transition frequency from ground to first excited state $E_{01}/\hbar = \omega_{01}$ is often calculated in terms of E_J, E_C as $\hbar\omega_{01} \approx \sqrt{E_J E_C} - E_C$, however to perform more accurate calculations in this thesis we use the 5th order expansion of the pertubative method shown in [73], which relates the qubit frequency and anharmonicity to E_J and E_C by

$$\begin{aligned}
\hbar\omega_{01} &= -E_C + 2\sqrt{2E_J E_C} - \frac{E_C\zeta}{4} - \frac{21E_C\zeta^2}{128} - \frac{19E_C\zeta^3}{128} - \frac{5319E_C\zeta^4}{32768}, \\
\hbar\alpha &= -E_C - \frac{9E_C\zeta}{16} - \frac{81E_C\zeta^2}{128} - \frac{3645E_C\zeta^3}{4096} - \frac{46899E_C\zeta^4}{32768}, \\
\zeta &= \sqrt{\frac{2E_C}{E_J}}.
\end{aligned} \tag{2.19}$$

2.3.3 Coupling the Resonator and Transmon

As was first proposed in [42], by connecting the LC and transmon circuits with a weak capacitive coupling (see Fig. 2.2(c)), one can achieve a similar Hamiltonian to the dispersive Jaynes-Cummings model. The key difference is that instead of a two-level system, the qubit is implemented with a transmon which is an anharmonic resonator. The effective dispersive Hamiltonian of the system with a resonator of frequency ω_r coupled with a coupling strength g to a transmon with transition frequency ω_{01} and anharmonicity α is

$$H_{\text{disp}}/\hbar = \tilde{\omega}_r \hat{a}^\dagger \hat{a} + \left(\tilde{\omega}_{01} + \frac{\alpha}{2}\left(\hat{b}^\dagger\hat{b} - 1\right)\right)\hat{b}^\dagger\hat{b} + 2\frac{g^2\alpha}{\Delta_0\left(\Delta_0 - \alpha\right)}\hat{a}^\dagger\hat{a}\hat{b}^\dagger\hat{b}, \tag{2.20}$$

so long as $g \ll \Delta_0$. Here $\Delta_0 = \omega_r - \omega_{01}$, is the resonator-qubit detuning, and the dressed frequencies are given by $\tilde{\omega}_r = \omega_r + (g^2/\Delta_0)$, $\tilde{\omega}_{01} = \omega_{01} - (g^2/\Delta_0)$. $\hat{a}$ and $\hat{b}$ are the annihilation operators for the resonator and transmon respectively. Considering only the first two levels of the transmon so as it treat it as a qubit leads to the approximate

Hamiltonian

$$H_{\text{disp}}/\hbar = \left(\tilde{\omega_r} - 2\frac{g^2\alpha}{\Delta_0\left(\Delta_0 - \alpha\right)}\hat{Z}\right)\hat{a}^\dagger\hat{a} - \frac{\tilde{\omega_{01}}}{2}\hat{Z}. \tag{2.21}$$

Defining the dispersive shift as $\chi = \frac{g^2\alpha}{\Delta_0(\Delta_0-\alpha)}$ we recover a form comparable to that of the dispersive cavity QED system Eq. (2.9), but with a different definition of χ modified by the anharmonicity of the transmon.

2.3.4 Tuning a Transmon with Magnetic Flux

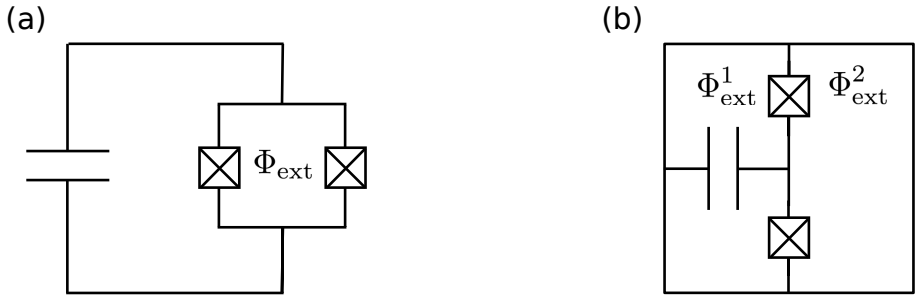

Figure 2.4: (a): The transmon can be made flux-tunable with an external field Φ_{ext} by replacing the Josephson junction with a DC SQUID. (b): Transmon with gradiometric SQUID loops, external flux can be threaded through either of the two loops, and is arranged such that only the flux difference $\Delta\Phi_{\text{ext}} = \Phi^1_{\text{ext}} - \Phi^2_{\text{ext}}$ will affect the current through the Josephson junctions.

The Josephson junction in the Transmon circuit can be replaced with two Josephson junctions in parallel forming a DC SQUID [74] as shown in Fig. 2.4(a). In this case, the inductive contribution to the Hamiltonian in Eq. (2.16) is modified to be the sum of the contribution from each junction,

$$H_{\text{ind}} = -E_{J1}\cos(\phi_1) - E_{J2}\cos(\phi_2), \tag{2.22}$$

where E_{Ji}, ϕ_i are the corresponding Josephson energies and phase differences across each junction. Because the DC SQUID forms a superconducting loop, in order to preserve the fluxoid quantisation the following relation must hold true of the difference between the phase drops across each junction,

$$\phi_1 - \phi_2 = \frac{\Phi_{\text{ext}}}{\Phi_0} \tag{2.23}$$

where Φ_{ext} is the external magnetic flux that is applied to the area within the superconducting loop, and $\Phi_0 = h/2e$ is the flux quantum. The dependence of H_{ind} on Φ_{ext} allows the frequency of the qubit to be tuned by varying Φ_{ext}. With the following substitutions,

$$\begin{aligned} E_{J\Sigma} &= E_{J1} + E_{J2}, \\ d &= \frac{E_{J2} - E_{J1}}{E_{J\Sigma}}, \\ \phi &= \frac{\phi_1 + \phi_2}{2} - \arctan\left(d \tan\left(\pi \frac{\Phi_{\text{ext}}}{\Phi_0}\right)\right) \end{aligned} \tag{2.24}$$

Eq. (2.22) can be recast as

$$H_{\text{ind}} = -E_{J\Sigma} \cos\left(\pi \frac{\Phi_{\text{ext}}}{\Phi_0}\right) \sqrt{1 + d^2 \tan^2\left(\pi \frac{\Phi_{\text{ext}}}{\Phi_0}\right)} \cos(\phi). \tag{2.25}$$

The entire prefactor in front of $\cos(\phi)$ can be collected into an effective Josephson energy E_J^{eff} which is dependent on Φ_{ext}. Eq. (2.19) shows that the qubit frequency depends explicitly on E_J, and so it can be tuned by an external magnetic field. Fig. 2.5 shows how the qubit frequency changes as a function of E_J^{eff}. The junction asymmetry, quantified by d, affects the overall achievable tuning range by limiting the minimum attainable E_J^{eff} to $E_J^{\text{eff}}(\pi) = dE_{J\Sigma}$. Despite the sacrifice of the tuning range, large junction asymmetries are often desirable in order to lower the susceptibility of the qubit to flux-noise [75], however large values of d also place upper limits on T_1 [69]. It is worth showing that for the case that the junctions are identical, the expressions reduce to

$$\begin{aligned} H_{\text{ind}} &= -E_J^{\text{eff}} \cos(\phi), \\ E_J^{\text{eff}} &= 2E_J \cos\left(\pi \frac{\Phi_{\text{ext}}}{\Phi_0}\right), \end{aligned} \tag{2.26}$$

Recovering the original form of H_{ind} in the single junction case but with the maximum Josephson energy given by $2E_J$.

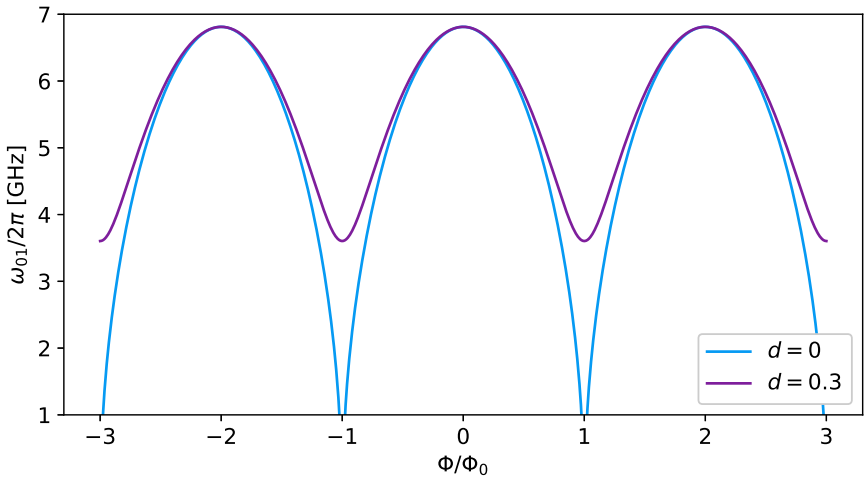

Figure 2.5: Qubit frequency calculated using Eq. (2.25) and Eq. (2.19) as a function of flux threaded through the DC SQUID Φ_{ext}. Tuning curves without junction asymmetry ($d = 0$) and with ($d = 0.3$) show how the tuning range decreases with increasing asymmetry.

The two Josephson junctions can also be arranged as in Fig. 2.4(b) to form a gradiometric SQUID. In this arrangement, there are two enclosed loops, and so two applied fluxes to consider Φ^1_{ext} and Φ^2_{ext}. The key idea is that the loops form a gradiometer that is sensitive to the difference in the flux through either loop, and is insensitive to homogeneous fields. In the case that both Φ^1_{ext} and Φ^2_{ext} are equal in amplitude and direction, reaction currents would be set up around the respective loops, which would have opposite directions along the wire-path on which the junctions are situated and would cancel. If instead Φ^1_{ext} and Φ^2_{ext} had opposite directions to one another, then the resulting counter-currents would add constructively along the path of the Josephson junctions. The result is that the SQUID is not tunable by global fields, but is instead tunable by the difference in the flux threaded through either loop, $\Phi_{\text{ext}} = \Phi_{\text{diff}} = \Phi^1_{\text{ext}} - \Phi^2_{\text{ext}}$. Using this to construct a transmon qubit [76] (as is done in chapter 7) results in a tunable qubit that is insensitive to changes in global flux, and only sensitive to the difference between the two. This has advantages in that it mitigates flux-noise that is homogeneous over the qubit area, and allows external flux to be delivered much more selectively if the flux-bias line is designed appropriately.

2.4 Cross-resonance

The cross-resonance interaction provides the basis of the two-qubits gates performed in this thesis. First proposed in [63, 64] it has frequently been utilised since for realising quantum logic with fixed frequency qubits with static couplings [29, 77]. Here we present an overview of the previously established physics, relevant for this thesis.

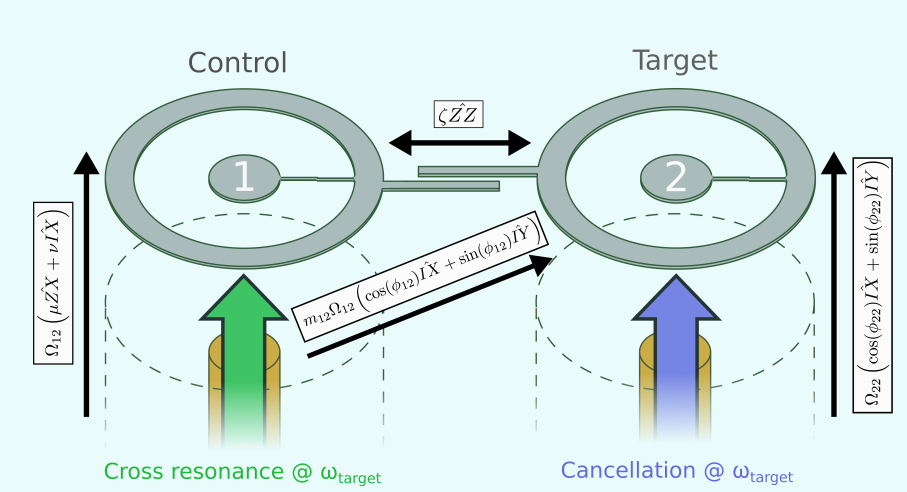

Figure 2.6: Schematic of the operation of the cross-resonance interaction. The qubits 1 and 2 are labelled as the control and target respectively. Applying a tone to the control qubit at the target qubit's frequency ω_{target} (green arrow) activates rotations about $\hat{ZX}$ and $\hat{IX}$ proportional to the cross resonance drive strength Ω_{12}. Crosstalk between the control drive pin and the target qubit generates additional rotations about $\hat{IX}$ and $\hat{IY}$. The unwanted $\hat{IX}$ and $\hat{IY}$ rotations can be counterbalanced and cancelled out by the application of a cancellation tone to the target qubit at ω_{target} (blue arrow). Lastly, there is an always-on rotation about $\hat{ZZ}$ due to the cross-Kerr shift between the two qubits.

Consider a system consisting of two coupled transmons, each with their own drive port, as in Fig. 2.6. We label one qubit the control, and the other the target. If the control qubit is driven at the frequency of the target, (which we refer to as a cross-resonance drive) then an $\hat{X}$ rotation on the target qubit is achieved, with a direction conditional on the $\langle\hat{Z}\rangle$ value of the control qubit. This allows for state-dependent qubit rotations to be performed between two-qubits, and thus entanglement. The Hamiltonian that describes

a system of two coupled qubits under a cross-resonance drive is given by[1]

$$\hat{H}/\hbar = \left(\frac{\Omega_{ZX}}{2}\hat{ZX} + \frac{\Omega_{ZY}}{2}\hat{ZY}\right) + \left(\frac{\Omega_{IX}}{2}\hat{IX} + \frac{\Omega_{IY}}{2}\hat{IY}\right) + \frac{\Omega_{ZZ}}{2}\hat{ZZ}. \tag{2.27}$$

$\hat{ZX}$ and $\hat{ZY}$ are the conditional rotations of the target dependent on the state of the control with respective rates Ω_{ZX} and Ω_{ZY}. The relative values of these two rates depends on the phase of the drive, and under normal operation this is ideally tuned such that Ω_{ZX} is maximised and Ω_{ZY} is zero. The next grouping of terms accounts for the crosstalk, i.e. direct driving of the target around $\hat{X}$ or $\hat{Y}$, either due to stray coupling between the control qubit's drive port and the target qubit, or due to the quantum crosstalk inherent of two coupled qubits. This crosstalk can be actively cancelled out by the application of a cancellation tone to the target qubit, as Fig. 2.6 shows. The last term $\frac{\Omega_{ZZ}}{2}\hat{ZZ}$ represents the constant rotation about $\hat{ZZ}$ due to the cross-Kerr shift ζ of one qubit on the other, and is exactly analogous to the state dependent dispersive shift between qubit and resonator. In contrast to the previous terms which are activated by the cross-resonance drive, this term is given by the static dispersive coupling between the two qubits and is always on. The drive rates of each term are given by:

$$\Omega_{ZZ} = \zeta, : \tag{2.28}$$

$$\Omega_{ZX} = \Omega_{12}^{X}\mu, \tag{2.29}$$

$$\Omega_{ZY} = \Omega_{12}^{Y}\mu, \tag{2.30}$$

$$\Omega_{IX} = \Omega_{12}^{X}\nu + m_{12}\left(\Omega_{12}^{X}\cos\phi_{12} + \Omega_{12}^{Y}\sin\phi_{12}\right) + \Omega_{22}^{X}, \tag{2.31}$$

$$\Omega_{IY} = \Omega_{12}^{Y}\nu + m_{12}\left(\Omega_{12}^{Y}\cos\phi_{12} - \Omega_{12}^{X}\sin\phi_{12}\right) + \Omega_{22}^{Y}. \tag{2.32}$$

Here Ω_{12}^{X} and Ω_{12}^{Y} are given by the amplitude of the applied cross-resonance drives in either quadrature, Ω_{22}^{X} and Ω_{22}^{Y} are given by the amplitudes of any cancellation tone applied directly to the target qubit. Equations Eq. (2.31) and Eq. (2.32) make clear the distinction between a quantum crosstalk with proportional amplitude ν, which arises from

[1] In this thesis we use the shorthand notation for operators $\hat{PP} = \hat{P}_{\text{control}} \otimes \hat{P}_{\text{target}}$, i.e. the first symbol in the two-qubit refers to the control qubit and the the second symbol the target.

the coupled-qubit Hamiltonian, and the classical crosstalk with proportional amplitude m_{12} and relative phase ϕ_{12}, which arises from the direct driving of the target from the control qubit's drive port. The cross-Kerr shift term and the relative amplitudes μ and ν depend solely on parameters of the two-qubit system. Considering up to the second level of the transmon, these are given by:

$$\chi_{ZZ} = \frac{J^2(\alpha^1 + \alpha^2)}{(\Delta_{12} + \alpha^1)(\Delta_{12} - \alpha^2)}, \tag{2.33}$$

$$\mu = -\frac{J}{\Delta_{12}} \frac{\alpha^1}{\Delta_{12} + \alpha^1}, \tag{2.34}$$

$$\nu = -\frac{J}{\Delta_{12}} \frac{\Delta_{12}}{\Delta_{12} + \alpha^1}, \tag{2.35}$$

where the superscripts 1 and 2 label the circuit parameters of the control and target qubit respectively, J is the qubit-qubit coupling, and $\Delta_{12} = \omega_1 - \omega_2$ is the qubit-qubit detuning. The cross-resonant interaction is the key circuit behaviour utilised in this work in order to perform a two-qubit CNOT gate. The physics of the system under these driving conditions is also necessary in order to determine the qubit drive-port selectivity later in Subsec. 6.2.3.

2.5 Decay and Decoherence

In any physical realisation of a device, the system acting as the qubit will not be totally isolated and will have some coupling to systems in the external environment, be it the control ports, other circuits, cavity modes or organic residues. Interactions with such systems can lead to depolarisation of the qubit state, leading to mixing of the qubit state towards the maximally mixed state $\langle \hat{X} \rangle = \langle \hat{Y} \rangle = \langle \hat{Z} \rangle = 0$, and ultimately a loss of the information stored in the qubit. Graphically one can think of this as a shrinking of the surface of the Bloch sphere (and the state-space for the qubit) towards the origin. There are two possible depolarization channels, longitudinal relaxation (i.e. energy decay) with characteristic time T_1, and transverse relaxation (i.e. accumulation of random phase)

with characteristic time T_2. This section describes in more detail the concepts used to understand these depolarization channels.

2.5.1 Energy Relaxation and the T_1 time

In nearly all implementations of cQED, the logical states of the qubit are encoded into the energy eigenstates of a quantum system, with $|0\rangle$ usually corresponding to the ground state and $|1\rangle$ some higher excited state. Unwanted changes to the energy stored in the quantum system will lead to unwanted and classical changes to the qubit logical state. This happens through any process where there is emission or absorption of an excitation in the qubit. This longitudinal relaxation, is characterised by a time T_1 called the qubit lifetime, or equivalently by the longitudinal relaxation rate $\Gamma_1 = T_1^{-1}$. Γ_1 is related to both the decay rate from excited to ground state, as well and absorption rate from ground to excited state.

$$\Gamma_1 = \frac{1}{T_1} = \Gamma_{1\downarrow} + \Gamma_{1\uparrow} \tag{2.36}$$

In the absence of high-levels of noise at or near the qubit frequency, and with the qubit in a sufficiently cool environment (such that $e^{-\frac{\hbar\omega_{01}}{k_B T}} \ll 1$), the longitudinal relaxation rate is dominated by the decay rather than absorption such that $\Gamma_1 \approx \Gamma_{1\downarrow}$.

2.5.2 Decoherence and the T_2 time

In the Bloch sphere picture of the qubit state, the qubit phase is represented by the azimuthal coordinate of the state ϕ. The process of randomisation of this phase is called decoherence, or dephasing. The accumulation of unwanted phase is brought about by noise processes that change the qubit frequency, and cause the qubit state to precess around the Bloch sphere. Additionally, any T_1 event will set the qubit state in $|0\rangle$ or $|1\rangle$ and so will entirely destroy the phase information. In an ensemble sense (i.e. considering the average measured state of multiple identically prepared and evolved systems) the result of decoherence processes on a qubit prepared on the equator of the Bloch sphere is the transverse relaxation of the qubit state towards the maximally mixed state $\langle\hat{X}\rangle = \langle\hat{Y}\rangle =$

$\langle \hat{Z} \rangle = 0$. Similar to the characteristic time T_1, this transverse relaxation is characterised by a time T_2 called the qubit coherence time, or equivalently by the dephasing rate $\Gamma_2 = T_2^{-1}$. From the Bloch-Redfield picture of decay and decoherence [78] the observed Γ_2 in any experiment depends on the contribution of the longitudinal relaxation and pure dephasing rates,

$$\Gamma_2 = \frac{\Gamma_1}{2} + \Gamma_\phi, \tag{2.37}$$

sometimes written explicitly in terms of characteristic times $1/T_2 = 1/2T_1 + 1/T_\phi$. The pure dephasing rate Γ_ϕ accounts for dephasing by any processes that directly change the qubit frequency and cause the accumulation of random phase. If the effects of such processes could be entirely eliminated then the coherence time of the qubit state is given by $T_2 = 2T_1$. To provide a more complete picture of decoherence, we briefly discuss both the contributing terms of Eq. (2.37).

Contribution from T_1

The expression $\Gamma_2 = \Gamma_1/2 + \Gamma_\phi$ captures the fact that longitudinal relaxation contributes to phase decay, and while this result can be derived from Bloch-Redfield theory the idea is more intuitive. Any longitudinal relaxation process collapses the qubit state and so the phase information is lost. In the $|0\rangle$ state the qubit is insensitive to T_1 events, whereas in the $|1\rangle$ the state it relaxes at the rate Γ_1, so in the superposition state $(|0\rangle + |1\rangle)/\sqrt{2}$ the state decays at half this rate, thus the contribution of T_1 events to T_2 is $\Gamma_1/2 = 1/2T_1$.

Contribution from T_ϕ

The pure dephasing characterised by T_ϕ, comes from any process that might change the qubit frequency and cause accumulation of random phase on the Bloch sphere through small rotations about $\hat{Z}$. The rate of dephasing in any experiment always depends both on the power spectrum of noise, and the pulses sent to the qubit. In an experiment the coherence of the qubit state is observed to decay in time, and is analytically described by

the coherence function $W(t)$. Following the analysis of [79], it is practical to write this as

$$W = e^{-\xi(t)}. \tag{2.38}$$

The form of $\xi(t)$ crucially depends both on the power spectrum of noise on the qubit frequency $S_Z(\omega)$, as well as the applied pulse scheme of the experiment being carried out. This is captured in its definition,

$$\xi(t) = \int_0^\infty \frac{1}{2\pi} S_Z(\omega) \frac{F(\omega t)}{\omega^2} d\omega. \tag{2.39}$$

Here, $F(\omega t)$ is a weight function that captures the noise-filtering of the pulse-scheme applied, and is obtained from a Fourier transform of the scheme as in [79, 80]. Relevant for this thesis are the weight functions for the Ramsey and spin-echo sequences[2] (explained and demonstrated in Subsec. 5.3.3)

$$\begin{aligned} F_{\text{Ramsey}}(\omega t) &= 2\sin^2\left(\frac{\omega t}{4}\right), \\ F_{\text{Echo}}(\omega t) &= 8\sin^4\left(\frac{\omega t}{4}\right), \end{aligned} \tag{2.40}$$

which are presented graphically in Fig. 2.7(a). Note that while the spin-echo sequence filters the effects of low-frequency noise, it will make the qubit more sensitive to noise at the frequency that is the inverse of the experiment length[3]. Conversely a Ramsey experiment is not sensitive at all to noise with frequency given by the inverse experiment length as the unwanted rotation will complete a whole period over the course of the experiment and undo its influence. By employing pulse schemes that shape the filter function so as to increase the sensitivity of the qubit to noise at particular frequencies, the spectrum S_Z can be directly measured, as in [79].

[2]These are calculated with the approximation that the pulses take no time, which is valid so long as the pulse durations are much smaller than the total free evolution time. To incorporate the finite width of the pulses, one can instead use the expressions derived in [81].

[3]It is worth noting that F depends on the spacing of pulses in the sequence, and so in an experiment where this value is swept, such as the typical Ramsey and Echo experiments, the filter function changes.

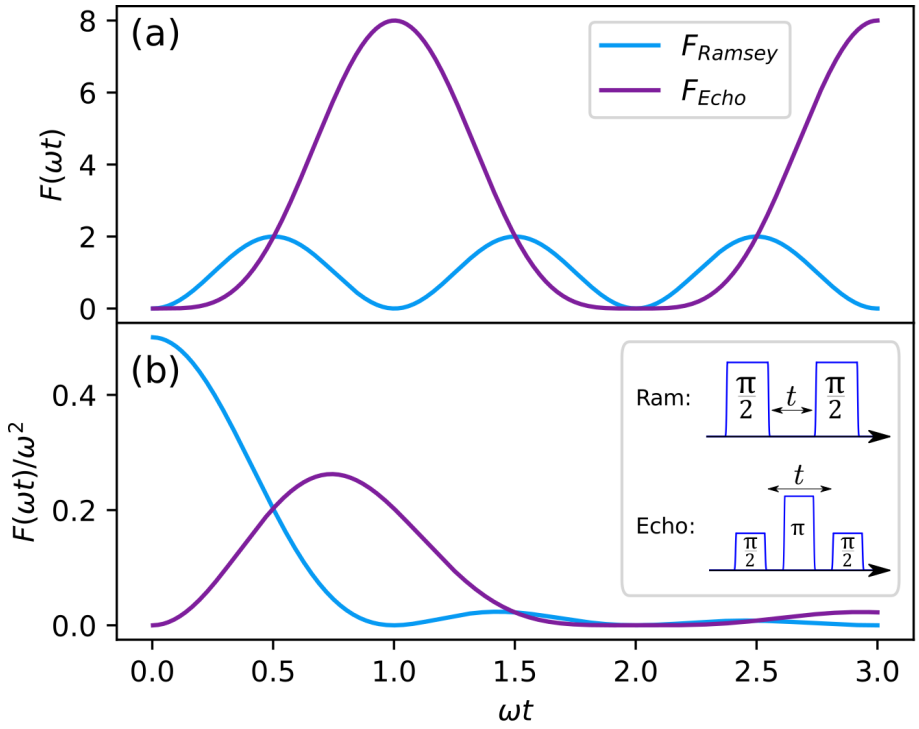

Figure 2.7: (a): The filter function $F(\omega t)$ on the noise PSD S_z for Ramsey and Echo pulse sequences (depicted in the inset). Here ω is the frequency of the noise and t is the experiment length (b): A plot of $F(\omega t)/\omega^2$, which is the filtering term that S_z is multiplied by in Eq. (2.39). Note the contrast between F_{Ramsey} and F_{Echo} in which F_{Echo} is more effective at filtering noise with low frequency compared to the inverse of the experiment length ($\omega \ll 1/t$), but is more susceptible to noise when these time-scales are similar ($\omega \approx 1/t$).

We now turn our attention to the other important term in Eq. (2.39) $S_z(\omega)$ which is the noise power spectral density (PSD). The form of S_z depends on the contributions to noise on the qubit frequency. We consider the two most common forms of S_z, which represent white noise from uncorrelated noise in the system, as well as $1/f$ noise correlated over long time scales and commonly found in electronic systems. The white noise spectrum is constant-valued across all frequencies $S_Z(\omega) = S_{\text{w}}$, whereas $1/f$ noise depends on the noise frequency as the name suggests $S_Z(\omega) = S_{1/f}/\omega$. Given a form of S_z one can work through Eq. (2.38) to recover the dephasing profile of the qubit state under these noise conditions,

$$W_{\text{white}}(t) = e^{-\frac{t}{T_2}},$$

$$W_{1/f}(t) \approx e^{-\left(\frac{t}{T_2}\right)^2},$$

where in both cases T_2 is defined as the characteristic time for W to fall to $1/e$ of its original value. In this thesis we consider only these forms of S_z however any functional form is possible, and can lead to non trivial dephasing profiles of the qubit.

Flux noise

In making a transmon flux tunable by way of a DC SQUID, the transmon is now susceptible to flux noise that directly affects its transition frequency, and so leads to an additional contribution to pure dephasing denoted by $\Gamma_\phi^{\text{flux}}$. Following the analysis of [69], to first order (valid for small noise amplitudes) this can be represented as

$$\Gamma_\phi^{\text{flux}}(\Phi_{\text{ext}}) = \left|\frac{\partial\omega_{01}}{\partial\Phi_{\text{ext}}}\right| \int_0^\infty \frac{1}{2\pi} S_Z^{\text{flux}}(\omega) d\omega. \tag{2.41}$$

That is, the gradient of the slope of the flux tuning curve (as in Fig. 2.5) multiplied by the RMS value of the flux contribution to S_Z. We can take this analysis further by presuming a symmetric SQUID with an E_J given by Eq. (2.26), and by assuming that S_Z^{flux} has a $1/f$ form of PSD, which is typically observed for flux noise [82, 83], producing

$$\Gamma_\phi^{\text{flux}}(\Phi_{\text{ext}}) \approx \frac{\hbar A}{\Phi_{\text{ext}}} \sqrt{\left|2E_{J\Sigma}E_C \sin\left(\frac{\Phi_{\text{ext}}}{\Phi_0}\right) \tan\left(\frac{\Phi_{\text{ext}}}{\Phi_0}\right)\right|}, \tag{2.42}$$

where A is the RMS flux noise calculated from the integral of $1/f$ noise (a logarithmic factor has been neglected as it is close to unity). At $\Phi_{\text{ext}} = 0$ we are at the insensitive part of the tuning curve (called the flux sweet-spot) where the gradient of the slope is zero, and so $\Gamma_\phi^{\text{flux}}$ is minimised. To calculate the expected dephasing time at this point one must carry out the same analysis as above to the next order (taking the second derivative of the curve). Several external factors can produce stray magnetic fields that lead to flux noise, external fields in the environment are always present and can be mitigated with appropriate shielding, noise on the amplitudes of the control electronics driving the flux-lines as well as any currents induced in the leads to the lines will also contribute, so low-noise sources and good filtering are required, and spins from TLSs adsorbed onto the

sample surface close to the DC SQUID will also contribute.

2.6 Measurement-Induced Dephasing and Stark Shift

Several experiments in this thesis require an understanding of the effect of photon population in the resonator on the coupled qubit. The partial entanglement between the two means the presence of photons in the resonator acts to both dephase the qubit by extracting information about its state, as well as shift the qubit via the Stark shift effect. The theory of such physics in the strong dispersive limit was first presented in [84], and experimental demonstrations of the predicted AC stark shift (in the limit $\chi \ll \kappa$) [85] and number splitting (in the limit $\chi \not< \kappa$) [86] were carried in the same period. In this section we briefly outline the physical models describing this, as it was first presented in [84]. We consider a system of qubit coupled to resonator, where the resonator is subject to a continuous drive at fixed frequency and power, and the system is in the steady-state (i.e. no parameters of the system are changing in time, and it has been driven for a long enough time scale such the mean photon population of the resonator is static).

2.6.1 Gaussian-approximation: $\chi \ll \kappa$

We first look at the system in the limit that $\chi \ll \kappa$. In this limit the resonator linewidth is much broader than the dispersive shift, and so each photon in the resonator only partially measures the qubit state. In general, fluctuations δn around the mean photon number in the resonator $\bar{n}$ will cause the qubit state to accrue random phase, leading to dephasing of the qubit. In this limit, a Gaussian approximation of the form of the phase accumulation is made, resulting in the following form of the qubit absorption spectrum (the measured signal response as an additional drive at frequency ω is applied)

$$S(\omega) = \frac{1}{2\pi} \sum_j \frac{(-2\tilde{\Gamma}_m/\kappa)^j}{j!} \frac{\Gamma_j/2}{(\omega - \omega_{01} - 2\bar{n}\chi)^2 + (\Gamma_j/2)^2}. \tag{2.43}$$

Here $\Gamma_j = 2(\Gamma_2 + \tilde{\Gamma}_m) + j\kappa$, and $\tilde{\Gamma}_m$ is the measurement induced dephasing rate defined in [84]. Essentially the spectrum is a sum over j photon numbers of each Lorentzian resonator response, with different weights and linewidths, all centred on the AC Stark shifted qubit frequency $\omega_{\rm ac} = (\omega_{01} + 2\bar{n}\chi)$.

2.6.2 Number splitting: $\chi \not\ll \kappa$

In the limit that $\chi \ll \kappa$ is not true, now the dispersive shift is more than or comparable to the resonator linewidth, and even a single photon is enough to fully determine the qubit state. One cannot make the same approximations and use the above expression, instead the latter expressions [84] are obtained by solving the master equation using a positive-P-function method. In this limit the mean photon number in the resonator depends on the qubit state, as the dispersive shift of the resonator is enough to impact the effectiveness of the resonator drive. Now the average number of photons in the resonator when the qubit is in the excited ($\bar{n}_+$) or ground ($\bar{n}_-$) state is given by

$$\bar{n}_\pm = \frac{\epsilon_{\rm rf}^2}{\kappa^2/4 + (\Delta_r \pm \chi)^2} \tag{2.44}$$

where $\epsilon_{\rm rf}$ is the amplitude of the drive field seen by the resonator, and Δ_r is the detuning of the drive from the undressed resonator frequency ω_r. The expressions for the measurement-induced dephasing are given by

$$\Gamma_m = \frac{D_s \kappa}{2} \tag{2.45}$$

where D_s is given by

$$D_s = \frac{2(\bar{n}_+ + \bar{n}_-)\chi^2}{\kappa^2/4 + \chi^2 + \Delta_r^2}. \tag{2.46}$$

$D_s = \left|\alpha_+^s - \alpha_-^s\right|^2$ can be understood as a measure of the distinguishably of the resonator states when the qubit is in ground or excited, and the larger its value the more projective a measurement is in the $\hat{Z}$ basis. The form of Eq. (2.45) simply describes measurement-induced dephasing as proportional to the product of the information obtained per photon

(D_s), with the rate of photons leaving the resonator κ. Finally, the absorption spectrum of the qubit is given by

$$S(\omega) = \frac{1}{\pi}\sum_{j=0}^{\infty}\frac{1}{j!}\mathrm{Re}\left(\frac{(-\mathrm{A})^{\mathrm{j}}\mathrm{e}^{\mathrm{A}}}{\Gamma_{\mathrm{j}}/2 - \mathrm{i}(\omega-\omega_{\mathrm{j}})}\right), \tag{2.47}$$

where

$$\begin{aligned}
\Gamma_j &= 2(\gamma_2 + \Gamma_m) + j\kappa, \\
\omega_j &= \tilde{\omega}_{01} + B + j(\chi + \Delta_r), \\
A &= D_s\frac{\kappa/2 - i\chi - i\Delta_r}{\kappa/2 + i\chi + i\Delta_r}, \\
B &= \chi(\bar{n}_+ + \bar{n}_-) - \chi D_s.
\end{aligned} \tag{2.48}$$

It is worth noting that we recover Eq. (2.43) in the limit $\chi \ll \kappa$. A key distinction from Eq. (2.43) is that the responses corresponding to different photon numbers j are centred at separate frequencies ω_j. The average qubit frequency (the AC Stark shifted frequency) occurs at

$$\omega_{\mathrm{ac}} = \tilde{\omega}_{01} + B + (\chi + \Delta_r)D_s = \tilde{\omega}_{01} + 2\chi\bar{n}_- \tag{2.49}$$

Chapter 3

Experimental Methods

In this chapter we detail the setup of the experiment as well as the device packaging developed to control and measure devices fabricated in this project. The experiments are carried out at cryogenic temperatures in the millikelvin range and controlled using a microwave electronics setup. In addition one of the key aspects of the coaxmon architecture is the 3D wiring of the circuits with an extensible design. Sample holders were developed to control and measure the devices according to this scheme.

3.1 Control and Measurement Setup

In this section we outline two experimental setups used to measure fixed frequency multi-qubit devices, and flux tunable devices. We cover the microwave electronics used for device control and signal processing.

3.1.1 Setup for multi-qubit experiments

The experimental setup used to simultaneously control and measure four qubits is shown in Fig. 3.1 and a summary of components in Table 3.1. Microwave pulses at the IF frequency are defined by a field programmable gate-array (FGPA) and produced by a digital-to-analogue converter (DAC). For the case of the qubit control signal, these pulses are up-converted with the internal IQ mixer of a microwave signal generator. In order to be efficient with microwave generators, the up-conversion for readout signals follows a

different scheme. The output from one signal generator is routed to a microwave splitter so that the same tone can be used to provide the local oscillator signal for the IQ mixers used in both the up-conversion and down-conversion of the readout signal.

All measurements are carried out at 10 mK inside a dilution refrigerator from Oxford Instruments. The main cooling power is provided by a pulse-tube system, but in order to reach such low temperatures these cryostats utilize the energy absorbed in the phase transition process between the concentrated and dilute phases of a mixture of ^{3}He and ^{4}He. The cooling is distributed over several plates, with the final plate reaching base temperatures of 10 mK. The device sample holders are mounted to OFHC copper brackets at the base-plate of the fridge, inside magnetic shields made from high magnetic permeability mu-metal. Signals are delivered to the device by way of coaxial input lines, attenuated at different stages to achieve a low electron temperature.

Routing the output of devices to a 6-port electromechanical switch enables different devices to be measured during fridge operation. The switch is controlled by voltage pulses from an external source. The outgoing signal passes through a 12 GHz low pass filter (LPF), an $8-12$ GHz band pass filter (BPF), and two circulators before connecting to the output lines. The signal is first amplified by a high electron mobility transistor (HEMT) amplifier at the 4K stage with a gain of 39 dB. The output signal is again amplified and filtered at room temperature before it is down-converted in a heterodyne detection scheme, measured at the analogue-to-digital converter (ADC), and processed by the FPGA. The down-converted signal is processed into the real (I) and imaginary (Q) field quadratures corresponding to the in- and out-of-phase components $S = I + iQ$, and can equivalently be described in terms of the amplitude and phase of the complex expression $S = Ae^{i\phi}$.

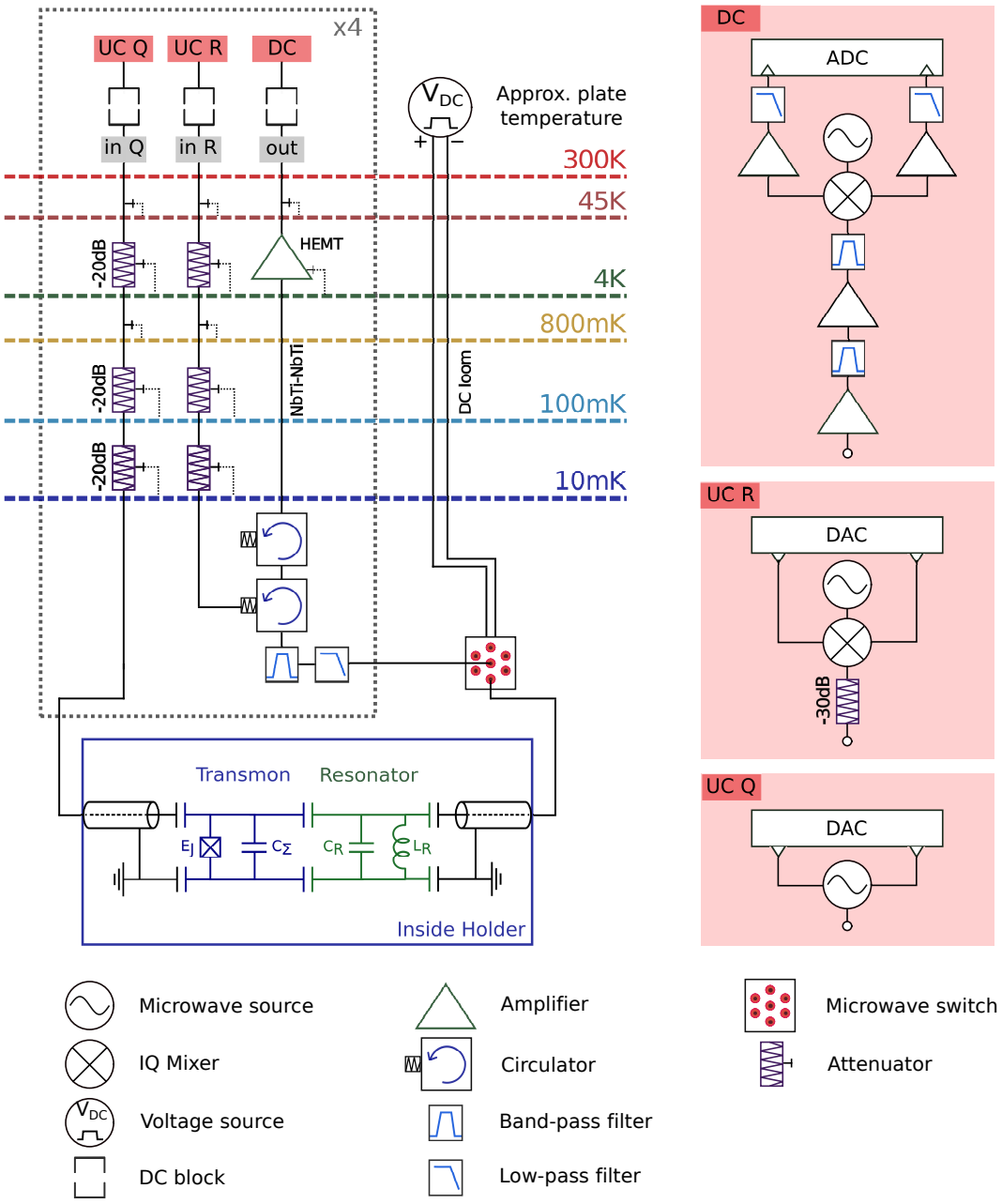

Figure 3.1: Schematic of the experimental setup for multi-qubit experiments. Control and measurement signals are generated by up-conversion chains (UC R for measurement, UC Q for control) and are transmitted via attenuated coaxial lines. The output signals are filtered by LPFs and BPFs and amplified by a HEMT amplifier. At the down-conversion chain (DC) the signal is mixed down and processed with a heterodyne detection scheme and the real and imaginary component of the signal is analysed with the FPGA.

Block	Device/Component	Manufacturer / Model
Upconversion (UC)	Microwave Signal Generator	Rohde & Schwarz SMF100A
	IQ mixers	Marki-microwave EVAL-MMIQ-0416L
	Power combiner/splitter	Mini-Circuits ZX10-2-126-S+
	DC-Block	Aeroflex Inmet 8039
Inside fridge (IF)	Magnetic shield	Amuneal Amumetal 4K
	Microwave switch	Radiall SP6T Coaxial Subminiature
	Circulator	Raditek 8-12-Cryo with magnetic shield
	Band-pass filter	Keenlion KBF-8/12-2S OFHC
	Low pass filter	K&L coaxial filters 6L250-00089
	HEMT amplifier	Low Noise Factory LNF-LNC1-12A
Downconversion (DC)	Wideband amplifier (1)	Mini-Circuits ZX60-183A+
	Wideband amplifier (2)	Mini-Circuits ZVA-183+
	Low pass filter	Mini-Circuits VLFX-300
Flux bias line (FBL)	Current source	Keithley 6221
	Arbitrary waveform generator	Textronix 5014C
	Bias Tee	Arnitzu K251 Ultra Wide Band
	Low pass filter	Mini-Circuits VLF-2250+

Table 3.1: Summary of components used in the experimental setup. The same signal generator, DC block and IQ mixer used for upconversion are used for downconversion.

3.1.2 Setup for flux tuning experiments

Flux-tunable devices required a modified setup that is shown in Fig. 3.2. Since the flux-tunable device holder has just one microwave port, the same port is used for both control and measurement of a qubit. To achieve this the control and measurement input signals are combined with a microwave splitter and sent to the device through the measurement input line. A current source provides the DC current for the flux bias line (FBL). The current is transmitted to the 10 mK stage with a superconducting loom, and is filtered with a home-made LPF with cutoff around 60 Hz, placed at the 4 K stage. The AC current for the FBL is produced by an arbitrary waveform generator (AWG). This is then transmitted by coaxial cable and attenuated outside and inside the fridge to reduce noise and thermalise the signal. The AC and DC components are combined at the base of the fridge by a bias tee, and then filtered once more with a 2.25 GHz LPF. As with the previous setup, the device sample holders are mounted to OFHC copper brackets at the base-plate of the fridge, inside a magnetic shield made from mu metal. In addition the sample holder is wrapped in Aluminium foil, to provide another measure of shielding from

global magnetic field. A set of photographs of the experimental setup inside the dilution refrigerator, including the setup for fixed frequency and tunable devices, are shown in Fig. 3.3.

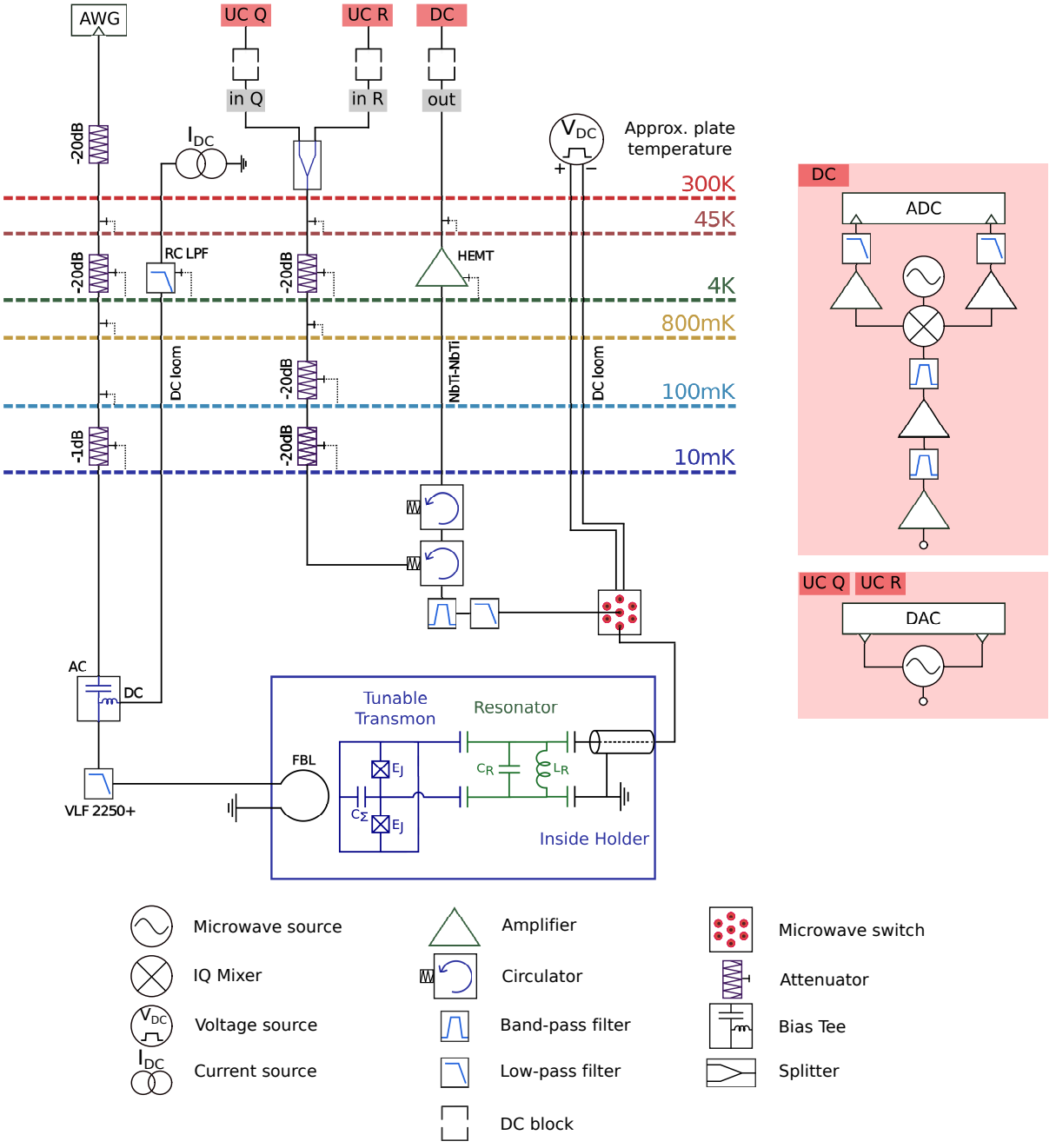

Figure 3.2: Schematic of the experimental setup for flux tuning experiments. Qubit microwave control and readout is performed as it was for fixed frequency devices, however since the sample holder contains only one microwave port, both control and measurement signals are combined at room temperature with a microwave splitter and transmitted via the same coaxial line. Both DC and AC currents are applied to the flux bias line (FBL). The DC component is transmitted via a DC loom filtered with an RC LPF at the 4 K plate, and the AC component via a coaxial line. Both components are combined with a bias tee and filtered with another LPF before reaching the FBL.

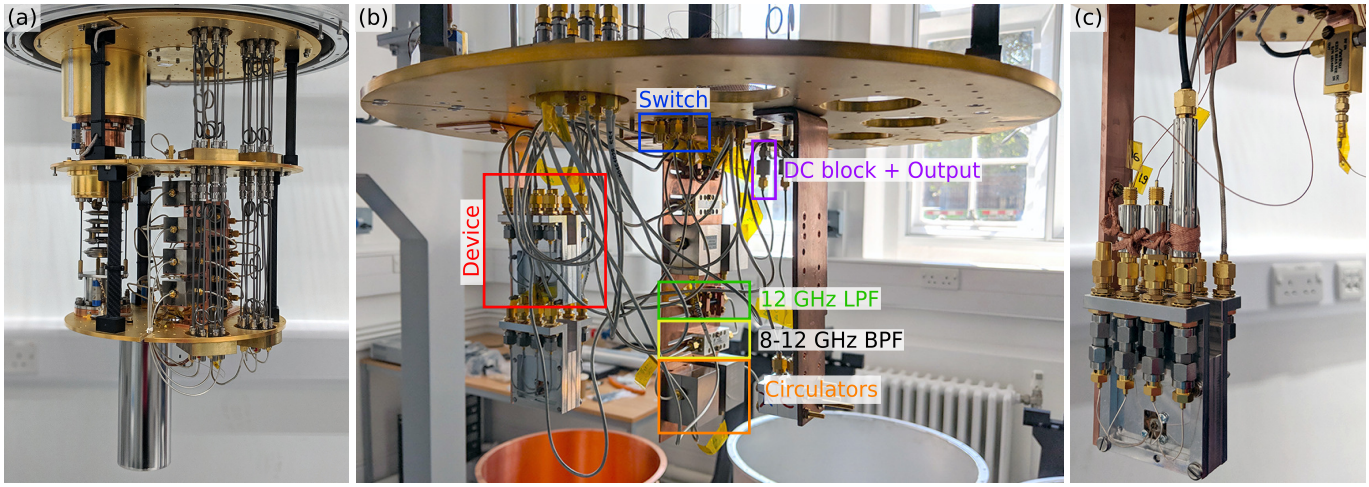

Figure 3.3: (a): The inside of the Triton 500 dilution refrigerator. An experiment enclosed in a mu-metal magnetic shield is attached to the base plate. (b): Base plate of the Triton XL, with a setup for multi-qubit experiments. Microwave components are labelled including the low pass filters (LPF) and band pass filter (BPF). (c): Image of the sample holder for flux tunable devices, mounted to an OFHC copper bracket at the base of the Triton 500. The flux bias line ports are visible and are connected to 1 GHz or 2 GHz LPFs, thermalised with copper braid. The bias-tee is visible in the top right.

3.2 Sample Holder Design

One of the key advantages of the coaxmon architecture is the 3D delivery of control and measurement signals delivered via microwave wiring built into the sample packaging following an extensible scheme. The holder design and the environment it provides are part of the definition of the circuit QED system. The coupling of the driving pins to their respective circuits set the photon decay rates κ, and the separation between the circuit plane on the chip and the sample holder will determine capacitances of different circuits to ground. Additionally the ability to selectively deliver microwave signals depends on the layout of the drive ports as well as the geometry of the holder. An added benefit of the out-of-plane connectivity of this architecture is that the device requires no wire-bonds to be mounted, greatly simplifying the loading procedure, as well as allowing the same device to be loaded and unloaded multiple times. Here we give a brief overview of the designs of the three sample holders used in this thesis, for single-qubit, multi-qubit and flux-controlled devices. Ultimately, the packaging design must be accounted for when determining whether a wiring scheme is indeed extensible, we shall how the wiring of the

multi-qubit and flux-driven holders were improved from the single-qubit holder.

3.2.1 1-qubit holder

The sample holder for single-qubit devices is show in Fig. 3.4, and is very similar to that used to measure coaxial LC resonators in [87]. Chips are mounted in 5×5 mm square-slots with circular cutaways beneath in order to protect the bottom circuit from contacting the holder. Indium is placed in the circular cutaways at the corners of the chip to mechanically fix and aid in thermalisation of the devices. The control and measurement pins are constructed from 0.375 mm diameter copper-beryllium wire inserted and soldered into the inner stud of a field-replaceable SMA connector. When mounted, the pins form the inner conductor of the coaxial ports, with the cylindrical hole of the sample holder acting as the outer. There are ports on both the top and bottom of the holder to act as the measurement and control ports respectively. The holder contains four separate slots for chips, which makes it possible to measure up to four single-qubit devices in the same cool down.

3.2.2 4-qubit holder

To control and measure multiple qubits on a 5×5 mm chip, it is necessary to have a wiring density to match the appropriate circuit density on the device. This is not achievable with the 1-qubit holder design, as the smallest dimensions of the SMA connectors used are the same size as the whole chip. In fact the smallest microwave connectors available at the time of writing are 3×3 mm, and would not be suitable for this device size (5×5 mm as before). As a solution, the SMA connector is removed entirely and instead the pin is replaced directly with UT-47 coaxial cable. One end of the cable is stripped back so that the centre conductor is exposed, forming the centre conductor of the drive port, and an SMA connector is assembled on the other end. The end is connected to an SMA bulkhead connector attached to feed-through plate, and this forms the interface for wiring the sample holder. With this approach, multiple cables can be packed almost as close as the diameter of the cable (≈ 1.1 mm), and fixed in position by soldering them to a copper

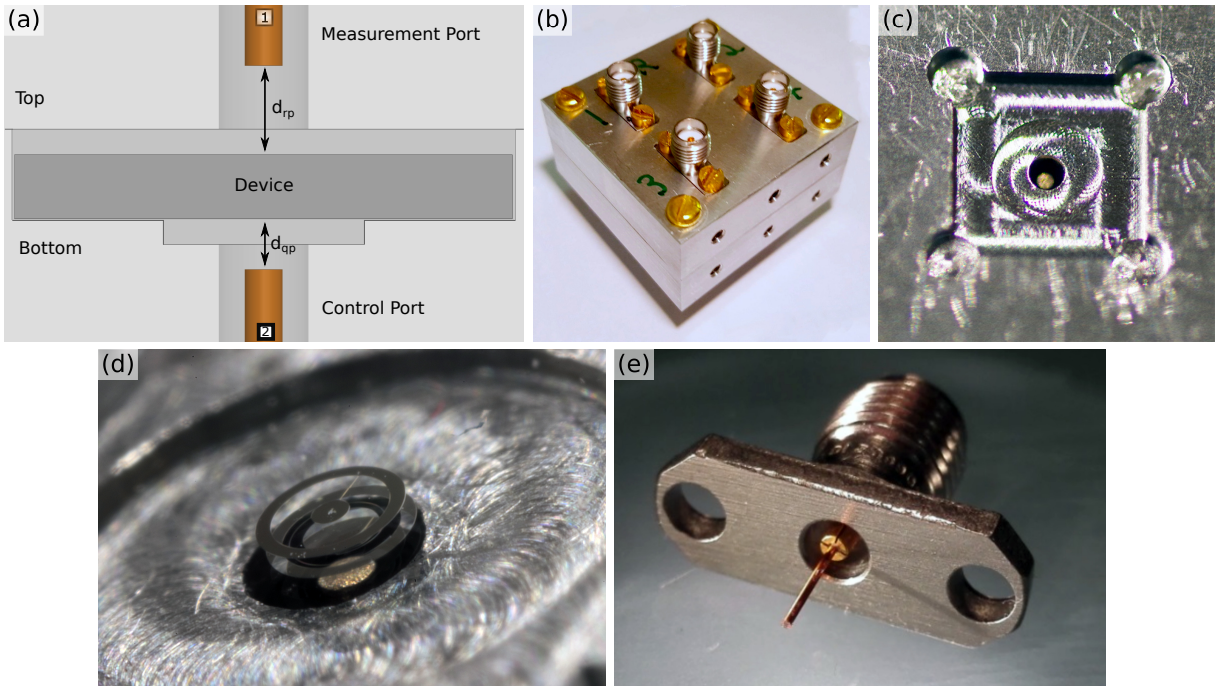

Figure 3.4: Single-qubit holder. (a): Side view of a device enclosed in the sample holder, with control wiring on both sides of the chip. The device sits in a square chip slot milled into the bottom piece of the sample holder, with a cylindrical recess beneath it protecting the circuits patterned on the bottom of the chip in these regions. The separation of pin to circuit is adjusted to set the coupling of the line to the circuit. $d_{\mathrm{rp}} = 0.4$ mm was found to give $\kappa \approx 1$ MHz, and d_{rq} is set to 0.7 mm to ensure the radiative decay rate of the qubit was less than ≈ 1 kHz. (b): Optical image of the enclosed sample holder, showing the measurement ports for each of the four device slots. The four control ports are on the underside of the holder. (c): Optical image of a chip slot. (d): Optical image of a chip in a slot. The sapphire substrate is transparent, and the qubit circuit can be seen on top with the LC resonator underneath. (e): Image of a drive pin used to control and measure the device.

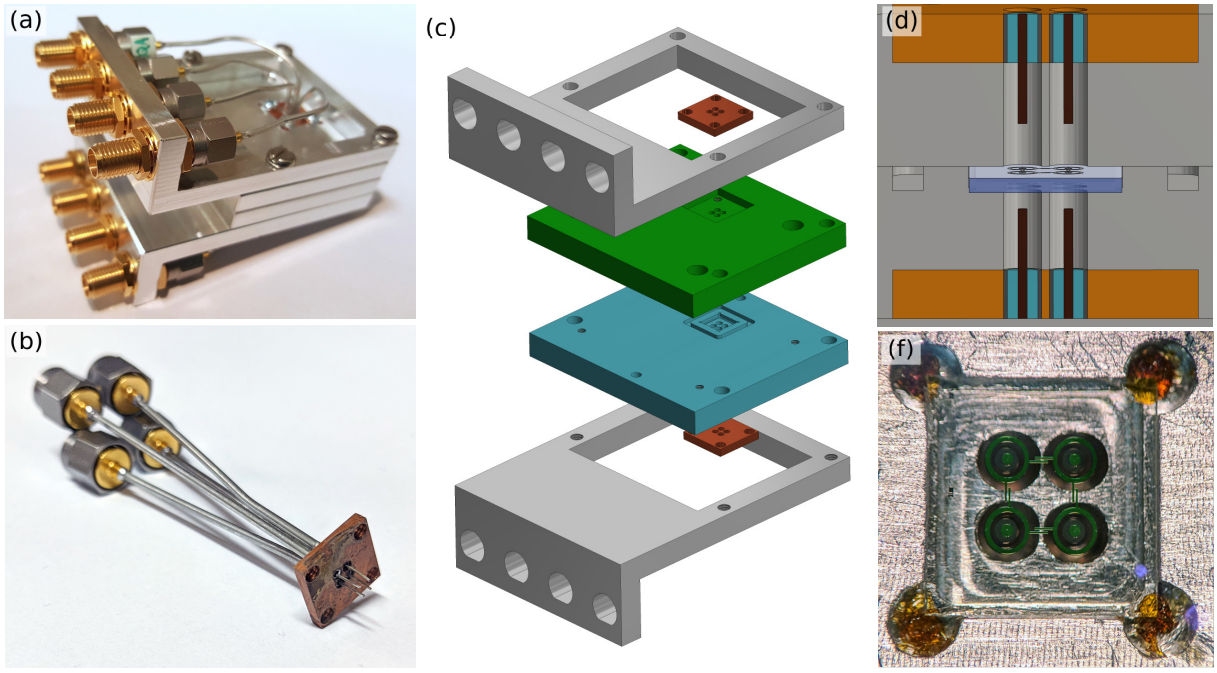

Figure 3.5: 4-qubit device holder. (a): Optical image of the assembled sample holder. (b): Image of the coaxial drive lines after being fixed to the copper piece. The near-ends of the cables have been stripped back to expose the centre conductor and protrude from the copper piece. This is then inserted into a slot in the top of the sample holder, and the connectorised ends bent to attach to the bulkhead connectors as they are in (a). (c): Exploded CAD design of all 6 components of the sample holder (without cables and connectors). (d): CAD image of a tilted side-view of a four-qubit device in the holder. The holder is cutaway to reveal the nearest set of drive ports with pins. (e): Optical image of a four-quit device in the chip-mounting slot of the holder. The qubits are false coloured green for visibility.

plate. This scheme is fully extensible, as by having the cable connections on a separate piece, the plane of connectivity of the sample holder is entirely separated from the device plane, and is free to have any topology or spacing. The 4-qubit sample holder is shown in Fig. 3.5. As a proof of principle the wiring was packed as closely as possible, given the constraints of machining a separation of 1.5 mm was chosen. It consists of two aluminium pieces with feed-throughs for the driving pins and with a square-slot for mounting the device area on the piece housing the resonator ports, two outer pieces that serve as the interface board with bulkhead SMA connectors, and two copper pieces onto which the wiring cables can be soldered to. The chip is mounted into the holder qubit-side up, and fixed in place with GE varnish at the corners. The chip sits on a shelf such that it rests on its edges and the bottom face is suspended 100 μm from the face of the holder. The depth of the recess is such that the gap between the top of the holder and the top face

of the chip is 200 μm. A trench is milled out around the chip mounting area which is filled with indium to ensure a good electrical connection between the two halves of the sample holder when they are closed. The lengths of the measurement pins are set so that they are spaced 400 μm from the resonator circuits to achieve a κ of $\approx$ 1 MHz, and the control pins are spaced 1000 μm from the qubits to achieve sufficient coupling without limiting T_1 through radiative losses [88, 89]. There are several small changes that could improve this sample holder. In particular the total area where the device is thermalised is quite minimal (it is only thermally fixed at the chip corners) and might be contributing to the circuit temperatures measured in Sec. 6.4. This could be mitigated by increasing the contact area, or by replacing the shelf and chip-gaps with a design whereby the chip is clamped directly, with etched grooves present only where there is metal on the circuit. Additionally both the proximity of the circuits and the presence of the chip-holder gaps affect drive-port selectivity, and simulations show there are gains to be made from increased separation of the circuits to 2 mm as well as by reducing or removing the chip-holder gaps altogether with the scheme just mentioned.

3.2.3 4-qubit holder with off-chip fast-flux lines

Flux-tunable devices require a source of magnetic field in to provide magnetic flux through the DC-SQUIDs in the circuit. This is typically achieved in two ways, first an external coil can provide sufficient flux even with a separation of several millimetres from the SQUID-loops, however this approach requires the sample holder material to not be superconducting (which would otherwise shield external field). In addition due to their size it is very difficult to make a network of coils selective, and it not possible to generate DC pulses or AC flux from the coil as its large inductance acts as a low-pass filter with approximately a kHz frequency cut-off. Because of this external coils are typically used to provide a constant magnetic field in conjunction with the second approach which is a flux-bias line (FBL). FBLs are wires lithographically defined on the same chip as the SQUIDs and as such can be brought very close to the SQUID-loops and provide sufficient flux without the line having such a large inductance, allowing it to handle AC signals.

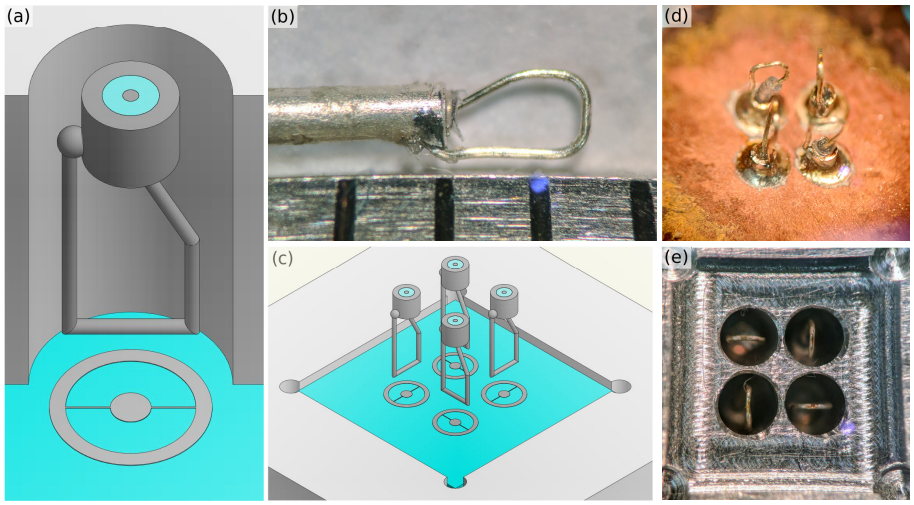

Figure 3.6: Four qubit holder with flux delivery. (a): CAD schematic of a flux bias line (FBL) and qubit with gradiometric SQUID loops. A cut of the sample holder is taken to reveal the FBL in the port. The FBL is constructed from a coaxial cable by forming the centre conductor into a loop and soldering the end to the outer jacket. (b): Optical image of an FBL, the markings on the ruler have a 1 mm spacing. (c): CAD image of the arrangement of the FBLs above device with four tunable qubits. The lid piece is removed from the model so that the FBLs are visible. The FBLs are arranged 90° rotated from neighbouring ports to improve flux selectivity. (d): Optical image of four FBLs, arranged as discussed and soldered to the copper piece. (e): Optical image of the chip-mounting slot, with the tops of the FBLs visible in each port.

Improved filtering must be used with FBLs to mitigate sources of flux noise as they do not have a natural filter like the external coil. Additionally FBLs can heat the chip where there are any resistive regions such as any bond contact (for this reason DC operation is usually avoided) and a lot of care must be taken with the current path and surrounding ground plane in order to achieve flux control selectivity. Lastly, it's worth mentioning that FBLs require design space on the chip and require a low resistivity DC contact (typically a wire-bond) to an external launch.

Flux control of gradiometric coaxial shaped circuits has already been demonstrated in [76] with an on-chip FBL. Here we seek to provide the same flux control in the coaxmon architecture. The challenge is to provide selective DC and AC flux control on a grid of gradiometric SQUIDs, within a superconducting sample holder and without compromising on the extensibility of the wiring scheme and port spacing. Additionally, we still wish to avoid wire-bonds and so DC connectivity to the chip is not viable. To meet all these

requirements, off-chip FBLs[1] were developed to provide both DC and AC flux through the gradiometric SQUID-loops, they are positioned vertically above the qubits and take the same footprint as the original drive ports. The FBLs were produced by shorting the centre conductor of UT-20 coax cable to its outer jacket to form a loop, such that when current flows through the part of the loop parallel to the device plane it will produce flux through the chip. Since the inductance of the loop is small enough it allows for fast AC driving, and since it is off-chip the heating of the device is mitigated when current is passed through the line and the line can be operated in DC as well. The sample holder for flux-tuning experiments was manufactured from a re-purposed 4-qubit holder, with the qubit control cables replaced with off-chip FBLs. In order to optimise for selectivity of flux delivery, the four flux lines were arranged in an alternating layout such that the loops of neighbouring lines were perpendicular to one another. Up to four qubit flux-tunable devices could be mounted and measured with this holder. For details of the simulation and operation of this sample holder, see Chapter 7.

[1]Other designs for off-chip FBLs have been the subject of recent works [90].

Chapter 4

Fabrication of Devices

In this chapter we present the design and processes used to fabricate devices in this thesis. We first present the circuit designs and how specific parameters were targeted. We then give an overview of considerations to enable double-sided fabrication, as well as optimisations made in order to produce high coherence devices with predictable and precise static frequencies. Achieving precision in setting the frequencies of qubits requires accurate and consistent fabrication of Josephson junctions, and the final section of this chapter will discuss tests and optimisations of junctions to reduce the frequency spread of fabricated devices.

4.1 Circuit Design

In this section we present the lithography patterns of both the LC resonators and coaxial transmons, and explain how the target parameters of each device are tuned. The LC resonator (shown in Fig. 4.1(a)) consists of a concentric pad and ring, connected by a geometric inductor that follows the path of an archimedian spiral. The geometry of the pads is fixed according to the dimensions shown in order to set the capacitance across the inductor, and so the resonance frequency $\omega_r = (LC)^{-1/2}$ is set by adjusting the length of the spiral inductor. The geometric inductance of the spiral is given by [91]

$$L(l, w, t) = 2l \left(\ln \left(\frac{2l}{w+t} \right) + 0.5 + 0.2235 \left(\frac{2+t}{l} \right) \right) \times 10^{-7}\,\mathrm{H}, \tag{4.1}$$

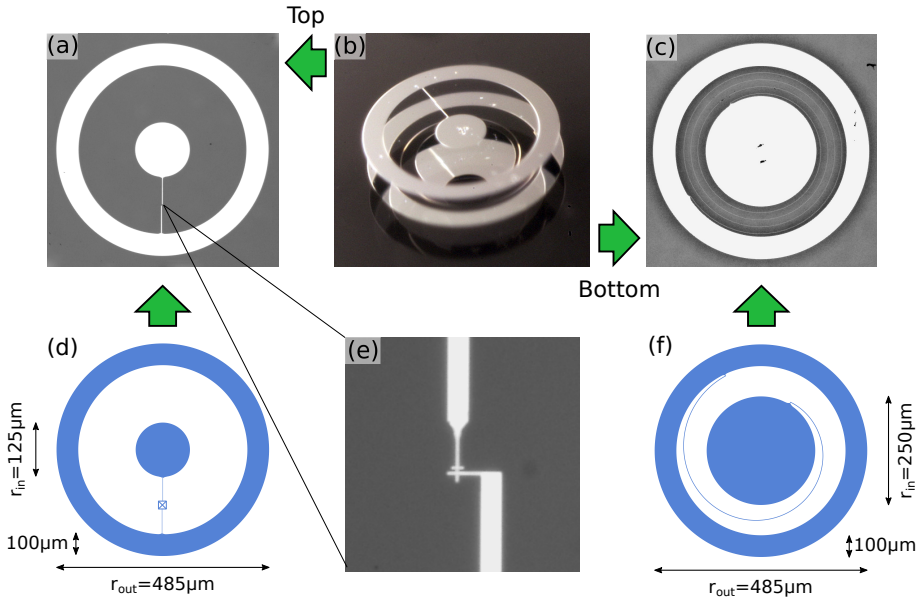

Figure 4.1: Design and layout of a unit cell. Optical images of fabricated circuits are shown in (a) and (c). (b): A qubit-resonator unit cell, with transmon on the top side of the clear sapphire substrate and the LC circuit on the bottom side. (d): Lithography pattern of a coaxial transmon. The Josephson junction is replaced with its circuit symbol so that it can be identified at this scale. (e): Optical image of the Josephson junction in (a). (f): Lithography pattern of an LC resonator.

where l, $w = 3$ μm, $t = 80$ nm are the spiral length and width, and film thickness respectively. The thickness t is chosen to be sufficiently large such that the kinetic inductance of the inductor does not contribute significantly to the overall inductance ($< 1\%$). This formula can be used to approximately set the LC frequency, however in practice it was found that a full finite element simulation was required in order to accurately model how the resonator frequency varies with inductor length to within 100 MHz. It is important to perform the simulation of the circuits within an accurate model of the sample holder as the capacitances of each metal island to ground will modify the effective capacitance across the inductor.

The coaxial transmon circuit is designed similarly with a concentric ring and pad connected by a single Josephson junction. In our designs, we generally fix the dimensions of the outer ring, and adjust the radius of the inner circuit to fine tune the capacitance C_Σ shunting the Josephson junction, and hence the anharmonicity of the transmon. Just as in the case of the resonator, when obtaining C_Σ from a finite element simulation it is important to enclose the device within a model of the sample holder to account for ground

capacitances. Then given a value of C_Σ, the frequency of the qubit is determined by the Josephson inductance by fabricating the junction with a target resistance as explained in Subsec. 4.4.2. Two transmons are coupled capacitively by way of extrusions of the outer ring that extend towards the target circuit as shown in 6.1, this is discussed further in Sec. 6.1.

4.2 Double-Sided Fabrication

To accommodate fabricating circuits on both sides of the substrate, the procedures involved require measures to protect prefabricated circuits on the backside of the chip, as well as to mitigate contamination and damage of the backside substrate. In fact no extra significant fabrication steps are needed to achieve this, and the measures outlined below were found to be robust to damage and contamination.

Protection layers of resist

In order to protect the backside of the substrate during the fabrication process, as a first step during spin-coating the backside was spun with a protection layer of resist. For photolithography this was a single layer of AZ1505 and for electron-beam lithography a single layer of copolymer, both spun with the same parameters used for applying them to the main resist stack. The ≈ 500 nm layer was found to be sufficient in protecting the backside from scratches and damage, and is removed during the liftoff procedure along with any accumulated contamination. A complication this can add is affecting the flatness of the chip during e-beam lithography (which affects the beam focus), however as long as care was taken not too apply too much resist solution during spin-coating, this was never found to be a significant factor.

Chip holders and surfaces

Measures were taken to prevent the backside of the substrate making contact with any surfaces during fabrication, particularly considering the substrate cleaning and liftoff processes where there is no protective layer of resist. To that end, several pieces were man-

ufactured to hold the chips so that only the edges of the backside surface rested on the pieces and any important areas were suspended freely. For device storage and chemical processing, several PTFE holders were designed as shown in Fig. 4.2. As for electron-beam lithography, aluminium holders were used to ensure a conducting container, however these pieces were later abandoned as the protection layer was found to be sufficient. Lastly for transient processes (N_2 blow-drying, inspection under the microscope, baking on a hot-plate), ordinary brass M4 washers were used as surfaces to rest the chip on.

Top-bottom alignment of circuits

To correctly align circuits on the top and bottom of the chip, global alignment markers were put down on either side of the substrate to ensure alignment of circuits to within 1 μm. Correct alignment of the markers was achieved by using both the top and bottom optics available in the EVG620 mask aligner. The markers on the qubit side were made from gold such that they could also be used for alignment during electron-beam lithography.

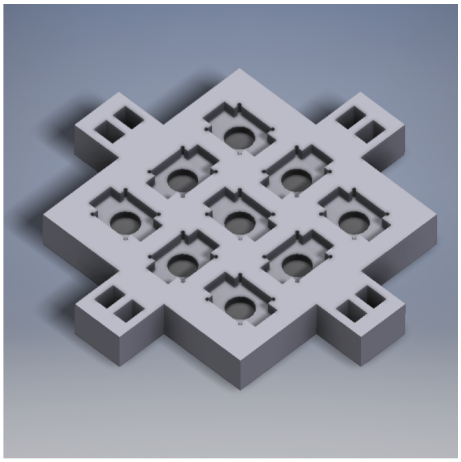

Figure 4.2: CAD image of a piece used to hold nine 5 mm chips inside a beaker whilst keeping the bottom faces protected. The part itself is made from PTFE.

4.3 Fabrication Processes

In this section we outline the key procedures used for device fabrication, and highlight considerations made when designing this process. For a more detailed explanation of how

each procedure works (such as electron-beam lithography and metal evaporation), see Chapter 5 of [87]. Device fabrication in this project consists of two lithography steps, one photolithography step to define the LC resonators, and one electron-beam lithography step to define the transmons. Naturally the main recipe used to create devices evolved continuously throughout this project, as we aimed to make optimizations to improve both device throughput, junction statistics and qubit lifetimes. The considerations reported here, and the recipe outlined in Appendix A were used to create the four-qubit devices measured in this project.

4.3.1 Photolithography

A photolithography process, developed by a member of the group Shuxiang Cao, is used to define the LC resonators as well as alignment marks on both sides of the substrate. It is a liftoff process with a two-layer resist stack of PMGI and AZ1505 photoresist (in order to create an undercut to improve liftoff). Fabricating the LC resonators this way has two advantages. First, it allows for a whole wafer of chips with resonators to be batch produced, and secondly we can take advantage of the top and bottom optics in the mask aligner to align markers on the qubit side of the wafer to markers on the resonator side, and thus align the qubit circuits to the resonators on the opposite side of the chip when it comes to defining them with e-beam lithography. After this procedure is completed, protection layers are spun on either side of the wafer which is then diced into 5×5 mm chips.

4.3.2 Substrate and surface cleaning

In general, the participation of the qubit mode's electric field with lossy material will lead to energy decay of the qubit, and so we wish to remove to unwanted dielectric material such as resist residues to avoid such events. First considering the substrate material itself, we use sapphire (Al_2O_3) due to its low dielectric loss tangent. To clean the substrate surfaces of organic matter and protection layers of resist, three steps of sonication in Acetone are used to remove the majority of the residue, followed by a soak in dimethyl-

sulfoxide (DMSO) which much more effectively strips the substrate of remaining residues. Any residual organic contaminants on the sample surface at this stage will have negative consequences on later steps, including poor spinning of resist, and thin residues under metal layers reducing circuit internal quality factors.

4.3.3 Spin-Coating of Resist

The resist stack for junction devices consists of (from bottom to top) copolymer (AR-P 617.08), PMMA950k (AR-P 672.045) and Electra92 (AR-PC 5090). The Electra is a conducting polymer that provides a conducting surface layer on the insulating sapphire chip to avoid charge accumulation during e-beam lithography. The copolymer and PMMA together will define the mask for fabricating the device. Since copolymer is much more sensitive than PMMA to the primary, secondary and backscattered electrons from the e-beam, it can be exposed to effectively "undercut" the PMMA layer and create free-standing "Dolan Bridges" with widths on the order of 100 nm. The copolymer is spun with settings that achieve a comparably large thickness (600 nm) compared to the PMMA (250 nm), in order to increase the height of the free-standing bridge (and thus increase the range of possible junction sizes).

4.3.4 Electron-beam Lithography

An JEOL JBX-5500 series ZC (50 kV) electron-beam lithography (EBL) system was used to write the devices in this thesis. Both the Josephson junction, and the qubit capacitor pads were written in the same ebeam step. The junction is created using the standard Dolan bridge technique [92], with a "cross-T" pattern whose form is shown in Fig. 4.3. Two different doses are used, a primary dose of 700 μC/cm^2 to expose both the PMMA and copolymer layer, and a lower dose of 160 μC/cm^2 to expose only the copolymer and create undercut areas below the PMMA layer. These undercut areas prevent metal build-up during steep-angled shadow evaporation which can make liftoff more difficult.

Similarly, the capacitor pads were written with the same primary dose of 700 μC/cm^2.[1] To save time, the capacitor pads are written with a 1000 μm writefield and a large aperture providing 10 nA current (Aperture 3 on this system). The junctions however are written with a 100 μm writefield and a 0.1 nA current (Aperture 1) to achieve sufficient resolution for defining multi-qubit devices. It goes without saying that an accurate an calibration is critical for achieving the necessary feature precision and avoid writing artefacts such as stitching errors. It is worth mentioning that due to the limitations of the system hardware and software used in this project, achieving the correct focus for features required extra consideration. In particular the lack of an appropriate cassette for 5×5 mm chips meant that the chip surface was usually not sufficiently flat (such that the range of heights of the chip exceeded the depth of focus of the electron-beam), and there was no ability perform automatic focal-plane adjustments. To accommodate this, focus values obtained from burning contamination dots were found at each corner of the chip, and a plane of focus was defined to manually calculate the appropriate focus at the location of written junctions.

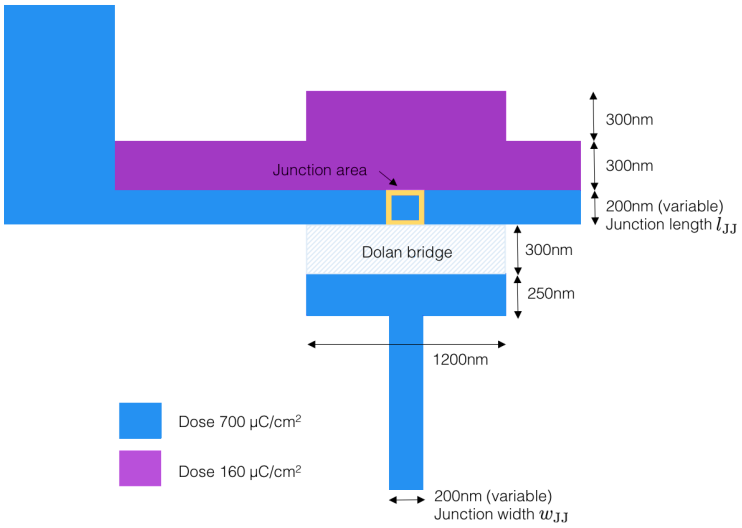

Figure 4.3: Lithography pattern for a Josephson junction. Writing this pattern with the appropriate doses in an e-beam lithography (EBL) system will form a Dolan bridge, which provides the mask for making Josephson junction via shadow angle evaporation. Key dimensions are shown, and the two dimensions labelled the Junction width w_{JJ} and Junction Length l_{JJ} can be varied to modify the resulting area of the Josephson junction.

[1] It is advisable to check that the value of the doses are still appropriate every few months as many aspects of the fabrication process can drift over time.

4.3.5 Development

A very conventional development process is carried out to remove exposed resist, whereby the electra is first removed with Di water, before developing the resist in a 1:3 mixture of MIBK:IPA, and a rinse in IPA only. The processing is carried out in a hot bath at 25°C in order to keep the development as consistent as possible, as the temperature of the developer will change the development rate. For a good development, the procedure should be carried out as close to exposure possible (higher junction resistance spreads and failure rates are observed after a few days). The developed free-standing bridges are robust and can be left after development for weeks without any degradation of the structure.

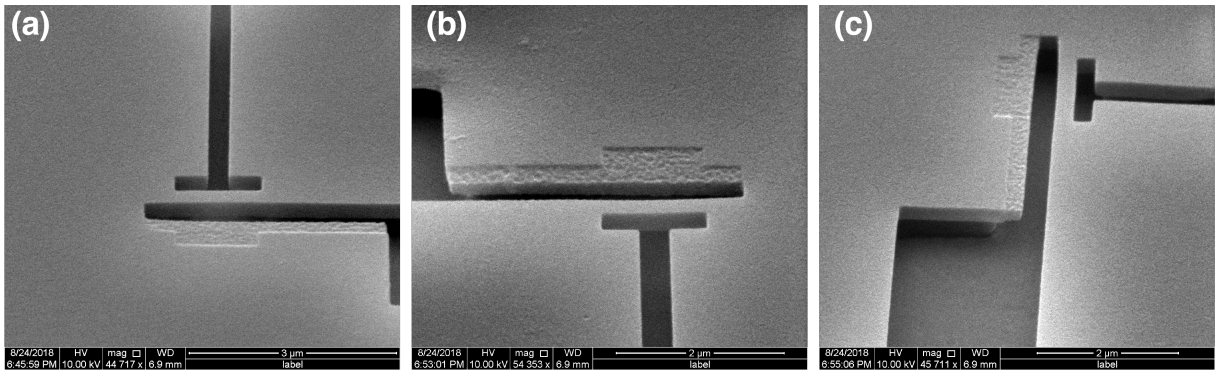

Figure 4.4: SEM images of the fabrication of a Josephson junction after development, revealing the form of the Dolan bridge as well as the intentionally undercut areas.

4.3.6 Descumming

Development is not a clean process, and typically leaves some amount of resist residue on the substrate surface that is to be metallised. To remove these residues a descumming procedure is necessary after development. In this project this was achieved with a short O_2 plasma ash in a PT7160 RF plasma barrel etcher. Informed by previous works [93, 94] different etch powers and times were used to create devices. Four-qubit devices were descummed using a power of 40 W for 20 s at an O_2 pressure of 0.5 mbar. These values were set to achieve a sufficient etch rate based on qualitative SEM images (Fig. 4.5) such that residue levels are visibly reduced and the structure of the junction is not affected. In future it would be beneficial to optimise this analysis through a quantitative study

of the remaining residues, possibly utilising atomic-force-microscopy (AFM) to map the topography of the developed region. This procedure was found to be vital in improving T_1 times (from $\mathcal{O}(1\ \mu s) \rightarrow \mathcal{O}(10\ \mu s)$) and junction resistance statistics (see Subsec. 4.4.2), and was carried out just before loading the chip into the evaporator.

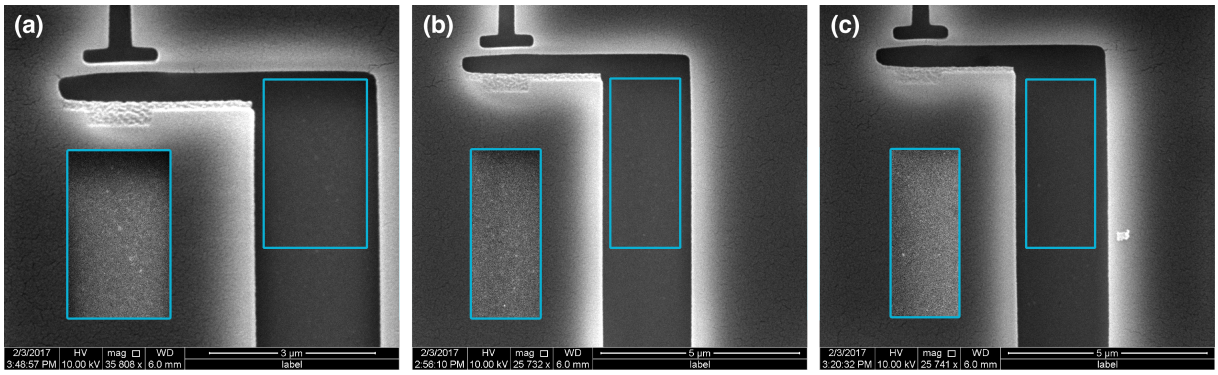

Figure 4.5: SEM images of the fabrication of a Josephson junction after development with (a): no O_2 plasma ash, (b): plasma ash at 40 W for 67 s, (c): plasma ash at 10 W for 207 s. The areas within the blue rectangles are duplicated with a higher contrast in order to make remaining residues in the developed regions more visible, with residue levels appearing reduced for junctions with an etch.

4.3.7 Metal Deposition

Metallisation of the chip surface is carried out by shadow evaporation in a home built electron beam evaporator. First 60 nm of aluminium (Al) is evaporated at 60° to the chip surface normal, then the Al is oxidised in an environment of 15/85% oxygen/argon, at a set pressure and time to achieve a target oxide-thickness (and thus junction resistance). The chamber is then pumped back to base pressure and a second 70 nm Al layer is deposited at 0° to the surface normal, before another oxidation step to "cap-off" the exposed Al with an aluminium oxide layer grown in controlled conditions. The result of this process is a Josephson junction with the top and bottom layers of Al as the electrodes. The base pressure of the evaporation chamber was $\approx 2 \times 10^{-7}$ mbar, however to improve the environment of the chamber during evaporation (in particular to reduce the levels of water, which is a catalyst for the oxidation reaction) a titanium pump was carried out before the first evaporation. This involves evaporating a small amount of titanium into the chamber (not on the chip), which then binds with water molecules in the environment

before sticking to the chamber walls. A residual gas analyser was used to determine that this lowers the water pressure from 2×10^{-7} mbar to order 10^{-8} mbar for the duration of an evaporation.

4.3.8 Liftoff

Liftoff of the residual resist and Al film was carried out in warm acetone. Since the soak in acetone doesn't remove all resist, the device is then rinsed with IPA before sitting in warm DMSO to clean the chip of remaining residues. This extra cleaning step is very important as the acetone soak alone is not enough to remove all the resist (see Fig. 4.6), and residues can lead to poor T_1 times and a higher rate of junction failures. A further potential issue in liftoff is that any metal that connects from the top of the resist to metal attached to the substrate will be very difficult to remove, and will lead to poor liftoff where structures still remain or tear. This can happen if an incorrect dose is used, or an insufficiently big undercut box is written, so care must be taken to determine these values correctly.

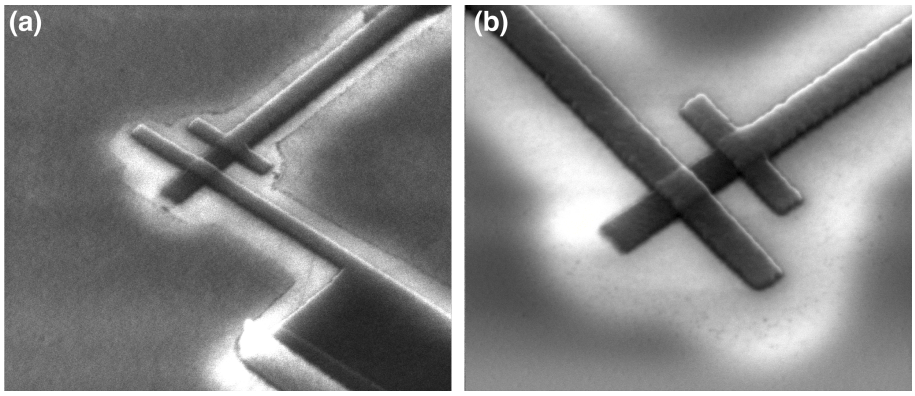

Figure 4.6: SEM of fabricated Josephson junctions after liftoff. (a): No post-clean has been performed, and a shadow or residue can be seen around the perimeter of the fabricated features. (b): A post clean in 60°C DMSO was carried out, and no residue shadow is observed.

4.4 Room Temperature Junction Characterisation

Production of Josephson junctions with accurate and consistent target resistances is crucial to fabricating devices with an acceptable rate of success. Since the value of E_C more

or less sets the transmon anharmonicity, we instead set the qubit frequency by tuning E_J by way of the junction resistance. The normal resistance of an Al-AlO_2-Al Josephson junction R_n is related to the junction critical current by the Ambegaokar-Barato relation [95]

$$I_c = \frac{\pi \Delta(0) k_B T_c}{2 q_e R_n} \tag{4.2}$$

where $\Delta(0) = 1.76$ J is the superconducting energy gap at $T = 0$ K, and $T_c = 1.26$ K is the critical temperature of the superconducting Al. We can relate this to a frequency by converting to the Josephson energy $E_J = \frac{\Phi_0 I_c}{2\pi}$ and using Eq. (2.19) to calculate ω_{01}. A value of $C_\Sigma = 68.7$ fF is used to determine E_C. This value was obtained from the calculated mean of measures of E_C experimentally determined from 6 different qubits with identical geometries. There are two ways of setting the junction resistance through fabrication, modifying the junction thickness (through the oxidation step during evaporation), or modifying the junction dimensions to set the area of the junction. When fabricating a device with multiple junctions of different resistances, it is necessary to change the lithographically defined junction dimensions since all the junctions will undergo the same oxidation. In this section we briefly outline measurement and analysis of junction resistances and spreads. We first present a discussion of how junction resistance spread affects device yield, before showing results of junction target resistances and spreads across multi-junction test chips.

4.4.1 Resistance Spread and Device Yield

Specific gate implementations and circuit connectivity of multi-qubit devices will place constraints on the target and acceptable deviations of qubit frequencies. In this project, we aimed to build a linear chain of up to 4 fixed frequency qubits, with fixed static couplings. In order to perform 2-qubit gates via cross-resonance [63, 64] with sufficient fidelity, the detuning between coupled qubits must lie within a certain range. In this case we targeted detunings of 500 MHz with an acceptable tolerance of 400 MHz $<$ x $<$ 700 MHz, any larger cross-resonance will be driven too slowly, and any smaller and the collision between the f_{12}^1 and f_{01}^2 will lead to a larger value of the unwanted $\hat{ZZ}$ term (see Sec. 6.1 for a

more detailed explanation).

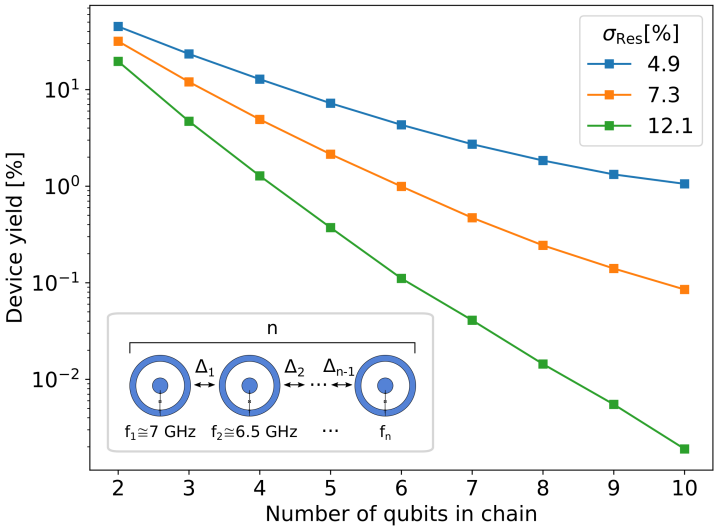

Figure 4.7: Results from a statistical simulation of the probability of success of fabrication of a linear chain of n qubits with highest frequency 7 GHz given a resistance spread σ_{res} (a depiction of this model is shown in the inset). Success is defined as all detunings between neighbouring qubits being within the band 400 MHz $<$ x $<$ 700 MHz. The simulation is carried out with values of σ_{res} of reported values from industrial efforts [96] = 4.9%, the average spread across all test chips fabricated in this thesis using the optimised fabrication procedure = 7.3%, and the average spread of test chips without the fabrication optimisations = 12.1%.

Fig. 4.7 shows the results of a statistical simulation of the success rates, with success defined according to the conditions above, of producing a linear chain of n qubits with highest frequency 7 GHz for different uncertainties of the junction resistance (resistance spread σ_{res}). Gaussian probability distributions are assumed for each junction resistance, centred on the resistances corresponding to each target frequency. The device yield falls sharply with the number of qubits, as one expects, with a predicted yield of 5% for a four-qubit chain with a standard deviation of 7.3%. At our level of fabrication, this is an acceptable figure, however a reduced resistance spread or higher fabrication output is necessary to reach acceptable yields for circuits with larger numbers of qubits. It is worth noting that this model doesn't scale no matter how good the resistance spreads are, and motivates the investigation of modularity in devices with large numbers of qubits. This analysis is idealised and doesn't take into account any other sources of error, such as uncertainties in the qubit coupling, charging energy and oxidation level, however it is

the resistance spread that dominates the determination of the frequency detunings which is why it is given the most attention here.

4.4.2 Measurements of Resistance Spread

It is necessary to find the correct oxidation parameters, and junction dimensions, in order to make junctions with the correct resistances for each target frequency. This is achieved by measuring the resistances of multiple test-junction chips to find an acceptable level oxidation, and the appropriate junction sizes to use given this oxidation that produce the target resistances.

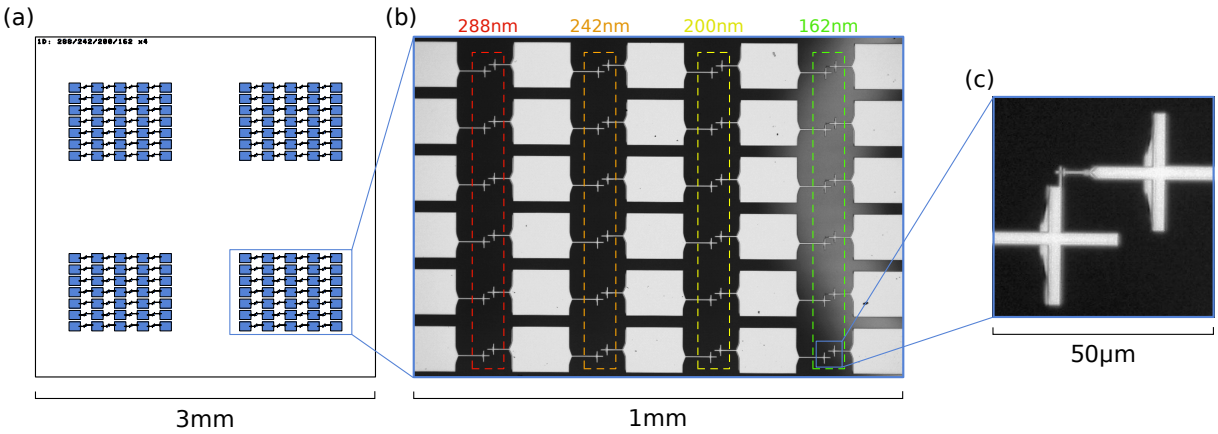

Figure 4.8: (a): GDS pattern for a device with test junctions, identical copies of each array of test junctions are placed at the locations of each qubit in a four qubit device. Each array consists of 4 columns and 7 rows of junctions, so each test chip contains 112 junctions each. (b): An optical image of an array of test junctions. The w_{JJ} dimension of the Josephson junctions in each column is varied to target the set of resistances corresponding to those of a four qubit device with the targeted detunings between qubits. l_{JJ} for all junctions is set at 200 nm. (c): An optical image of a Josephson junction.

Fig. 4.8 Shows an example of a chip with test-junctions. A block of junctions is patterned at four different locations on the chip, corresponding to the locations of qubits on a four-qubit device. Within each block are four different sizes of junction arranged in columns, with seven copies of each junction to obtain a measure of the resistance deviation. Contact pads for the DC probes are put down so that each junction can be measured independently. The motivation for spreading the different junctions sizes across the chip rather than devoting each block to one junction size is to give us the ability to

distinguish between random variation of the resistances, and drifts of mean resistances across the device plane due to the chip not being flat during e-beam.

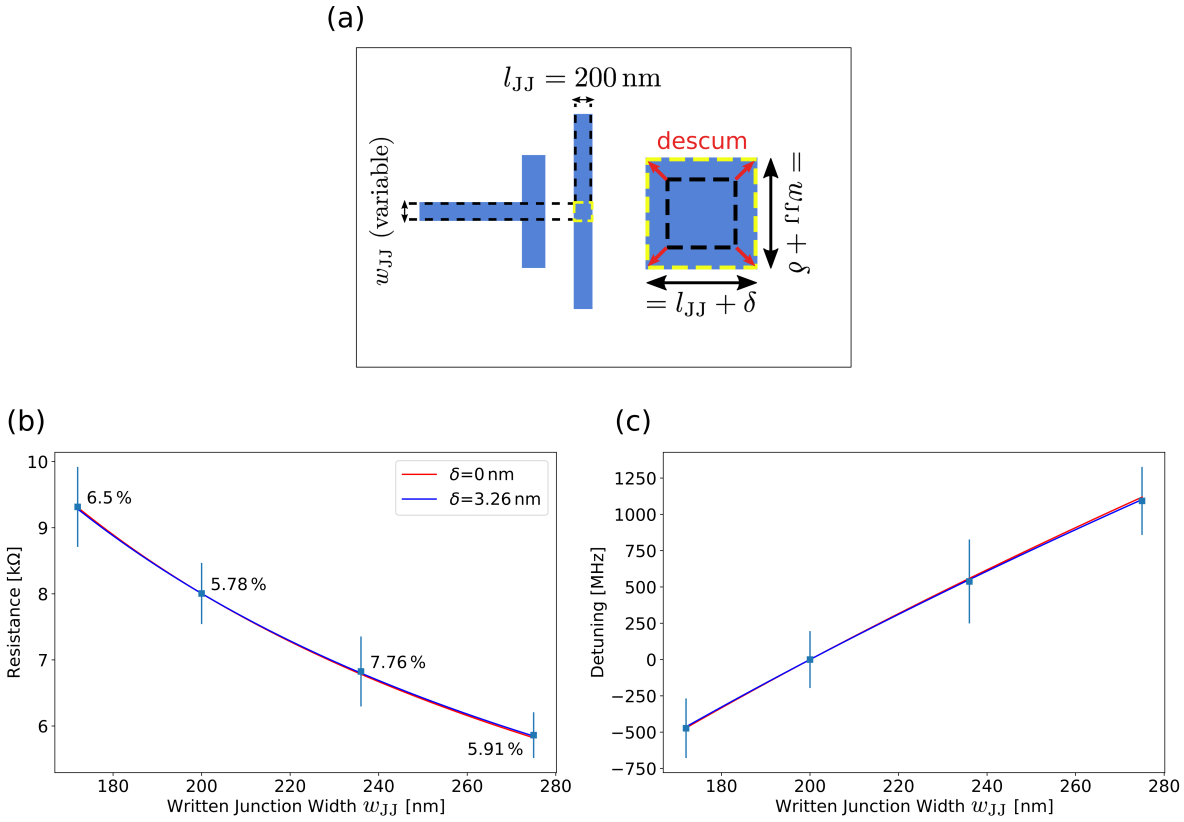

Figure 4.9: Measurements of resistance spread. (a): Depiction of the simple model of the expanding junction area. The area of the Josephson junction (highlighted with a yellow dashed line) is lithographically defined by the dimensions l_{JJ} and w_{JJ} labelled in the figure. A precise writing of these features would result in an area with those exact dimensions, represented by the black dashed line, however in the model we consider the elongation of both dimensions by an equal amount δ as a result the descumming procedure, which etches resist isotropically. (b): Measured resistances versus w_{JJ} for an individual test chip. The error bars are the standard deviation of the set of measured values for that junction size, and the point annotations are the deviations in percent. Solid lines are theory plots of the resistance model presented in the main text, with the red line not considering any expansion offset δ and the blue line with a value of δ obtained from a fit. (c): The same data in (b) is converted into a frequency as explained in the main text, and the detuning from the reference junction (i.e. the junction with w_{JJ}) 200 nm is calculated. Error bars are upper and lower bounds converted from the spread in resistance values.

Fig. 4.9 shows the the measured resistances of such a chip, with an average resistance deviation of 6.5% in this case. In order to model how junction size relates to resistance, the resistances are fitted to the model $R = R_{\mathrm{ref}} \frac{(l_{\mathrm{ref}}+\delta)(w_{\mathrm{ref}}+\delta)}{(l_{JJ}+\delta)(w_{JJ}+\delta)}$. Here l_{ref}, w_{ref} are a reference junction length and width (chosen to both be 200 nm in this case) to compare the other

junctions with dimensions l_{JJ} and w_{JJ} to, R_{ref} is the measured resistance of the junction with the reference dimensions, and δ approximately corrects for increases to the dimensions as a result of the descumming procedure. A good agreement is observed to the model that accounts for an increase in junctions dimensions by 3.26 nm in this case. The resistance values are then converted into their respective frequencies, and the detunings from the frequency of the reference junction are plotted. In this instance we achieve the targeted detuning of 500 MHz between pairs, however the overlap of the error bars even for the junction spread of 6.5% seen here indicates the challenge of meeting frequency targets.

Whilst the fitted resistance curve is used to adjust the junction sizes so as to set the mean values of the resistances, the standard deviation of the resistances depends on the precision of fabrication. In this project, two additional considerations were found to make the most significant improvements to the resistance spread, namely the inclusion of a 40 W, 20 s O_2 plasma ash descum post-development, and the use of the finest aperture when defining features with EBL. From a fabrication round of several test-chips, the average value of the junction resistance spread across 7 test-chips prepared with a descum and finer aperture was 7.3%. This compares to the average value across two test-chips without the descum and a lower resolution aperture of 12.1%. We evaluate the effectiveness of the descumming procedure by comparing the value of 7.3% to the mean spread of junctions on a test chip prepared identically except without a descum, in which we found a value of 9.6%. The other key improvement was to switch from using a larger aperture in the e-beam (Aperture 2) to the finest aperture (Aperture 1), with the intent being to make use of the finer resolution and precision this allows. The average resistance spread across two test-chips written with Aperture 2 was 9.1%. It is worth mentioning that to achieve a consistent write across the chip when using the finer beam aperture, one must account for the much smaller depth of field it has (as the focus of the beam is more sensitive to changes in the sample height). If the chip surface is not level there will be a difference in the focus on different parts of the device plane, and this will result in junctions sizes (and resistances) having a uniform drift over the chip surface. Mitigating

this can be achieved by ensuring the chip is as flat as possible, and by calculating the plane of focus to correct the beam focus value as it writes across an uneven chip surface.

	descum	No descum
Aperture 1	7.3%	9.6%
Aperture 2	9.1%	12.1%

Table 4.1: Values of the average resistance deviation σ_{res} obtained from measurements of junction resistances across many test-chips. The descumming procedure was a 40 W 20s O_2 plasma ash post-development. The Aperture refers to the finer (Ap.1) and larger (Ap.2) beam apertures of the EBL system which have higher and lower resolutions respectively.

4.4.3 Junction Ageing

The resistance of Josephson junctions has been found to increase over time after fabrication, according to an empirical power law that saturates after a few days [97]. This increase in resistance is known as "ageing" and while its cause is not fully understood, a correlation between higher levels of ageing and a lack of junction descumming has been observed [93], and has been attributed to organic residues contaminating the junction barrier. Thus there are two reasons to reduce ageing, the first to prevent drifting of measured resistances in case they deviate from the already obtained target values, and the second to confirm the reduction of residues present in the device that may limit T_1. Fig. 4.10 shows the measured ageing of junctions on a test chip prepared with a plasma ash with power 40 W for 20s. Each set of junctions with different sizes ages by approximately 20% over the course of 10 days. In general devices produced with aperture 1 and a plasma ash with power 40 W for 20 s had a typical ageing of 15% compared to devices without any descum which had an ageing of 94%. The comparatively higher average ageing of the non-descummed junctions indicates that resist residues contribute significantly to the ageing process and that ageing can be used as a metric of the cleanliness of the junction after

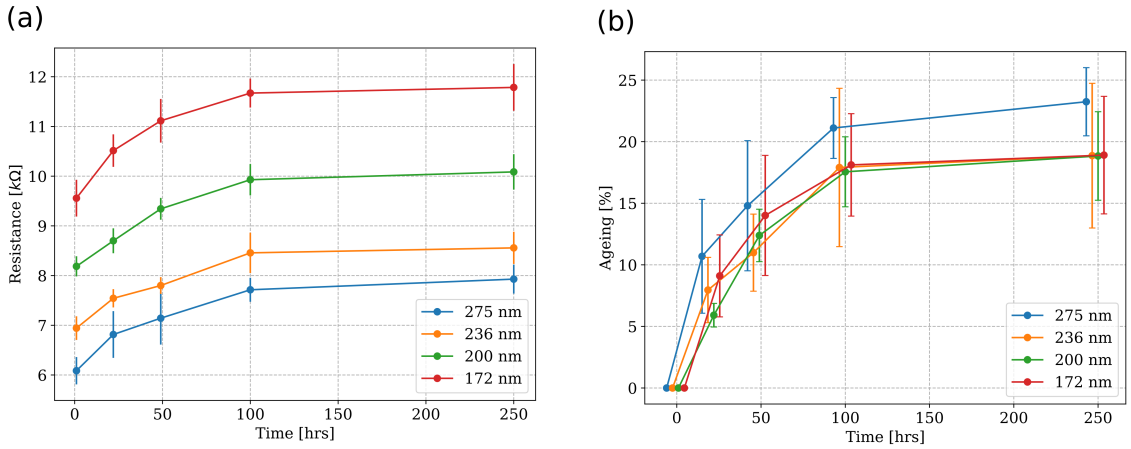

Figure 4.10: Measured ageing of a subset of 7 junctions for each junction size on one test chip across the span of 10 days. (a): Measured resistance over time, organised by written junction size. Points are connected for clarity and error bars are the measured resistance spreads. The ageing has mostly saturated over the course of this time. (b): Calculated ageing of of the same junction resistances in (b) over time. Points are slightly offset on the x-axis for clarity.

fabrication.[2] To help reduce drift over time due to ageing, the junctions can be pre-aged. This is achieved by gently heating the junction on a hotplate at ≈ 100°C for 2 min, which accelerates the ageing process to the point of saturation. When using this technique one must be careful of the increase in junction resistance spread as not all junctions will age by the same amount. As seen in Fig. 4.10(b), the standard deviation of junction ageing on the test-chip in question is $\approx 5\%$, and the propagation of this uncertainty will increase junction resistance spread after such ageing. Hence we chose instead to mitigate ageing of real devices by storing samples in dry vacuum containers.

4.5 Future Improvements

There has been a great deal of work in the community on improving device fabrication to reduce sources of internal loss and improve device yield. Whilst the recipe used in this thesis was consistently capable of producing multi-qubit devices with T_1 of $\mathcal{O}(10\ \mu\text{s})$, there

[2] When calculating average ageing it is important to calculate the average of each junction's increase $\mathbb{E}((x_i^{\text{aged}} - x_i^{\text{init}})/x_i^{\text{init}})$ rather than the increase of the average resistances before and after ageing $(\mathbb{E}(x_i^{\text{aged}}) - \mathbb{E}(x_i^{\text{init}}))/\mathbb{E}(x_i^{\text{init}})$, as the latter is not the same, and will under-represent the correct value when the initial resistances are different.

are many potential modifications based on current literature that could be implemented. Improving qubit lifetimes (and so the upper bound on coherence) can be achieved by reducing the internal loss of the circuits. Switching from a liftoff process to an etch process for defining the qubit capacitor pads has been found to improve internal quality factors [98], and additionally the capacitor pads can be made of a material with higher T_C than aluminium, such as titanium-nitride, to reduce quasiparticle loss [99]. Since the Josephson junction itself must still be made with a liftoff process, both these processes require a well calibrated argon milling of the device before an evaporation in order to establish a good electrical connection between the pads and junction [100]. Additionally we could investigate a UV ozone descum that would take place in the evaporation chamber right before metallisation, and has been found to reduce losses [98]. Annealing of the substrate surface has also been found to be beneficial [101] in ensuring an atomically flat substrate surface and removing surface carbon that might contaminate the circuits. We can also consider switching to a silicon substrate, using conventional substrate preparation through chemical cleans such as RCA to remove organic compounds and hydrogen-fluoride to remove the silicon oxide layer and passivate the surface [102, 103]. The advantage of silicon is that we can perform trenching of the substrate after circuit fabrication [104, 103] to reduce coupling of the circuit to dielectric material at interfaces. Generally, reducing the presence of dielectrics is one means of reducing internal losses. Another means is reducing the coupling of circuits to these dielectrics, investigation of the participation of the field of the circuits at various interfaces can be carried out and the circuit design adjusted accordingly to reduce the participation ratios[3] [105]. In order to obtain devices with the correct frequencies, we can increase device throughput by switching to wafer-scale fabrication. Additionally device yield is increased with reduced junction resistance spread, which can be improved from optimisations to the junction lithography, descumming, and metallisation.

[3]Even with all these measures, it is worth bearing in mind that fabrication improvements alone will not mitigate all sources of loss, and one still needs focus on reducing radiative and quasiparticle losses through modifications in the circuit design and experimental setup.

Chapter 5

Experimental Demonstration of a Single-Qubit Unit Cell

In this chapter we present the design and experimental validation of the fundamental unit cell of the coaxial architecture explored in this thesis. We begin by presenting the design and layout of a unit cell, comprised of a single qubit coupled to a resonator for readout. We then fully characterise the system Hamiltonian of a fabricated device with parameters that place it in the dispersive regime. We use spectroscopy to identify the resonator frequency, as well as the internal and external quality factors. We then perform spectroscopy of the qubit, including a technique employing two-spectroscopic tones to identify the single and multi-photon transition frequencies of transmon. We determine the dispersive shift using pulsed spectroscopy of the resonator, and use all the prior information to determine the resonator-qubit coupling. We perform measurements of the AC Stark shift and number splitting of the qubit transition frequency on two different devices, and show how either experiment is used to calibrate resonator drive power with mean photon number in the resonator. Lastly we demonstrate the coherence of a device with measurements of Rabi oscillations, as well as of energy relaxation and dephasing of the qubit state. Some of the results presented in this chapter have been previously reported in [62].

5.1 Unit Cell Design

The unit cell of the architecture demonstrated in this thesis is depicted in Fig. 5.1. It consists of a superconducting charge qubit in the transmon regime [69] with coaxial electrodes, which we call the coaxmon (similar in geometry to the concentric [76] and aperture [106] transmons) coupled to a lumped element LC microwave resonator fabricated on the opposite side of the chip. The device is controlled and measured via coaxial drive ports, perpendicular to the plane of the chip (see Fig. 5.1 (a)), whose distance from the chip can be modified to change the external quality factor of the circuits. These drive ports can be used for independent control of the qubit and measurement of the resonator in reflection, or to measure the device in transmission by applying a signal at the control port and measuring at the measurement port.

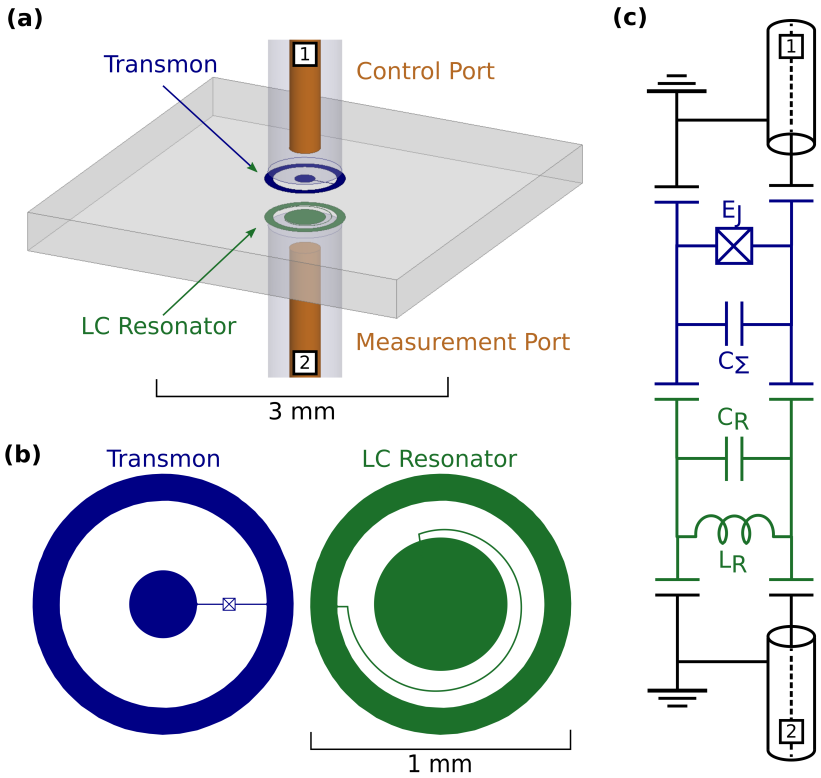

Figure 5.1: (a): CAD design of the unit cell, with transmon qubit and lumped element resonator on opposing sides of a substrate, and control and measurement ports perpendicular to the chip plane. (b): Designs of the transmon and resonator. In the transmon the two electrodes are connected by a single Josephson junction, whereas the electrodes of the resonator are connected by an inductor line. (c): Equivalent circuit of the device, showing the resonator inductance and capacitance, L_R and C_R, the junction Josephson energy E_J and effective capacitance over the junction C_Σ.

Fig. 5.1(c) shows an equivalent circuit of the device, (with capacitances between non-neighbouring voltage nodes omitted). Since the unit cell can be entirely represented with a lumped element model, key circuit parameters can be calculated with an electrostatic simulation. A Maxwell simulation of the device and its packaging produces a capacitance matrix that can be solved using the procedure in [65]. From this a simulated qubit-resonator coupling of $g/2\pi = 420$ MHz was found, which compares to the experimentally determined value of 418 MHz.

The target parameters of the device can be tuned by adjusting the circuit geometry. The transmon anharmonicity can be set by changing the radius of the transmon centre pad, thus altering C_Σ, and the frequency of the qubit is determined by the Josephson inductance (set with the junction resistance as explained in the previous chapter). The resonator frequency is determined by adjusting the length of the spiral inductor. The separation of the drive port centre pin and its corresponding circuit can be adjusted to set the value of, or an upper-bound on, the excitation decay rate of a circuit via that port. The resonator measurement port pin is set such that a target resonator photon-decay rate κ is achieved, and the separation of the transmon and control port pin is increased to a large enough value that T_1 is not limited through energy relaxation via this channel [88, 89]. It is necessary to simulate the circuits enclosed in a model of the sample holder to determine these target values since the ground capacitance provided by the enclosure plays a vital role in determining the circuit coupling as well as the effective capacitance between nodes. For more details of the circuit design see Sec. 4.1, and for the sample holder and wiring see Subsec. 3.2.1.

5.2 Characterising the Hamiltonian with Spectroscopy

The physics of a qubit coupled to a resonator, implemented with superconducting circuits, is described by circuit QED [42, 43] (as outlined in Sec. 2.2). When the detuning of the qubit transition frequency ω_{01} and resonator frequency ω_r is much larger than the qubit-resonator coupling g, the device is in the dispersive limit of circuit QED. In this section we use techniques in spectroscopy to characterise the system Hamiltonian of several single-

qubit devices with parameters such that they can be operated well into the dispersive regime. To fully characterise the system Hamiltonian of such devices, one need only extract the parameters ω_r, ω_{01}, and χ from the dispersive Jaynes-Cummings Hamiltonian

$$H_{\text{disp}} = \hbar(\omega_r + \chi\hat{Z})\hat{a}^\dagger\hat{a} + \frac{\hbar}{2}(\omega_{01} + \chi)\hat{Z} \tag{5.1}$$

where

$$\chi = \frac{g^2\alpha}{\Delta_0(\Delta_0 - \alpha)}, \tag{5.2}$$

recalling the qubit-resonator detuning $\Delta_0 = \omega_r - \omega_{01}$ and the transmon anharmonicity α. In addition to these Hamiltonian terms we wish to also determine the parameters of the quantized circuit system, namely the Josephson Energy E_J and the Charging Energy E_C, which relate to the Josephson Junction inductance and the effective shunting capacitance across it respectively. In order to check the validity that we are in the strong dispersive limit, it is also necessary to characterize the decay rates present in the system, namely the photon decay rate in the resonator κ and the excitation decay rate of the transmon T_1. The former is characterised in this section, however the latter requires time-resolved experiments and is characterised in the next section.

5.2.1 Resonator Frequency and Quality Factor

The most straightforward approach to characterizing the readout resonator of the system is to measure its transmission spectrum S_{21}. To achieve this, a continuous-wave microwave tone at f_{dr} is applied to the device from the control port, and the resulting transmitted amplitude at the analogue-to-digital converter (ADC), V_{ADC}, is read. Fig. 5.2(a) shows the resonator transmission spectrum at low probe drive power $P_r = -30$ dBm (such that we populate the resonator with a mean number of photons less than the critical photon number $\bar{n} < n_{crit}$ and avoid non-linear behaviour). Fitting the data to a root-Lorentzian curve

$$\left|\sqrt{S_{21}(f_{dr})}\right| = \left|\frac{a}{1 + 2iQ_L(f_{dr} - f_{r0})/f_{r0}}\right| + b \tag{5.3}$$

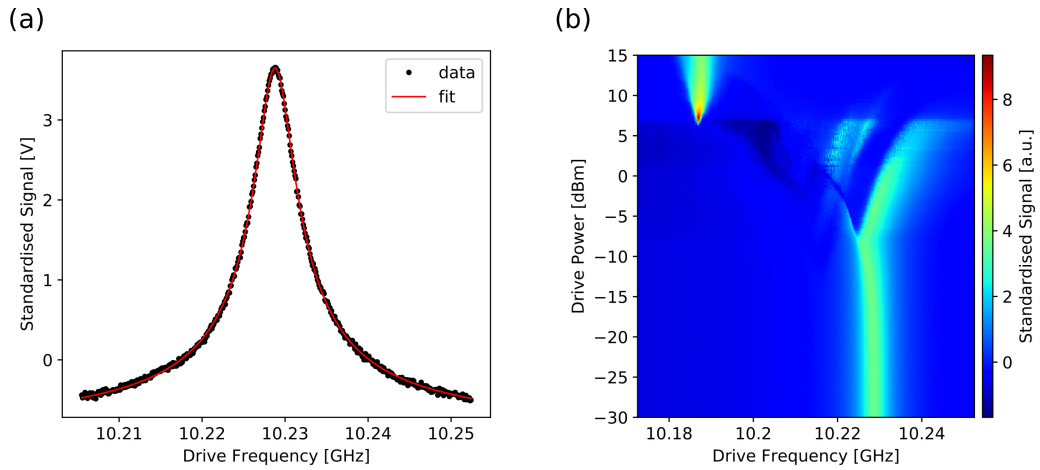

Figure 5.2: Continuous-wave (CW) resonator spectroscopy. (a): Transmitted signal amplitude at the ADC against the frequency of the applied tone at low power, −30 dBm. The root-Lorentzian response of the resonator is fitted to Eq. (5.3) to find $\omega_{r0}/2\pi = 10.229$ GHz and $\kappa = 4.8$ MHz. (b): Resonator spectroscopy for different drive powers of the spectroscopic tone, at high powers the uncoupled resonator frequency $\omega_C/2\pi = 10.19$ GHz is observed, and shifts to the dressed frequency f_{r0} as the drive power is lowered.

(where a and b are fit factors) allows us to extract the resonance frequency $\omega_{r0}/2\pi = f_{r0} = 10.229$ GHz and loaded quality factor $Q_L = 2145$. Both these values allow us to determine the photon decay rate of the resonator $\kappa = f_{r0}/Q_L = 4.8$ MHz. This rate determines the readout rate of the resonator, and it is necessary to optimize this value in order to obtain the largest rate without limiting the transmon T_1 through Purcell decay [88, 89].

We then perform resonator spectroscopy across a range of drive powers to reveal the shift from the resonator's ground-state frequency ω_{r0} back to the resonator bare frequency ω_C (the undressed frequency if the resonator was not coupled to the qubit), with increasing drive power [107, 108]. The same spectroscopy of the resonator is carried out as in Fig. 5.2(a), and the power of the spectroscopy drive is also swept as the second dimension. The results are shown in Fig. 5.2(b). Since the measured signal power increases with input power, the standardised signal is instead presented so that all traces can be compared across the same signal range. In this case $\omega_C/2\pi = 10.20$ GHz and a total power-dependent shift of 41 MHz is observed (note that this is not the same as the dispersive shift). The resonator responses in the intermediate power range are non-trivial

and multi-peaked, reflecting the rich physics in this regime that requires more generalised physical and numerical models to explain that are beyond the scope of this thesis. However it is worth noting that explorations of the system and the non-linearities that arise in these limits produce results that are relevant to the way these devices can be operated [109, 110].

At this point it is worth briefly clarifying the difference between ω_C, ω_r and ω_{r0}. ω_{r0} is the dressed frequency of the resonator when the transmon is in the ground state $|0\rangle$, and the resonator is weakly driven ($\bar{n} < n_C$) such that we are in the dispersive limit. $\omega_C = 1/\sqrt{LC}$ is the bare resonator frequency, and is the resonance we would find if the LC circuit was not coupled to the transmon. We are able to recover this frequency when driving the resonator at very high power (10 dBm) as the dispersive approximation breaks down and the dispersive couplings reduce to zero. Finally $\omega_r = \omega_{r0} + \chi$ (not to be confused with $\omega_{r1} = \omega_{r0} + 2\chi$) is the term that appears in the Hamiltonian Eq. (5.1). If the qubit were a true two-level system then it would be the case that $\omega_C = \omega_r$, however the transmon has many more than two levels, and so the dressing of the resonant frequency is more complex [42, 69].

It is necessary to also measure the reflection spectrum of the resonator S_{11} for two reasons, the first being that during actual operation of the device the resonator is probed in reflection via the measurement port and so determining the appropriate power for readout needs to be evaluated this way. The second reason, more relevant for the aims of this section, is that it is the only way to determine the external and internal quality factors Q_e and Q_i, relating to photon decay through the measurement port, and via internal losses respectively. In principle this is also possible in transmission if the insertion loss (the signal attenuation all the way down to the port) is very well calibrated however this is difficult to determine with sufficient accuracy.

Fig. 5.3 shows the magnitude and phase of the S_{11} spectrum of the resonator. The real (I) and imaginary (Q) parts of the spectrum signal can be plotted in the complex

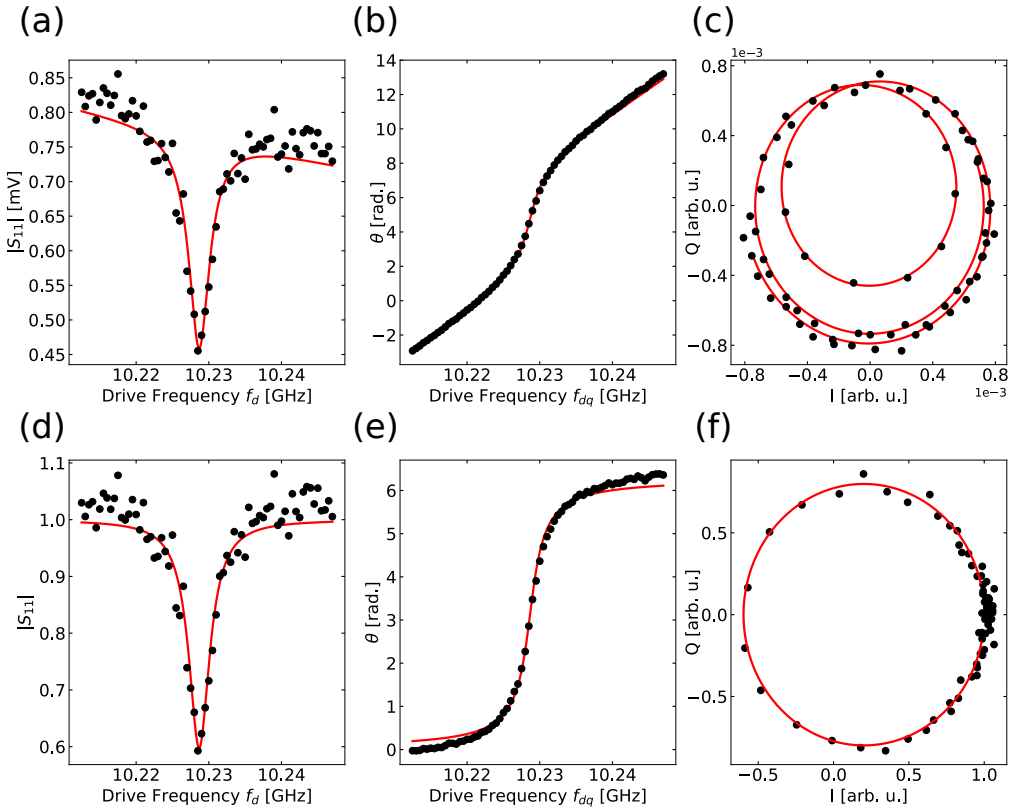

Figure 5.3: Spectroscopy of the resonator in reflection, (a)-(c) show the magnitude, phase and complex plot respectively of the same measured signal. Solid lines are corresponding projections of a fit of the data to Eq. (5.4). (d)-(f) show the same data only divided by the fitted line response terms in Eq. (5.4) to highlight the response of the resonator.

plane and are fitted to the model

$$S_{11}(f_{dr}) = \left(c_0 + c_1\left(\frac{f_{dr}-f_{r0}}{f_{r0}}\right)\right) e^{i\left(c_2+c_3\left(\frac{f_{dr}-f_{r0}}{f_{r0}}\right)\right)} \left(1+\left(\frac{-p_0}{1-2iQ_L\left(\frac{f_{dr}-f_{r0}}{f_{r0}}\right)}\right)\right). \tag{5.4}$$

This model is derived following the methods in [111, 112] for the response of a a 1-port system. Here c_0, c_1, c_2, c_3, are cable coefficients to account for the zero and first order effects of the lines on the magnitude and phase of the signal respectively, Q_L is the loaded quality factor, and p_0 is the maximum change in magnitude from the baseline. Q_i is found from $Q_i = Q_L(1+\kappa_{cc})$ where $\kappa_{cc} = p_0/(1-p_0)$ is the coupling coefficient of line to resonator. Q_e then accounts for the remaining losses and can be obtained from the inverse sum $1/Q_L = 1/Q_e + 1/Q_i$. In the end the fit allows us to extract the parameters $\omega_{r0}/2\pi = 10.23$ GHz, $Q_e = 3230$ and $Q_i = 12800$. A robust routine to fit the reflected spectrum was developed by Peter Spring and Matthias Mergenthaler and is used to fit

the data in Fig. 5.3.

In order to achieve efficient qubit readout, we require $Q_e \ll Q_i$ (i.e. that the majority of readout photons are captured by the readout port). This practically achieved by setting the measurement port coupling to the resonator to fix the value of Q_e and mitigating intrinsic losses in the resonator through the reduction of dielectric residues and sources of quasiparticles to increase Q_i. Typical internal quality factors for our coaxial resonators are $\mathcal{O}(10^5)$, and so we set $Q_e \approx 10^4$, both to achieve efficient readout but also to set the readout rate κ to be sufficiently high without significantly reducing T_1 through Purcell loss [88, 89]. Optimising readout in circuit QED requires further consideration, and is the subject of works such as [113, 114, 115, 116].

5.2.2 Qubit Frequency and Anharmonicity

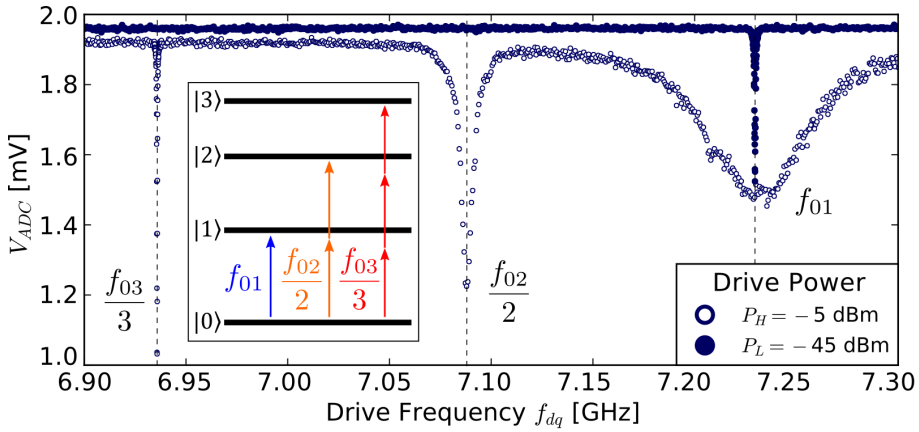

Figure 5.4: Pulsed qubit spectroscopy for two different qubit drive powers. At -45 dBm only the $f_{01} = 7.230$ GHz transition is visible. At a drive of -5 dBm, two multi-photon transition frequencies $f_{02}/2$ and $f_{03}/3$ become visible and the f_{01} transition is power broadened.

Qubit spectroscopy is employed to determine the transition frequencies of the transmon. The measurement drive is fixed at frequency ω_{r0} and an additional drive at frequency f_{dq} is swept. By measuring the dispersive qubit state-dependent frequency shift of the resonator (see subsection 5.2.3), we can identify transitions between different energy levels of the transmon. The experiment presented in Fig. 5.4 was carried out with an 8 μs drive pulse immediately followed by an 8 μs measurement pulse at frequency ω_{r0} and power $P_r = -35$ dBm, averaging the data 10^6 times. Fig. 5.4 Shows the results of the

spectroscopy at two different drive powers. At low drive power $P_L = -45$ dBm, we observe only the qubit transition at $f_{01} = 7.23$ GHz, whereas at higher power $P_H = -5$ dBm, the linewidth of the f_{01} transition is Rabi-broadened, and we observe two additional spectral lines below f_{01}, as expected of a transmon qubit. We observe a two-photon transition at $f_{02}/2 = 7.08$ GHz and a three-photon transition at $f_{03}/3 = 6.93$ GHz to higher energy levels of the transmon, illustrated by the figure inset. From this we can get an estimate of the transmon anharmonicity $\alpha = 2f_{01} - f_{02} = 294$ GHz[1]. When carrying out pulsed spectroscopy this way, care must be taken that the length of the qubit drive pulse is a few times greater than the decay rate T_{Rabi} such that the qubit is in a mixed state at the end of the pulse and not an arbitrarily populated state (consider the case where the drive duration results in a 2π rotation around the Bloch-sphere and no population change is detected).

Correctly identifying the nature of transitions is important in order to correctly characterise the system, and can be difficult (especially for transition frequencies with similar values, such as f_{12} and $f_{03}/3$). While in principle the number of photons involved in a transition can be determined from the dependence of its linewidth on drive amplitude (given roughly by the driven Rabi-rate, proportional to $\sqrt[n]{\epsilon}$ where ϵ is the field amplitude and n is the number of photons involved in the transition), we can instead identify the nature of the transition more directly with the application of a second spectroscopic tone swept across the same range of frequencies as f_{dq}. We refer to this technique as "two-tone spectroscopy" and has previously been employed to measure the Autler-Townes splitting of a driven transmon [117].Fig. 5.5 shows the results of two-tone spectroscopy on the same device as in Fig. 5.4, with zoom-ins on the f_{01}, $f_{02}/2$, and $f_{03}/3$ transitions. Each transition f_{t} can be driven in either of two ways. First by one drive directly, for multi-photon transitions the signal generator can sometimes provide multiple photons of the same frequency simultaneously. In the plot these come up as the horizontal and vertical spectral lines at $f_{dq2} = f_{\text{t}}$ and $f_{dq1} = f_{\text{t}}$ respectively, and an absence of any other lines is a

[1]In practice this estimation of α can be off by tens of MHz depending on the cleanliness of the spectroscopy and the validity of the transmon approximation $E_J \gg E_C$. A more appropriate way to determine this parameter (and the method used in this thesis) is to perform Ramsey interferometry on the transmon f_{12} transition.

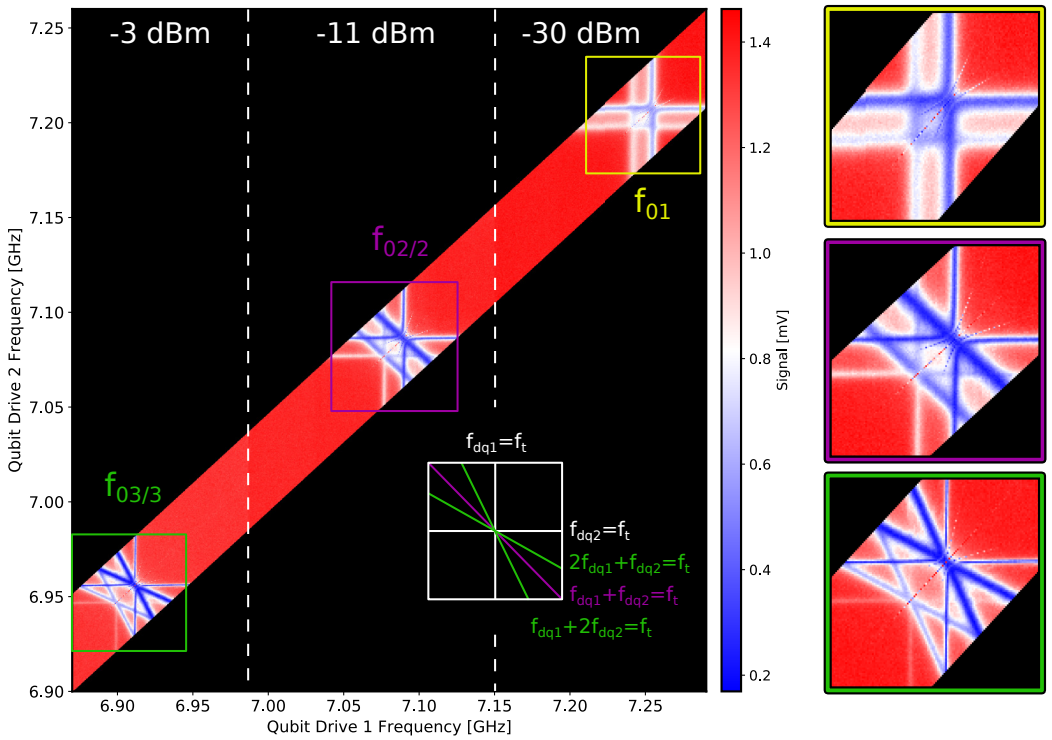

Figure 5.5: Two-tone qubit spectroscopy of device 1Q3. Two individual qubit drives are swept revealing the f_{01}, $f_{02}/2$ and $f_{03}/3$ transitions, the photon-count of each transition can be identified from the spectral signatures. The power of the spectroscopic tones f_{dq1}, f_{dq2} are chosen for each transition so that they are visible and not too power-broadened. To achieve this three powers were used $P_{01} = -30$ dBm, $\mathrm{P}_{02/2} = -11$ dBm, $\mathrm{P}_{03/3} = -3$ dBm, and traces measured with these powers are grouped into regions indicated by dashed lines. On the right hand side are zoom-ins of the f_{01}, $f_{02}/2$ and $f_{03}/3$ transitions (top to bottom). Since the experiment was carried out with CW tones, the resonator is populated during driving and so the dispersively shifted version of each spectral line is also visible.

demonstration of a one-photon transition. The second way is by the two drives providing multiple photons with a sum of energies equal to that of the transition. For the case of a two-photon transition, one photon from drive 1 and one photon from drive 2 can sum to give the correct energy, i.e. $f_{dq1} + f_{dq2} = f_\mathrm{t}$ which gives rise to a spectral line at $f_{dq2} = -f_{dq1} + f_\mathrm{t}$. For the case of a three-photon transition, one of the drives provides two photons while the other provides one, which gives rise to two spectral lines at $f_{dq2} = -2f_{dq1} + f_\mathrm{t}$ and $2f_{dq2} = -f_{dq1} + f_\mathrm{t}$. Each pattern in Fig. 5.5 has a duplicate image shifted by 2χ below in frequency as this experiment was carried out with a CW drive to the resonator, meaning that the resonator was populated with some number of photons as the qubit was being driven and so the dispersively shifted transition frequencies are

also visible. It is worth noting that these experiments were carried out by probing the resonator in transmission (i.e. driving from the control port) however one must be careful when performing the same experiment in reflection to look at the real or imaginary part of the measured signal and not the magnitude, since the the real and imaginary parts of the amplitude response of the resonator can take on both positive and negative values due to interference with the background signal, meaning that the signal magnitude is not necessarily linear with qubit population.

With knowledge of f_{01} and α we can determine the transmon parameters E_J and E_C. Using the fifth order expansion form of the treatment given in [73] the system of equations

$$\begin{aligned} hf_{01} &= -E_C + 2\sqrt{2E_JE_C} - \frac{E_C\zeta}{4} - \frac{21E_C\zeta^2}{128} - \frac{19E_C\zeta^3}{128} - \frac{5319E_C\zeta^4}{32768} \\ \hbar\alpha &= -E_C - \frac{9E_C\zeta}{16} - \frac{81E_C\zeta^2}{128} - \frac{3645E_C\zeta^3}{4096} - \frac{46899E_C\zeta^4}{32768} \\ \zeta &= \sqrt{\frac{2E_C}{E_J}} \end{aligned} \tag{5.5}$$

can be solved to determine $E_J/h = 26.3$ GHz and $E_C/h = 268$ MHz, giving a ratio $E_J/E_C = 98$ confirming we are comfortably in the transmon limit $E_J \gg E_C$.

5.2.3 The Dispersive Shift and Qubit-Resonator Coupling

The term $(\omega_r + \chi\hat{Z})\hat{a}^\dagger\hat{a}$ in Eq. (5.1) captures an important behaviour of the system, namely the qubit-state dependent shift of the frequency of the resonator. If the qubit is in its excited state, the resonator frequency will shift down in frequency from ω_{r0} by 2χ where χ is the dispersive shift (more accurately called the resonator-qubit cross-Kerr). A demonstration of this is shown in Fig. 5.6. The transmission spectrum S_{21} is probed with a 1 μs pulse at a low power of $P_r = -50$ dBm, and the transmitted amplitude V_{ADC} is measured. We find the Lorentzian response of the resonator centred on $f_{r0} = 10.23$ GHz, with quality factor $Q = 2080$ (blue curve). We repeat the transmission measurement of the LC resonance after preparing the qubit in its first excited state with an $\hat{X}_\pi$ pulse prior to a measurement pulse. (see Fig. 5.6 orange curve). The response is fitted to the weighted sum of two Lorentzians in the complex plane (Eq. (5.3)), from which we extract

the dispersive shift of the resonator $2\chi/(2\pi) = -12.68\,\text{MHz}$. We then use this to derive the qubit-resonator coupling $g/(2\pi) = 418\,\text{MHz}$ from Eq. (5.2).

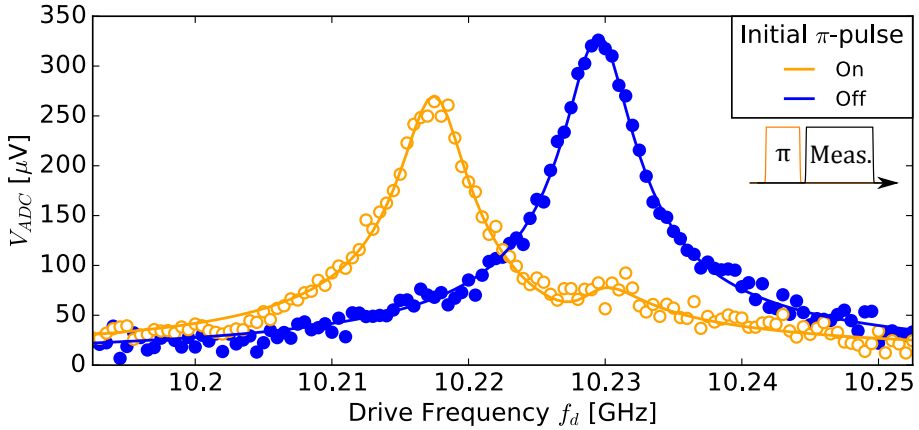

Figure 5.6: Resonator spectroscopy in the low photon number limit. Transmitted signal amplitude at the ADC measured with a 1 μs pulse at f_d, with (orange) and without (blue) a π-pulse applied to the qubit immediately prior to the measurement pulse (pulse scheme inset). The data (circles) are fitted (solid lines) to the magnitude of the sum of two complex Lorentzians given by Eq. (5.3)

This experiment also serves to demonstrate the principle of dispersive readout [46, 85, 47] that was employed previously in the qubit spectroscopy. One can see that by measuring the transmitted response from a tone at f_{r0}, one will be able to determine from the magnitude of the signal whether the qubit is $|0\rangle$ (330 μV) or $|1\rangle$ (90 μV).

5.2.4 Stark shifts and Number Splitting

Just as the qubit state shifts the resonator frequency by 2χ, so too is the qubit frequency shifted by 2χ for each photon present in the resonator state[2]. Here we show two experimental demonstrations of this in two limits, where $\chi \ll \kappa$, and where that inequality is invalid, and we then show how this can be used to map drive power to mean photon number in the resonator in both cases.

[2]This is the case so long as the resonator is driven at ω_{r0}, see Subsec. 2.6.2.

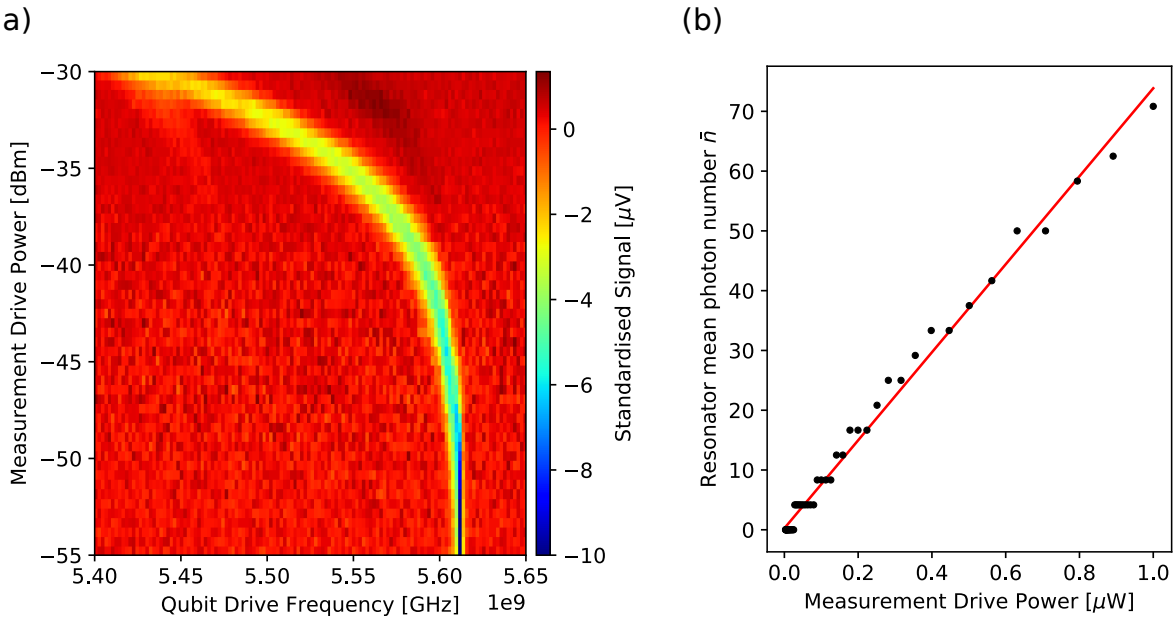

Figure 5.7: (a): Observation of the AC Stark shifting of the qubit f_{01} transition frequency on the device 1Q1. CW qubit spectroscopy is performed with increasing power of the resonator tone at f_{r0}. The average qubit frequency shifts down with increasing resonator drive power and so resonator population $\bar{n}$. The average qubit frequencies are estimated by taking the minimum values of each spectroscopy trace, rather than fitting the spectrum. These values were used to produce (b): resonator population plotted against applied power. The solid line is a fit to the data revealing the expected linear relationship. The data appears discretized due to the frequency resolution of the experiment in (a).

In the limit that $\chi \ll \kappa$, the form of the qubit spectral line is given by Eq. (2.43). The relevant term in the denominator tells us that when the resonator is populated with $\bar{n}$ photons, the qubit transition will be found at the ac Stark shifted qubit frequency $\omega_{\text{ac}} = \omega_{01} + 2\chi\bar{n}$. This allows us to calibrate the average photon number in the resonator $\bar{n}$ by mapping it to the shift in the average qubit frequency. Measurements of the AC Stark shift and resonator photon number calibration were first performed in [85], and we employ the same methods to produce the results shown in Fig. 5.7. Continuous-wave qubit spectroscopy is performed across a range of different measurement drive powers on a device (1Q1) with $\kappa = 3.13$ MHz, $\chi = 1.20$ MHz. The qubit drive power is set low enough that the spectral line is not Rabi-broadened (in this case, $P_q = -50$ dBm), and the resonator is driven at ω_{r0}. During the experiment, the resonator will be populated with $\bar{n}$ photons, and so the qubit will be found at the average frequency ω_{ac} (along with broadening of the spectral line due to increased dephasing from measurement). The central frequency

of each spectrum is extracted and plotted on a linear power scale, showing the expected dependence of $\bar{n}$ to drive power is linear as long as we are in the low photon number limit $\bar{n} < n_{\text{crit}}$. From the slope of the fit, and the value of χ, one can arrive at the calibration $\bar{n}/P_r = 73.6\ \mu\text{W}^{-1}$.

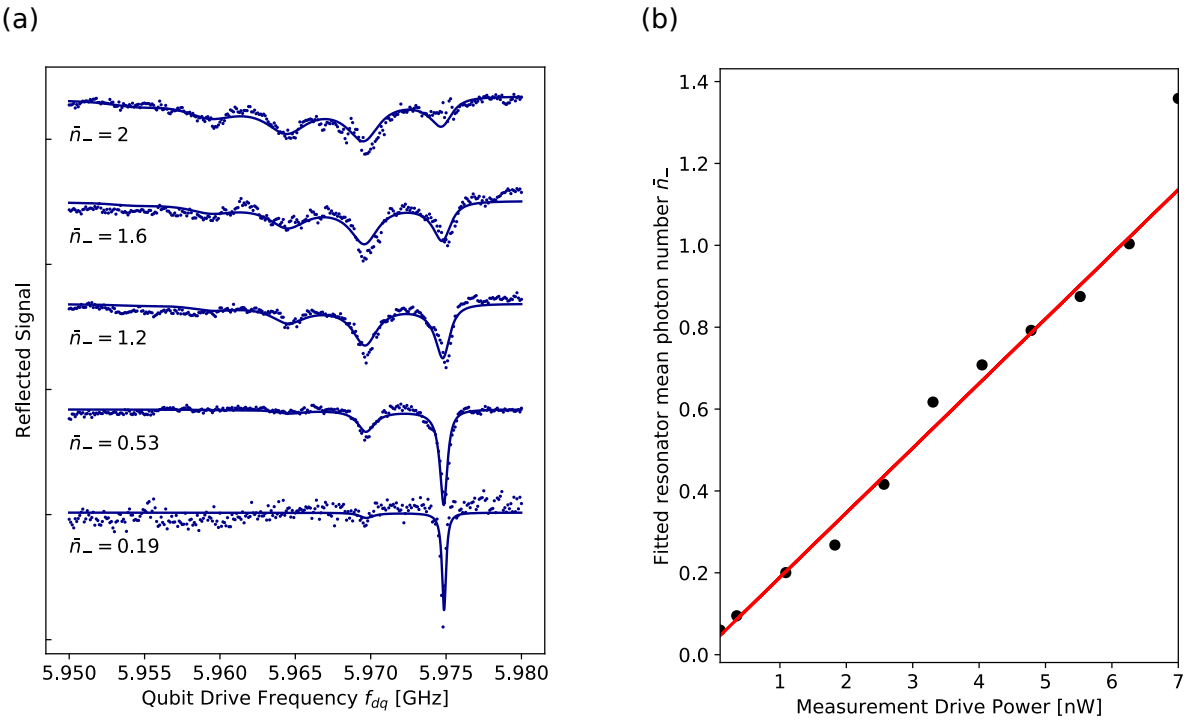

Figure 5.8: (a): Observation of the number splitting of the qubit f_{01} transition frequency on the device 2Q1:2. CW qubit spectroscopy is performed with increasing power of the resonator tone at f_{r0}. Traces are vertically offset for visibility from the lowest resonator power to the highest (bottom-top). In this limit, clear discrete peaks are observable corresponding to integer photon number populations in the resonator. Peaks are also broadened with increasing power due to increased measurement-induced dephasing. Solid lines are fits of the data to Eq. (2.47) with ϵ_{rf} as the free parameter, and the calculated $\bar{n}_-$ is shown for each trace. (b): Fitted $\bar{n}_-$ plotted against applied measurement power revealing the expected linear relationship.

In the case that the condition $\chi \ll \kappa$ is not met, we cannot use the above expressions and a more full treatment is needed. In this limit, called the strong dispersive limit, we expect to see individually resolvable peaks in the qubit spectrum corresponding to different numbers of photons in the resonator. This was first proposed in [84], and can be seen in the derived absorption spectrum described by Eq. (2.47), where each photon number j produces a Lorentzian line-shape centred at $\omega_j = \tilde{\omega}_{01} + B + j(\chi + \Delta_r)$ [84], and so each peak will be separated by $(\chi + \Delta_r)$ (commonly the resonator is driven at ω_{r0} such

that $\Delta_r = -\chi$ and the separation is 2χ, however it is important to note that driving at different detunings from the ω_r will give different separations).

This form of spectrum is refereed to as "number splitting", these features were first shown in [86] and we employ the same method to produce the spectra shown in Fig. 5.8(a). As in the previous Stark-shift experiment, continuous-wave qubit spectroscopy is carried out at a range of different measurement drive powers, however this time on a different device (2Q1:Q2) with $\kappa = 0.82$ MHz, $\chi = -2.6$ MHz. Again the resonator is driven at ω_{r0} such that $\Delta_r = -\chi$, and a low qubit drive power is used to avoid extra broadening of the spectral lines. The split spectrum is revealed with peaks separated by 2χ with different weights depending on $\bar{n}_-$, also note the increased broadening of each peak with power, that eventually removes the visibility of the peaks.

Looking at the form of the spectra, it is immediately clear that relating the drive power to photon number is not as simple as in the Stark-shift experiment, and instead the full spectrum must be fitted to Eq. (2.47) with the experienced driving field ϵ_{rf} as the fit parameter and all other terms determined independently. An extra complication to consider is that in this limit, the mean photon number in the resonator depends on the qubit state, as the dispersive shift of the resonator is enough to impact the effectiveness of the resonator drive. The average number of photons in the resonator when the qubit is in the excited ($\bar{n}_+$) or ground ($\bar{n}_-$) state is given by Eq. (2.44), and in this experiment we have chosen to calibrate $\bar{n}_-$ as we are driving the resonator at ω_{r0} where $\bar{n}_-/\bar{n}_+$ is maximised ($= 162$ in this case). The values of $\bar{n}_-$ extracted from each spectra are plotted against the applied power in Fig. 5.8(b), again revealing the expected linear relationship between drive power and photon number. The slope directly gives $\bar{n}_-/P_r = 6.3\ \mathrm{nW}^{-1}$.

5.3 Demonstrations of Coherence

In this section we focus on time-resolved experiments to demonstrate the coherence of device 1Q3, as well as characterise the energy relaxation time T_1, and phase coherence times T_2^*, T_2^E of the qubit. In each experiment the qubit population is extracted by fitting the signal-time response to cavity Bloch equations (see Appendix C).

5.3.1 Rabi Oscillations

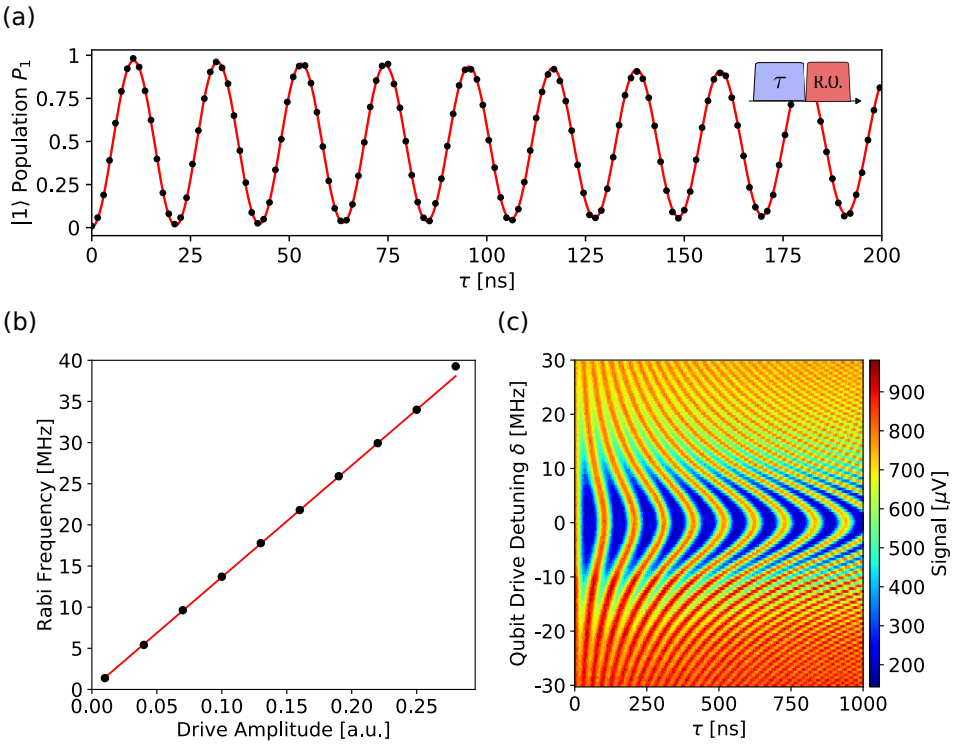

Figure 5.9: Demonstrations of Rabi oscillations on device 1Q3. (a): Qubit population as a function of Rabi-pulse width τ (pulse scheme inset) revealing Rabi oscillations. The solid line is a fit to a decaying cosine $P_1 = A\cos(\Omega_0\tau)e^{-\tau\Gamma_R}$ finding $\Omega_0 = 47$ MHz. (b): Fitted Rabi frequencies from several traces plotted against applied drive amplitude, revealing the expected linear relationship as given by Eq. (5.6). (c): Rabi oscillations as a function of qubit drive detuning δ, the Chevron pattern expected from Eq. (5.8) is visible.

Under a steady-state drive at ω_{01}, the qubit state will rotate about the $\hat{X}$-axis on the Bloch sphere at a frequency Ω_0, causing the qubit state to oscillate between $|0\rangle$ and $|1\rangle$. These oscillations of the qubit state between ground and excited are called Rabi oscillations and Ω_0 is called the Rabi frequency. It is given by

$$\Omega_0 = \frac{\vec{E}\cdot\vec{d}}{2}, \tag{5.6}$$

where $\vec{E}$ is the amplitude of the drive field seen by the qubit (and is proportional to the applied drive amplitude) and $\vec{d}$ is the effective dipole moment of the qubit, which comes from the geometry of the system. The Rabi oscillations shown in Fig. 5.9(a) were performed by applying a square pulse at the qubit frequency ω_{01} with a fixed amplitude and varying pulse length $\Delta\tau$, followed by a measurement pulse of width 16 μs. The

reflected signal was measured and the qubit population extracted as outlined in Appendix C. Each point was averaged 10^6 times and the average population is plotted against the corresponding pulse length. The oscillation of the qubit state between ground and excited is revealed, together with a slight exponential decay of the signal amplitude. The decay rate of Rabi oscillations under a steady-state drive (with assumptions about the form of noise from the Bloch-Redfield picture [78]) can be obtained from the simplified expression

$$\Gamma_{\mathrm{R}} = \frac{3\Gamma_1 + 2\Gamma\phi}{4}. \tag{5.7}$$

The inclusion of both the decay and dephasing rates Γ_1 and Γ_ϕ can be understood from the fact that as the qubit state is driven about the $\hat{X}$-axis of the Bloch sphere, it makes excursions through the $\hat{Z}$ eigenstates (where relaxation processes have the most significant effect on the qubit state) and the XY plane (where dephasing processes have the most significant effect).

To verify that the oscillations we measure are indeed Rabi, we perform two further experiments that vary an additional parameter in each case. The first is to demonstrate the linear dependence of the Rabi frequency with drive amplitude as given by Eq. (5.6) and shown in Fig. 5.9(b). Several Rabi oscillations are produced by varying the amplitude of the driving pulse in each experiment, and the fitted frequencies are plotted against the drive amplitude showing the expected linear dependence. The second parameter that can be swept is the frequency of the driving pulse ω_{dq} such that we drive at a detuning $\delta = \omega_{01} - \omega_{dq}$. Under these conditions the off-resonant Rabi frequency Ω is given by

$$\Omega = \sqrt{\Omega_0^2 + \delta^2}. \tag{5.8}$$

Fig. 5.9(c) shows a plot Rabi oscillations against the detuning of the drive. The chevron pattern predicted by Eq. (5.8) is revealed as the Rabi frequency increases with larger detunings of the drive.

5.3.2 Qubit Relaxation Time T_1

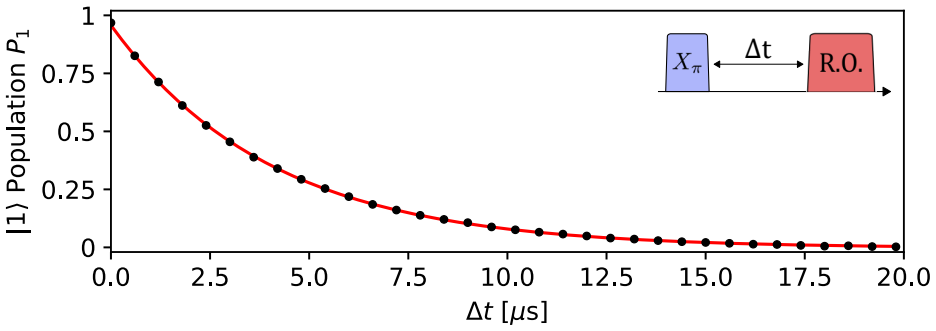

Figure 5.10: A T_1 experiment carried out on 1Q3 (pulse scheme inset). The curve is fitted to an exponential decay as described in the main text and $T_1 = 4.1$ μs is extracted.

The qubit relaxation time $T_1 = 1/\Gamma_1$ is measured by first preparing the qubit in the excited state with an $\hat{X}_\pi$ pulse, followed by a delayed measurement pulse. Sweeping the value of the delay tracks the decay of the qubit state in time, and under typical noise conditions gives rise to an exponential decrease. The time constant of this decay is the relaxation time T_1. Such an experiment is performed in Fig. 5.10 and is fitted to the function $P_1 = a + be^{-\Delta t/T_1}$, where a and b are fit parameters to account for the starting population and fully-relaxed population respectively. A good agreement is found to this form of decay and a relaxation time of $T_1 = 4.10$ μs is extracted.

5.3.3 Qubit Coherence Times T_2^* and T_2^E

The coherence time of the qubit is measured with a Ramsey interferometry experiment (sometimes called free-induction decay FID). The qubit Bloch-vector is first brought to the equator with an $+\hat{X}_{\pi/2}$ pulse. The system is then allowed to evolve for varying delay Δt, the free evolution time, before another $+\hat{X}_{\pi/2}$ is applied to project the $\langle\hat{Y}\rangle$ component of the state back into the measurable $\hat{Z}$ basis. Often, the frequency of the applied qubit pulses are detuned from the qubit frequency by a fixed amount in order to set the periodicity of the fringes in the Ramsey experiment (since the Bloch sphere is a representation in the frame rotating at the drive frequency, the qubit state will precess around the $\hat{Z}$-axis at a frequency given by the detuning of the drive from ω_{01}). Dephasing

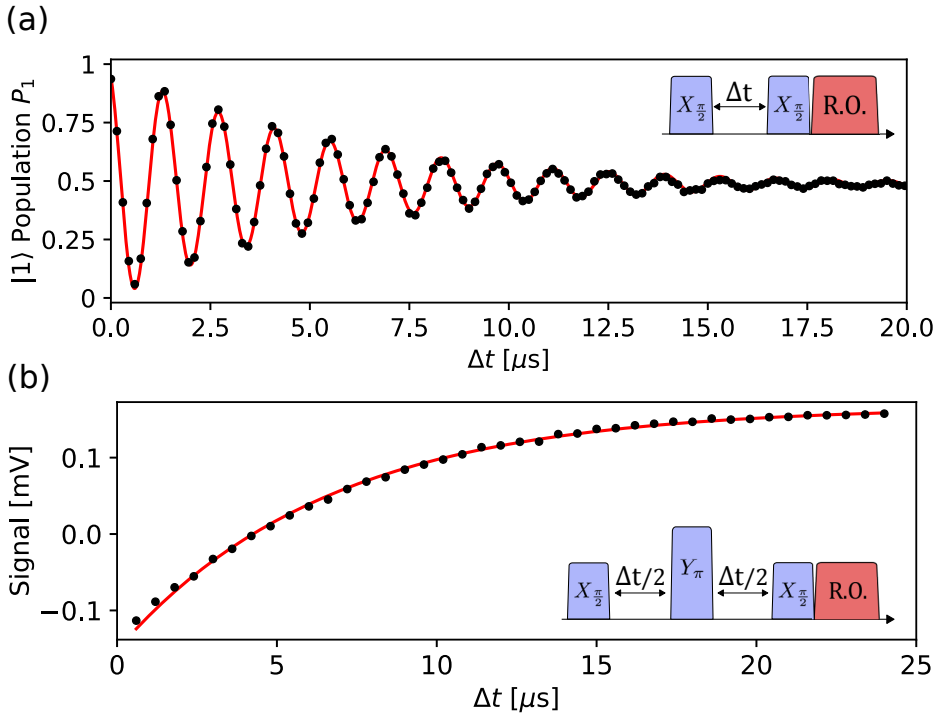

Figure 5.11: Measurements of the coherence of qubit 1Q3. (a): Ramsey oscillations performed with the qubit drive detuned 4.5 MHz from f_{01} reveals a $T_2^* = 5.65\,\mu$s from the fitted oscillating decay $P_1 = a + b\cos(\omega t - \phi)e^{-\Delta t/T_2^*}$ (pulse scheme inset). (b): A spin-echo experiment (pulse scheme inset), the data is fitted to the same form of exponential decay as in the T_1 experiment and a $T_2^E = 6.67\,\mu$s is found.

of the state is brought about by energy relaxation events, and pure dephasing processes (i.e. direct changes to the qubit frequency) as captured by $1/T_2^* = 1/2T_1 - 1/T_\phi$ where $1/T_\phi = \Gamma_\phi$ is the pure dephasing rate. Both these processes will cause the state to accrue random amounts of phase during the free evolution, and in an averaged measurement we will see the qubit state tend towards a purely mixed state. The projected measurement results in a decaying sinusoidal curve, as shown in Fig. 5.11. The result is fitted to the function $P_1 = a + b\cos(2\pi\delta\Delta t - \phi)e^{-\Delta t/T_2^*}$ and a good agreement to an exponential decay with time constant $T_2^* = 5.65\ \mu$s is found[3]. The other piece of information that can be obtained from the fit is the qubit-drive detuning δ, and thus the qubit frequency. The sensitivity to small frequency offsets inherent of any interferometry experiment is why a Ramsey experiment is one of the best ways of deducing the qubit frequency and is the method employed in this thesis for the task.

[3]It is important to remember the decay of the state coherence is only exponential if the frequency noise spectrum affecting the qubit is white (constant valued). For example a $1/f$ noise spectrum, commonly found for frequency tunable qubits, gives rise to a Gaussian decay $e^{-(\Delta t/T_2^*)^2}$, and in the case of more exotic noise spectra there may not be a meaningful time constant at all.

The coherence time can be extended by applying modified pulse sequences that essentially filter the noise spectrum $S_Z(\omega)$ seen by the qubit. There are many such sequences [80], referred to as dynamical decoupling schemes, and they are interesting as they can be used to directly measure $S_Z(\omega)$, and can be built in to other sequences to improve fidelities of logical operations. The simplest of schemes is the spin-echo, which consists of a Ramsey experiment with a Y_π pulse situated midway in between the two $X_{\pi/2}$ pulses. The effect of the pi-pulse is to "refocus" any deviations away from the desired Bloch vector by reversing the direction of any noise drives after the pulse, essentially undoing their effects. This approach works for low-frequency fluctuations in the qubit frequency, where "low" is less than the inverse of the free-evolution time (intuitively, this only works if the direction and amplitude of the noise doesn't change significantly over the course of the experiment, a more concrete analysis of the filtering effects is given in [79, 80]). Such an experiment is carried out in Fig. 5.11(b) and shows a good agreement with an exponential fit, with decay time $T_{2\text{Echo}} = 6.6\ \mu$s, with $T_2^E > T_2^*$ telling us that there is a some contribution to the noise spectrum at low frequencies ($\lesssim 1$ MHz), however since $T_2^E < 2T_1$ there is still some pure-dephasing due to high frequency processes, for example possible photon shot-noise in the readout resonator.

5.4 Conclusions

In this chapter we have presented a new double-sided coaxial implementation of circuit QED. We demonstrated multiple versions of a single qubit unit cell and showed that it was possible to carry out conventional cQED experiments to determine key properties of the dispersive Jaynes-Cummings Hamiltonian. We found it was possible to obtain a qubit resonator coupling of $g/(2\pi) = 418\,\text{MHz}$. We further showed demonstrations of qubit coherence, finding characteristic times of $T_1 = 4.1\ \mu$s, $T_2^* = 5.65\ \mu$s, and $T_{2\text{Echo}} = 6.6\ \mu$s.

Chapter 6

Extension to Multi-Qubit Circuits

In this chapter we demonstrate the extension of the coaxmon architecture to multi-qubit circuits. The ability to arrange single qubit unit cells in a 2D plane without further constraints imposed by the wiring design is a key motivation behind its development, and so we show the viability of this approach on devices with two and four qubits with fixed dispersive couplings. We first perform a full characterisation of measurement and control drive port selectivity, as well as the circuit cross-coupling between qubits and resonators of differing unit cells. Having established this, we then show an evaluation of two-qubit gates via a calibrated cross-resonance (CR) interaction [77], performed on two and four qubit devices. We then turn out attention to the environment of devices with multiple qubits, and perform measurements of qubit temperatures and upper-bound estimates of resonator temperatures. Finally we explore methods to evaluate the noise environment affecting the qubits, such as repeated lifetime and coherence measurements, spin-locking, and T_2 spectroscopy.

6.1 Device Layout and Parameters

Within this project, devices of two and four coupled qubits were designed, fabricated and characterised. To realize devices with multiple qubits, single qubit unit cells (see Chapter

5) are placed adjacent to one another[1]. Each qubit remains coupled to an individual resonator on the opposing surface of the substrate, with individual control and measurement lines. Fig. 6.1 shows the design patterns of the transmon circuits for 2-qubit and 4-qubit devices. Qubits were separated with a 1.5 mm pitch and coupled capacitively by way of finger capacitors in the outer electrode design. The spatial configuration was chosen to be a 2×2 grid for the 4-qubit devices in order to demonstrate the extensibility of the architecture to 2D connectivities. The qubit-qubit coupling is adjusted by the changing length of the overlap of the finger capacitors. To calculate the expected coupling, a lumped-element electrostatic simulation in Maxwell is performed to obtain the capacitance matrix of the system, which is then used to find the system Hamiltonian and can be solved to get the value of the coupling (the values used for this thesis were obtained from the following works [118, 65]).

The two main parameters that define the interaction between two qubits are the qubit-qubit coupling J, and the qubit-qubit detuning $\Delta_q = \omega_{01}^1 - \omega_{01}^2$. Different designations of these parameters will be required depending on the method used to implement logic gates in the device. In this project, we aim to implement CNOT gates between the qubits by way of the cross-resonance interaction [63, 64], and so we must choose parameters that enable high fidelity unitary operations. For a review of the cross-resonance interaction in this thesis, please see Sec. 2.4. In the particular case of cross-resonance, there are three factors to consider, the cross-resonance ratio μ from Eq. (2.29), the quantum crosstalk ratio ν from Eq. (2.31), and the cross-Kerr shift between the two qubits ξ from Eq. (2.28) (the analogue of the dispersive shift between qubit and resonator). We wish for ν to be small relative to μ. We also wish for the always-on entanglement at a rate of ξ to be smaller than the cross-resonance activated entanglement at a rate of $\Omega_{12}^X \mu$ in order to have a reasonable on-off ratio of the gate.

While increasing the amplitude of the drive Ω_{12}^X will increase the rate of the entangling operation, there are other practical considerations when the amplitude of the drive is large compared to the detuning of other transitions in the device such as driving of higher

[1]For details of the packaging that provides control and measurement wiring to such a device with an extensible scheme, please see Subsec. 3.2.2.

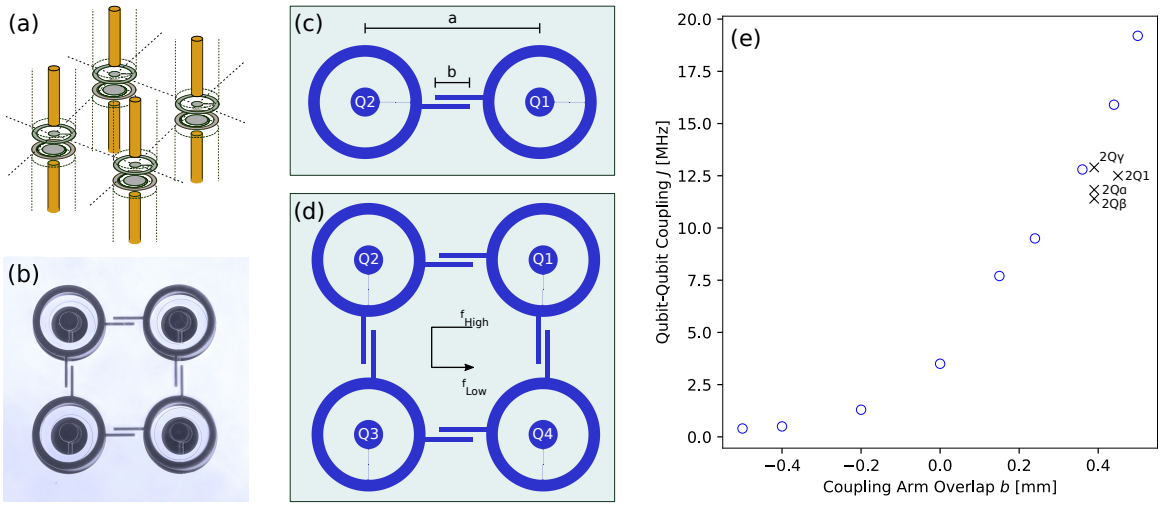

Figure 6.1: Depictions of multi-qubit circuit design and layout. (a): Visual depiction of the extension of the coaxmon architecture to a 2D array of unit cells. (b): An optical image of a four-qubit device. (c): Circuit layout of the qubit side of the two-qubit device, the unit-cell is spaced with a pitch of $a = 1.5$ mm, and the qubit-qubit coupling is set by the overlap of the coupling arms b, which has a value of 295 μm in this instance. (d): Layout of the four-qubit device, circuits are arranged as a 2D grid however the arrangement of coupling with frequency is a 1D chain from highest to lowest frequency, with primary pairs $1 \leftrightarrow 2$, $2 \leftrightarrow 3$ and $3 \leftrightarrow 4$. $1 \leftrightarrow 4$ is also connected however we do not expect to be able to utilize this due to the large detuning between Q1 and Q4. (e): Values from a simulation of the coupling of a two qubit device as in (c) with overlap b. Experimentally determined values are in close agreement with simulated results. Note that for the four qubit device, a different simulation had to be used due to the contributions to the effective capacitance due to the presence of the other qubits.

transitions and off-resonant driving of the control qubit. It is therefore desirable to have a sufficiently large μ to avoid strong driving. Optimising for these conditions naturally presents a challenge. The relationship between μ, ν, and ξ with Δ_q (as given by Eq. (2.33)-Eq. (2.35)) is shown in Fig. 6.2 holding all other qubit parameters fixed.

Due to the minimisation of ν/μ one might choose to target $\Delta_q < \alpha^1$ such that the second qubit's frequency lies in the straddling regime of the first. However a drift of greater than ± 50 MHz will lead to a frequency collision between the two and a much higher ζ. This imposes tight constraints on the qubit fabrication, in particular the setting of the Josephson energy via the junction resistance needs to be precise in order to have a sufficient yield of potential devices after fabrication (see Subsec. 4.4.1 for a detailed analysis). As we can actively reduce the effects of crosstalk during operation [77], we can relax these tight constraints by instead targeting a different parameter regime with $\Delta_q > \alpha^1$, with target

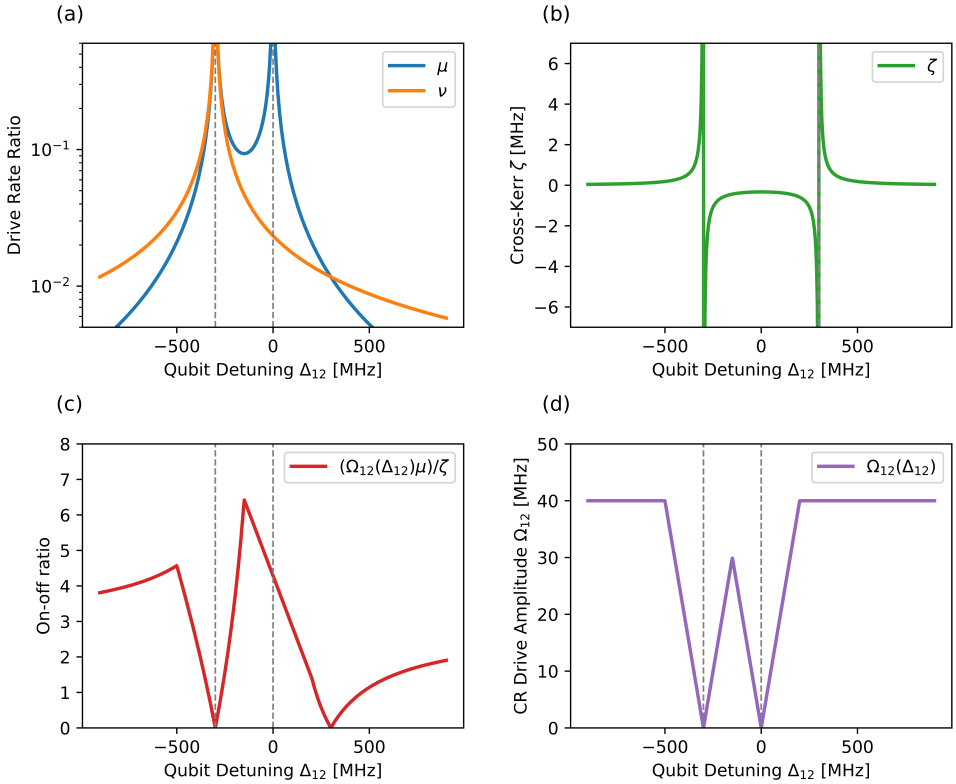

Figure 6.2: (a)-(b) Variation of μ, ν and ζ from Eq. (2.33)-Eq. (2.35) with qubit-qubit detuning Δ_q for qubits with fixed anharmonicity $\alpha = 300$ MHz and coupling $J = 7$ MHz. (c) On-off ratio $\frac{\Omega_{ZX}}{\Omega_{ZZ}} = \frac{\Omega_{12}(\Delta_q)\mu}{\zeta}$ given the prior circuit parameters. An upper bound estimate of the maximum drive rate Ω_{12} is calculated on the principle that it must be considerably smaller than lower frequency qubit's detuning from the two poles at $\Delta_q = 0, \alpha^1$, and that it be sufficiently low such that we do not have off-resonant driving of the control qubit or leakage to higher excited states. The expression $\Omega_{12}(\Delta_q) = \min\left(\min\left(|\Delta_q - \alpha^1|, |\Delta_q|\right)/5, 40 \text{ MHz}\right)$ is used here to quantify this constraint. For clarity, a plot of this expression is shown in (d).

values $J = 7$ MHz and $\Delta_q = 500$ MHz such that $\mu = 2.1\%, \nu = 3.5\%$ and $\zeta == 180$ kHz. In this regime, there is a larger range of detunings of ≈ 400 MHz $- 700$ MHz that we find to have a sufficiently high on-off ratio (see Fig. 6.2(c)), with cross-resonance ratios of $0.8\% \leq \mu \leq 5.3\%$ ensuring such on-off ratios can be achieved without very large drive amplitudes. We are less concerned about the larger ratio of ν/μ as crosstalk can be actively cancelled during operation [77].

6.2 Port Selectivity and Circuit Cross-Coupling

Crosstalk is the process by which a drive applied to one channel creates an undesired signal or effect on a separate channel. Characterising crosstalk in multi-qubit superconducting

circuits is becoming increasingly important. Control-wiring crosstalk can cause coherent control errors that become increasingly impractical to correct in larger scale circuits, and cross-coupling between circuits can create unwanted measurement induced dephasing on one qubit during readout of another. Selective control and coupling is intrinsic to the architecture explored in this thesis, due to the mode-matching of coaxial circuit elements to out-of-plane 3D wiring. In addition, there is no reason for the crosstalk and cross couplings to get worse as the device is extended to larger arrays of qubits. However, in any multi-qubit circuit the electromagnetic fields associated with individual circuit elements and control signals will never be perfectly confined, and so this warrants investigation. In this section we present a careful characterisation of resonator and qubit drive port crosstalk, as well as measurement crosstalk due to circuit cross-coupling, on device 4Q3. We first utilise measurement-induced dephasing to directly characterize resonator drive port crosstalk, as well as to determine the cross-couplings of resonators and qubits in differing unit cells. We then incorporate a detailed understanding of the two-qubit Hamiltonian in order to extract the qubit drive port crosstalk, distinguishing between the quantum crosstalk that arises from the qubit-qubit coupling, and the classical crosstalk due to a direct coupling between the drive port and qubit. Finally we present results from finite-element simulations to better understand the sources of classical qubit drive port crosstalk.

6.2.1 Resonator Port Selectivity

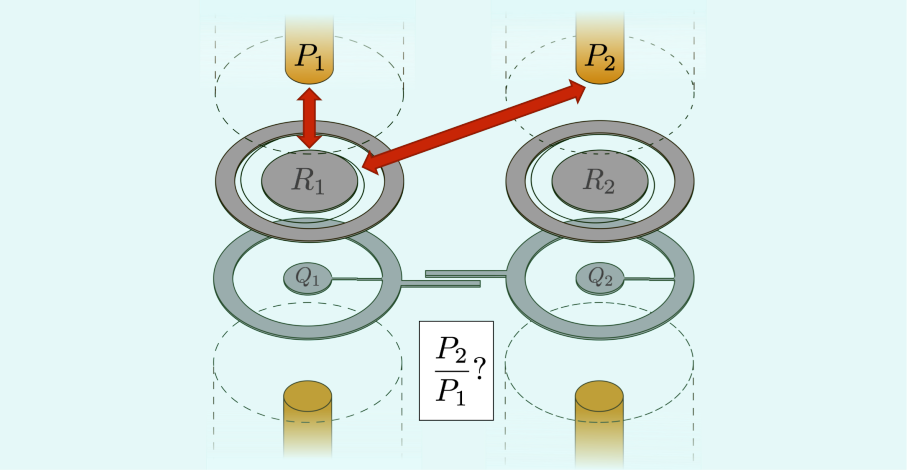

Figure 6.3: Depiction of the definition of resonator port selectivity between measurement port 2 and resonator R_1. It is the ratio of powers P_1 and P_2, applied to measurement ports 1 and 2 respectively, needed to populate R_1 with a single photon.

We define the resonator port selectivity X_{ij}^R between ports i and j as the ratio of the powers needed to populate resonator i with the same number of photons from the resonator's local port i, compared to the distant port j. Expressed in dB this is

$$X_{ij}^R = 10 \log_{10} \left(\frac{\eta_{ii}}{\eta_{ij}} \right) \tag{6.1}$$

where η_{ij} is the applied power at port i required to put one photon in resonator j. To determine the ratio η_{ii}/η_{ij}, the proportionality of the measurement-induced dephasing rate Γ_m with the applied power is exploited, similar to experiments carried out in [106, 119, 120]. The objective of the experiment shown in Fig. 6.4 is to the compare the Γ_m per unit power when a signal is applied from a local v.s. a non-local measurement port.

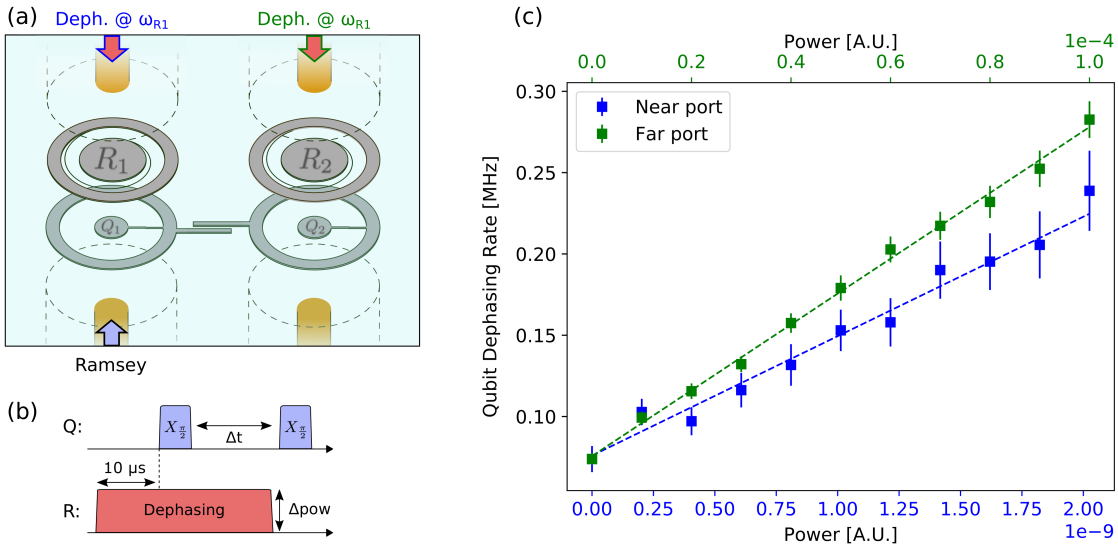

Figure 6.4: Determination of the resonator port selectivity for port 4 → resonator 1 on 4Q3. (a) Two sets of Ramsey experiments are carried out, the first with the dephasing tone applied from the near port 1 (blue) and the second from the far port 4 (green). (b) Pulse scheme for the Ramsey experiments used to generate each point in (c), a dephasing pulse is applied with a chosen power, 10 μs before the start of a conventional Ramsey sequence on Q_1. (c) Measured dephasing rates from a set of Ramsey experiments with varying dephasing pulse powers when the pulse is applied from the near port 1 (blue data and bottom x-axis) and the far port 4 (green data and top x-axis). Points are extracted dephasing rates from the Ramsey traces and dashed lines are linear fits. The ratio of the gradient of the two slopes directly gives $X_{ij}^R = -46$ dB.

Given a signal applied at drive port m, the measurement-induced dephasing per unit power is measured by a series of Ramsey experiments with a dephasing pulse applied to the resonator during the qubit's free evolution (Fig. 6.4(b)). The dephasing pulse is applied to the resonator at the frequency ω_{r0} in order to maximise dephasing per photon. Crucially, the dephasing pulse begins several decay periods $1/\kappa$ before the first $\hat{X}_{\pi/2}$ pulse (10 μs in this case), to ensure the system is in the steady state during the free-evolution time of the Ramsey experiment[2]. A sweep of Ramsey experiments are performed, with different dephasing pulse powers, and the total dephasing rate Γ_2 is determined as the inverse of the fitted T_2^*. The same set of Ramsey experiments are performed for the two cases where the dephasing pulse is applied to resonator i from port i, and from port j, and the extracted Γ_2s can be plotted against the dephasing pulse power as in Fig. 6.4(c).

[2]By steady-state we mean that there is no ringing of photon population in the resonator, which occurs when the dephasing tone is first applied and decays away at a rate proportional to κ. For more details see [84]

We first verify that relationship between dephasing and power is linear, as expected from Eq. (2.45), which confirms that we are driving weakly enough such that $\bar{n} \ll n_{\text{crit}}$. The slope of each trace tells us the dephasing rate per unit power, which is proportional to η_{ij}, and thus the ratio η_{ii}/η_{ij} is given directly by the ratio of the slopes. In this case we extract a selectivity of $X^R_{41} = -46$ dBm .

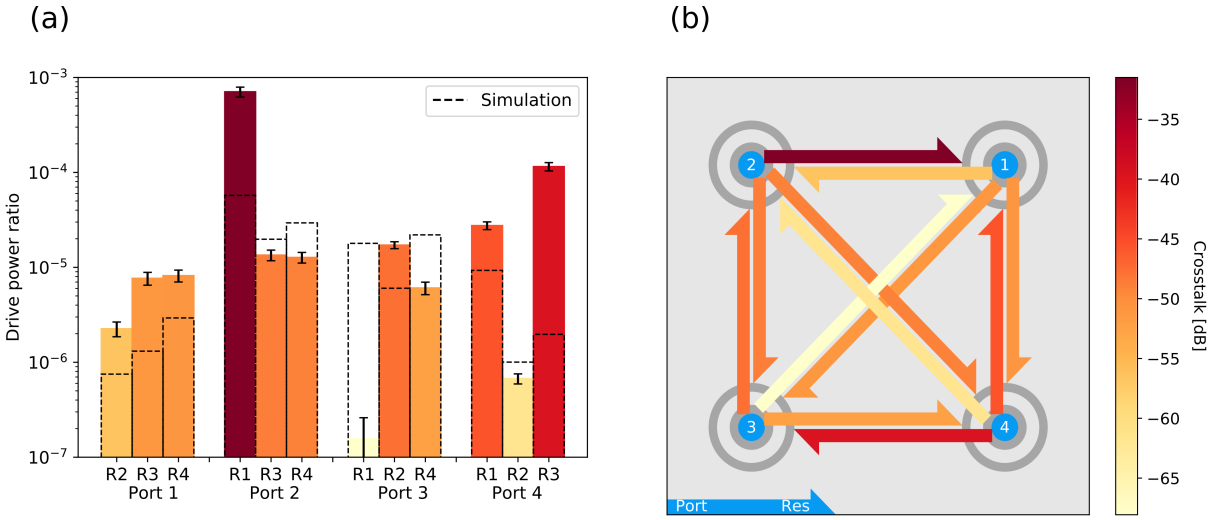

Figure 6.5: Measured values of resonator-port crosstalk between all pairs in 4Q3, the same data is plotted in both (a) and (b). (a) Power ratios measured by experiment (solid bars) as well as simulated values (dashed outlines). Bar colouring reflects the magnitude of crosstalk according to the same colour bar in the neighbouring plot. (b) Geometric depiction of the measured crosstalk, arrows indicate the crosstalk between port to resonator as indicated by the scheme arrow in the bottom left.

X^R_{ij} can be determined for every resonator-port combination in order to build up the resonator port selectivity matrix X^R. The results of this analysis on device 4Q3 are shown in Fig. 6.5. There are a couple of points to note, firstly there is not much of a pattern of difference in crosstalk between neighbouring and diagonal pairs, which indicates that although the circuit-pin separations are different in the two cases, the crosstalk balance is likely more influenced by other factors. In particular, the asymmetry of the couplings between drive pins and resonators, as reflected by the varying values of κ for each resonator. This asymmetry is due to inaccuracies of setting the pin-circuit separations during sample holder assembly. The most separated pin at port 2(as reflected by the lower values of κ of resonator 2) is the source of noticeably higher levels of crosstalk when compared to the least separated pin at port 1. This analysis is reflected in the

simulation results (which accounted for the differences in κ). One item that remains unexplained is the relatively larger level of crosstalk between port 2 $\rightarrow$ resonator 1, and could be due to further sample holder imperfections or quantum effects not accounted for in simulation. From a performance point of view, these results show that the resonator drives are highly selective (would produce an error of $\approx 10^{-3}$ in the worst case), however not so directly informative as the device is not typically operated this way (we typically only drive a resonator port at the frequency of its corresponding resonator to perform readout). Instead these results will be informative of what we should expect from the qubit port selectivity, explored in subsection6.2.3, as the wiring setup and circuit shapes are almost the same.

6.2.2 Resonator-Qubit Cross-Coupling

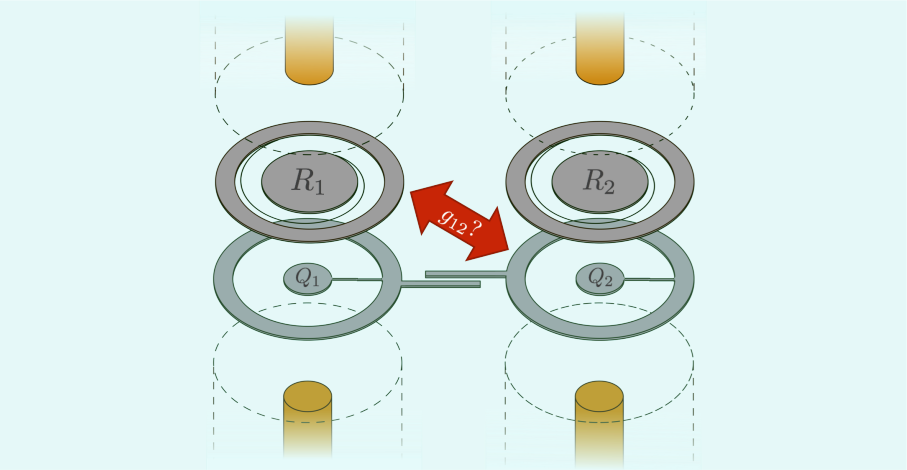

Figure 6.6: Depiction of the circuit cross-coupling between resonator R_1 and qubit Q_2, labelled as g_{12}.

Another aspect of the 3D layout of this architecture to evaluate is the cross-coupling between neighbouring qubit and resonator. In particular given resonator R_1 and qubit Q_2, we wish to know the coupling rate g_{12}. Stray coupling between these circuits can lead to unwanted measurement-induced dephasing of a Q_2 while the state of the Q_1 is read, and so it is important that g_{12} is much smaller than the coupling between qubit and resonator within a unit cell g_{11}. In order to determine g_{12} we can measure the dispersive shift as a result of this cross coupling χ_{12}, and determine g_{12} using Eq. (5.2). Since we

expect g_{12} to be small, we expect χ_{12} to be too small to measure with a single-excitation spectroscopy experiment as in Subsec. 5.2.3. Instead, a larger number of photons will need to be put into R_1 before the shift can be resolved. A similar study has been previously demonstrated on a 2D circuit QED architecture in [120]

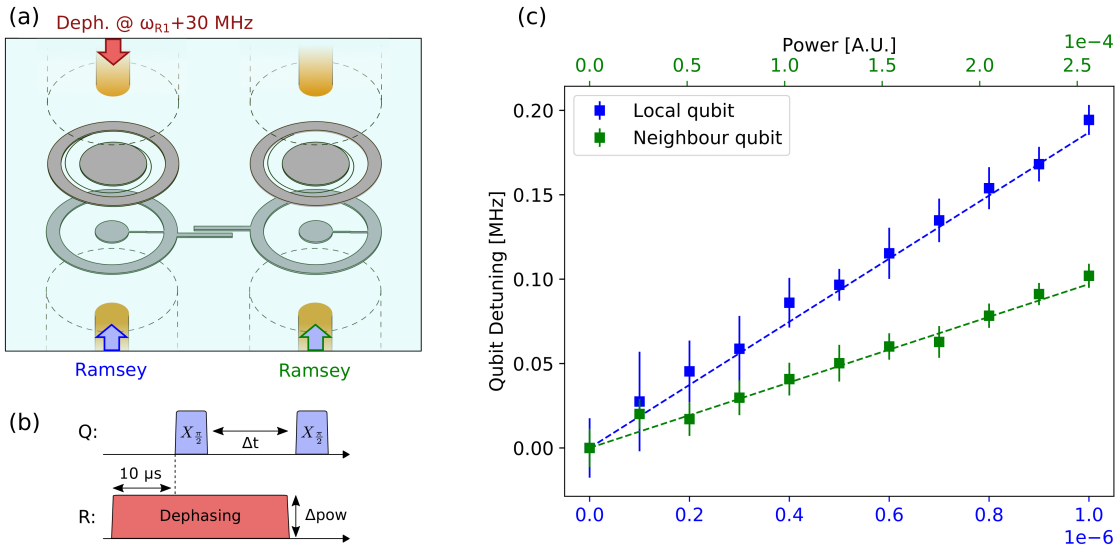

Figure 6.7: Determination of the cross-coupling g_{12} between resonator 1 and qubit 2 on 4Q3. (a) Two sets of Ramsey experiments are carried out, the first on the local qubit Q_1 (blue) and the second on the neighbouring qubit Q_2. The dephasing pulse to R_1 is intentionally detuned by +30 MHz (see main text). (b) Pulse scheme for the Ramsey experiment used to generate each point in (c), a dephasing pulse is applied with a chosen power, 10 μs before the start of a conventional Ramsey sequence applied to the qubit in question. (c) Measured dephasing rates from a set of Ramsey experiments with varying dephasing pulse powers. The two traces account for the measuring dephasing rates of the local qubit Q_1 (blue data and bottom x-axis) and the neighbouring qubit Q_2 (green data and top x-axis). Points are extracted dephasing rates from the Ramsey traces and dashed lines are linear fits. As explained in the main text the ratio of the gradient of the two slopes is used to calculate the cross-coupling $g_{12} = 19$ MHz.

Fig. 6.7 shows the principle and demonstration of the experiment used to determine g_{12}, which is similar to the methods employed in [106, 119, 120]. As with the resonator-port selectivity, it involves a calibration measurement followed by a determination measurement. In both cases, Ramsey experiments are performed with a dephasing pulse applied before and during the qubit's free-evolution in order to populate the resonator with a steady-state average photon number $\bar{n}$ (the pulse scheme is shown in Fig. 6.7(b)). A set of Ramsey experiments is carried out with a varying amplitude of the dephasing pulse in order to populate the resonator with different numbers of photons, and the AC

Stark-shifted qubit frequencies are extracted from the Ramsey oscillations. According to Eq. (2.49) the relationship between the mean photon number in the resonator and the AC Stark shift is linear. Crucially the resonator is driven detuned, such that the drive is several χ away from ω_{r0} (in this case +30 MHz). This is to more effectively populate the resonator ambiguous of qubit state, and achieve a lower measurement-induced dephasing rate for the same $\bar{n}$ compared to the resonant drive case, thus allowing for longer Ramsey experiments with a better determination of frequency. For the calibration experiment, the Ramsey interferometry is performed on Q_1 (blue) and for the determination experiment on Q_2 (green). Fig. 6.7(c) shows the results of both experiments, with the expected linear dependence of AC-stark shift on drive power in both cases.[3] From Eq. (2.49) we can arrive at the expression $\chi_{11}/\chi_{12} = \frac{\partial\omega_1}{\partial P}/\frac{\partial\omega_2}{\partial P}$, i.e. the ratio of the dispersive shifts is the ratio of the gradients of the two slopes. Since we experimentally determine the two slopes, as well as χ_{11} from spectroscopy experiments, we can simply solve for $\chi_{12} = -13$ kHz in this experiment, and using Eq. (5.2) compute the corresponding value of $g_{12} = 19$ MHz.

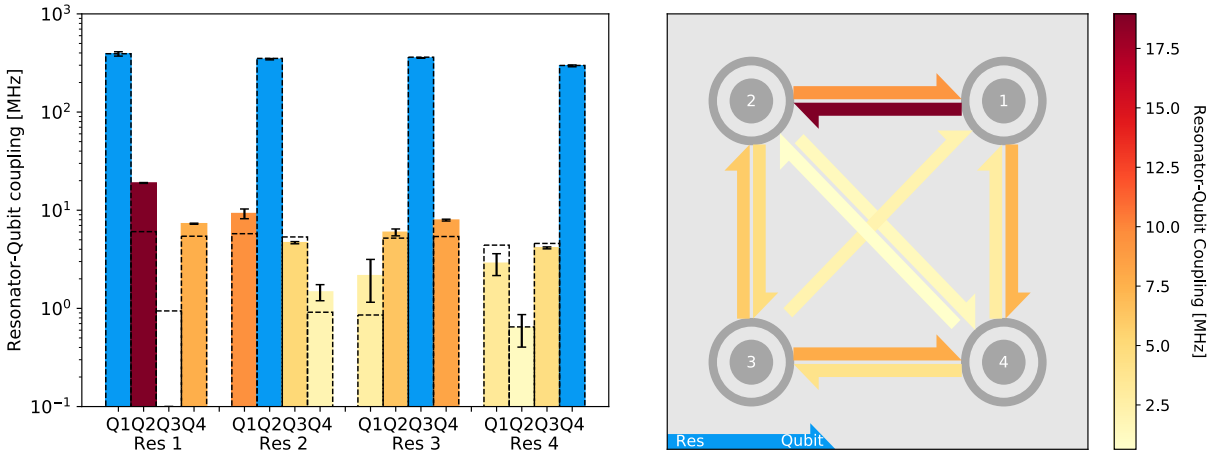

Figure 6.8: Measured values of resonator-qubit cross-coupling between all pairs in 4Q3, the same data is plotted in both (a) and (b). (a) Coupling values measured by experiment (solid bars) as well as simulated values (dashed outlines). Solid blue bars are the measured couplings between resonator-qubit unit cell pair, other bar colourings reflect the magnitude of crosstalk according to the same colour bar in the neighbouring plot. (b) Geometric depiction of the measured cross-coupling, arrows indicate the crosstalk between resonator to qubit as indicated by the scheme arrow in the bottom left.

[3]Interestingly the powers used in the determination experiment are beyond that producing the critical photon number n_c, and yet we still see a linear dependence. In fact the linearity can continue past n_c due to the competing effects of the higher-order terms [84].

g_{ij} can be determined for every resonator-qubit pair in order to build the full coupling matrix of the system, show in Fig. 6.8. We observe that the cross-couplings are ≈ 60 smaller than the couplings within unit cells, with average values 5.9 MHz for the cross-coupling and and 346 MHz within cells. To evaluate this result, we calculate the measurement induced dephasing rate on a qubit with 5.9 MHz cross-coupling to a resonator, with $\kappa = 5$ MHz and that is driven such that $\bar{n}_- = 1$, and find a value of $\Gamma_m \approx 5 \times 10^{-6}$ MHz. This can be compared to the rate of ≈ 13 MHz for a qubit with coupling to the resonator of 346 MHz. From the results we also observe that the cross-coupling is larger between neighbouring qubits than between next-nearest neighbours (diagonals). This is to be expected due to the qubit-qubit coupling between neighbouring cells, which results in an increased indirect coupling between resonator and neighbouring qubit due to the combination of the direct coupling between the resonator and its own qubit, and the direct coupling of the qubit to the neighbouring qubit. A simple analytical calculation using $g_{rq}g_{qq}\left(\frac{1}{\Delta_{rq}} + \frac{1}{\Delta_{qq}}\right)$ on the values for all 8 nearest neighbour pairings produces an average indirect coupling of 2.8 MHz. Note that one next-nearest neighbour cross-coupling could not be determined, as the measurement became non-linear before an appreciable shift in the qubit frequency could be observed.

6.2.3 Qubit Port Selectivity

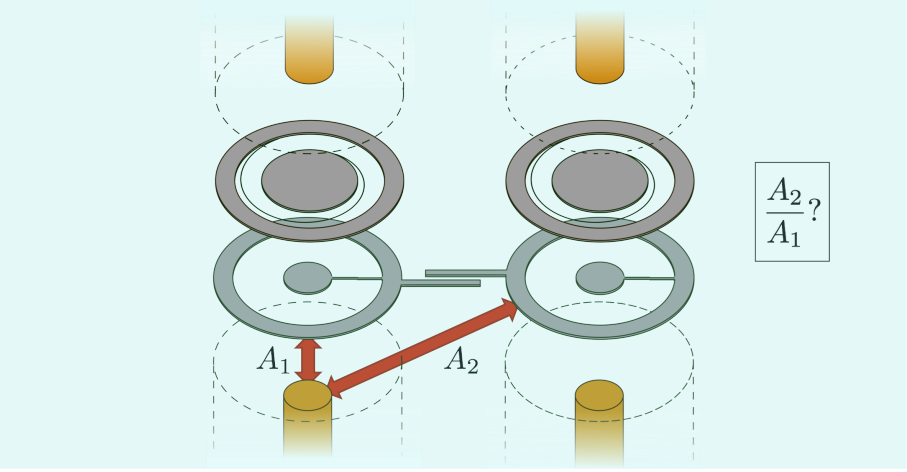

Figure 6.9: Depiction of the definition of qubit port selectivity between control port 1 and qubit 2. It is the ratio of signal amplitudes A_1 and A_2, applied to control port 1 needed to achieve the same Rabi drive rate on both Q_1 and Q_2.

We define the qubit-port selectivity X_{ij}^{Q} between a control port i and a target qubit j as the ratio of amplitudes required to obtain the same rabi rate on the target qubit j from a port i compared to driving the port's local qubit. This ratio is the same as m_{12} from equations Eq. (2.31) and Eq. (2.32). We can define it in dB with

$$X_{ij}^{Q} = 20\log_{10}\left(\frac{\epsilon_{ii}}{\epsilon_{ij}}\right) = 20\log_{10}\left(m_{12}\right), \tag{6.2}$$

where ϵ_{ij} is the amplitude applied to port i in order to get a 1 MHz Rabi-rate on qubit j.

The principles of the experiment to determine the value X_{ij}^{Q} are necessarily different from those used in the last two experiments. If one naively attempts to directly drive qubit j from port i, then extra rotations of the target qubit from the cross-resonance interaction will arise in addition to the direct driving of the target. In addition, some of the direct drive rotation will arise from the quantum crosstalk inherent of the two-qubit coupled system, however we only wish to measure the drive rate as a result of direct coupling between the control's drive port and the target qubit.Thus, X_{ij}^{Q} must be obtained by measuring all of the drive rates in the Hamiltonian given by Eq. (2.27), and then solving the corresponding system of equations for m_{12}.

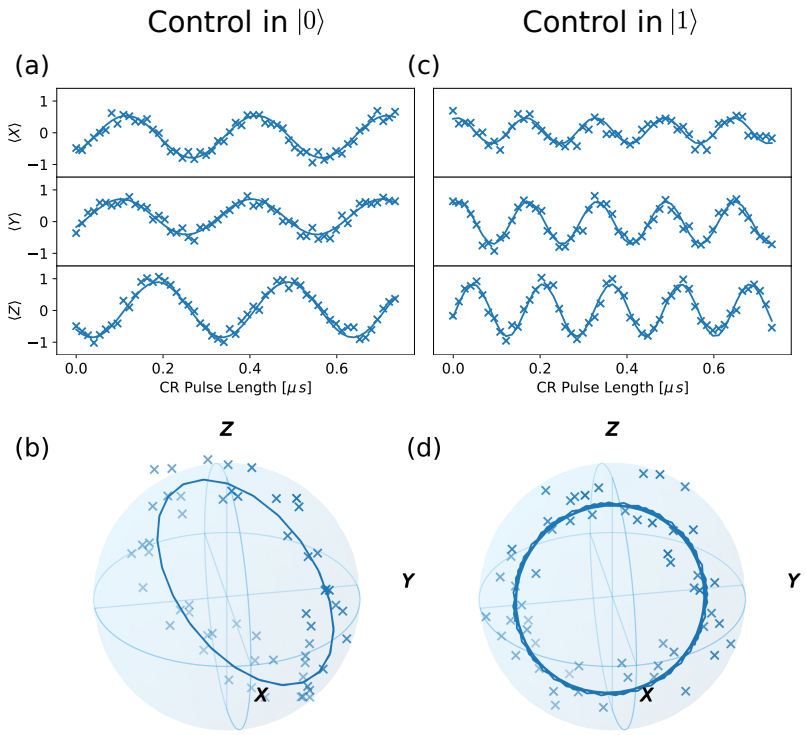

Figure 6.10: Tomography of the target qubit during cross-resonance when the control qubit is in $|0\rangle$ ((a)/(b)) and $|1\rangle$ ((c)/(d)). (a)/(c) Tomography of the target qubit during a cross resonance drive applied to the control qubit. Points are data and solid lines are projections of the fits carried out in (b)/(d) respectively. (b)/(d) Bloch sphere representation of the data gathered in (a)/(c), the data points are first fitted to find an axis of rotation, and then a rotation rate, phase and amplitude as represented by the solid lines.

The determination of the Hamiltonian terms is achieved via Hamiltonian tomography of the two-qubit system when subject to a cross-resonance drive, i.e. a tone with the frequency of the target qubit is applied to the control qubit's port. In order to distinguish between rotations caused by the cross-resonance terms ($Z\hat{X}, Z\hat{Y}$) and the crosstalk terms ($I\hat{X}, I\hat{Y}$), the tomography is performed with the control qubit in the ground, and then excited state. In the two tomography experiments with the control qubit in $|g\rangle$ and $|e\rangle$, the rotation rates of the target qubit about $\hat{X}$, $\hat{Y}$ and $\hat{Z}$ can be determined and the

two-qubit Hamiltonian terms extracted with,

$$\begin{bmatrix} \Omega_{ZX} \\ \Omega_{ZY} \\ \Omega_{ZZ} \end{bmatrix} = \frac{1}{2} \left(\begin{bmatrix} \Omega_X^{|g\rangle} \\ \Omega_Y^{|g\rangle} \\ \Omega_Z^{|g\rangle} \end{bmatrix} - \begin{bmatrix} \Omega_X^{|e\rangle} \\ \Omega_Y^{|e\rangle} \\ \Omega_Z^{|e\rangle} \end{bmatrix} \right), \tag{6.3}$$

$$\begin{bmatrix} \Omega_{IX} \\ \Omega_{IY} \\ \Omega_{IZ} \end{bmatrix} = \frac{1}{2} \left(\begin{bmatrix} \Omega_X^{|g\rangle} \\ \Omega_Y^{|g\rangle} \\ \Omega_Z^{|g\rangle} \end{bmatrix} + \begin{bmatrix} \Omega_X^{|e\rangle} \\ \Omega_Y^{|e\rangle} \\ \Omega_Z^{|e\rangle} \end{bmatrix} \right). \tag{6.4}$$

These Hamiltonian terms by themselves are sufficient to make a calculation of m_{12}, however in order to make for a more convincing and accurate determination it is beneficial to perform the same pair of tomography experiments for different amplitudes of the applied cross-resonance drive in order to demonstrate the linear relationship between drive amplitude and the drive rates $\Omega_{ZX}, \Omega_{ZY}, \Omega_{IX}$ and Ω_{IY}. In addition, for each tomography experiment, the phase of applied cross-resonance tone is initially tuned up such that Ω_{ZX} is maximised and Ω_{ZY} minimised (this was implemented to make the calculation of m_{12} more simple by assuming $\Omega_{ZY} = 0$, however in the end of the full calculation was used). The results of such a sweep are shown in Fig. 6.11, the linear relationship between drive amplitude and rotation rate is clear. To account for variation in the accuracy of the determination of the cross-resonance drive phase, the magnitude of the cross-resonance and crosstalk drive rates are also plotted to obtain a more fair measure of the linearity.

In order to calculate m_{12}, we solve the following set of non-linear equations for $m_{12}, \phi_{12}, \Omega_{12}^X$ and Ω_{12}^Y given calculated values of μ and ν, and drive ratios obtained from

the fitted slopes:

$$\Omega_{ZX} = \Omega_{12}^{X}\mu, \tag{6.5}$$

$$\Omega_{ZY} = \Omega_{12}^{Y}\mu, \tag{6.6}$$

$$\Omega_{IX} = \Omega_{12}^{X}\nu + m_{12}\left(\Omega_{12}^{X}\cos\phi_{12} + \Omega_{12}^{Y}\sin\phi_{12}\right), \tag{6.7}$$

$$\Omega_{IY} = \Omega_{12}^{Y}\nu + m_{12}\left(\Omega_{12}^{Y}\cos\phi_{12} - \Omega_{12}^{X}\sin\phi_{12}\right). \tag{6.8}$$

Values of μ and ν are calculated from Eq. (2.34), Eq. (2.35) based on the two-qubit parameters determined from separate experiments.[4] For the experiment shown in Fig. 6.11, we obtain values of $m_{12} = 1.60\% \pm 0.01$, and $\phi_{12} = -0.867 \pm 0.006$.

These experiments were used to measure the qubit-port selectivity across all ports and qubits of device 4Q3, producing the results shown in Fig. 6.12. It is important to note that this procedure could not be used on qubit pairs detuned by > 1 GHz due to the limited IF bandwidth of the control electronics, and on 4Q3 this applies to the next nearest-neighbour pairs Q1↔Q3, Q2↔Q4, as well as the far detuned neighbours Q1↔Q4. To obtain a value, the tomography was performed with the control qubit in ground only, and the measured rotation was taken to entirely be attributed to $I\hat{X}$ and $I\hat{Y}$. This approximation assumes that $\mu \ll m_{12}$ which is fair in these cases as the qubit detunings are large, and for the case of next-nearest neighbouring qubits which are not directly coupled, an even smaller qubit-qubit coupling compared to directly coupled pairs.

[4]Note that it is also possible to not assume knowledge of μ and ν and instead use values for Ω_{12}^{X}, and Ω_{12}^{Y}, however without tunable qubits it is not possible to get an accurate determination of the transfer function of the line, and thus a reasonable estimate of these values.

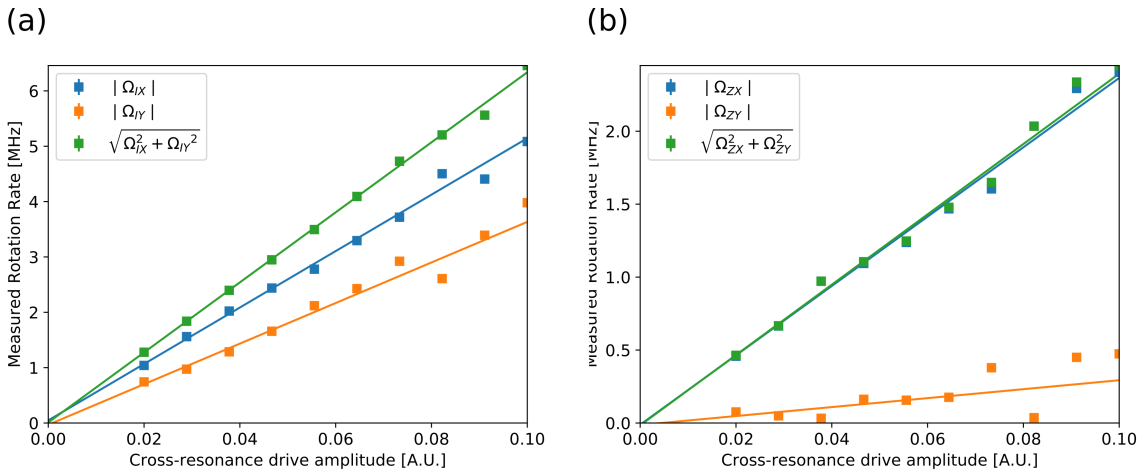

Figure 6.11: Plots of the measured Hamiltonian-term drive rates with cross-resonance drive amplitude used to determine the qubit port selectivity between port 1 and qubit 2 on 4Q3. (a) shows measurements of direct driving terms Ω_{IX} and Ω_{IY} responsible for crosstalk, and (b) shows measurements of conditional driving terms Ω_{ZX} and Ω_{ZY}. The magnitude of the direct and conditional rotation rates are plotted in green, and confirm the linear relationship between cross-resonance drive amplitude with rotation rate. Points are data and solid lines are linear fits. The fitted gradients, as well as the calculated cross-resonance parameters μ and ν, are used to determine the crosstalk from direct coupling of the target to the control qubit's port, with a value of $m_{12} = 1.6 \pm 0.01\%$ in this instance.

The values of m_{12} determined from the experiment on 4Q3 range from $1.1\% - 6.7\%$, with a mean value of 3.2%. This is comparable to the mean value of the calculated quantum crosstalk $\bar{\nu} = 2.79\%$ showing that this system experiences significant classical crosstalk. These values when converted to dB are also comparatively larger than the measured resonator-port selectivity. Interestingly close agreement to these values can be obtained from the classical simulation, and in Subsec. 6.2.4 we use this to conclude the significant difference is the presence of coupling arms in the case of the qubits. One aspect of the results is visible in Fig. 6.12(b) but is not reflected in simulation is that the value of m_{12} is always larger when the qubit chosen as the control has the higher frequency of the pair, i.e. the drive port selectivity to the lower frequency qubit of the two was always worse. We were unfortunately not able to obtain a satisfactory explanation of this phenomenon.

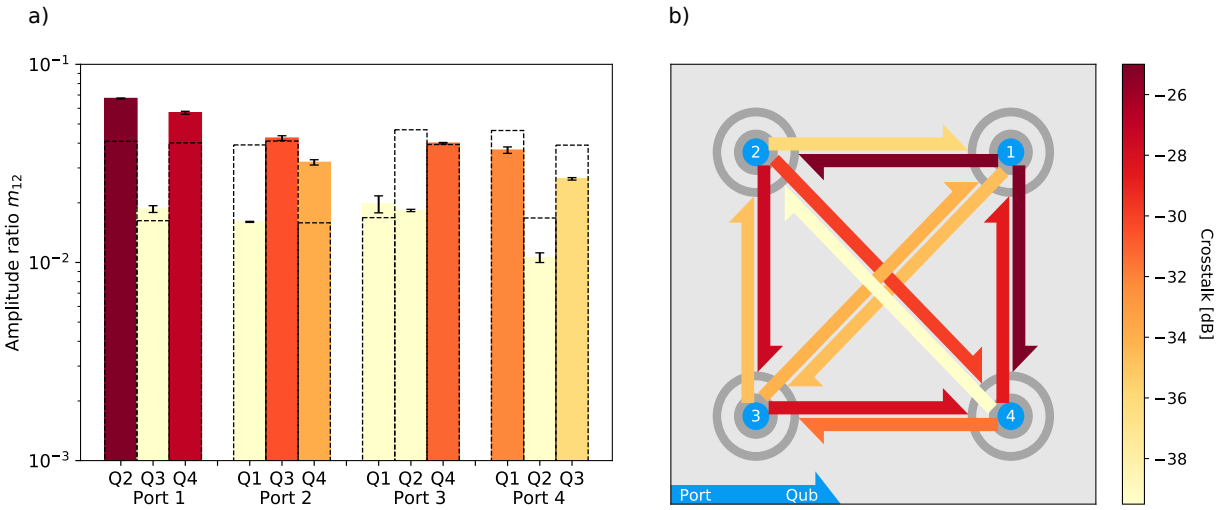

Figure 6.12: Measured values of qubit-port crosstalk between all pairs in 4Q3, the same data is plotted in both (a) and (b). (a) amplitude ratios m_{12} measured by experiment (solid bars) as well as simulated values (dashed outlines). Bar colouring reflects the magnitude of crosstalk according to the same colour bar in the neighbouring plot. (b) Geometric depiction of the measured crosstalk, arrows indicate the crosstalk between port to qubit as indicated by the scheme arrow in the bottom left.

6.2.4 Simulations of Selectivity

All the results in the three preceding sections were compared against selectivity values obtained from the same finite-element simulation. Using the method outlined in [121], a driven terminal simulation was carried out for each qubit and resonator frequency, with circuit ports defined at each inductor or Josephson junction and drive ports at each control pin. The extracted multiport impedance matrix was analysed with the derived impedance response formulas to determine the drive port selectivity (using eq. 22 of [121]) and circuit cross-coupling (using eq. 38 of [121]).

The geometry of the simulation was matched to the geometry of the sample holder and circuit design. There were two further modifications in order to more closely match the experiment, first the separation of the resonator drive pins to the circuits was modified from the design value of 400 μm such the the simulated photon decay rates κ matched the measured values for each resonator (this accounts for inaccuracies in setting the separation of the pins). Secondly the self-capacitance of the resonators (the effective capacitance across the inductor) was adjusted such that the qubit-resonator couplings matched when calculated using the impedance response formulas. The fitted values with average 180 fF

were consistent with experimentally determined values obtained from other experiments.

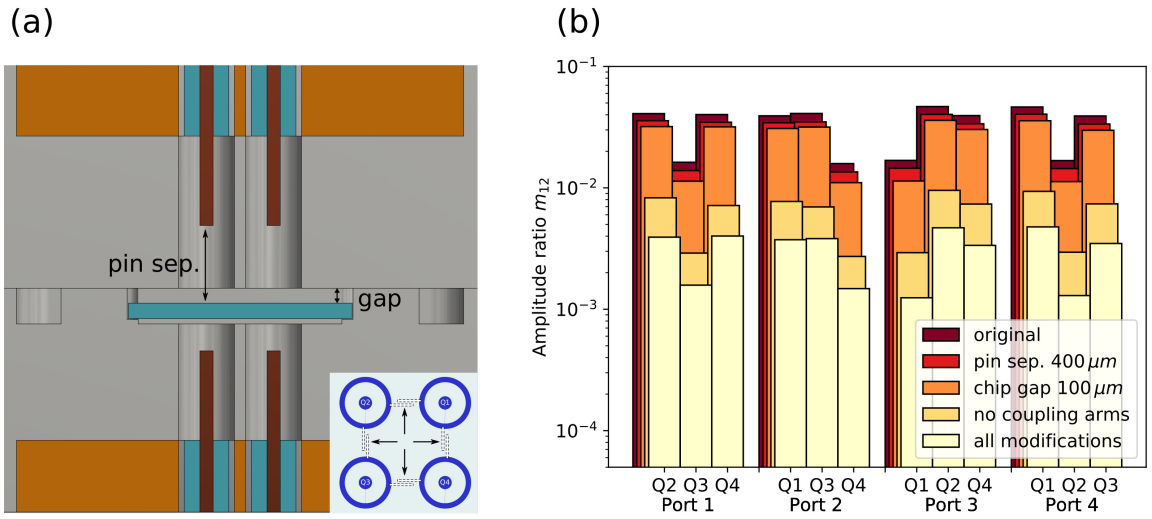

Figure 6.13: (a) Side cutout view of the chip inside the sample holder, with key features indicated by arrows. Inset: A depiction of the circuit layout of a four qubit device with the coupling arms highlighted in white. (b) Simulated qubit port selectivity values with each of the geometry adjustments mentioned in the main text, "all modifications" incorporating all three changes. For comparison, the average value of the resonator drive port selectivity from the original simulation is 3.2×10^{-3} when expressed as an amplitude ratio.

One benefit of the agreement between values from theory and experiment is that we can use the simulation to investigate how the measured values relate to the design. In particular we performed simulations to investigate the disparity between the resonator and qubit drive port selectivity, which had average values of -52 dB and -33 dB respectively despite the geometry of circuit to drive port being similar in the two cases. In terms of the packaging and design, there were three clear differences between the control of resonators and qubits, the separation of the circuits to the drive pins (400 μm v.s. 1100 μm respectively), the size of the gap between the circuit face and the sample holder (100 μm v.s. 200 μm), and finally the presence of the qubit coupling arms. We performed three more simulations, each evaluating the impact of modifications in accordance with each difference, namely reducing the pin separation to 400 μm, the chip gap to 100 μm and removing the coupling arms. In addition, a fourth simulation was carried out incorporating all three modifications. The calculated values of the selectivity are shown in Fig. 6.13(b), which reveal that by far the most significant contribution to the difference

in selectivity is the presence of the coupling arms. However it is still the case that the other two modifications also contribute, as the selectivity is improved when all modifications are considered. These values can compare to the average value of the resonator drive port selectivity from the original simulation, which when expressed as an amplitude ratio has value 3.2×10^{-3}. In future, the design of the coupling arms can be changed, for example to interdigitated capacitors, such that they do not extend as close to the other qubit's driving pin, and the chip gap can also be reduced. The qubit control pins cannot be brought as close as 400 μm as this will likely limit T_1 through Purcell loss, however there are many more modifications that can be made to improve selectivity further such as simply increasing the unit-cell pitch.

In addition to the drive port selectivity disparity, the effects of a 50 μm offset of the chip with respect to the drive ports was simulated, to investigate the effects of misalignment between circuits and drive ports with 50 μm being the maximum amount of displacement allowed for by the sample holder. However only very small changes ($\Delta X_{ij}^{Q} < 1$ dB) or asymmetries ($X_{ij}^{Q} - X_{ji}^{Q} < 1$ dB) were produced from such a shift.

6.3 Two-Qubit Gates using Cross Resonance

This architecture employs fixed frequency transmon qubits with static dispersive couplings. One means by which a two-qubit gate can be realised under these conditions is that of the cross-resonance interaction. First proposed in [64], cross-resonance has been used to perform high-fidelity entangling operations between qubits [122, 123, 29] by utilising a $Z\hat{X}$ rotation to form a CNOT gate. In the extension to multiple qubits, we have targeted circuit parameters to achieve two-qubit gates between directly coupled pairs with the cross-resonance interaction. In this section we present direct measurements of two-qubit parameters, as well as the results to date on calibrated $Z\hat{X}_{\frac{\pi}{2}}$ gates performed on several fabricated devices.

6.3.1 Measurement of Coupling J

Optimisation of the fidelity of a two-qubit gate with cross-resonance requires a precise characterisation of the two-qubit Hamiltonian. Whilst Δ_q can be obtained from simple spectroscopy of both qubits, an estimate of J can be found by measuring the qubit-qubit cross-Kerr shift ξ and make a calculation using Eq. (2.33). To that end, a two-qubit Ramsey experiment [65] was performed on the pair of qubits in question. By comparing the frequency of the Ramsey oscillations with and without the paired qubit in the excited state, the magnitude and sign of 2ζ is determined. Performing full tomography of the qubit state also allows us to measure Ω_{ZI} and Ω_{IZ}, the qubit detunings from the centre frequency $\omega_{01}+\zeta$. We choose to drive cross-resonance at this frequency to avoid a constant single qubit error term developing on both qubits, that would otherwise appear in the process tomography of the two qubit system.

For some devices, the Ramsey lifetime was too short to perform this method or the value of ζ was too small determine with this method. In these cases a simultaneous echo sequence was used to take advantage of the longer lived T_2^E coherence time (see inset of Fig. 6.14(c)). As in the conventional spin echo experiment, the effect of the simultaneous echo is to filter away the effects of any slow noise on the qubit frequency and inaccuracy in qubit frequency calibration. However with this scheme the effects of the $\zeta\hat{ZZ}$ term will still be included since it picks up two negative signs in total, one from each echo, and is not cancelled out. Fig. 6.14(b) shows this measurement on 4Q3:2 $\leftrightarrow$ 3, determining $\zeta = 0.09(2)$ MHz. The downside of this approach is that full tomography is not possible, and in particular Ω_{ZI} and Ω_{IZ} will not be determined but rather must be calculated based on single qubit Ramsey experiments and the measured ζ. This technique was sufficient to measure ζ between two directly coupled qubits, however it proved insufficient to measure the predicted low values of $\zeta \approx 2$ kHz between next-nearest neighbours, as the coupling is smaller (simulated to be ≈ 2 MHz, see Subsec. 6.2.4) and the detuning larger than with coupled pairs. As a confirmation, the same experiments were carried out on the next nearest-neighbour pairs in 4Q3 which produced no apparent oscillation over ≈ 30 μs suggesting ζ is below ≈ 30 kHz. The sensitivity of this technique would be improved by

longer spin echo coherence times T_2^E

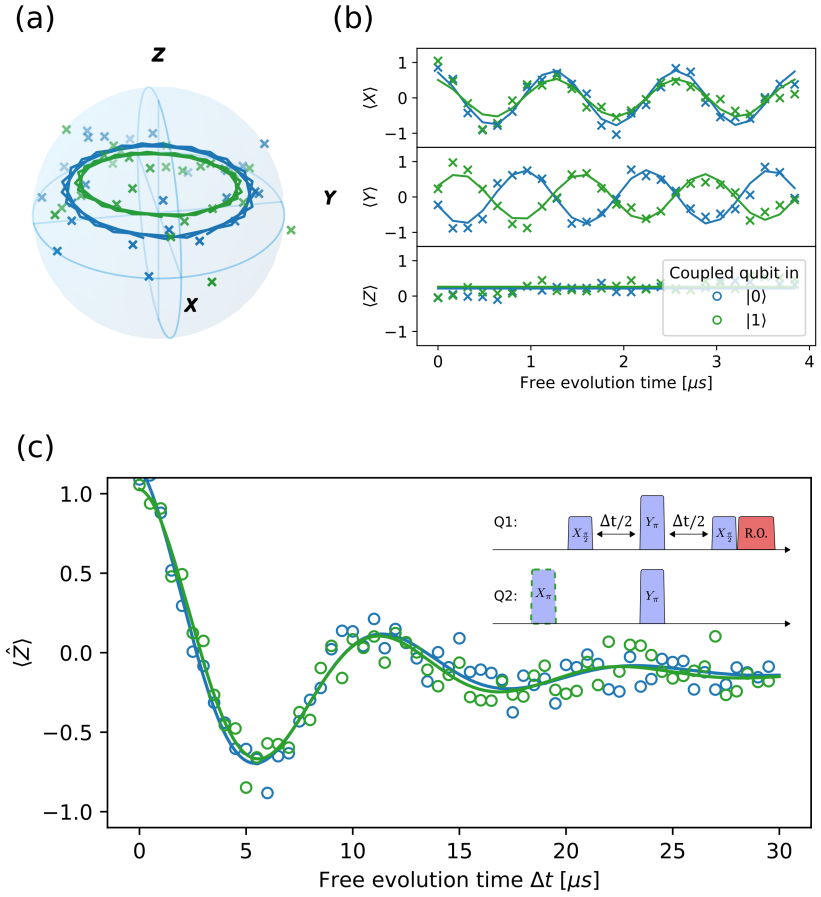

Figure 6.14: Demonstrations of the two methods of measuring the qubit-qubit coupling J. (a) Results from a target qubit of a two-qubit Ramsey experiment performed with the control qubit in ground and excited. The device pair is 4Q3:2 $\leftrightarrow$ 1, and we extract values of $\Omega_{ZI} = -11$ kHz, $\Omega_{\mathrm{ZI}} = -4$ kHz and $\Omega_{ZZ} = -750$ kHz. (b) shows the projection of the data and fit in (a) onto the axes of the Bloch sphere. (c) Measurement of Ω_{ZZ} using the simultaneous echo experiment performed on pair 4Q3:2 $\leftrightarrow$ 3 determining $\Omega_{ZZ} = 90$ kHz. Inset: the pulse scheme of the experiment, two versions are performed with and without the initial $\hat{X}_\pi$ pulse on the coupled qubit.

6.3.2 Performing cross-resonance and two qubit gates

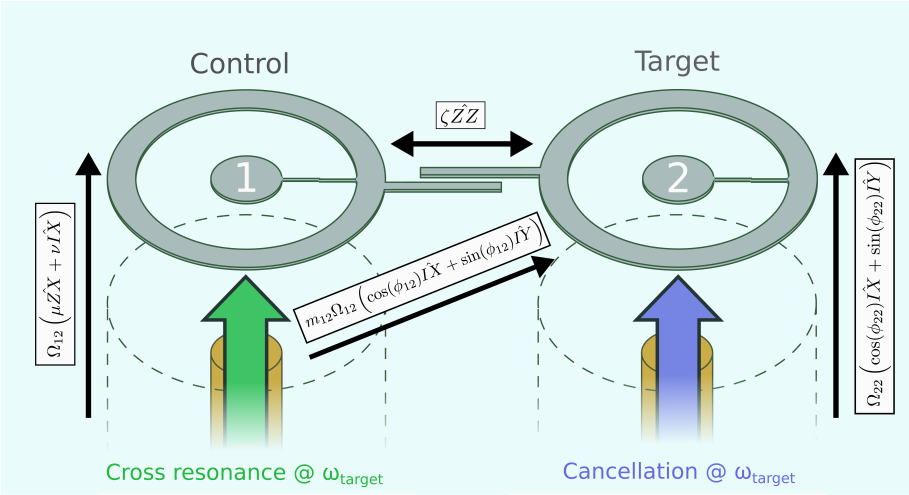

Figure 6.15: Schematic of the operation of the cross-resonance interaction. The qubits 1 and 2 are labelled as the control and target respectively. Applying a tone to the control qubit at the target qubit's frequency ω_{target} (green arrow) activates rotations about $Z\hat{X}$ and $I\hat{X}$ proportional to the cross resonance drive strength Ω_{12}. Crosstalk between the control drive pin and the target qubit generates additional rotations about $I\hat{X}$ and $I\hat{Y}$. The unwanted $I\hat{X}$ and $I\hat{Y}$ rotations are counterbalanced and cancelled out by the application of a second cancellation tone to the target qubit at ω_{target} (blue arrow). Lastly, there is an always-on rotation about $Z\hat{Z}$ due to the cross-Kerr shift between the two qubits.

We first give an overview of how cross-resonance is used to construct a CNOT gate between two qubits. As explained in Sec. 2.4, a cross-resonance drive consists of driving a "control" qubit at the frequency of a coupled "target" qubit. The resulting cross-resonance interaction generates a rotation about $\hat{X}$ on the target qubit, with the sign of the rotation dependent on the state of the control qubit, i.e. a rotation about $Z\hat{X}$. The operating scheme is depicted in Fig. 6.15. Whilst in principle the cross-resonance drive is all that is necessary, there is in fact also direct driving of the target qubit both from a quantum crosstalk that arises from the cross-resonance interaction as well as classical crosstalk due to direct coupling between the control line and the target qubit, generating rotations about $I\hat{X}$ and $I\hat{Y}$. To negate these effects, a second resonant tone is applied to the target qubit, to counter-rotate and cancel this crosstalk[5]. Utilising this interaction to form a CNOT

[5]whilst the quantum crosstalk will be entirely in phase with the cross-resonance drive, i.e. a rotation about $I\hat{X}$, the phase of the classical crosstalk can vary depending on the phase difference resulting from the different path lengths between the control line to the qubits, and so rotations about $I\hat{Y}$ are usually also observed.

gate involves performing the circuit $(\hat{ZX}_{-\frac{\pi}{2}})(\hat{IX}_{\frac{\pi}{2}})(\hat{ZI}_{\frac{\pi}{2}})$ shown in Fig. 6.16(a). The $\hat{ZX}_{-\frac{\pi}{2}}$ gate is generated by the application of a calibrated cross resonance and cancellation tone for a fixed gate time. Whilst this can be achieved with the simplest scheme shown in Fig. 6.16(b), in this thesis we use an echo scheme (Fig. 6.16(c)) first shown in [29]. The refocusing of rotations from this echo scheme actively cancels out any unwanted rotations about $\hat{IX}$, $\hat{ZI}$, and small unwanted rotations about and $\hat{ZZ}$ and $\hat{IY}$ to first order [29]. In our devices a large $\hat{IY}$ error is typical (see Subsec. 6.2.3) and so active cancellation of the crosstalk generating this error is critical in order for the $\hat{IY}$ rotation to be small enough for the echo scheme to be effective. One caveat of this scheme is that since $\hat{ZZ}$ does not commute with the $\hat{ZX}$ operation, an effective $\hat{IY}$ rotation proportional Ω_{ZZ}/Ω_{ZX} is generated that is not cancelled by the scheme [65]. This error could be removed with a post $\hat{IY}$ rotation, but this was not done here. An additional benefit is the reduction of decoherence errors due to the refocusing of slow noise processes as in the T_2^{Echo} experiment.

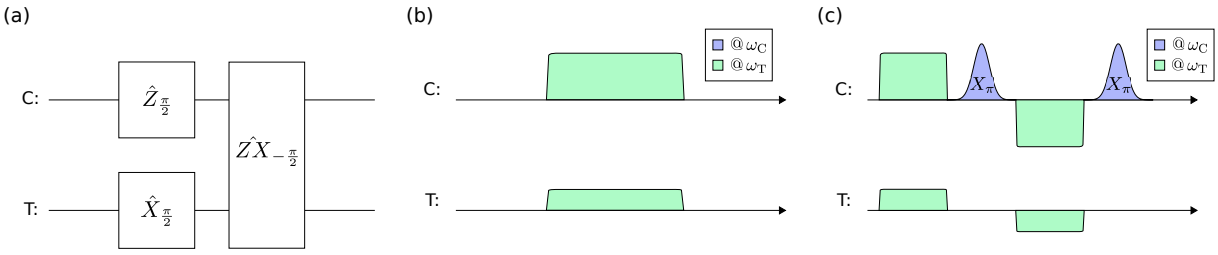

Figure 6.16: (a) Circuit for performing a CNOT gate using a $\hat{ZX}_{-\frac{\pi}{2}}$ pulse. (b)-(c) $\hat{ZX}_{-\frac{\pi}{2}}$ pulse sequences for the simple and echo cross resonance schemes respectively, with a cross resonance pulse applied to the control qubit (C) and a cancellation tone to the target (T). The inversion of the pulses in (c) signify a 180° phase difference.

Performing a $\hat{ZX}_{\frac{\pi}{2}}$ gate with high fidelity requires a tune-up procedure that can accurately determine the appropriate amplitudes and phases of both the cross-resonance and cancellation drives. Developing this procedure was the work of Andrew Patterson and an in depth explanation can be found in [77, 65], however for clarity we present an overview of the procedural steps.

1. First full state-tomography of the two-qubit system under a cross-resonance drive and with the control in $|0\rangle$ and $|1\rangle$ is carried out (the same experiment as the one used in Subsec. 6.2.3). From this a measure of the drive rates $\Omega_{ZX}, \Omega_{ZY}, \Omega_{IX}$ and

Ω_{IY} is obtained. With knowledge of these drive rates, we can make corrections to the phase and amplitude of the cross-resonance drive in order to achieve a $Z\hat{X}_{-\frac{\pi}{2}}$ rotation in the target time with minimal $Z\hat{Y}$ rotation. The tomography experiment is then repeated with a cancellation tone in order to find the appropriate phase and amplitude of the cancellation such that there is minimal direct driving of the target about $I\hat{X}/I\hat{Y}$. This tomography is repeated several times until the parameters are sufficiently in range.

2. Whilst in principle this tuned-up pulse sequence performs a $Z\hat{X}_{-\frac{\pi}{2}}$ rotation, we instead wish to use the echo scheme [29] outlined earlier. This tune-up is carried out with several stages of repeated gate tomography [77, 29] again calibrating the amplitude and phase of Ω_{12} and Ω_{22} but this time to produce a $Z\hat{X}_{-\frac{\pi}{4}}$ rotation, again with minimal rotation around $Z\hat{Y}$, $I\hat{X}$ and $I\hat{Y}$. Repeated gate tomography provides a much more sensitive measure of the coherent error from the pulses allowing the pulse to be tuned up with greater accuracy.

3. The previous steps cover how the tune-up works for a fixed gate time and pulse shape, and the gate fidelity of the $Z\hat{X}_{\frac{\pi}{4}}$ operation is then evaluated using process tomography [124] and two-qubit interleaved randomised benchmarking [125, 126]. This tuneup procedure is repeated for different gate times and pulse times in order to maximize the value of the fidelity. For long gate times, decoherence becomes the main limitation, and for short times we drive the qubit hard enough such that higher transmon levels and off-resonant driving of the control qubit become relevant. Similarly the pulse shape will have a trade-off between gate length and driving of higher levels of the transmon, due to the limited anharmonicity of the qubits.

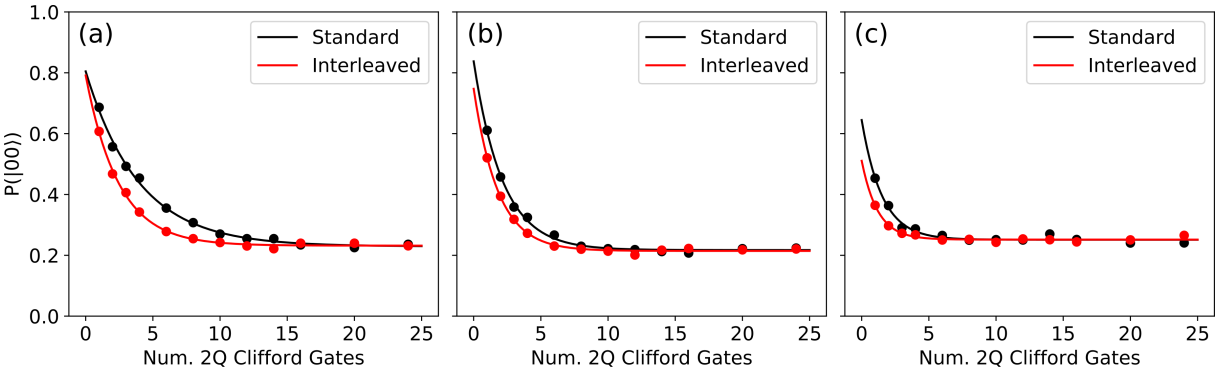

Figure 6.17: Standard and interleaved randomised benchmarking of $Z\hat{X}_{\frac{\pi}{2}}$ gates for the primary qubit pairs on 4Q3. The curves are fitted to an exponential decay and the interleaved gate fidelity calculated according to $F_U = (1 + (d-1)\,\beta_U/\beta)\,/d$, where d is the number of 2Q Clifford gates, and β_U, β are the decay constants for the interleaved and standard benchmarking traces respectively.

Tuneup of two-qubit gates were carried out on four devices in this project, 2Q1 and 4Q1, 4Q2 and 4Q3 (the procedure was unsuccessful for all but the $1 \leftrightarrow 2$ pairs of 4Q1 and 4Q2 due to the low Ramsey lifetimes T_2^* of qubits on these devices). The best fidelities as measured by interleaved two-qubit randomised benchmarking [126] are shown in Table 6.1. These demonstrations show that multi-qubit logic can be implemented within this architecture. Whilst these values are notable, it is worth evaluating possible limitations to the gate fidelities.

We first consider the coherent error due to a significant $\hat{ZZ}$ term. Due to the non-commutation of $\hat{ZZ}$ and $\hat{ZX}$, one effect of the echo scheme is to transform a small $\hat{ZZ}$ error into a smaller effective $\hat{IY}$ error proportional to $\zeta/8$ (a derivation of this is shown in [65]). This issue was significant for pairs of qubits with larger ζ such as 2Q1 and 4Q3:1↔2. This could in principle be corrected with a post rotation, however such a correction was not done here. The next issue is the balance between decoherence and leakage error. The former comes from longer gates and the latter from shorter (higher amplitude) gates. In principle we would like to make our gate as short as possible such that coherence is not the dominant source of error, however leakage error sets the limit of when the gate is too short. In this work, we considered a drive amplitude of 40 MHz to be the upper bound of how hard we could drive before these effects became significant. To improve this limit on cross-resonance gate speed, "efficiency" is important, i.e. we would like a large

	2Q1	4Q1	4Q2	4Q3		
	2↔1	2↔1	2↔1	2↔1	2↔3	4↔3
F_U [%]	97 ± 0.7	95.6 ± 1.2	90.5 ± 3.0	89.3 ± 1.4	93.8 ± 1.8	87.7 ± 5.7
Ω_{ZX} [MHz]	3.0	1.2	2.0	1.0	0.35	0.35
J [MHz]	12.5	5.24	4.87	7.6	6.9	6.8
Δ_q [MHz]	510	557	278	346	628.1	571.5
ζ [MHz]	-0.55	-0.09	0.78	-0.75	-0.09	-0.123
μ [%]	0.91	0.35	0.92	0.96	0.34	0.40

Table 6.1: Gate fidelities F_U, rotation rates Ω_{ZX}, and two-qubit parameters for all $\hat{ZX}_{-\frac{\pi}{2}}$ gates calibrated in this thesis. The pairs are labelled as control↔target. The given errors on the gate fidelities are 90% confidence intervals.

μ ratio such that for the same drive strength we have proportionality more $\hat{ZX}$ rotation. Improving this means achieving the target J and Δ_q parameters when fabricating the device, and so fabrication precision is critical.

6.4 Circuit Temperatures

Residual thermal population of modes in a superconducting device, be it qubits, readout resonators or couplers, gives rise to state preparation and gate errors and induces dephasing of qubit states. In this section we demonstrate conventional methods on multi-qubit devices for directly measuring the residual population in a qubit and an upper bound on the population in the resonator.

6.4.1 Qubit Temperature

Any thermal excitation of qubits can be problematic when using a multi-qubit device for logic. Amongst other issues, they can prevent the correct initialisation of a register (where all qubits are expected to be in their ground states) and can create unwanted dephasing on coupled neighbouring qubits. This motivates a measurement of the qubit temperatures, or more explicitly the residual thermal population in higher energy levels of the qubit. While large thermal populations ($P_1 \gtrapprox 20\%$) can be evaluated by comparing

the heights of the ground and excited peaks in resonator spectroscopy, this method fails to give accurate results when the residual population is smaller.

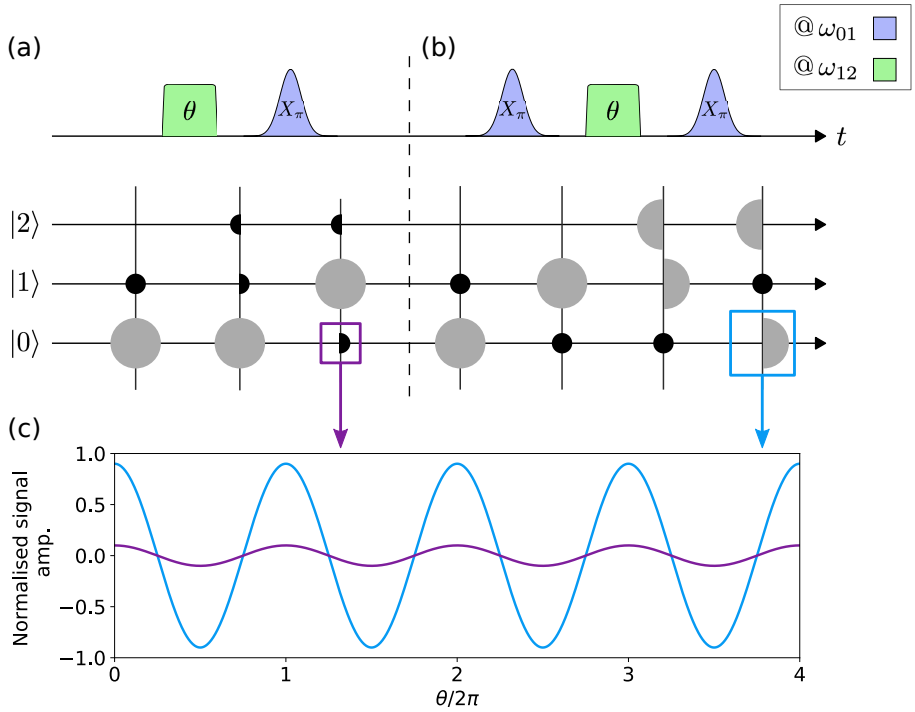

Figure 6.18: Outline of the Rabi population method experiment. Image adapted from [127]. (a)-(b): Pulse sequences used to measure the qubit excited state population using the Rabi population method (RPM), with the qubit the qubit prepared without (a) and with (b) an initial inverting $\hat{X}_\pi$-pulse. Circles represent state populations proportional to their radii. (c): Calculated Rabi traces from either experiment corresponding to a qubit with a 10 % population in $|1\rangle$.

In this thesis we employ the Rabi population method (RPM), previously demonstrated in [127, 128]. The principle of the experiment is based on the linear relationship between the amplitude of a Rabi oscillation and the amount of population being oscillated. In the simplest form of the experiment, two traces are taken. In the first trace, an $\hat{X}_\pi$ pulse is applied to swap the populations in $|0\rangle$ and $|1\rangle$, followed by a pulse of width τ at the ω_{12} transition frequency to drive Rabi oscillations between $|1\rangle$ and $|2\rangle$, and then finally another $\hat{X}_\pi$ pulse to map the population in $|1\rangle$ back to $|0\rangle$. The result of this is to perform a Rabi oscillation between $|0\rangle$ and $|2\rangle$ (the latter of which is assumed to be totally unpopulated). The second trace has the same pulse sequence as the first, without the initial $\hat{X}_\pi$ pulse, so as to measure the Rabi oscillation between $|1\rangle$ and $|2\rangle$. The linear relationship between oscillation amplitude and driven population then allows the fitted

amplitudes of both Rabi oscillations to be compared to get P_1, the residual population in $|1\rangle$,

$$P_1 = \frac{A_1}{A_0 + A_1}, \tag{6.9}$$

where A_0 and A_1 and the amplitudes of the Rabi traces with and without the initial $\hat{X}_\pi$ pulse respectively.

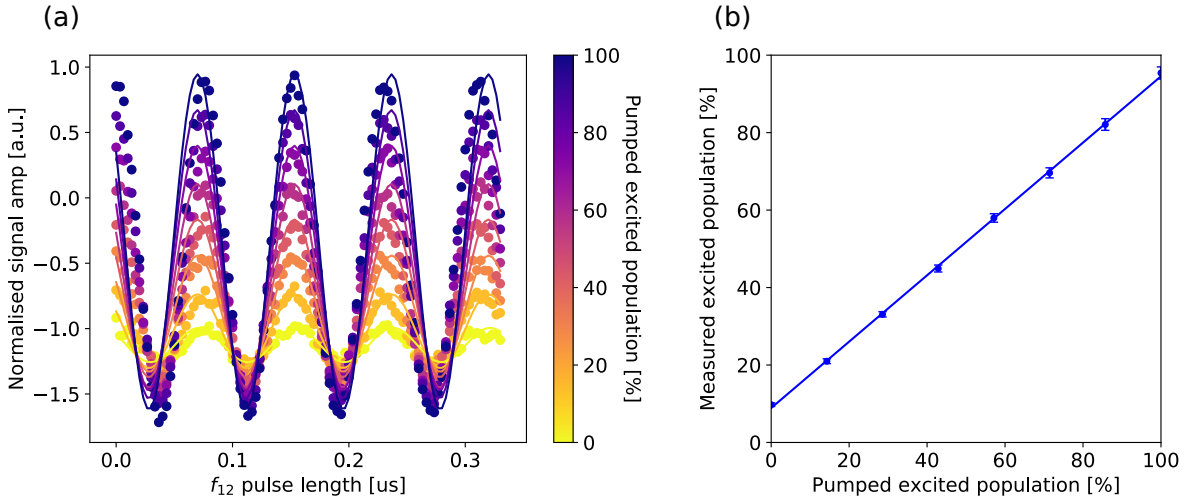

Figure 6.19: Results of an RPM experiment on 2Q1:Q1. (a) Time-Rabi oscillations between $|1\rangle$ and $|2\rangle$, with different initial populations in $|1\rangle$ created by a prior pulse at ω_{01}. Solid lines are fitted to a decaying sinusoid $P_2 = A\sin(\Omega_0\tau)e^{-\frac{\tau}{T_R}}$. (b) Excited state populations calculated from the fitted amplitudes in (a) as Eq. (6.9), plotted against the initially pumped population prior to the Rabi experiment. The intersection of the linear fit with zero pumped population is taken as the residual thermal population, $P_e = 8.5\%$ in this case.

The experiment shown in Fig. 6.19 demonstrates the slightly modified protocol used in this thesis. Since the A_1 is usually very small due to the hopefully small amount of residual population being driven, its determination is more strongly affected by the lower signal to noise ratio. In order to mitigate this and provide a more complete picture, additional Rabi traces with linearly-stepped initially pumped populations are also recorded (this is achieved by linearly sweeping the amplitude of the initial $\hat{X}_\pi$ pulse). Fig. 6.19(a) shows such as set Rabi oscillations on the $|1\rangle \leftrightarrow |2\rangle$ transition, from which one can observe the increasing amplitudes with initially pumped population as well as matching frequencies. The fitted amplitudes can be extracted and used to determine the population in $|1\rangle$ after the initial populating pulse, from a slight modification of the earlier formula

$P_n = A_n/(A_0 + A_1)$. Fig. 6.19(b) shows the calculated populations in $|1\rangle$, plotted against the initially pumped populations. The y-intercept of the linear fit is taken as the residual population in $|1\rangle$, which can be converted to a circuit temperature by assuming a Boltzmann thermal distribution $T_{\text{qubit}} = -h\omega_a \ln(k_B P_1)$ (for this device we find $P_e = 8.5$ % and $T_{\text{qubit}} = 126$ mK). Amongst devices in this thesis measured with this technique, we found a range of qubit temperatures of $65 - 153$ mK, with typical temperatures of ≈ 100 mK (see Appendix B).

When using this technique one must be mindful of some potential issues. Firstly RPM makes the assumption that there is no residual population in $|2\rangle$ or higher levels, and any population there will be discounted from the experiment. If there is significant population in $|2\rangle$ then the total population will be under-represented and the residual thermal population overestimated. Secondly, any decay present in the time-Rabi[6] trace has to be accounted for, and can harm the accuracy of the fit to amplitude.Typically this leads to an underestimation of the amplitude, and so an overestimation of the residual population. Thirdly, the fidelity of the pi-pulses used puts a limit on the lowest residual that can be measured, as the population transfer will not be 100% efficient. This puts a lower bound on the residual population that can be measured of $1 - F_\pi^2$ as two pi-pulses are used in this scheme.

6.4.2 Resonator Temperature

Residual photon population in resonator due to thermal excitations results in an additional source of dephasing for qubits. Stochastic shifts of the qubit frequency due to fluctuations of photon number about the mean value $\bar{n}_{\text{th}}$ give rise to a measurement-induced dephasing rate [129, 130]

$$\Gamma_\phi^{\text{th}} = \frac{\bar{n}_{\text{th}} \kappa \chi^2}{\kappa^2 + \chi^2}. \tag{6.10}$$

Moreover, the dephasing events occur on a time-scale set by κ, often set ≥ 1 MHz for faster readout, so a spin echo pulse scheme will not be sufficient to filter out this contribution. Whilst the effects of shot-noise can be mitigated by ensuring $\chi \ll \kappa$ (reducing

[6] A Rabi experiment where the pulse duration is swept

the information extracted per photon), this comes at a cost of reducing readout efficiency, and so there have been many efforts to lower the temperature of resonators through thermalisation and attenuation [131, 129]. A direct measurement of $\bar{n}_{\text{th}}$ can be obtained from the relative height of the dispersively-shifted peak in pulsed qubit spectroscopy if it is sufficiently high, however measuring small residual populations is much more difficult than for the qubit, as we cannot perform measurements such as RPM. Instead the more common approach in the field is to determine an upper bound[7] of the residual population by attributing the dominant sources of noise at higher frequencies in the power spectral density (PSD) of noise on the qubit frequencyS_Z, to this shot noise. This is achieved by performing a spin-echo experiment as in 5.3.3 to measure the pure dephasing rate Γ_ϕ in the absence of low frequency noise, and then using Eq. (6.10) to determine what value of $\bar{n}_{\text{th}}$ would generate this dephasing rate. This value can then be converted to a temperature by assuming a Boltzmann thermal distribution as in the previous subsection, $T_{\text{res}} = -h\omega_{r0}\ln(k_B\bar{n}_{\text{th}})$. The typical range of values found in recent external experiments are far above the 10 mK operating temperature of most dilution refrigerators, with $6 \times 10^{-4} \leq \bar{n}_{\text{th}} \leq 0.15$ corresponding to 55 mK $\leq \text{T}_{\text{res}} \leq$ 140 mK [129]. As a demonstration, we perform this analysis on the measured $\bar{T}_\phi$ of all four qubits of 4Q3 (Table 6.2) and find similar values of temperature with mean 115 mK indicating that the circuits are indeed significantly hotter than the base temperature of the cryostat.

[7]To directly measure $\bar{n}_{\text{th}}$ or to validate that it is the dominant source of high frequency noise one can directly measure the noise power spectral density S_z as is done in Subsec. 6.5.2.

	Q1	Q2	Q3	Q4
T_{res} [mK]	112	106	120	120
$\bar{n}_{\text{th}}$ [$\times 10^{-2}$]	0.79	0.74	1.65	2.39
κ [MHz]	8.48	3.0	2.92	6.62
T_1 [μs]	6.31	5.83	6.6	24.82
T_2^E [μs]	9.60	9.7	8.7	14.59
T_ϕ^E [μs]	40.3	57.7	25.5	20.7

Table 6.2: Measured circuit parameters and calculated upper bounds on resonator temperatures for all qubits of 4Q3.

6.5 Sources of Decoherence

Characterising decay and decoherence on multi-qubit devices is an important part of developing larger scale circuits. In this section we present characterisations of lifetimes and dephasing on multi-qubit circuits, as well as employing spin-locking and T_2-spectroscopy in order to evaluate the noise environment.

6.5.1 Measurements of Decay and Decoherence

Decay and decoherence times of superconducting qubits have been found to vary over time, as several studies have found [132, 133, 134]. Variations in T_1 have been experimentally attributed to coupling of the qubit to two-level systems (TLS) themselves coupled to a bath of thermal fluctuators (TF), and T_ϕ is susceptible to any change in sources contributing to the noise power spectrum S_Z including coupling to coherent TLS [132, 135].The significance of these temporal drifts is that it is necessary to measure the distributions of the characteristic time constants T_1 and T_2 from many repeated traces in order to fully characterise the decay and decoherence experienced by the qubit.

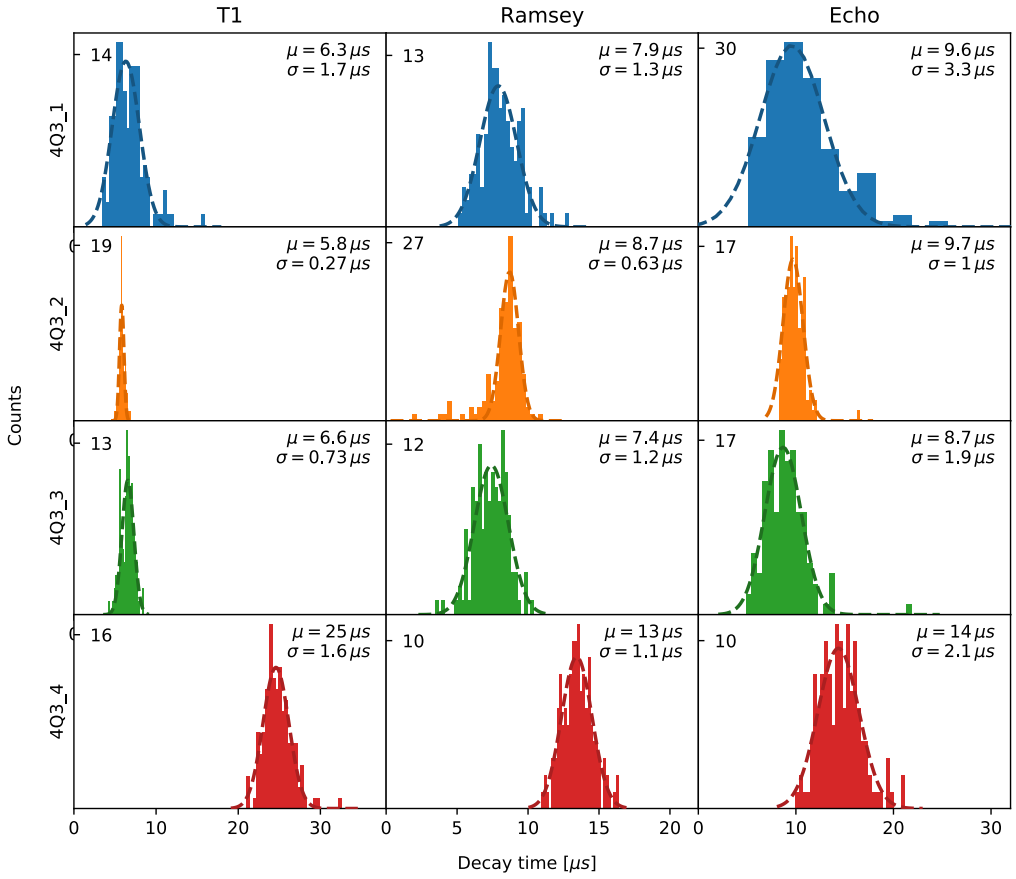

Figure 6.20: Histograms of characteristic times T_1, T_2^* and T_2^E for all four qubits of 4Q3 measured over the course of a 12 hour experiment. Each histogram is generated from the binning of 134 measured values, and the histogram values are fitted to Gaussian distributions (dashed lines) producing the reported mean μ and standard deviation σ.

Here we study the variation of T_1, T_2^*, and T_2^E on all four qubits of 4Q3 over the course of a 12 hour experiment. For each of the four qubits, in order from Q1-Q4, T_1, T_2^* and T_2^E are measured one after another. This set of experiments was repeated until 12 hours had passed, resulting in 134 traces for each experiment for each qubit and an average time step between experiments of 27 s. We first look at the distributions of each characteristic time presented in Fig. 6.20. Each set of histogram data are fitted to a Gaussian distribution in order to characterise the mean characteristic time μ and the spread in measured values σ. Different spreads are measured, finding a range of $\sigma/\mu = 5\% - 27\%$ in the case of T_1.

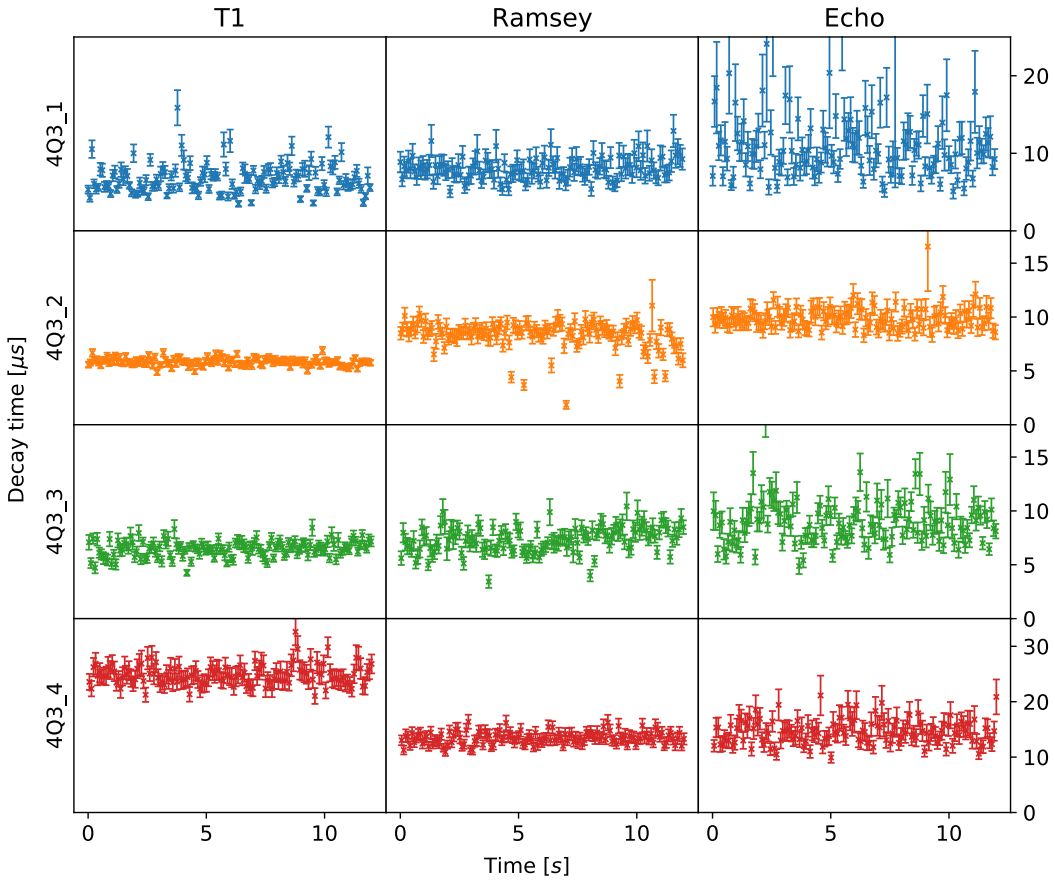

Figure 6.21: Measured values of T_1, T_2^* and T_2^E plotted against time of measurement for all four qubits of 4Q3.

Taken from the same data set, the variation of each of the characteristic times in time is shown in Fig. 6.21. To estimate the power spectral density (PSD) of these variations we use Welch's method [132, 133]. We find that the variation of the characteristic times follow a white noise profile, which is confirmed for the frequency range $10^{-5} - 10^{-3}$ Hz (see Fig. 6.22). We then attempted to find time correlations between T_1 and T_ϕ, and T_2^* and T_2^E for each qubit (Table 6.3), as well as T_1, T_2^* and T_2^E between qubits (Table 6.4), however no value of $|r^2|$ was found above 0.25.

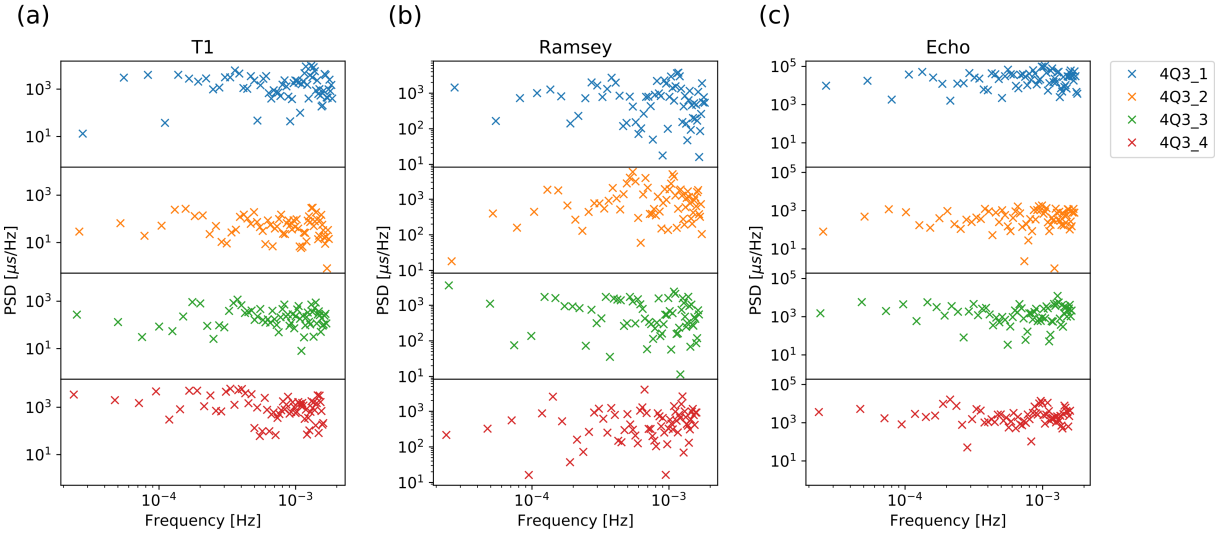

Figure 6.22: Calculated power spectral densities (PSDs) of fluctuations of T_1, T_2^* and T_2^E in time for all four qubits of 4Q3 PSDs are calculated using Welch's method with a Hanning window.

Table 6.3: Linear regression r^2 values of the time correlations between pairs of characteristic times for each qubit on 4Q3.

	T_1, T_ϕ^*	T_1, T_ϕ^E	T_2^*, T_2^E
Q1	0.1	0.01	0.01
Q2	-0.06	-0.09	0.13
Q3	-0.25	0.01	0.23
Q4	-0.04	-0.16	0.03

Table 6.4: Linear regression r^2 values of the time correlations between each pair of qubits on 4Q3, for each of the characteristic times T_1, T_2^* and T_2^E.

	T_1	T_2^*	T_2^E
Q1, Q2	0.10	-0.06	0.19
Q1, Q3	-0.12	0.07	0.07
Q1, Q4	0.13	-0.10	0.00
Q2, Q3	0.04	0.00	0.11
Q2, Q4	0.15	0.04	0.02
Q3, Q4	0.06	-0.01	-0.04

A further set of information that can be obtained is the drift in each qubit's frequency over time. This is extracted from the measured detuning from the Ramsey experiments and plotted in Fig. 6.23(a). The frequencies of the four qubits are found to drift by differing amounts, both in the form of a slow diffusive drift (most pronounced for 4Q3:2) as well as discrete switching (most pronounced for 4Q3:3). The calculated Allan deviation [136] of the data(Fig. 6.23(b)) is used to provide a quantitative measure of the frequency

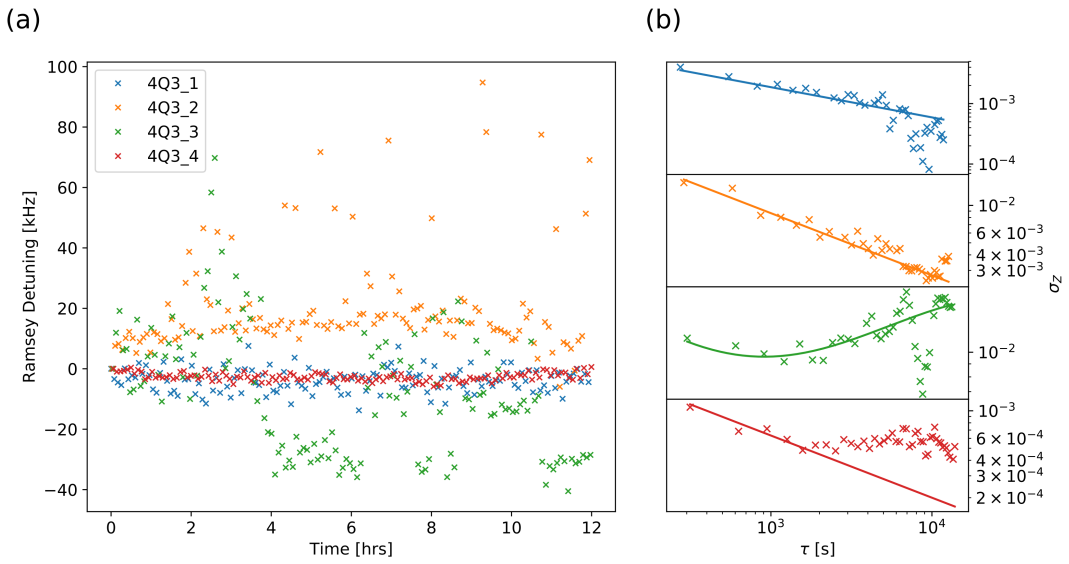

Figure 6.23: (a): Qubit frequency drift plotted against time of measurement. 4Q3:3 exhibits clear signs of discrete frequency shifts not seen for any of the other qubits. (b): Calculated Allan deviations of each trace in (a), points are data and solid lines are fits to white noise models, except for 4Q3:3 which contains an additional Lorentzian component (see main text). The tails of the spectra of 4Q3:3 and 4Q3:4 deviate from the white noise model and could not be fitted with the inclusion of any other power-law process.

stability. Whilst the spectra for 4Q3:1, 4Q3:2 appear to have a white noise profile of amplitude 7×10^{-3}, 1.5^{-1} respectively in the region $10^2 < \tau < 10^4$, the tails of the spectra for 4Q3:3 and 4Q3:4 clearly deviate from the linear relationship expected of white noise. It is not possible to fit these profiles with the inclusion of 1/f noise either, however it is possible to model the spectrum of 4Q3:3 as white noise plus a Lorentzian contribution, as is done in [132], which could be attributed to coupling of the qubit to a TLS.

6.5.2 Spin-Locking

Whilst Ramsey and Echo experiments can give us an accurate measure of the characteristic dephasing times T_2^* and T_2^E, they do not necessarily give us detailed information about the form of noise processes affecting qubit coherence. We can instead directly measure the noise power spectral density (PSD) affecting the qubit frequency $S_Z(\omega)$ which gives rise to the dephasing. There exist several techniques to measure $S_Z(\omega)$ [137, 138, 139, 140, 141, 142], many utilising dynamical decoupling schemes such as the Carr-Purcell-Meiboom-Gill sequence (CPMG) to measure the noise spectrum under free-evolution.

Such techniques can provide an accurate measurement of the noise PSD, but can also be challenging to perform reliably and analyse. A simpler scheme is to measure $S_Z(\omega)$ under driven evolution with a technique known as spin-locking [137, 141]. It has a simple pulse-scheme that is easily tuned and processed. This technique has been demonstrated on superconducting qubits before [137, 141, 79]. Here we use it to measure the noise PSD affecting the qubits in 4Q3, and in particular attempt to evaluate the contribution from residual thermal population in the resonator to T_2^E, as well as detect signatures of coupling to coherent two-level systems.

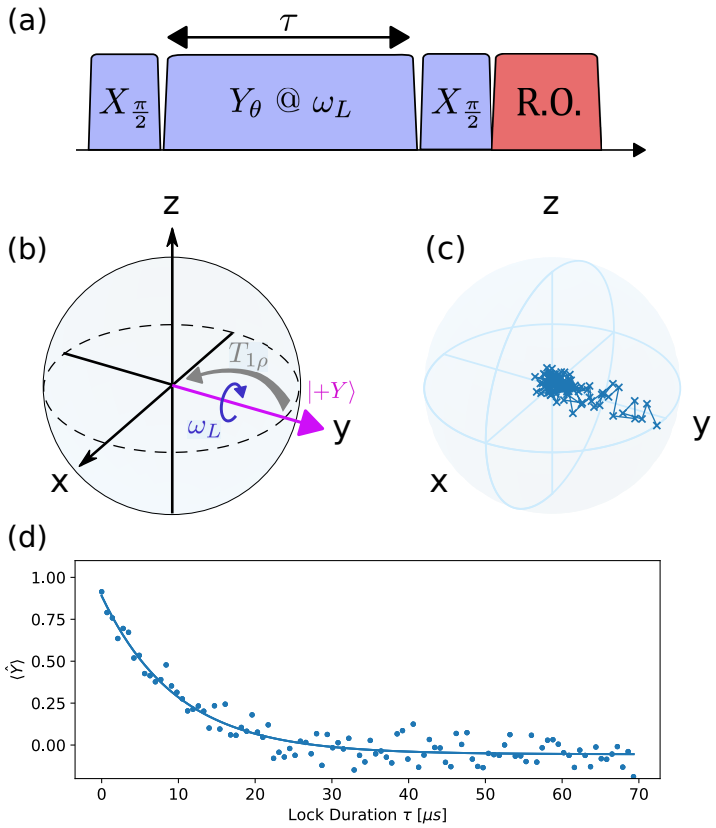

Figure 6.24: (a) Pulse sequence for a spinlocking experiment. An $\hat{X}_{\frac{\pi}{2}}$ pulse maps the qubit to the $|+Y\rangle$ eigenstate before the locking drive $\hat{Y}_\theta$ is applied with drive rate ω_L for a varying amount of time τ. A final $\hat{X}_{\frac{\pi}{2}}$ projects $\langle\hat{Y}\rangle$ onto the $\hat{Z}$ axis before the qubit state is read out. (b) Bloch sphere representation of spinlocking, the qubit-state is rotated about the $\hat{Y}$ axis at the locking rate ω_L, dephasing processes cause depolarisation of the qubit state towards the centre of the Bloch sphere at a rate $T_{1\rho}$. (c) Bloch sphere plot of the results of a spinlocking experiment with full tomography applied such that $\langle\hat{X}\rangle$ and $\langle\hat{Z}\rangle$ are also measured. Data points are connected by lines to make the evolution of the qubit state in time more clear. (d) $\langle\hat{Y}\rangle$ values from the same data used in (c). An exponential decay is fitted to produced the depolarising rate $T_{1\rho} = 9.8$ μs

A schematic of spin-locking is shown in Fig. 6.24(a). The principle of the technique

is that the effects of noise processes are cancelled out by the presence of a faster rotating "locking" drive. An $\hat{X}_{\frac{\pi}{2}}$ brings the qubit state to the $\hat{Y}$-axis at $|+Y\rangle$, and a Rabi drive around $\hat{Y}$ is then applied for a varying duration Δt, before a tomography $-\hat{X}_{\frac{\pi}{2}}$ maps $\langle\hat{Y}\rangle$ onto the $\hat{Z}$-axis. Nominally the Rabi drive does nothing, as the qubit state is rotated about the axis upon which it sits, however any noise on the qubit frequency such that it causes the qubit state to precess around the $\hat{Z}$ axis will cause it to deviate from the $\hat{Y}$-axis and dephase the qubit. If the frequency of the noise process is many times slower than the locking frequency ω_L, then the qubit state will have performed multiple rotations about $\hat{Y}$ before one period of the noise process has been completed, and the precession caused by the noise is essentially filtered out due to the refocusing caused by the locking rotation. Noise that is similar to or faster than ω_L will still contribute to dephasing, and in particular noise at ω_L will be the dominating contribution. In this driven frame, the qubit state will relax towards the mixed state with a simple exponential law characterised by the longitudinal relaxation under driven evolution, $\Gamma_{1\rho}$. From the Bloch-Redfield equations, $\Gamma_{1\rho}$ is connected to the noise PSD by

$$S_Z(\omega_L) = 2\Gamma_{1\rho}(\omega_L) - \Gamma_1. \tag{6.11}$$

where $\Gamma_{1\rho}(\omega_L)$ is the longitudinal relaxation rate observed during a locking drive of frequency ω_L. It is the ability to sample S_Z at particular frequencies, simply by setting the frequency of the locking drive, that makes this technique very practical to implement. A series of spin-locking experiments can be carried out at different locking frequencies in order to build up a picture of the noise PSD. Fig. 6.25 shows the results of such an experiment on each qubit of 4Q3. First a calibration must be obtained between the amplitude of the locking pulse and the the resulting locking frequency or drive rate. To that end a time-Rabi experiment is first performed with a defined Rabi pulse amplitude and its drive rate Ω_0 is fitted. With this calibration known, spin-locking is carried out on each qubit over different frequency ranges, resulting in the blue traces of Fig. 6.25. To demonstrate the impact of residual population in the resonator, and validate our modelling of the resulting noise, each spin-locking experiment is repeated but this time with an extra pulse

to the readout resonator with power −33 dBm before and during the spin-locking drive, such that the resonator has some average population $\bar{n}_{\text{res}}$ during the experiment. These produce the green traces in Fig. 6.25.

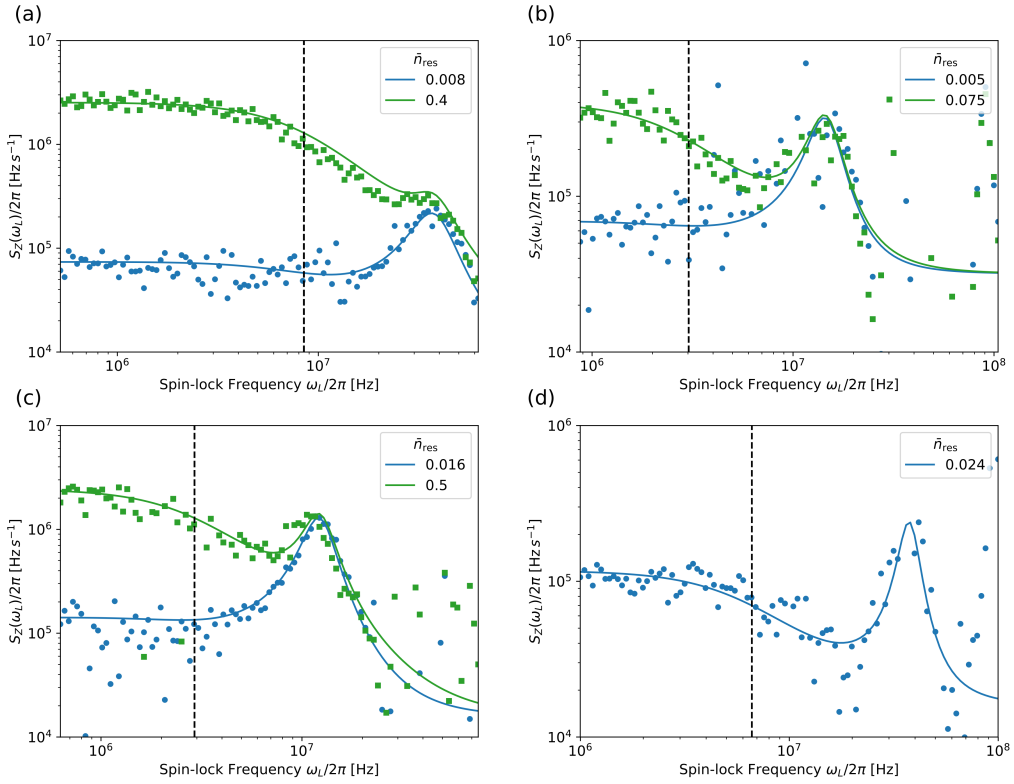

Figure 6.25: Results of spinlocking experiments on device 4Q3 for (a) Q1, (b) Q2, (c) Q3, and (d) Q4. Blue traces correspond to the conventional experiment as in Fig. 6.24(a) and green traces have an additional pulse applied to the readout resonator at a power of −33 dBm in order to make the effect of resonator shot-noise more pronounced. Lines are fitted theory models of $S_Z = S_Z^{\text{Res}}(\bar{n}_{\text{res}}, \omega_L) + S_Z^{\text{TLS}}(\omega_L) + S_Z^{\text{white}}$ defined in the main text. Extracted values of $\bar{n}_{\text{res}}$ for each trace are used as labels, including the traces without the additional application of the resonator pulse indicating residual thermal population of the resonators. The dashed lines are placed at the values of κ for each resonator.

Each trace is fitted to the model of $S_Z(\omega) = S_Z^{\text{res}}(\omega) + S_Z^{\text{TLS}}(\omega) + S_Z^{\text{white}}$ which considers a linear combination of three contributing components, shot noise from the resonator S_Z^{res}, noise from coupling to coherent TLS S_Z^{TLS} and a constant white noise S_Z^{white}. We briefly explain the form of the two frequency dependent contributions. Firstly, shot noise from residual thermal population in the resonator causes dephasing of the qubit due to the AC Stark-shifting of the qubit frequency. Its contribution to S_Z is given by [79]

$$S_Z^{\text{Res}}(\omega) = (2\chi)^2 \frac{2\eta\bar{n}_{\text{res}}\kappa}{\omega^2 + \kappa^2} \tag{6.12}$$

where $\eta = \kappa^2/(\kappa^2 + 4\chi^2)$ is a factor that scales the effective photon population seen by the qubit. This is the form of a Lorentzian centred at $\omega_L = 0$ and with linewidth κ, and such profiles can be seen in Fig. 6.25 with the dashed lines indicating the previously measured value of κ also marking the -3 dB cutoff of the Lorentzians. The profile of S_Z also contains Lorentzian bumps centred at non-zero values of ω_L. Such features cannot be explained by the model for resonator shot-noise, and must be generated by a different noise process. In a different work [141], similar signatures were found and argued to be the result of coupling to coherent TLS [143]. This could be the mechanism responsible for the features seen in this work, however to conclusively show this would require future work, and we are primarily concerned with simply identifying the form of the PSD. As in [141], the bump-like features are fitted to a Lorentzian

$$S_Z^{\mathrm{TLS}}(\omega) = A\frac{\gamma^2}{((\omega - f_{\mathrm{TLS}})^2 + \gamma^2)} \tag{6.13}$$

where f_{TLS}, γ are the TLS frequency and coherence time respectively. We find that the PSD of each qubit contains one significant Lorentzian, with central frequencies ranging from $12.1 - 37.4$ MHz and linewidths of $2.39 - 10.3$ MHz. A summary of the fitted noise parameters is given in Table 6.5. The estimated thermal photon of the resonators are in good agreement with the upper-bounds determined in Table 6.2, and comparable values of white noise are found.

		Q1	Q2	Q3	Q4
$\bar{n}_{\mathrm{th}}/10^{-2}$		0.8	0.5	1.6	2.4
S_Z^{white} [kHz]		7.96	31.8	15.9	15.9
S_Z^{TLS}	A [MHz]	0.21	0.29	1.27	0.22
	f_{TLS} [MHz]	36.6	14.3	12.1	37.4
	γ [MHz]	10.3	3.18	2.39	4.77

Table 6.5: Summary of parameters of the noise PSD $S_Z = S_Z^{\mathrm{Res}} + S_Z^{\mathrm{TLS}} + S_Z^{\mathrm{white}}$ obtained from fits to the measured data in Fig. 6.25.

We briefly give an evaluation of the spinlocking method as it was found in this thesis. This method has enabled us to perform an accurate measure of the noise PSD in the range 10^6 Hz $- 10^8$ Hz, however the method has its limitations. There are limits on the possible values of ω_L meaning we can only determine S_Z in a particular range. The locking frequency cannot be so low that it is similar to Γ_2^* or else the locking condition will be broken, and high values of ω_L led to non-trivial decay profiles possibly due to leakage of population to higher levels of the transmon. The lower limit makes it difficult to evaluate the contribution of noise from coupled qubits which typically have noise time-scales given by Γ_1. Other works [141] use slightly modified pulse schemes to correct for transient errors or pulse miscalibration, and these were trialled in these experiments however little improvement was found.

6.5.3 T_2 Spectroscopy

In this subsection we are concerned with finding hidden modes in the qubit environment that our qubits may be coupled to. Such modes might be cavity resonances or transition frequencies of two level systems that couple to the qubit strongly. Residual population in these modes can lead to Measurement-induced dephasing (just as it does for the readout resonator), and can also create unwanted mediated couplings between qubits as well as increased drive line crosstalk. It is thus desirable to ensure there are no unintended extra modes in the qubit environment, especially given the novel chip packaging used in this architecture, and to validate this we use T_2 spectroscopy [144].

T_2 spectroscopy consists of performing a series Ramsey or Echo experiments with a simultaneous continuous-wave (CW) dephasing tone, and the frequency of the dephasing tone ω_{deph} is varied in each T_2 experiment to "scan" for coupled modes in the system. If the dephasing tone becomes resonant with a mode that is sufficiently coupled to the dephasing drive port, it will be populated by the drive, and will induce dephasing in the qubit if it also has coupling to the mode. Fig. 6.26 shows the results of T_2 spectroscopy on both qubits of 2Q1. For each qubit, a 20 dBm CW dephasing tone is applied at the port of the neighbouring qubit, i.e. if we are measuring the T_2 of Q1, the tone is

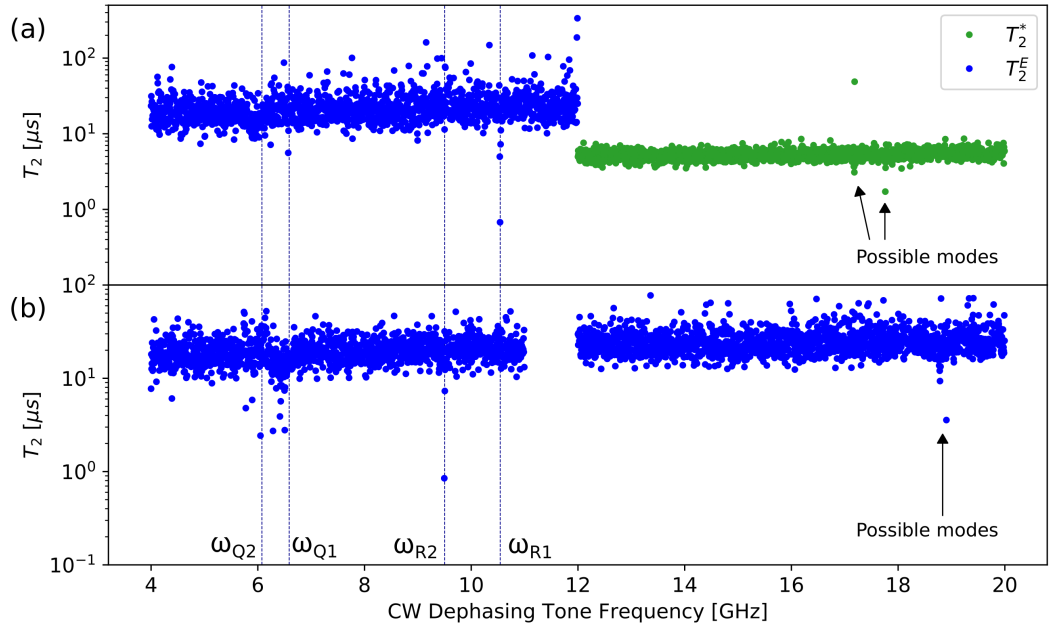

Figure 6.26: T_2 spectroscopy carried out on (a) 2Q1:Q1 from the drive port of 2Q1:Q2, and (b) 2Q1:Q2 from the drive port of 2Q1:Q1, primarily using echo spectroscopy. Dashed lines indicate known modes of the system, which are the resonator and qubit frequencies. The power of the CW dephasing was 20 dBm. Data was not obtained for 2Q1:Q2 in the range $11 - 12$ GHz, and only Ramsey spectroscopy was carried out for 2Q1:Q1 for $12 - 20$ GHz. Arrows indicate the presence of possible modes above 17 GHz.

applied to the port of Q2 (and vice-versa). Initially these experiments were performed with a Ramsey sequence measuring T_2^*, however later we switched to performing an echo sequence measuring T_2^E to take advantage of the increased lifetime (which sets the noise floor). The echo version was not carried out for Q1 in the range $12 - 20$ GHz due to time constraints. The spectrum for both qubits is relatively flat, with dephasing clearly induced as the tone is brought resonant with the coupled readout resonators and qubit frequencies. Above 17 GHz, there is evidence of possible modes for both qubits. A finite-element simulation of the holder and device (using Ansys HFSS) indicates the presence of cylindrical modes underneath the drive ports at 16.5 GHz, however these were also predicted to have very low quality factors of order 1, and so should not be observable by this method. The lowest frequency box mode of the cavity was found to be at 30 GHz with a quality factor of 2000, however this was out of the range of the experimental hardware.

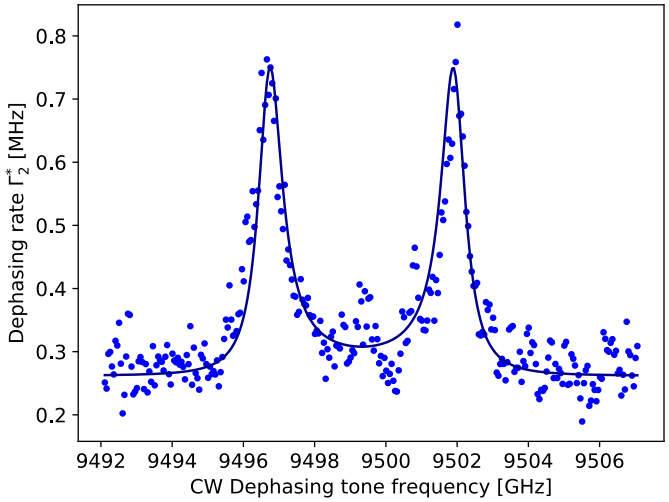

Figure 6.27: Dephasing rate Γ_2^* against dephasing tone frequency near the readout resonator frequency. The solid line is a fit to Eq. (2.45) with ϵ_{rf} as a free parameter and other values determined from prior experiments.

As a demonstration of the technique we can look at the dephasing spectroscopy near the readout resonator, shown in Fig. 6.27. The increased dephasing rate can be seen as the dephasing tone is brought into resonance with the modes ω_{r0}, ω_{r1}, corresponding to the frequency of the resonator when the qubit is in $|0\rangle$ and $|1\rangle$ respectively. Since the qubit is in an equal superposition of the two states during the measurement, both resonances are found with equal weight, with the predicted splitting of 2χ. The experiment can be directly modelled with Eq. (2.45), with ϵ_{rf} as the fit parameter and $\kappa = 0.81$ MHz, $\chi = -2.6$ MHz, and $\omega_r = 9.499$ GHz determined from prior measurements. An agreement to the data is observed with a fit of $\epsilon_{\text{rf}} = 0.2$ MHz, validating the principle of the experiment.

6.6 Conclusions and Future Work

In this chapter we have performed a full characterisation of the extension of the coaxmon architecture to arrays of four unit cells. We began by describing the circuit design of two and four qubit devices, and explained how qubit frequencies and qubit-qubit couplings were chosen to achieve a target Hamiltonian for performing two-qubit gates with cross-resonance. We showed that fabricated versions of such devices were able to achieve $\hat{ZX}_{-\frac{\pi}{2}}$

of 97%, and all gate fidelities between directly coupled and appropriately detuned qubits above 87% on a four qubit device. Following this we performed a full characterisation of the drive port selectivity and resonator-qubit cross coupling, finding average values of -52 dB for the resonator port selectivity, and -33 dB for the qubit port selectivity, and that cross couplings were ≈ 60 times smaller than that within a unit cell. Next we showed measurements of the temperatures of qubits, in this case finding an excited state population of $P_e = 8.5\%$, and estimates for the resonator temperatures of ≈ 110 mK. Finally we turned out attention to measurements of decay and decoherence in a four qubit device, presented statistics of these features over a 12 hour measurement. We measured the noise PSD S_z directly using spin-locking to show both that the echo coherence times are limited by the resonator temperature as well as the presence of Lorentzian features in the PSD of all four qubits. We then performed T_2 spectroscopy to show there are no cavity modes present in the system below 17 GHz.

All aspects of this set of characterised parameters are fertile ground for improvement. CR gate fidelities can be improved by increasing the accuracy of frequency setting and increased qubit coherence. Once junction resistance spreads are sufficiently low, the straddling regime of the CR Hamiltonian can be targeted to minimise quantum crosstalk. Drive port selectivity (classical crosstalk) can be improved in future sample holder designs with tighter control of shielding between unit cells, an increased spacing of unit cell, and modifications to the circuit design. The resonator-qubit cross-coupling can also be improved with increasing separation and isolation of unit cells. Improving circuit temperatures requires careful thermalisation of both the chip to the sample holder, as well as a careful study of the thermal load supplied by the drive lines and possible adjustments thereof. Improved decay and decoherence times lies in improved fabrication and device shielding, however this analysis can be extended to gather more statistics across multiple devices to understand more deeply the noise processes affecting qubits, and to utilise spin-locking as a tool to understand which driving rates should be avoided for high fidelity operation.

Chapter 7

Introducing Flux-tuning

The ability to tune the frequency of qubits is significant as it allows for more relaxed device constraints on the uncertainty of junction resistance, and is a key operating principle behind many two-qubit gate implementations [145, 146, 147, 148]. Tuning is typically achieved by threading magnetic flux through a SQUID-loop that replaces the Josephson junction, as was previously discussed in Subsec. 2.3.4. In this chapter we present experiments demonstrating DC and fast-flux control of coaxial superconducting circuits with an out-of-plane wiring scheme.

The challenge of providing flux control in this architecture is to enable selective DC and AC flux control on a grid of tunable qubits within a superconducting sample holder, without compromising on the extensibility of the wiring scheme and port spacing. To that end, the packaging shown in Subsec. 3.2.3 was developed to provide flux control to a device with up to four tunable qubits with a gradiometric design similar to [76]. Here we show experiments on two different gradiometric designs demonstrating that the qubits are tunable, with a mutual inductance to the flux bias lines (FBLs) such that current ranges of $\mathcal{O}(100\ \mu\text{A})$ cover a period of the tuning curve. We show coherence times of 2.51 μs at the sweet spot, with DC flux selectivity values all $< 0.5\%$, as well the ability to perform dynamic and parametric tuning of the qubit frequency.

7.1 Circuit Design and Flux Delivery

7.1.1 Delivering flux

In this approach we make the transmons tunable by including gradiometric SQUID loops into the design. Recall from Subsec. 2.3.4 that a gradiometric design differs from the conventional DC squid design in that it consists of not one but two superconducting loops through which to thread magnetic flux, and that given the appropriate arrangement it is the difference in the threaded flux between the two loops that tunes the effective Josephson energy of the transmon. The decision to use gradiometric SQUIDs was partly motivated by the relatively large separation between qubit and flux-line. Since we wish to provide the flux from an off-chip line, the separation of line to SQUID-loop (400 μm in this case) is greater than that of typical values found in devices with on-chip FBLs (of order 10 μm). To get a reasonable mutual inductance, the SQUID-loops must also be larger however this comes with a proportional increase in the amount of flux-noise picked up by the loops. The advantage of opting for a gradiometric design in this case is that it is first-order insensitive to global flux-noise (i.e. magnetic field that threads the same amount of flux through both loops) so we reduce the sensitivity to external fields. The other key motivation behind using gradiometric SQUID loops was the highly selective flux control this allows us to implement, as is shown later in Subsec. 7.2.4.

In order to check that sufficient flux could be threaded through the two SQUID-loops, magnetostatic simulations of the setup were carried out in Maxwell. Fig. 7.1 shows the simulated magnetic field from such a simulation given an applied current of 1 mA through the coil. The total differential flux threaded through the gradiometric SQUID was $\Phi_{\text{diff}} = 18.6\,\Phi_0$. Remarkably this value is very close to the experimentally determined value of $18.290(8)\,\Phi_0$, further agreements were found between simulation and experiment for different circuit designs (see Table 7.1). In principle, the line could be brought closer in order to have a greater mutual inductance to the circuit, however the challenge is that this can increase the capacitive coupling of the circuit to the line, and reduce T_1 by Purcell limiting the qubit [88, 89]. This can in principle be overcome by symmetrising

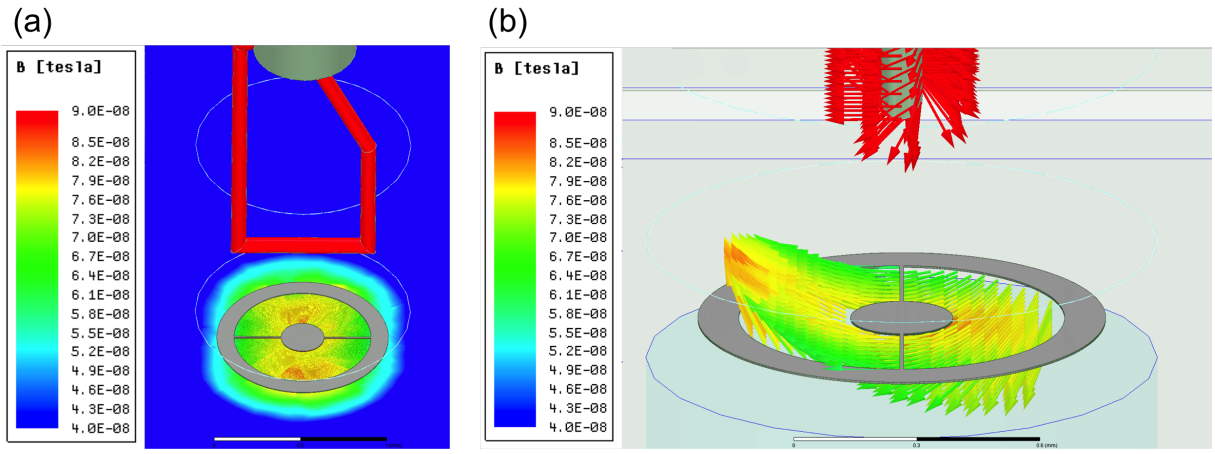

Figure 7.1: Magnetostatic simulations in Maxwell of the magnetic field produced by a 1 mA current applied to the FBL, and threaded through a gradiometric SQUID. (a): A plot of the field magnitude normal to the surface of the chip $|B_z|$. The integral of the field in the areas enclosed by the gradiometric loops gives the total amount of flux quanta captured with this value of applied current. (b): A vector plot of the field from the same simulation as (a), revealing the asymmetry of the field direction through the two loops. Note that in both (a) and (b) the value range of the colour bar was chosen to best display the field at the circuit, and the field strength at the FBL is much higher than the maximum value of this range.

the capacitance between the line and the inner and outer pad of the qubit [149], however due to the technical limitations of fabricating the flux-lines, we instead opted to pull back the flux-line to a safe separation as determined by calculating the Purcell loss from a finite-element simulation.

7.1.2 Circuit design

Two different shapes of circuit were explored in this project. The first "original" circuit was based off of the original coaxmon design, only with a second junction lead to form the gradiometric SQUID-loops. Device SQ1:1 had this shape. Whilst promising initial results were found with this device, the circuit shape was determined to not be appropriately matched to the magnetic field from the FBL, as the SQUID loops did not cover areas with the most field and did cover areas with comparatively little (see Fig. 7.1(a)). With values from simulation we extract a differential flux per unit current and area of $45.2\,\Phi_0\,\mu\mathrm{A}^{-1}\mathrm{mm}^{-2}$. Learning from this, a second "modified" circuit design was explored in order to achieve higher coherence times by reducing the area of the SQUID-loops whilst

still capturing sufficient flux from the FBL (see Fig. 7.1(b)). All three qubits on device SQ2 had variants of this shape, and differential flux efficiencies were found in the range $57.5 - 63.4\,\Phi_0\,\mu\mathrm{A}^{-1}\mathrm{mm}^{-2}$.

To aid with the circuit design and comparison, a numerical model was built to estimate the magnitude of the component of the magnetic field perpendicular to the chip plane when a current is applied to the flux-line. This was modelled analytically as the component of the field around a wire with finite length l, that is perpendicular to a plane parallel to the wire with separation d,

$$|B_Z(x,y,d,l)| = \frac{x}{x^2+d^2}\left(\sin\left(\tan^{-1}\left(\frac{l/2-y}{\sqrt{x^2+d}}\right)\right)+\sin\left(\tan^{-1}\left(\frac{-l/2-y}{\sqrt{x^2+d}}\right)\right)\right). \quad (7.1)$$

Here we used values of $d = 0.4$ mm, and $l = 0.7$ mm to produce the scalar field shown in Fig. 7.1. From this we see that there are two maxima of magnetic field amplitude at displacements of $\pm d$ from the y-axis and $x = 0$. Looking at the overlay of the original design 59% of the loop area (between -0.2 mm $<$ y $<$ 0.2 mm) captures only 2.6% of the total available flux, and the areas with the greatest field amplitude do not lie within the SQUID loops. In response the modified circuit design was developed, with a more appropriate shape to capture the field whilst minimizing the total loop area. The perimeters of the centre pad and inside of the outer ring are given by

$$\begin{aligned} r_{\mathrm{pad}}(\theta) &= a_p\cos(\theta)+b_p \\ r_{\mathrm{ring}}(\theta) &= a_r\cos\big(\sin^2(\theta)\big)+b_r. \end{aligned} \quad (7.2)$$

It should be noted that this shape was not optimised for the the field but merely chosen as it was easily parametrised. By integrating the field over the enclosed areas defined by the ring and pad, a relative measurement of the amount of captured flux was calculated. In fact, after determining a conversion factor, the simulation results of captured flux were found to be in close agreement with this simple analytical model, and so the analytical model was used in the end to determine the captured flux. By varying a_p, b_p, a_r, b_r in the equations Eq. (7.2), one could optimise for 3 different constraints, the total area of

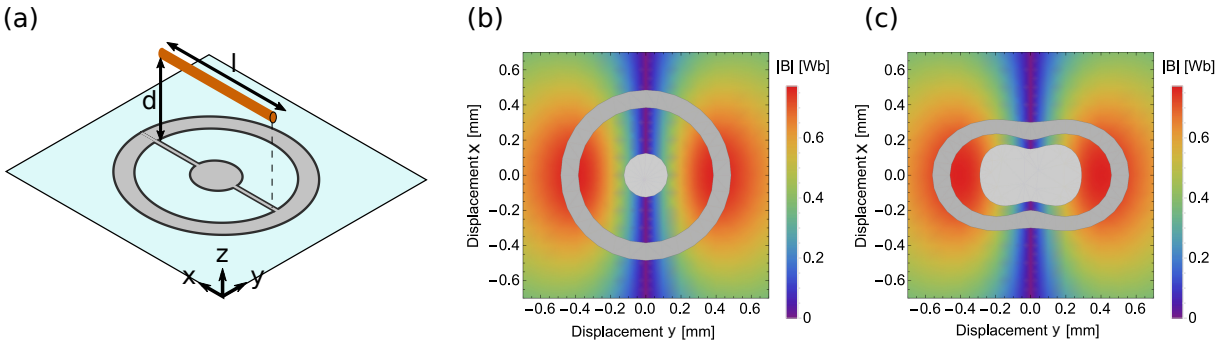

Figure 7.2: Numerical simulations of $|B_z|$, the magnitude of the magnetic field normal to the chip plane, using Eq. (7.1). (a): Visual definition of the analytical model used to generate Eq. (7.1), we consider the perpendicular component of the field from a finite wire of length l, through a plane of separation d. In our model we use values of $l = 0.7$ mm, $d = 0.4$ mm. (b): A plot of $|B_z|$ with an overlay of the original design for the tunable transmon. It is clear that the SQUID loops do not efficiently capture the magnetic field, both missing areas higher field amplitudes as we as including areas with lower field amplitudes. (c) A plot of $|B_z|$ with an overlay of the modified design of the tunable transmon with an area of 0.19 mm^2. The shape is chosen such that the SQUID loops more efficiently capture the magnetic field so that the loop area can be minimised. In this case the design captures an amount of flux that is 62% of the value captured in the original design given the same current through the FBL, whilst the loop area is 29% of the original.

the loop (assumed to be proportional to flux-noise), the total flux-captured (a measure of the mutual inductance between line and circuit), and the effective capacitance across the junctions (defining the charging energy E_C). The effective capacitance was determined by way of electrostatic Maxwell simulations of the same set up as in the magnetostatic simulations. Optimising these parameters proves a challenge, as we wish to have a sufficient mutual inductance (large matched area) with low levels of flux-noise (small area) and a sufficiently high qubit anharmonicity (greater separation between the ring and pad). To investigate this device SQ2 was designed and fabricated, and consisted of three different parametrised circuits with the inner-ring radius amplitude a_r varied with three different values, corresponding to "large" ($a_r = 0.4$ mm), "medium" ($a_r = 0.26$ mm) and "small" ($a_r = 0.2$ mm) designs with total loop areas of 0.39 mm^2, 0.19 mm^2, and 0.12 mm^2, compared to 0.42 mm^2 for the standard design[1]. The other parameters were kept fixed for all three designs at $b_r = 0.2$ mm, $a_p = 0.2$ mm, and $b_p = 0.09$ mm. To find the

[1]It is worth noting for comparison that the concentric transmon [76] had a loop area of 0.04 mm^2 and conventional non-gradiometric SQUIDs have a typical area of 1×10^{-4} mm^2, 3 orders of magnitude smaller than this design.

anharmonicity of each circuit, the capacitance matrix of the system was first simulated using an electrostatic simulation in Maxwell. This was then inverted to find the system Hamiltonian, values were assigned to the inductive terms in order to find the normalisation factors, and the full Hamiltonian was solved to determine the anharmonicity as in [65]. For the large, medium and small parametrised designs, the anharmonicities were simulated to be 147 MHz, 137 MHz and 131 MHz respectively, compared to experimentally determined values of 172 MHz, 132 MHz and 129 MHz. Full details of all four devices can be found in Table 7.1 and a visual schematic in Appendix B. We find that the experiment ranges of current needed to sweep through one period of the flux tuning curve are comparable to values from simulation. The largest discrepancy is identified for SQ2:1, found at half the simulated value, and in fact smaller than the value found for SQ2:2, which had larger loop areas. This discrepancy could be due to inaccuracies in setting the separation of the FBL and the qubit, or it could be due to inaccuracies of the model which fails to take into account the screening effects of superconductivity. Taking the simulated period together with the total area, we find the efficiency of flux capture is increased with the modified design compared to the original, as was intended, finding values of $57.5\,\Phi_0\,\mu A^{-1}mm^{-2}$, $60.9\,\Phi_0\,\mu A^{-1}mm^{-2}$, $63.4\,\Phi_0\,\mu A^{-1}mm^{-2}$ for SQ2:1,2,3 respectively compared to $45.2\,\Phi_0\,\mu A^{-1}mm^{-2}$ for SQ1.

	SQ1	SQ2		
Qubit	Q1	Q1	Q2	Q3
Shape	Original	Modified	Modified	Modified
Pad amp. a_p [mm]	0	0.2	0.2	0.2
Ring amp. a_r [mm]	0	0.2	0.26	0.4
Pad rad. b_p [mm]	0.125	0.09	0.09	0.09
Ring rad. b_r [mm]	0.385	0.2	0.2	0.2
Total area [mm^2]	0.412	0.121	0.191	0.388
Period [μA]	109.3 (107.5)	142.5 (287.4)	170 (172)	59.1 (81.3)
Anharmonicity [MHz]	-264 (-247)	-129 (-131)	-132 (-137)	-172 (-147)

Table 7.1: Design parameters and measured (simulated) values for the different circuit designs implemented in this thesis. The shapes of the circuits are defined with Eq. (7.2). Device SQ2 consists of three different variants of the modified design corresponding to a small area (SQ2:1), medium area (SQ2:2) and large area (SQ2:3).

7.1.3 Sources of flux noise

There are three distinct possible sources of flux-noise in the system. First there is the presence of global external fields, i.e. any field generated outside of the experimental setup. There are many such sources, including any electronics such as monitors, or even earth's magnetic field and is usually mitigated with the inclusion of appropriate magnetic shielding. The second source is noise on the flux-line used to bias the qubit. In this vein, low noise sources must be used, and appropriate filtering on all lines connected to the coil is necessary. Typically DC looms that are passed down are formed into twisted pairs to counter-act any induced current in the wires, and on-chip FBLs typically incorporate an on-chip low-pass filter. The third source is field generated by spins of two-level systems on the surface of the chip [150]. Mitigation is usually achieved by clean fabrication and passivation of the sample surface such that surface spins do not accumulate [151, 152]. Considering sources of flux-noise in this experiment was important in achieving reasonable coherence times.

In order to evaluate noise on the line, extensive work was carried for the masters

project of Jacquelin Luneau [153]. It was demonstrated that the noise level of the lines was sufficiently low, given appropriate filtering (shown in the experimental setup in Fig. 3.3) and with the use of a low noise Keithley 6221 current source. The measured power-noise spectrum was measured [153] and used to estimate upper bounds on the contribution to the noise power-spectral-density (PSD) of both the white and $1/f$ noise contributions, $S_Z = S_Z^{\text{white}} + S_Z^{1/f}/f$. We found $S_Z^{\text{white}} \leq 10^{-23}$ A^2/Hz, and $S_Z^{1/f} \leq 10^{-19}$ A^2, which would put and approximate limit on T_2^* of 70 μs if the noise values matched the maximum.

Perhaps surprisingly, despite the presence of a superconducting holder and the use of a gradiometric SQUID design, a significant mitigation of global flux-noise was found with the addition of a mu-metal magnetic shield (compared to without). For device SQ1:1 (which had the original design), T_2^* was too small to characterise without a shield and 300 ns with one. For device SQ2:1 (which the the modified design with smallest loop area) T_2^* increased from 200 ns to 2.11 μs (T_1 also increased from 15.5 μs to 37.7 μs indicating the presence of flux-noise at the qubit frequency). This indicates at least that the dominant causes of flux-noise in the initial unshielded versions of both experiments were likely to have been global fields. In future, techniques such as those utilised in [154] can be used to determine the relative contributions of global and local flux noise.

7.2 DC Characterisation

7.2.1 Flux-dependent spectroscopy

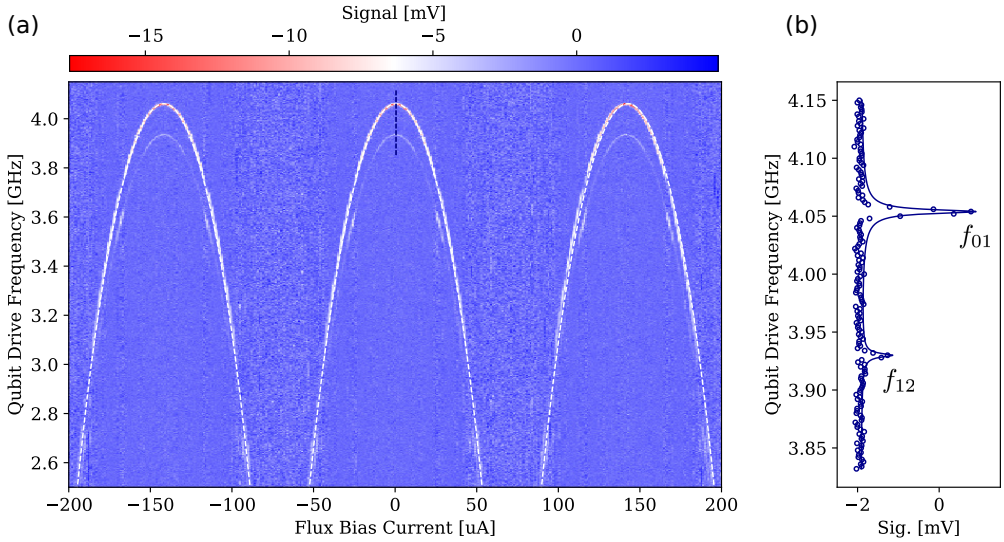

Figure 7.3: (a): Qubit spectroscopy of SQ2:1 as a function of current applied to the FBL. The variation of the f_{01} transition with current is fitted to Eq. (7.3) to reveal a periodicity of 142.2 μA, and offset of -0.4 μA, an $E_{J\Sigma}$ of 18.2 GHz and an asymmetry factor d of 0.05. The signal traces are standardised to account for the variation of the resonator frequency with current. The f_{12} is also visible indicating the qubit has a measurable excited state population. (b): A zoom-in of a trace taken at the flux sweet-spot revealing both the f_{01} and f_{12} transitions, revealing an anharmonicity of 129 MHz. The trace is fitted to the complex sum of two Lorentzians and the resulting peak heights indicate an excited state population of 21%, corresponding to a qubit temperature of 126 mK.

As an external flux is threaded through the SQUID loops in a transmon, the Josephson energy, and thus the qubit frequency is modified as in Eq. (2.22). Since the dressed frequencies of the resonator and qubit are functions of their detuning, modifying this detuning by changing the qubit's frequency will also modify the dressed frequency of the resonator. What this means from a practical perspective is that in order to perform qubit spectroscopy, a tracking measurement must be performed whereby the resonator frequency ω_{r0} is first determined. This is carried out by an automated script that sweeps through a range of currents applied to the FBL from the Keithley current source. For each current, resonator spectroscopy is first performed, and the frequency of the point with the lowest signal in the trace is taken to be the LC resonance. Qubit spectroscopy is then performed as in Subsec. 5.2.2 with the resonator drive tone set to the found resonance. In this way, qubit spectroscopy can be performed despite the shifting frequency of the

resonator with flux. Fig. 7.3 shows the results of such an experiment. The measured qubit frequencies are then extracted and fitted to the model $f_{01}(E_J(\Phi_{\text{ext}}), E_C)$ as defined in Eq. (5.5), with $E_J(\Phi_{\text{ext}})$ given by a slight modification to Eq. (2.22) to account for the differential flux trapped in the two gradiometric SQUID loops Φ_{off},

$$E_J(\Phi_{\text{ext}}) = E_{J\Sigma} \cos\left(\pi \frac{\Phi_{\text{ext}} - \Phi_{\text{off}}}{\Phi_0}\right) \sqrt{1 + d^2 \tan^2\left(\pi \frac{\Phi_{\text{ext}} - \Phi_{\text{off}}}{\Phi_0}\right)}, \tag{7.3}$$

where $\Phi_{\text{ext}} = \Phi_2 - \Phi_1$ is the difference in flux threaded between the two SQUID loops, Φ_{off} is an offset to account for trapped flux, $E_{J\Sigma} = E_{J1} + E_{J2}$ is the combined inductance of the two Josephson junctions, and $d = (E_{J2} - E_{J1})/E_{J\Sigma}$ is the junction asymmetry. A periodicity of $I_0 = M^{-1}\Phi_0 = 142.2\ \mu$A is found giving a corresponding mutual inductance of $M = \Phi_0/I_0 = 1.56 \times 10^{-11}$ H, and a value of $I_{\text{off}} = M^{-1}\Phi_{\text{off}} = 0.4\ \mu$A is also extracted. In addition, the SQUID is found to have an $E_{J\Sigma} = 18.2$ GHz, and an asymmetry factor $d = 0.05$ meaning the ratio of the two Josephson energies of the junctions that form the SQUID $E_{J1}/E_{J2} = 90\%$. A second peak corresponding to the f_{12} transition frequency[2] can also be observed in the spectroscopy, indicating that the qubit temperature is sufficient to have a reasonably significant population in the $|1\rangle$ state. From this trace we also determine the anharmonicity of 129 MHz at the flux sweet-spot allowing us to calculate $E_C = 120$ MHz. To estimate the qubit temperature, the Lorentzian fits of the f_{01} and f_{12} transition in the trace given by Fig. 7.3(b) can be compared with a ratio of their amplitudes $A_{01} = 2.84$ mV, $A_{12} = 0.77$ mV giving an estimate of the residual population in the first excited state of $A_{12}/(A_{01} + A_{12}) = 21\%$, corresponding to a temperature of 126 mK.

7.2.2 Demonstrations of coherence

Repeated measurements of decay and decoherence were performed on the qubit over a period of 10 hours, whist the qubit was tuned to the flux sweet-spot (where the coherence times are greatest). T_1, Ramsey and spin echo experiments were performed and

[2]This was verified to be the f_{12} transition and not a multiphoton transition by checking the power dependence of the presence of this peak

the resulting curves fitted to extract decay times. Each decay was fitted to an exponential profile, the validity of which was checked by observing the residuals of the fits (see Subsec. 7.2.3)[3]. The distribution of the measured decay times were fitted to Gaussian distributions, with mean values $\bar{T}_1 = 37.7\ \mu$s, $\bar{T}_2^* = 2.11\ \mu$s, and $\bar{T}_2^E = 2.51\ \mu$s. In addition, the qubit frequency was determined from the Ramsey experiments, and was found to drift by ≈ 20 kHz over the course of the full 10 hours.

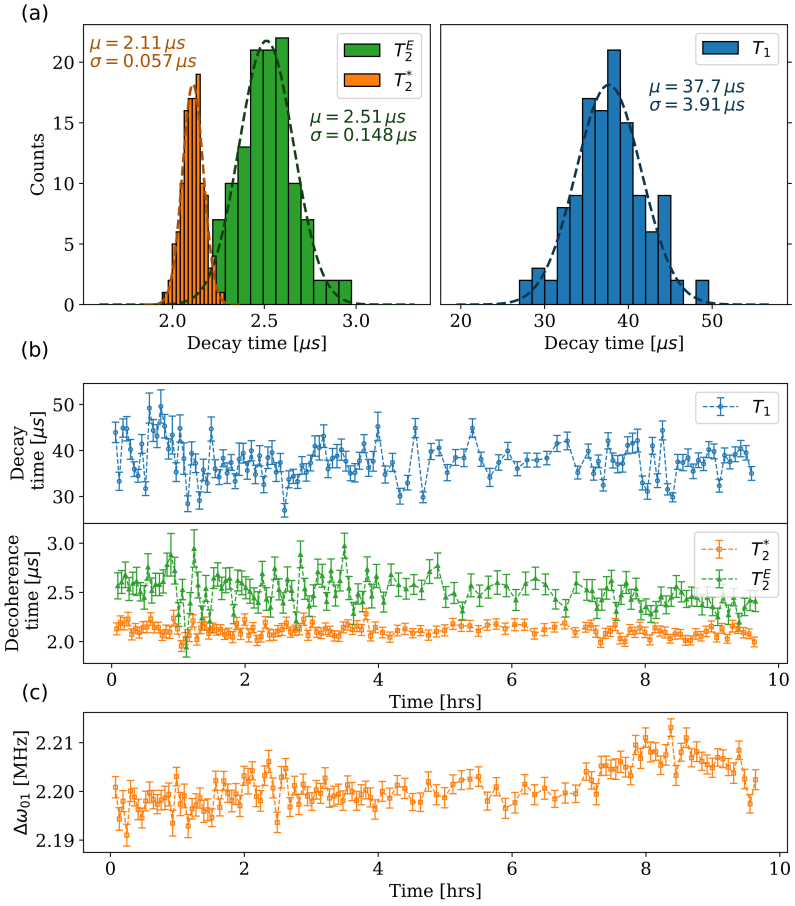

Figure 7.4: Results of T_1, T_2^*, and T_2^E experiments on SQ2:1 with 121 repetitions each, taken continuously over the course of 10 hrs. (a): Histograms of the measured decay times. The histogram data are fitted to Gaussian distributions to find the mean and standard deviations shown in the figure. (b): Measured decay times plotted against time of measurement. The average time step was 286 s however the time taken per measurement changed as the experiment progressed possibly due to a slowdown of the measurement software. (c): Frequency drift of the f_{01} transition as measured by the frequency of Ramsey oscillations. The qubit frequency is seen to change by ≈ 20 kHz over the course of the 10 hrs.

[3]An exponential profile is typically expected at the flux sweet spot where the coherence time isn't limited by flux-noise (which usually produces a Gaussian profile [83]) and instead by a white noise power spectrum [75].

7.2.3 Lifetimes versus flux

In order to investigate the effects of flux noise on the qubit, a tracking measurement was done to perform T_1 and spin-echo experiments on device SQ2:1 over a range of different qubit frequencies. We first focus on T_1 as a function of flux. First of all it is important to determine the appropriate decay profile of any lifetime measurement in order for the fitting to be meaningful. The decay can take on different forms depending on the spectrum of noise affecting the qubit, in particular we expect to see an exponential decay if the noise spectrum is white and a Gaussian decay if the noise spectrum has a $1/f$ profile. To perform this validation, each T_1 trace was fitted to both an exponential and a Gaussian decay, and plotted together with their residuals (Fig. 7.5(a)-(b) show an example fitting of one trace near the flux sweet-spot). By checking that the fit residuals were both lower and were free from consistent overestimation or underestimation, it was determined that an exponential decay was the appropriate profile to use across the full range of tuning values. Fig. 7.5(c) shows the relationship between the fitted T_1 lifetime and flux, over a range of flux values corresponding to $-0.43\,\Phi_0 < \Delta\Phi < 0.42\,\Phi_0$. The dependence of T_1 on flux in the region near the flux sweet-spot is revealed as the decay time decrease from ≈ 45 μs, before saturating out at ≈ 20 μs. Such a dependence could be either due to flux-noise at the qubit frequency which stimulates energy decay and absorption, however this seems unlikely as we expect the noise to get worse with increasing flux and not saturate. It is also possible that the changing qubit frequency is to blame, as the qubit may be brought closer to resonance with two-level systems or may be more strongly coupled to any other decay channel in the system.

We next look at T_2^E measured from spin echo experiments as a function of flux on the same device for the range $-0.17\,\Phi_0 < \Delta\Phi < 0.11\,\Phi_0$, similar to the procedures carried out in [82, 75]. As before, we wish to verify the appropriate decay profile of the traces, and determine whether to use an exponential or Gaussian fit (or possibly neither). This analysis is particularly pertinent to decoherence of tunable devices, as we expect flux noise to have a $1/f$ profile, however we also expect very little flux-noise at the sweet-spot. An analysis of the trace at the sweet spot as shown in Fig. 7.6(a) reveals that

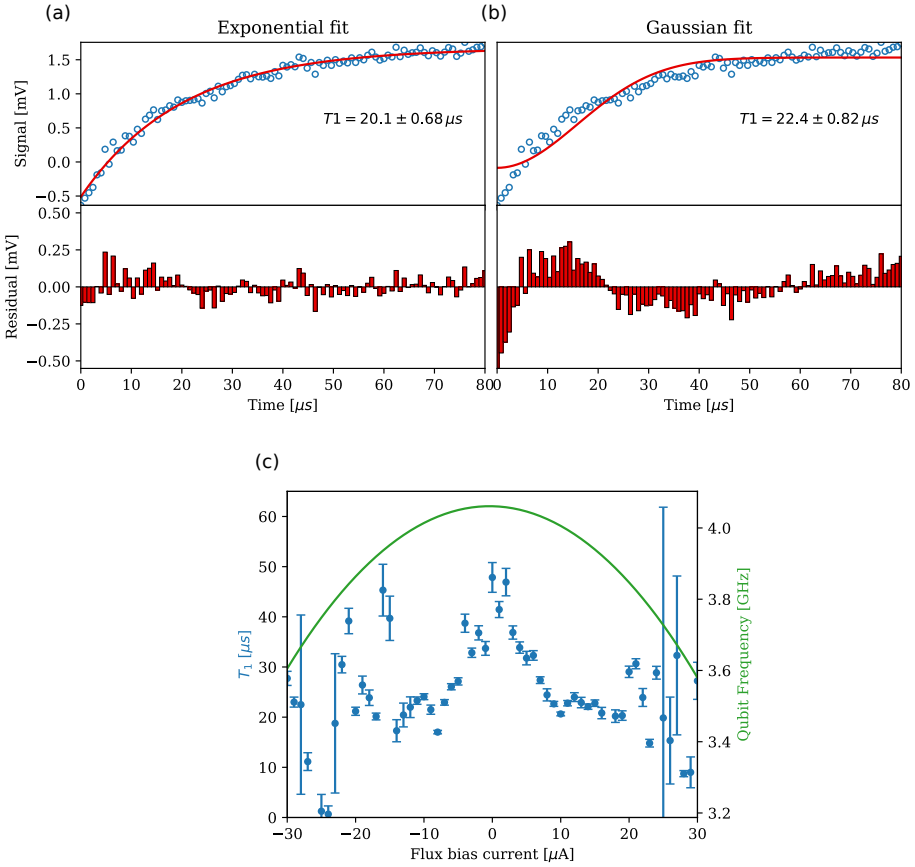

Figure 7.5: Measurements of T_1 versus current through the FBL for device SQ2:1. (a)-(b): To determine the appropriate model, we look at fits of an exponential ($\exp(-t/T_1)$) and Gaussian ($\exp((-t/T_1)^2)$) decay to the same trace of a T_1 experiment carried out at the flux sweet-spot. The fits are shown in the top plots, with points for data and solid lines for fits. The fit residuals are plotted underneath. Despite similar levels of error, the exponential fit is clearly more appropriate than the Gaussian, as revealed in the consistent over or under estimation of the Gaussian fit seen in the residuals. (c): Measured T_1 fitted with an exponential decay as a function of current to the FBL. For convenience, the qubit frequency as predicted from valued fitted in earlier experiments is shown. T_1 appears to decrease away from the sweet-spot, until saturating at ≈ 20 μs.

an exponential profile is more appropriate, however at a small tuning away from this at $\Phi = 0.04\,\Phi_0$ (Fig. 7.6(b)) a Gaussian profile is found to be more appropriate. Neither fits capture the the bump-like features present in both traces which indicates that the noise power-spectral-density (PSD) is more complex than simple white or $1/f$ noise. Since we cannot compare the T_2^E decoherence times determined from exponential and Gaussian fits with one another, and because there are clear signatures of noise processes that do not conform to the two considered models, we instead take a phenomenological approach to determining T_2^E. To this end, we interpolate the first quarter of each trace with an $\mathcal{O}(10)$ polynomial and calculate T_2^E as the time taken for this function to fall to $1/e$ of the visibility as determined by the minimum and maximum of the signal trace. The calculated values of T_2^E are shown in Fig. 7.6(c), revealing a clear dependence with flux. For comparison we perform a fit to a model of flux-noise following a $1/f$ dependence [69],

$$\Gamma_2^E = \frac{\Gamma_1}{2} + \Gamma_{\phi,\mathrm{flux}}^E + \Gamma_{\phi,\mathrm{oth}}^E, \tag{7.4}$$

$$\Gamma_{\phi,\mathrm{flux}}^E \approx \frac{A}{\hbar}\left|\frac{\partial E_{01}}{\partial \Phi}\right| = \frac{A}{\hbar}\frac{\pi}{\Phi_0}\sqrt{2E_{J\Sigma}E_C\left|\sin\frac{\pi\Phi}{\Phi_0}\tan\frac{\pi\Phi}{\Phi_0}\right|}. \tag{7.5}$$

Here, $\Gamma_{\phi,\mathrm{oth}}^E$ accounts for decoherence from other sources, and is taken as $1/T_{2,\mathrm{max}}^E = 0.37$ MHz. We extract an RMS flux noise amplitude of $A = 2.7\times10^{-4}\,\Phi_0$, which compares values of $10^{-5}-10^{-6}\,\Phi_0$ typically found for most tunable qubits with DC SQUIDs [82, 155].

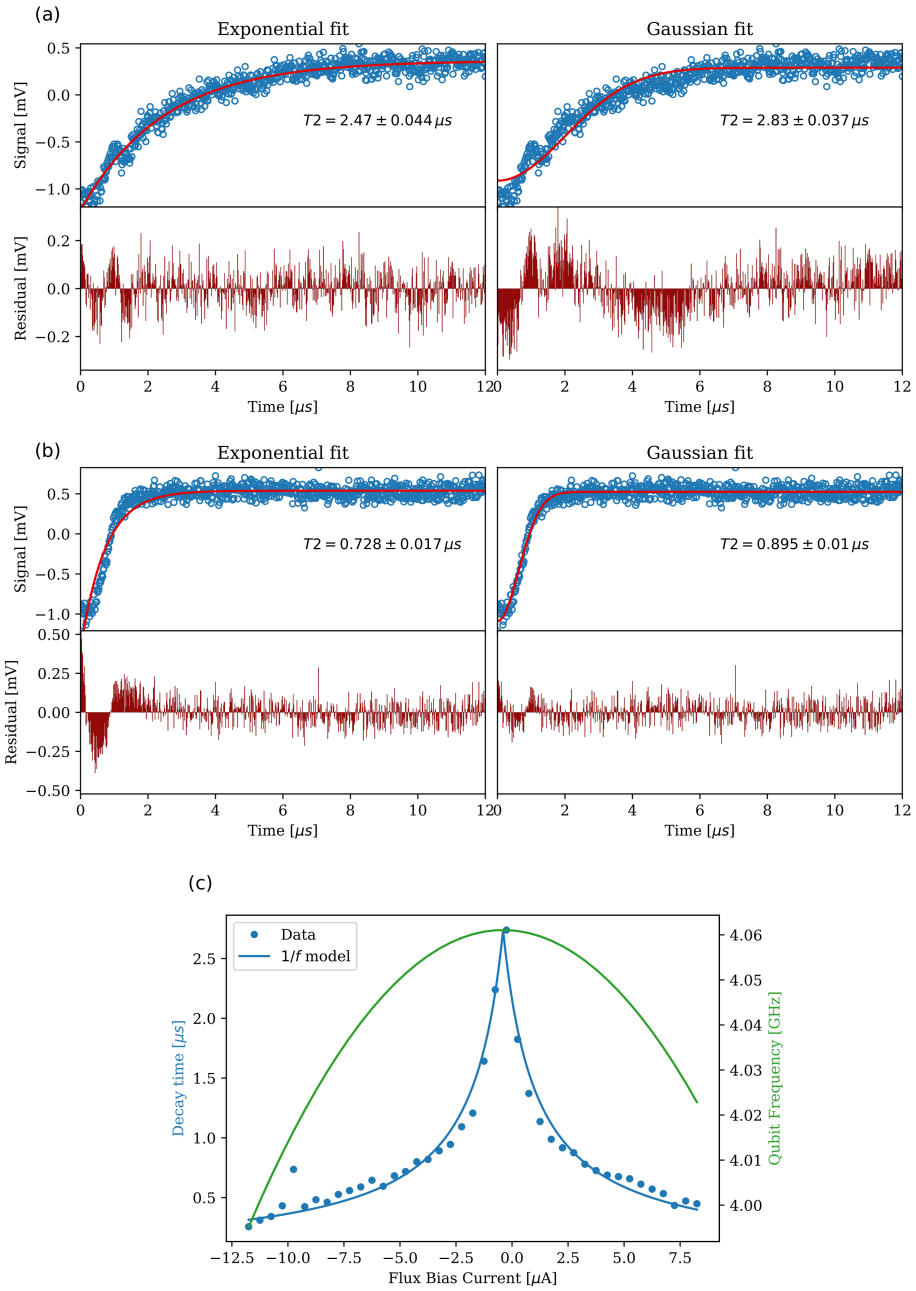

Figure 7.6: Measurements of T_2^E as a function of flux bias current. (a)-(b): Determination of the appropriate decay model at the sweet spot (a) and at $\Phi = 0.04\,\Phi_0$ (b). The traces of T_2^E experiments (points) are each fitted to both an exponential and Gaussian fit (solid lines) and are shown together with their fit residuals. (a): At the sweet spot an exponential fit is determined to be more appropriate due to the lower level of residuals, however small oscillations in the trace are observed that are not captured by either model. (b): Away from the sweet spot, a Gaussian fit is shown to be more appropriate however both models fail to account for an initial "bump" during the first 200 ns of the trace. (c) Flux bias current versus T_2^E, as determined by the $1/e$ decay time of the interpolated traces (points). For convenience, the qubit frequency as predicted from valued fitted in earlier experiments is shown. The blue solid line is a fit of the measured T_2^E to a model of the decay time given $1/f$ flux noise, we extract an RMS flux noise amplitude of $A = 2.7 \times 10^{-4}\,\Phi_0$.

7.2.4 DC crosstalk

In this subsection we evaluate the flux-line crosstalk from the neighbouring ports of the flux-line sample holder. As with microwave drive crosstalk [77], flux crosstalk can be problematic for device operation, in particular causing unwanted $\hat{Z}$ rotations on nearby tunable qubits. Achieving low levels of crosstalk with on-chip flux-lines requires appropriate spacing and careful routing and shorting of the control line so as to avoid spurious current paths in the device ground plane. Recent experiments that have taken such measures report typical values of order 1% [156, 157, 158, 159, 160]. In the case of this device, care has been taken in both the circuit design and packaging to achieve low levels of crosstalk. Firstly the qubits are tunable via gradiometric SQUID loops which require asymmetric amounts of flux through either loop to tune. Contributions to the magnetic field from distant sources will be more homogeneous near the qubit, and thus worse at tuning the qubit than the local line. These FBLs are mode-matched to the gradiometric design for efficient tuning, putting equal-in-magnitude and opposite-in-direction amounts of field through either loop. Lastly we take advantage of the need for an asymmetric flux profile by orienting the FBLs in the neighbouring ports perpendicular to the direction of the local FBL, i.e. the worst possible orientation for tuning neighbouring qubits. These steps counter the concerns arising from the larger separation between line and device, and larger SQUID-loop areas, than in conventional on-chip approaches.

An experiment to measure the crosstalk from the neighbouring (perpendicular-aligned) and diagonal (parallel-aligned) FBLs is shown in Fig. 7.7. The principle of the experiment is to measure the periodicity of the qubit frequency with DC current applied to the FBL when tuned from the local, neighbouring and diagonal ports. Since the periodicity is proportional to the mutual inductance [74], the ratio of the measured periods between the local and target lines directly gives the flux crosstalk. In each experiment, the value of current applied to the relevant FBL is swept and the qubit frequency is measured. To avoid potential inconsistencies in DC current source signal amplitude, the current is provided by the same source in all cases. To determine the qubit frequency at each value of current, Ramsey interferometry is performed and ω_{01} determined from a fit to the

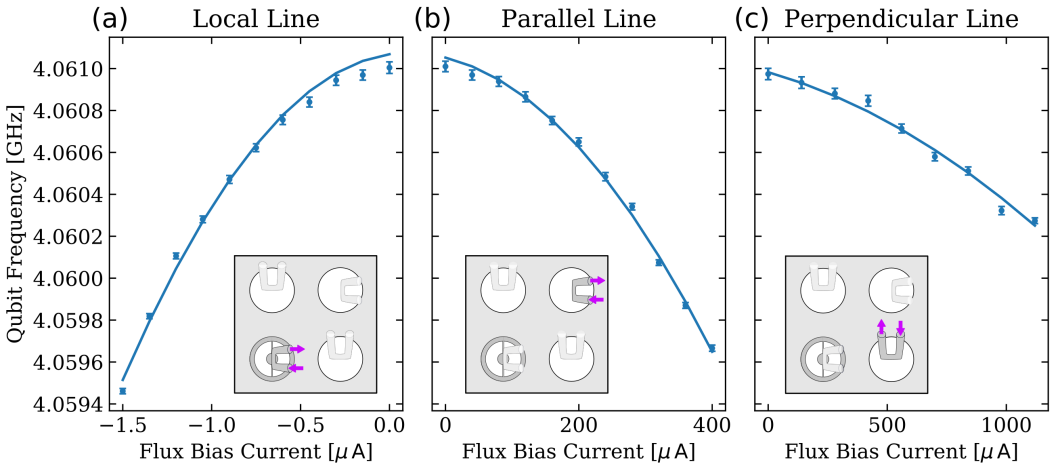

Figure 7.7: Measurements of DC crosstalk from proximal FBLs on device SQ2:1. In each experiment the qubit frequency is measured by determining the detuning from the drive when performing Ramsey oscillations (points). The qubit frequency changes as a function of DC current applied to the FBL, as this is fitted (solid lines) to Eq. (7.3) in order to extract the periodicity. (a): Calibration experiment where the qubit is tuned from its own FBL. (b): Current is instead applied to the FBL at the port diagonally across from the local port, orientated parallel to the local FBL. A comparison of the periodicities reveals a crosstalk of $0.33 \pm 0.015\%$ from this line. (c): Current is instead applied to the FBL at the neighbouring port, oriented perpendicular to the local FBL. A comparison of the periodicities reveals a crosstalk of $0.069 \pm 0.005\%$ from this line.

measured oscillations. The measured values are fitted to the model $f_{01}(E_J(\Phi_{\text{ext}}), E_C)$ as defined in Eq. (5.5), with $E_J(\Phi_{\text{ext}})$ given by

$$E_J(\Phi_{\text{ext}}) = E_{J\Sigma} \cos\left(\pi \frac{\Phi_{\text{ext}} - \Phi_{\text{off}}}{\Phi_0}\right) \sqrt{1 + d^2 \tan^2\left(\pi \frac{\Phi_{\text{ext}} - \Phi_{\text{off}}}{\Phi_0}\right)} \tag{7.6}$$

with Φ_0 and Φ_{off} as free parameters, and $E_{J\Sigma} = 18.24$ GHz, $\mathrm{E_C} = 129$ GHz, $\mathrm{d} = 0.05$, determined from independent experiments[4]. From the ratios of the periodicities, we extract crosstalk values of $0.33 \pm 0.015\%$ for the diagonal (parallel-aligned) line and $0.069 \pm 0.005\%$ for the neighbouring (perpendicular-aligned) line. This level of crosstalk is low compared to values of $1\% - 10\%$ found in recent experiments [156, 157, 158, 159, 160], and is the result of using gradiometric SQUIDs mode-matched to their respective FBLs.

[4]The justification for fitting Φ_{off} is that the amount of trapped flux in the SQUID loops drifts in time and can be changed by the switching of the current on the lines. However in this experiment all fits gave the same value of $\Phi_{\text{off}} = 1.4 \times 10^{-3} \Phi_0$.

7.3 Demonstrations of Fast-Flux Performance

7.3.1 Fast frequency switching

The presence of inductance and resistance in a coil acts as a low-pass filter on AC signals applied to it, with larger values leading to a lower cut-off frequency, and thus a longer time-scale of operation. For example, the large inductance of the long wound cable of external coils usually leads to a time-response of the order of milliseconds. Since the coil of the sample holder's off-chip FBL is not made of superconducting material, and since the line will have some inductance, it is necessary to investigate whether the time response of the FBL is sufficiently fast to perform quick operations on the qubit (on the time-scale of nanoseconds). The ability to quickly tune the qubit frequency to a desired value, hold it there, and return it to the original frequency, is necessary for certain gates such as the CZ gate implemented in [146].

To make a determination of this time-response, we perform flux-pulse spectroscopy (Fig. 7.8) and observe the switching speed of the qubit frequency, as is done in [155]. Pulsed spectroscopy of the qubit is performed with a Gaussian π-pulse to perform spectroscopy, followed by a flux-pulse, and finally a readout-pulse. In addition to the frequency of the spectroscopy pulse, the delay time of the start of the pulse with respect to the flux-pulse is swept. The flux-pulse quickly shifts the qubit frequency from its starting value and holds it there, during this time, the spectroscopy pulse is applied to the qubit and excites it depending on whether its frequency is resonant with the qubit at that particular delay. The flux-pulse is then switched off and the readout-pulse is applied at the value of the LC resonance when the qubit is in its starting frequency. The readout pulse is applied 7 μs after the end of the flux-pulse to ensure the qubit has returned to its original frequency, as there is a ring-down of the current on the line on the order of microseconds caused by the presence of a capacitor in the bias-tee. Another consequence of the capacitance of the bias-tee is the resetting of the charge once of the plates have been loaded (proportional to dV/dt) so to compensate for this the height of the flux-pulse has a linearly increasing slope to compensate for the accumulating charge on the capacitor

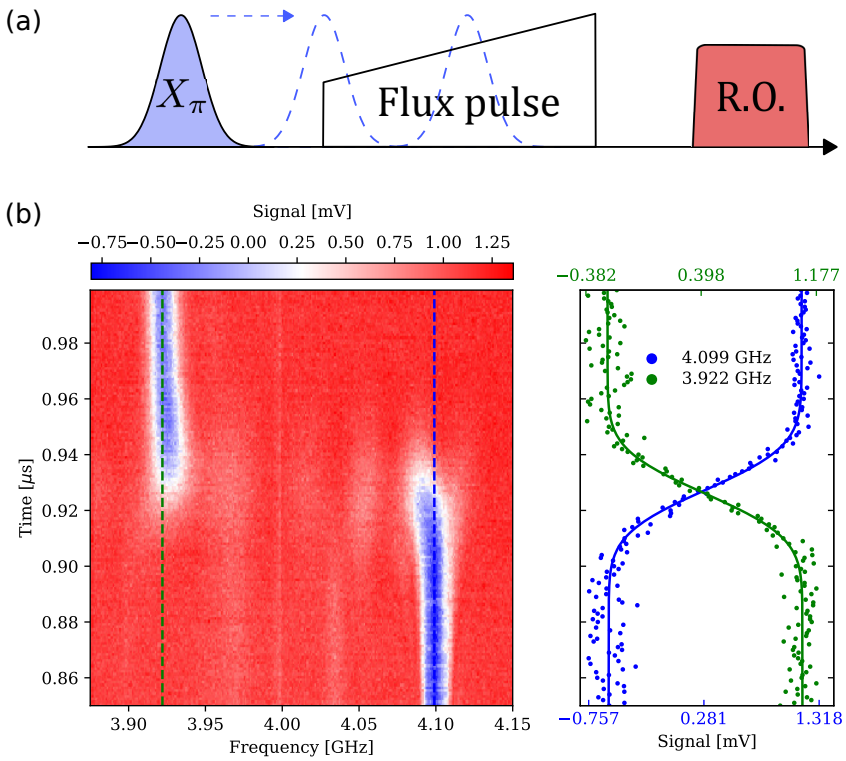

Figure 7.8: Measurement of dynamic tuning of the qubit of SQ2:1. (a): The pulse scheme of the experiment, a flux pulse is applied to suddenly detune the qubit from its start position and hold it at a new value for a fixed time. To perform spectroscopy of the frequency shift, a $\hat{X}_\pi$ pulse of width $\sigma = 12.5$ ns calibrated at $f_{01} = 4.099$ GHz is also applied to the qubit at some frequency and delay from the start of the flux pulse. The amplitude of the flux pulse is increased linearly after is starts to account for the effects of the capacitor in the bias-tee. The readout pulse is applied 7 μs after the end of the flux pulse such that the qubit frequency has returned to its original value and the resonator can be read out at the corresponding frequency. (b): Qubit spectroscopy as a function of spectroscopy pulse frequency and delay. The qubit frequency is seen to shift from 4.099 GHz to 3.922 GHz at $t \approx 0.93$ μs. (c): Traces of the measured signal at the original (blue) and switched (green) qubit frequencies corresponding to the dashed lines in (b). The shape of the traces is determined by the Gaussian shape of the spectroscopy pulse, the traces are fitted to error functions with width $\sigma = 12.5$ ns, and the difference between their centre values gives the frequency switching time, 1.23 ns$\pm$0.56 ns. Note the difference in scale of the two x-axes, as the rotation generated by the spectroscopy pulse is altered due to the frequency dependence of the of the qubit control line transfer-function, modifying the final pulse amplitude.

[161], and hold the qubit frequency at the switched value.

The experiment is performed and the switching of the qubit frequency as the flux-pulse is applied is revealed in Fig. 7.8(b). The qubit initially starts at 4.099 GHz and at $t \approx 0.93$ μs shifts to 3.922 GHz. The individual traces of both frequencies are plotted in Fig. 7.8(c), and a rising slope is observed due to the temporal width of the spectroscopy pulse (the amount of rotation is proportional to the integral overlap region between the spectroscopy and flux pulses). Both traces are fitted to error functions (i.e. the cumulative distribution function of the Gaussian) with $\sigma = 12.5$ ns, and the centre values taken as the times at which the middle of the spectroscopy-pulse is aligned to the start of the flux-pulse. The difference in these times is taken as the qubit frequency transit time for which we obtain a value of 1.23 ns $\pm$ 0.56 ns. From this we conclude that the switching time of the qubit frequency is on the order of nanoseconds.

7.3.2 $\hat{Z}$-rotations

To show that the FBL coherently shifts the qubit frequency and doesn't induce additionally dephasing during operation, it can be used to coherently accumulate a controlled amount of phase on the qubit, i.e. to perform rotations of the qubit state about the $\hat{Z}$-axis on the Bloch sphere. This could in principle be used to tune up a $\hat{Z}$-gate on the qubit, although other approaches exist [162].

Fig. 7.9 shows a demonstration of $\hat{Z}$ rotations. An echo pulse scheme is applied in order to take advantage of the longer coherence time T_2^E, and the free evolution time is fixed to 400 ns such that on average the qubit has experienced an 85% decoherence of its state after the scheme. A flux pulse is sent to the FBL such that it coincides with the center of the first free evolution period. The flux pulse causes the qubit frequency to change, accumulating phase that is proportional to the integral of the pulse. Finally the last qubit pulse acts to perform tomography of the qubit state in the $\hat{X}$ and $\hat{Y}$ bases in order to determine the evolution of the state on the equator of the Bloch sphere. The amplitude of the flux pulse is swept in order to accumulate varying amounts of phase and the measured signal is recorded. Because this experiment was carried out at the

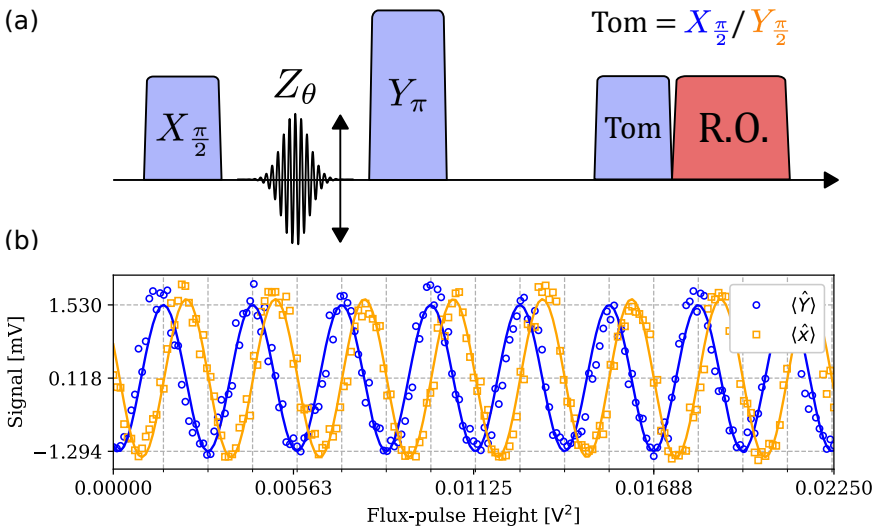

Figure 7.9: (a): Pulse scheme of a $\hat{Z}$-rotation experiment. The $\hat{X}_{\frac{\pi}{2}}$, $\hat{Y}_\pi$, and tomography pulses form a standard set for an echo experiment with a fixed total free-evolution time of 1 μs. At the centre of the first free-evolution period is a modulated flux-pulse of frequency 100 MHz inside a Gaussian envelope with width $\sigma = 20$ ns. To track the evolution around the Bloch sphere, the tomography pulse is switched between an $\hat{X}_{\frac{\pi}{2}}$ and $\hat{Y}_{\frac{\pi}{2}}$ pulse to measure the projections $\langle\hat{Y}\rangle$, $\langle\hat{X}\rangle$ respectively. (b): Measured rotations about $\hat{Z}$ on SQ2:1, points are data and solid lines are fits to sin oscillations. As a visual guide, grid lines are spaced according to the period of the fitted oscillations of $\langle\hat{Y}\rangle$. The phase difference between the two oscillations is found to be $87.0^\circ \pm 3.3^\circ$ in comparison to the expected 90°.

flux sweet-spot, the qubit frequency is approximately proportional to the square of the external flux, $\omega_{01} \propto \Phi_{\text{ext}}^2 \propto \text{V}^2$, so the flux pulse amplitude is stepped in V^2 increments. The total width of the flux pulse used in Fig. 7.9(b) was 20 ns (modulated at 100 MHz) meaning a 20 ns $\hat{Z}$-gate could principally be calibrated. Coherent oscillations of the qubit state about $\hat{Z}$ are observed in the $\hat{X}$ and $\hat{Y}$ bases, with a phase difference between the two of $87.0^\circ \pm 3.3^\circ$. The deviation from the expected difference of 90° could be due to imperfect calibration of the initial and final qubit pulses.

7.3.3 Transfer-function of the FBL

In this experiment we wish to characterise the frequency response of the FBL in transmission, and validate that a range AC signals can be applied to the line up to some sufficient cut-off frequency. A relatively flat transfer function ensures that square flux pulses can be applied with little convolution of the shape, and that flux pulses with modulations

of order 100 MHz can be applied as required by several two-qubit entangling schemes [145, 148].

To characterise the transfer-function we perform $\hat{Z}$-rotation experiments as in Subsec. 7.3.2 with different modulation frequencies ω_{mod} of the flux-pulse (see Fig. 7.10(a)). Then for each ω_{mod} we fit the Larmor frequency Ω_z of the measured $\hat{Z}$-rotations, and calculate the line-loss in dB using the formula

$$\Xi = 10 \log_{10} \left(\frac{c\,\Omega_z}{(V_{\text{src}}^{\text{max}})^2} \right), \tag{7.7}$$

where $V_{\text{src}}^{\text{max}}$ is the maximum applied amplitude of the flux-pulse and c is a constant with dimension [Power]^2 that amounts to a fixed offset to the measured line loss in dB, the choice of which is explained later in this subsection. We now briefly justify the form of Eq. (7.7). We are interested in the line loss $\xi = P_{\text{line}}/P_{\text{src}}$, where P_{line} is the power of the signal going through the FBL at the bottom of the fridge and P_{src} is the applied signal power i.e. the value set at the AWG. Since ξ is a power ratio, it is expressed in dB as $10 \log_{10}(\xi) = 10 \log_{10} (P_{\text{line}}/P_{\text{src}})$. Since we are performing the experiment at the flux-sweet spot (as in Subsec. 7.3.2), the detuning of the qubit, and so the total phase accumulated, is approximately proportional to the pulse amplitude squared. Since Ω_z is proportional to the phase accumulated we can write $P_{\text{line}} = c\,\Omega_z$ and substitute this into the previous equation to recover Eq. (7.7).

We perform a $\hat{Z}$-rotation for each modulation frequency, determine Ω_z and calculate the line loss with Eq. (7.7) to produce the measured transfer shown in Fig. 7.10(b). In order to obtain flux-pulse modulations above 200 MHz IQ pulses from the Tektronix AWG were upconverted using the SGS microwave sources. This result is the transfer of the entire line including the input line, bias-tee and 2 GHz low pass filter in addition to the FBL. To determine the transfer function of the line itself, we determine the transmission of the input lines as well as the bias-tee and filter in separate experiments under cryogenic conditions to form the line calibration shown in Fig. 7.10(b). The offset to the measured transfer (c in Eq. (7.7)) is determined from this calibration such that the measured transfer and the line calibration have the same value at low frequency, allowing us to compare

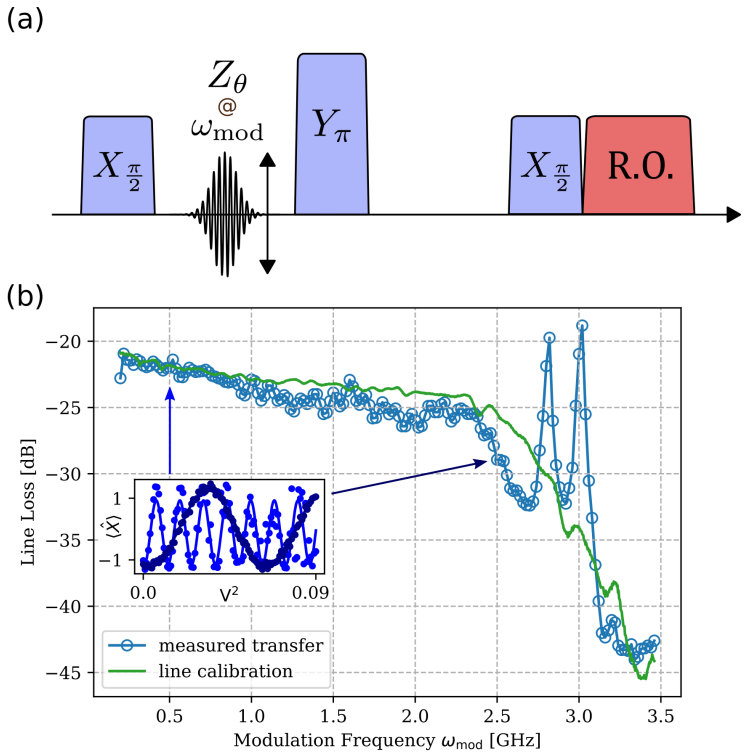

Figure 7.10: (a) Pulse scheme of the transfer function experiment, the $\hat{X}_{\frac{\pi}{2}}$, $\hat{Y}_\pi$, $\hat{X}_{\frac{\pi}{2}}$ pulses form a standard set for an echo experiment with a fixed total free-evolution time of 1 μs. At the centre of the first free-evolution period is a modulated flux-pulse of frequency ω_{mod} inside a Gaussian envelope with $\sigma = 100$ ns. (b) The measured transfer of the entire FBL chain as determined by the results of Z-rotation experiments (shown in the inset) and calculated with Eq. (7.7), as well as the loss of the measured line calibration consisting of the input line, bias-tee and 2 GHz low pass filter. The measured transfer trace is offset such that it matches the line calibration at low frequency.

the two traces more effectively. We see that the majority of the line loss is caused by the input lines and microwave components rather than the FBL. The total response is relatively smooth and flat, losing < 5 dB over a 2 GHz range, before decreasing due to the presence of the 2 GHz low-pass filter in the line. At $\omega_{\text{mod}} = 1.25\text{ GHz}, 2.0\text{ GHz}$, differences between the measured transfer and line calibration are observed signalling that there is some attenuation of signal due to the FBL at these frequencies. Higher than $\omega_{\text{mod}} = 2.5$ GHz there are two clear peaks of high transmission at $\omega_{\text{mod}} = 2.8$ GHz and 3.0 GHz that are not present in the line calibration. The cause of these peaks is not yet understood, however it is worth noting the qubit transition frequency is at 4.06 GHz meaning that this could correspond to the driving of a qubit transition, especially noting that the 200 MHz detuning between the two peaks is exactly twice the I.F. frequency

used for upconversion of the modulated flux pulse in this experiment.

7.4 Conclusions and Future Work

In this chapter we have presented the design and characterisation of a modification to the coaxmon architecture that allows for qubits with gradiometric SQUID loops to be selectively tuned with both DC and fast flux control provided by novel off-chip FBLs. The packaging, first explained in Subsec. 3.2.3, provides flux control without compromising on this architecture's wiring scheme extensibility or unit cell pitch, with FBLs mode-matched to their respective qubits and anti-matched to neighbours to achieve selective control. Flux is provided off-chip with no need for a galvanic connection to the device.

First we showed how magnetostatic simulations were used to predict the flux captured by the SQUID loops. We then outlined both the original and modified circuit designs that were explored, and how their shape determines the trade-off between total loop area, mutual inductance with the line, and qubit anharmonicity. We presented a careful characterisation of the qubits, primarily SQ2:1, tuned with both DC and AC flux signals. We found that the qubits follow the expected tuning curve of a transmon with reasonable periodicity 142.2 μA, and that with sufficient efforts to protect against flux-noise we measured $T_1 = 37.7$ μs and $T_2^E = 2.51$ μs. We also showed the low levels of DC flux crosstalk of $0.33 \pm 0.015\%$ when tuning the qubit from the diagonal port (parallel-aligned FBL) and $0.069 \pm 0.005\%$ from the neighbouring port (perpendicular-aligned FBL). We investigated the performance of the off-chip FBL, demonstrating that it could be used to perform fast switching of the qubit frequency on a time-scale < 2 ns, that it could be used to perform coherent $\hat{Z}$-rotations, and that the transfer function of the FBL was sufficiently flat and smooth over a 2 GHz range.

The next steps are to work towards improved qubit coherence. It is promising that a tunable qubit with the original design has been measured to have a sweet-spot T_2^E of 14.5 μs and an estimated $1/f$ RMS flux noise amplitude of $\mathcal{O}(10^{-5})\,\Phi_0$ in a packaging where the qubits are tuned with external coils instead of FBLs [163]. We wish to demonstrate that similar and improved coherence times can be realized inside a packaging with

fast-tuning, by improving filtering on the line and redesigning the FBL to route the current back up the fridge and make use of the twisted pairs of the DC loom. There are still optimizations to be made in terms of the design, precision, and ease of manufacture of the FBLs that would allow the lines to provide a larger amount of magnetic field through the chip-plane. Lastly we hope to make use of this method of flux delivery to explore different flux-tunable devices, two qubit gates that involve fast or parametric tuning, and qubit networks with tunable couplers, such that they can be incorporated into this scalable architecture.

Chapter 8

Conclusions and Outlook

8.1 Conclusions

In this thesis we have reported on the development of a new coaxial circuit QED architecture, that fulfils the requirement of extensibility by incorporating out-of-plane wiring into the sample holder. Single-qubit unit cells consisting of a transmon qubit and readout resonator with coaxial geometries are fabricated on opposing sides of a substrate, and selective control and readout of the qubits is achieved via a capacitance to coaxial wiring built into the device enclosure. Unit-cells of qubit and resonator can be arranged in a 2D array without modification of the wiring scheme.

Firstly, we explained the circuit and wiring design of the architecture, and the principle of how the design is scaled to 2D arrays of qubits without alteration to the wiring scheme. We detailed the techniques used to fabricate transmons and resonators on opposing sides of the same chips. Optimisations of this recipe enabled us to achieve qubit lifetimes in the range 10 μs $\leq$ T_1 $\leq$ 50 μs, and junction resistance spreads of 7%, giving rise to a sufficient yield of four-qubit devices.

Secondly, we demonstrated a first realization of a single-qubit unit cell of this architecture, fabricated with parameters that placed it in the dispersive regime of the Jaynes-Cummings Hamiltonian. We used spectroscopy to fully characterise the system Hamiltonian and show that reaching the strong coupling limit of this Hamiltonian is well within the scope of this architecture, finding parameters such as a qubit-resonator coupling of

418 MHz. We Further performed measurements of Rabi oscillations and of the characteristic relaxation and dephasing times to demonstrate the coherence of the qubit, finding $T_1 = 4.10\ \mu$s and $T_2^E = 6.67\ \mu$s.

Thirdly, we showed the viability of this approach at the multi-qubit scale, on devices with two and four dispersively coupled qubits. We explained how the qubit frequencies and couplings were optimised for cross-resonance, and showed that two-qubit gates with fidelities above 87 % could be performed on all primary pairs of a four-qubit device. We then performed a full characterisation of the drive port crosstalk and resonator-qubit cross-coupling, finding average isolations of 52 dB and 31 dB for the resonator and qubit ports respectively, and an average cross-coupling between circuits of 5.9 MHz. These values demonstrate the selective coupling that arises from the mode-matched circuits and wiring.

We utilised the Rabi Population Method to determine the temperature of qubits, and spin-echo traces to place upper bounds on the temperature of resonators, finding average values of ≈ 90 mK and ≈ 110 mK for qubits and resonators respectively. We then evaluated sources of decoherence in multi-qubit devices. We performed repeated measurements of characteristic times T_1, T_2^* and T_2^E to understand the time fluctuations of these parameters. We then utilised spin-locking to measure the underlying power spectral density of noise on the qubit frequency in the range $10^6\ \text{Hz} - 10^8\ \text{Hz}$, confirming resonator temperatures as the dominant source of decoherence during echo experiments, and finding Lorentzian peaks in the spectra which are characteristic of couplings to coherent two-level systems. Following this we used T_2 spectroscopy to scan for potential cavity modes that the qubits might be coupled to, finding none below 17 GHz.

Finally, we showed an extension of this architecture to incorporate frequency tuning of transmons with gradiometric SQUID loops via off-chip flux bias lines. An investigation of device coherence and flux line crosstalk was presented, finding $T_1 = 37.7\ \mu$s, $T_2^E = 2.51\ \mu$s at the flux sweet spot. Based on the change in coherence times with flux bias, we estimated an RMS $1/f$ flux noise amplitude of $2.7 \times 10^{-4}\Phi_0$. We also showed low levels of DC crosstalk with all values $< 0.4\%$. We then performed demonstrations of AC tuning of the

qubit frequency. We showed that the FBLs could be used to perform dynamic tuning of the qubit frequency on a time-scale < 2 ns. We then used the FBLs to perform coherent $\hat{Z}$-rotations, and extended this method to study the transmission of AC signals of up to 2 GHz through these FBLs, finding a sufficiently flat and smooth transfer function with < 5 dB loss over the range. This shows that dynamic tuning and parametric driving of the qubits are within the scope of this implementation.

8.2 Outlook

The architecture described in this thesis was developed primarily to be a platform for creating devices with many qubits. Whilst we have shown the viability of this approach on devices with four qubits, we can look ahead to how this approach can be further improved to yield circuits with larger numbers of qubits and larger varieties of designs.

In the near term, improvements to the device yield and coherence can be achieved through optimisation of fabrication, leveraging existing knowledge from literature as outlined in Sec. 4.5. To that end, the packaging and thermalisation of the device and control lines can be improved through light-tight enclosures, and appropriate high frequency filtering and attenuation of the microwave lines. Similarly, we can evaluate sources of flux-noise in the tunable-qubit framework to improve coherence times. Additionally it is worth working towards a redesign flux bias line wiring to achieve more positional precision, provide larger amount of fields, and provide a return path for the bias current to make use of twisted pairs to avoid induced currents in the bias line.

As designs scale to incorporate larger numbers of qubits there will be further challenges to focus on. As the substrate dimensions increase to incorporate such designs, it will be important to handle the presence of cavity modes that might couple to the qubits and act as a channel for Purcell loss. With the 5×5 mm sizes in this project there are no modes below 17 GHz however at dimensions of 10×10 mm there are modes at ≈ 10 GHZ that would be a cause for concern. This issue can be solved by utilising through-substrate vias [55] or by changing the mode structure of the holder [164]. A further objective that is useful for scaling devices is multiplexing of the qubit readout, so that many resonators can

be controlled and measured from one microwave input line with one channel of control electronics. There is scope to achieve this in this architecture by coupling many LC resonators to one drive port.

As the previous paragraph suggests, more will be needed than simple duplication of unit cells to produce devices with tens or hundreds of qubits. However given the flexibility of circuit design afforded by the simplicity of the device fabrication and packaging, there are many interesting research directions that can be investigated. One more immediately exciting area is the exploration of novel circuit designs and coupling buses that make use of the DC and AC flux control introduced into this architecture. Such circuits have been used to perform high fidelity two qubit gates [145], produce "protected" qubits with long-lived lifetimes [165, 166, 167] and explore models of physics [168] to name just a few possibilities. A further extension of this approach is the coupling of circuits between two or more chips. Such vertical coupling of circuits would increase the versatility of this architecture by coupling qubits to resonators or other qubits in this way, to achieve the benefits of flip-chip layouts without requiring bonding or galvanic connections between the chips. Finally there is scope to explore how microwave signals are delivered to devices of larger scale, for example by incorporating printed circuit boards into the packaging [61].

Appendices

Appendix A

Fabrication Recipe

The fabrication process of devices consists of one photolithography step to pattern the resonators across a 3 inch wafer, and one electron-beam lithography (EBL) step to pattern the qubits. The recipe has evolved throughout the course of this project, however we outline the procedure of the most recent recipe in Table A.1, which was used to create the four-qubit devices.

Step	Process
1	Photolithography • Pre-bake the substrate at 100°C for 5 min. • Spin AZ5214E at 500 rpm for 10 s, then at 3000 rpm for 45 s. • Bake at 110°C for 50 s. • Expose with a dose of 15 mJ/cm^2. • Develop with AZ726MIF for 60 s, rinse in DI water. • Liftoff in DMSO at 80°C for 60 min, then sonicate for 1 min with power 50% and frequency 37 kHz, then for 1 min with power 50% and frequency 80 kHz.
2	Wafer dicing • Dice wafer into 5 × 5 mm chips, be very careful to fully dice through substrate.
3	Chip preparation • Clean 2x chip holders, 2x washers with acetone and IPA • Carefully remove chip from prepared wafer, inspect resonator inductor lines for breaks • Stir chip for 30s in acetone to remove majority of protection resist, IPA rinse • Place chip in holder and sonicate resonator side (R-side) up in 50°C acetone for 5 mins @37kHz 70% pow, 1 min @80kHz 100% pow • Rinse chip in IPA and flip, placing it qubit side (Q-side) up into second chip holder in fresh beaker of acetone • Sonicate in 50°C acetone for 10 mins @37kHz 70% pow, 5 min @80kHz 100% pow • IPA rinse, N_2 blow dry chip on washer, inspect level of residue. • Place chip in holder, clean in DMSO @80C for 15 mins, Q-side up,rinse in warm DI water then IPA, N_2 dry
4	Spin coating of resist • Spin protection layer on R-side: Copolymer (AR-P 617.08) @ 3000 rpm for 45 s, bake at 180°C for 5 mins • 1st layer Q-side: Copolymer @ 3000rpm/45s, bake 180°C/5mins • 2nd layer Q-side: PMMA 950K (AR-P 672.045) @ 2500rpm/45s, bake at 180°C/5mins • 3rd layer Q-side: Electra92 (AR-PC 5090) @ 3000rpm/45s

5	EBL (JEOL JBX-5500 series ZC 50kV) • Mount chips in cassette Q-side up, ensure chips are level and firmly secured. • Write large features with 10 nA beam, 1 mm writefield, 700 μC/cm^2 dose • Write junctions with 100 pA beam, 100 μm writefield, 700 μC/cm^2 main dose and 160 μC/cm^2 undercut dose
6	Development • Remove Electra92 in DI water, N_2 blow dry • Development in 1:3 MIBK:IPA at 25°C for 45s, rinse in IPA for 15s, N_2 blow dry
7	Descum • O_2 plasma ash, RF300 (40 W) for 20 s, 0.5 mbar O_2
8	Evaporation (homebuilt e-beam evaporator) • Prepare chamber: Pump till base pressure 10^{-7} mbar, Al warmup recipe to mitigate outgassing of Al, Ti pump to lower water pressure to 10^{-8} • Al 60nm @ 60° to surface normal • Junction oxidation (typical values 4 mbar O_2 for 5 mins) • Al 70nm @ 0° to surface normal • Post oxidation, 20mbar for 2mins
9	Liftoff • Place chip in holder • Liftoff 30 mins-1 hour in acetone @ 60°C, IPA rinse • Clean in DMSO 30 mins @ 60°C, rinse in warm DI water, IPA, N_2 blow dry

Table A.1: Fabrication recipe used for multi-qubit devices.

Appendix B

Summary of Device Parameters

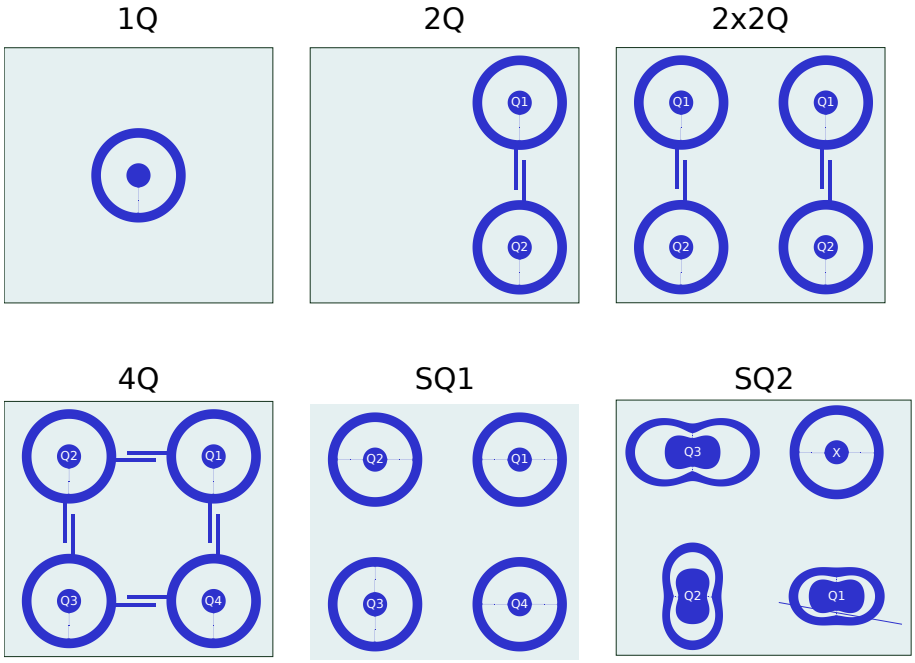

Figure B.1: CAD patterns of all devices measured in this thesis.

In this chapter we present the values from experimental characterisations of all relevant devices produced across the course of this project. CAD patterns for the qubit side of the chip for all devices are shown in Fig. B.1, with the resonator side containing LC circuits underneath each qubit as in the single-qubit unit cell. Four different single qubit devices were measured with values shown in Table B.2 before the focus of the project focused on multi-qubit devices. Initially, devices with two pairs of coupled qubits (2×2Q) were tested so as to have two independent two-qubit experiments on one chip. Due to fears of

circuit cross coupling we instead produced devices with one pair of coupled qubits (2Q), and the values of all these circuits are shown in Table B.3. Three four-qubit devices were made, with values in Table B.4. Due to an error in the code used to define the resonator mask, the first two devices had resonators 1.5 GHz lower in frequency than the intended target. This forced the qubit frequencies to be lower, which came with an increase in the charge dispersion affecting T_2^*. Finally two different devices were made to explore flux tunable designs. for SQ1, only qubit 1 was measured with sufficient depth to report, and in SQ2 the originally shaped transmon unfortunately had no working junctions, and so was omitted.

Symbol	Definition
d_{qpin}	Pin-qubit separation
d	Junction asymmetry factor
$\omega_c/2\pi$	Bare resonator frequency
$\omega_{r0}/2\pi$	Dressed resonator frequency
Q	Loaded resonator quality factor
Q_i	Internal quality factor
Q_e	External quality factor
$\kappa/2\pi$	Resonator photon decay rate
$\omega_{01}/2\pi$	Qubit frequency
$\Delta_0/2\pi$	Resonator-qubit detuning
$\alpha/2\pi$	Qubit anharmonicity
$\chi/2\pi$	Dispersive shift
E_J/h	Josephson energy
E_C/h	Charging energy
$g/2\pi$	Resonator-qubit coupling
T_1	Energy relaxation time
T_2^*	Ramsey decoherence time
T_2^E	Spin-echo decoherence time
$\mathrm{T_Q}$	Qubit temperature
$P_{1,\mathrm{therm}}$	Residual population in $\|1\rangle$
ζ	Qubit-qubit cross-Kerr
Δ_q	Qubit-qubit detuning
J	Qubit-qubit coupling

Table B.1: Relevant symbol definitions for this section.

Parameter	Unit	1Q1	1Q2	1Q3	1Q4
d_{qpin}	mm	0.3	0.3	0.7	0.6
$\omega_c/2\pi$	GHz	9.37	9.17	10.19	9.93
$\omega_{r0}/2\pi$	GHz	9.45	9.34	10.23	10.03
Q	$\times 10^3$	3.00	7.51	6.84	-
Q_i	$\times 10^3$	-	-	-	-
Q_e	$\times 10^3$	-	-	-	-
$\kappa/2\pi$	MHz	3.15	1.24	1.50	-
$\omega_{01}/2\pi$	GHz	5.61	8.46	7.23	8.41
$\Delta_0/2\pi$	GHz	-3760	-711	-2959	-1526
$\alpha/2\pi$	MHz	-129	-130	-294	-242
$\chi/2\pi$	MHz	-1.20	-32.70	-6.34	-35.66
E_J/h	GHz	33.6	73.4	26.3	41.1
E_C/h	MHz	122	126	268	227
E_J/E_C	-	275	583	98	181
$g/2\pi$	MHz	356	322	412	537
T_1	μs	2.20 / 0.190	0.566	4.1	1.46
T_2^*	μs	2.10 / 0.376	1.00	5.65	-
T_2^E	μs	-	-	6.67	-
$\mathrm{T_Q}$ / $P_{1,\mathrm{therm}}$	mK/%	-	-	70 / 0.7	-
Device Notes		No descum, Lifetimes decreased after two weeks	No descum	Plasma etch RF150 17s	Plasma etch RF150 17s

Table B.2: Single qubit devices.

		2 × 2Q0 Pair 1		2 × 2Q0 Pair 2 (2Qα)		2 × 2Q1 Pair 2 (2Qβ)		2 × 2Q2 Pair 2 (2Qγ)		2Q1	
Parameter	Unit	1	2	1	2	1	2	1	2	1	2
d_{qpin}	mm	0.9	0.9	0.9	0.9	1.1	1.1	1.1	1.1	1.1	1.1
$\omega_c/2\pi$	GHz	10.48	9.69	10.73	9.68	10.71	9.65	10.60	9.52	10.55	9.50
$\omega_{r0}/2\pi$	GHz	10.48	9.69	10.73	9.68	10.71	9.65	10.60	9.52	10.55	9.50
Q	$\times 10^3$	9.66	13.20	4.13	14.70	5.86	11.70	-	-	4.52	11.59
Q_i	$\times 10^3$	-	-	-	-	-	-	-	-	-	-
Q_e	$\times 10^3$	-	-	-	-	-	-	-	-	-	-
$\kappa/2\pi$	MHz	1.08	0.73	2.60	0.66	1.83	0.82	-	-	2.33	0.82
$\omega_{01}/2\pi$	GHz	7.97	7.84	7.98	7.74	6.67	5.92	7.33	6.10	6.59	6.08
$\Delta_0/2\pi$	GHz	-2508	-1852	-2750	-1941	-4038	-3730	-3277	-3424	-3958	-3425
$\alpha/2\pi$	MHz	-	-276	-282	-270	-308	-326	-300	-300	-299	-310
$\chi/2\pi$	MHz	-3.89	-6.80	-4.39	-7.19	-2.33	-2.17	-3.65	-2.75	-2.83	-2.72
E_J/h	GHz	-	32.19	32.70	32.00	21.90	16.80	26.50	18.90	18.14	14.89
E_C/h	MHz	-	255	260	250	277	288	273	268	299	310
E_J/E_C	-	-	126	126	128	79	58	97	71	61	48
$g/2\pi$	MHz	-	268	325	294	337	290	345	313	383	320
T_1	μs	1.70	1.50	4.65	7.28	8.77	13.28	10.18	11.24	29.80	36.80
T_2^*	μs	-	-	5.50	4.00	5.11	6.75	4.62	1.50	-	-
T_2^E	μs	-	-	-	-	-	-	-	-	48.80	65.00
T_Q / $P_{1,\text{therm}}$	mK/%	-	-	-	-	-	-	-	-	129 / 8.9	125 / 9.9
		$1 \leftrightarrow 2$		$1 \leftrightarrow 2$		$1 \leftrightarrow 2$		$1 \leftrightarrow 2$		$1 \leftrightarrow 2$	
ζ	MHz	-		3.86		-0.17		-0.07		-0.55	
Δ_q	MHz	129		243		756		1231		510	
J	MHz	-		11.83		11.40		12.90		12.50	

Table B.3: Two-qubit devices

		4Q1				4Q2				4Q3			
Parameter	Unit	1	2	3	4	1	2	3	4	1	2	3	4
$\omega_{r0}/2\pi$	GHz	9.48	9.04	8.62	8.13	9.46	9.04	8.62	8.14	11.30	10.84	10.28	9.74
Q	$\times 10^3$	54	23	67	42	61	-	44	18	1.3	9.0	3.5	1.5
Q_i	$\times 10^3$	133	89	331	179	268	-	94	27	-	-	-	-
Q_e	$\times 10^3$	92	31	84	55	79	-	83	54	-	-	-	-
$\kappa/2\pi$	MHz	0.18	0.39	0.13	0.19	0.16	-	0.20	0.45	8.48	1.20	2.92	6.62
$\omega_{01}/2\pi$	GHz	5.31	4.76	4.21	3.79	5.04	4.76	4.26	3.69	7.62	7.27	6.64	6.07
$\Delta_0/2\pi$	GHz	-4165	-4286	-4408	-4340	-4421	-4272	-4352	-4454	-3680	-3565	-3639	-3665
$\alpha/2\pi$	MHz	-328	-358	-360	-360	-310	-328	-330	-342	-266	-277	-294	-310
$\chi/2\pi$	MHz	-2.56	-2.32	-2.20	-2.03	-2.12	-2.07	-2.08	-1.94	-3.25	-2.82	-3.05	-2.20
E_J/h	GHz	13.8	10.7	8.7	7.2	13.2	11.4	9.3	7.2	31.5	27.9	22.6	18.3
E_C/h	MHz	285	302	297	290	270	281	279	277	246	254	266	276
E_J/E_C	-	48	35	29	25	49	41	33	26	128	110	85	66
$g/2\pi$	MHz	353	330	330	312	353	326	332	322	391	345	356	296
$\bar{T}_1$	μs	15.10	18.00	20-27	20-26	29.20	26.30	31.82	49.18	6.31	6.66	8.56	22.96
$\bar{T}_2^*$	μs	1.10	4.00	0.30	0.50	5.89	1.50	<1	<1	7.92	9.84	8.77	12.74
$\bar{T}_2^E$	μs	29.00	14.00	16.00	8.00	15.07	9.67	4.20	1.85	7.73	10.84	10.72	12.83
T_Q / $P_{1,\mathrm{therm}}$	mK/%	85 / 4.9	77 / 5.2	-	-	65 / 2.5	82 / 6.1			98 / 2.5	114 / 4.7	153 / 12.6	106 / 6.4
		$1 \leftrightarrow 2$	$2 \leftrightarrow 3$	$3 \leftrightarrow 4$		$1 \leftrightarrow 2$	$2 \leftrightarrow 3$	$3 \leftrightarrow 4$		$1 \leftrightarrow 2$	$2 \leftrightarrow 3$	$3 \leftrightarrow 4$	
ζ	MHz	-0.09	-0.08	-0.26		0.78	-0.10	-0.08		0.75	0.09	0.12	
Δ_q	MHz	557	544	427		278	499	575		346	628	572	
J	MHz	5.24	4.41	4.40		4.87	4.65	5.17		7.64	6.91	6.80	

Table B.4: Four-qubit devices.

		SQ1	SQ2		
Parameter	Unit	1	1	2	3
Loop Area	mm^2	0.412	0.121	0.191	0.388
Periodicity	μA	108	143	170	59
d	-	0.35	0.05	-	-
$\omega_{r0}/2\pi$	GHz	10.46	8.14	8.60	9.01
Q	$\times 10^3$	-	-	-	-
Q_i	$\times 10^3$	-	-	-	-
Q_e	$\times 10^3$	-	-	-	-
$\kappa/2\pi$	MHz	-	2.5	1.8	1.4
$\omega_{01}/2\pi$	GHz	6.86	4.11	4.92	5.01
$\Delta_0/2\pi$	GHz	-3598	-4029	-3689	-4003
$\alpha/2\pi$	MHz	-290	-129	-132	-172
$\chi/2\pi$	MHz	-2.17	-0.15	-0.54	-0.89
$E_{J\Sigma}/h$	GHz	24.2	18.6	25.6	21.0
E_C/h	MHz	264	120	124	159
E_J/E_C	-	92	155	206	132
$g/2\pi$	MHz	298	135	231	281
$\bar{T}_1$	μs	1.5	37.7	8.0	3.2
$\bar{T}_2^*$	μs	0.3	2.11	< 0.1	< 0.05
$\bar{T}_2^E$	μs	0.3	2.51	< 0.1	< 0.1
T_Q / $P_{1,\mathrm{therm}}$	mK/%	-	126 / 21	-	-
Device Notes		Third cooldown with magnetic shield	Second cooldown with magnetic shield	No magnetic shield	No magnetic shield

Table B.5: Flux-tunable devices (all parameters measured at flux sweet spot where relevant).

Appendix C

Cavity-Bloch Equations in Reflection

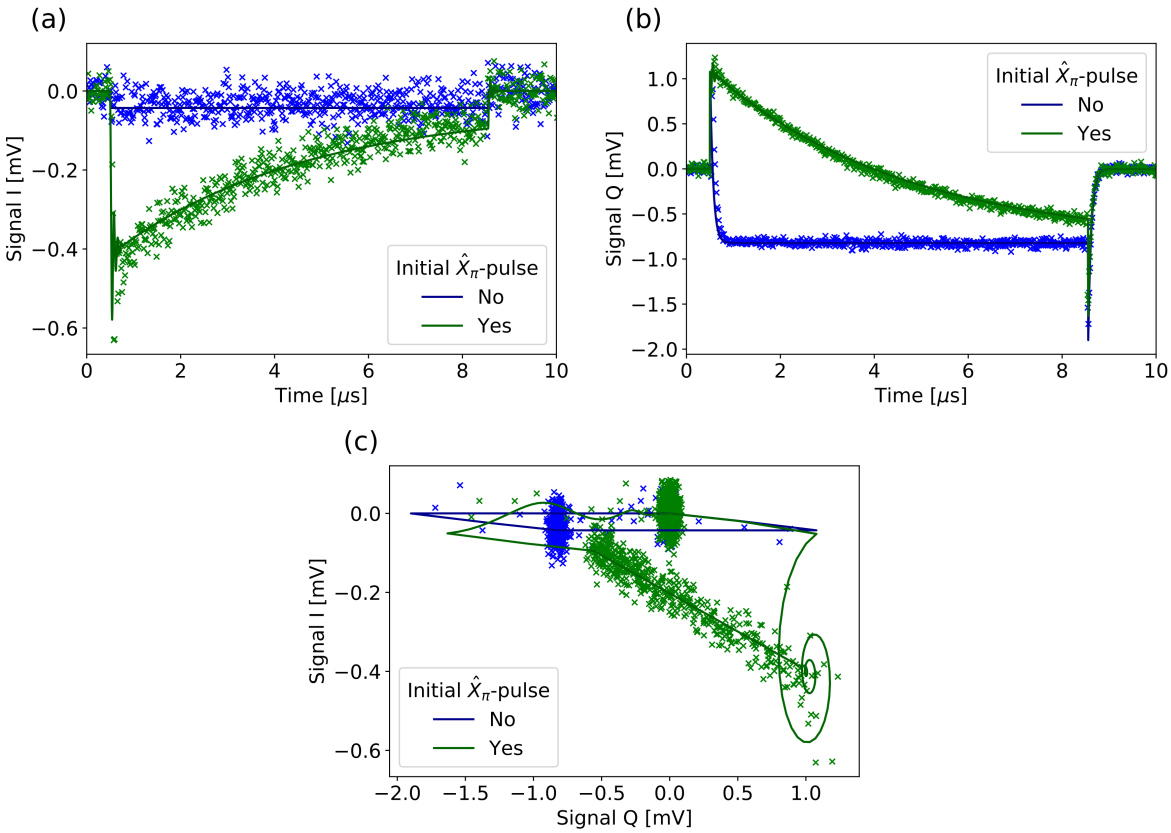

Figure C.1: Time resolved traces of the measured reflected signal after an 8 μs pulse to the resonator, with and without the qubit prepared in $|1\rangle$ by an initial $\hat{X}_\pi$-pulse. (a)-(b): The I and Q quadratures of the recorded signal plotted against time. Points are data and solid lines are fits to the data using the model described by Eq. (C.9) and Eq. (C.10). the data is first rotated in the IQ plane to maximise the signal range in Q. (c): The same data and fits as (a) and (b), plotted in the complex plane.

In order to meaningfully measure the qubit state during a time resolved experiment we wish to convert the measured signal into a qubit population value, i.e. an accurate measure of the $\langle \hat{Z} \rangle$ value of the qubit. In a time-resolved experiment, the qubit state is measured by way of dispersive readout, with a square pulse to the resonator of finite width. After down-conversion of the measured response, both the time-average values of the I and Q quadratures are used to infer the qubit state. In this section we explain how we map these measured signals to $\langle \hat{Z} \rangle$ using a slight modification of the protocol used in [47]. The Cavity-Bloch equations describe the time response of the measured signal from a driven resonator dispersively coupled to a qubit. It is obtained by solving the Lindblad-type master equation of the dispersive Jaynes-Cummings Hamiltonian and neglecting higher-order terms to lead to the set of eight coupled differential equations[47],

$$\frac{d\langle \hat{a} \rangle}{dt} = -i\Delta_{rm}\langle \hat{a} \rangle - i\chi\langle \hat{a}\hat{\sigma_z} \rangle - i\epsilon_m - \frac{\kappa}{2}\langle \hat{a} \rangle, \tag{C.1}$$

$$\frac{d\langle \hat{\sigma_z} \rangle}{dt} = \Omega\langle \hat{\sigma_y} \rangle - \Gamma_1 \left(1 + \langle \hat{\sigma_z} \rangle\right), \tag{C.2}$$

$$\frac{d\langle \hat{\sigma_x} \rangle}{dt} = -\left(\Delta_{as} + 2\chi\left(\langle \hat{a}^\dagger \hat{a} \rangle + \frac{1}{2}\right)\right)\langle \hat{\sigma_y} \rangle - \left(\frac{\Gamma_1}{2} + \Gamma_\phi\right)\langle \hat{\sigma_x} \rangle, \tag{C.3}$$

$$\frac{d\langle \hat{\sigma_y} \rangle}{dt} = -\left(\Delta_{as} + 2\chi\left(\langle \hat{a}^\dagger \hat{a} \rangle + \frac{1}{2}\right)\right)\langle \hat{\sigma_x} \rangle - \left(\frac{\Gamma_1}{2} + \Gamma_\phi\right)\langle \hat{\sigma_y} \rangle - \Omega\langle \hat{\sigma_z} \rangle, \tag{C.4}$$

$$\frac{d\langle \hat{a}\hat{\sigma_z} \rangle}{dt} = -i\Delta_{rm}\langle \hat{a}\hat{\sigma_z} \rangle - i\chi\langle \hat{a} \rangle + \Omega\langle \hat{a}\hat{\sigma_y} \rangle - i\epsilon_m\langle \hat{\sigma_z} \rangle - \Gamma_1\langle \hat{a} \rangle - \left(\Gamma_1 + \frac{\kappa}{2}\right)\langle \hat{a}\hat{\sigma_z} \rangle, \tag{C.5}$$

$$\begin{aligned}\frac{d\langle \hat{a}\hat{\sigma_x} \rangle}{dt} = &-i\Delta_{rm}\langle \hat{a}\hat{\sigma_x} \rangle - \left(\Delta_{as} + 2\chi\left(\langle \hat{a}^\dagger \hat{a} \rangle + 1\right)\right)\langle \hat{a}\hat{\sigma_y} \rangle - i\epsilon_m\langle \hat{\sigma_x} \rangle \\ &- \left(\frac{\Gamma_1}{2} + \Gamma_\phi + \frac{\kappa}{2}\right)\langle \hat{a}\hat{\sigma_x} \rangle,\end{aligned} \tag{C.6}$$

$$\begin{aligned}\frac{d\langle \hat{a}\hat{\sigma_y} \rangle}{dt} = &-i\Delta_{rm}\langle \hat{a}\hat{\sigma_y} \rangle - \left(\Delta_{as} + 2\chi\left(\langle \hat{a}^\dagger \hat{a} \rangle + 1\right)\right)\langle \hat{a}\hat{\sigma_x} \rangle - i\epsilon_m\langle \hat{\sigma_y} \rangle \\ &- \left(\frac{\Gamma_1}{2} + \Gamma_\phi + \frac{\kappa}{2}\right)\langle \hat{a}\hat{\sigma_y} \rangle - \Omega\langle \hat{a}\hat{\sigma_z} \rangle,\end{aligned} \tag{C.7}$$

$$\frac{d\langle \hat{a}^\dagger \hat{a} \rangle}{dt} = -2\epsilon_m \mathrm{Im}\langle \hat{\mathrm{a}} \rangle - \kappa\langle \hat{\mathrm{a}}^\dagger \hat{\mathrm{a}} \rangle \tag{C.8}$$

where we have used the notation $\hat{\sigma}_z = \hat{Z}$, $\hat{\sigma}_x = \hat{X}$, $\hat{\sigma}_y = \hat{Y}$, Δ_{rm} is the detuning of the resonator drive tone from ω_r (usually $= -\chi$), Δ_{as} is the detuning of the qubit drive tone from the undressed qubit frequency ω_a (usually $= \chi$), ϵ_m is the measurement tone

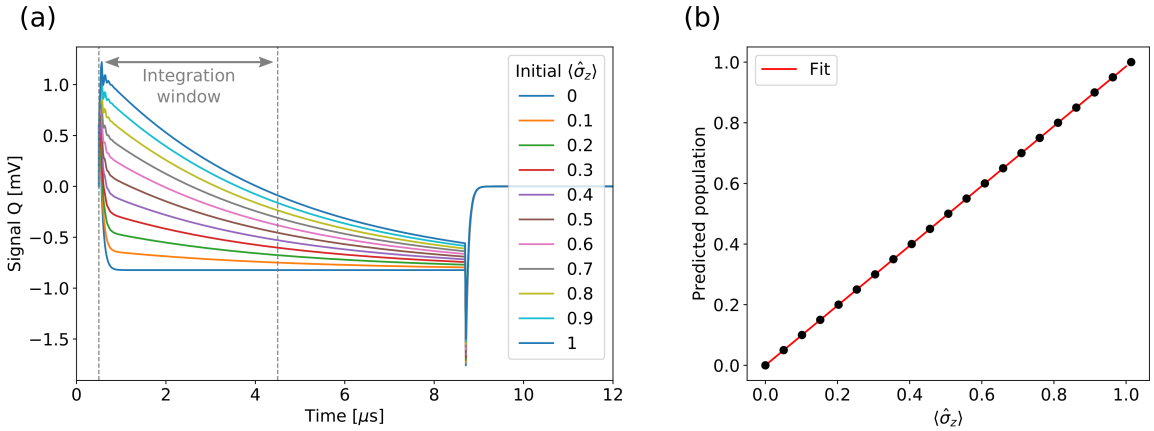

Figure C.2: (a): Simulated Q quadratures of the reflected responses of a device with the same parameters as in Fig. C.1 for several different initial qubit populations at $t = 0$. An appropriate window to integrate over is chosen from the data traces optimising for signal-to-noise. (b): The mapping between initial qubit population and predicted population, obtained from the normalised integrations obtained in (a). The mapping is found to be linear (although not simply $y = x$) and the fit can be used to convert the integrated values of experimental traces into $\langle\hat{\sigma}_z\rangle$.

amplitude, Ω is the qubit tone amplitude, and κ,χ,Γ_1,Γ_ϕ are the resonator decay rate, qubit-resonator dispersive shift, qubit decay rate and qubit pure dephasing rate, as usual. The set of equations can be solved numerically to obtain with values of κ,χ,Γ_1,Γ_ϕ obtained from experiment, and $\epsilon_m(t)$, $\Omega(t)$ defining the envelope of the resonator and qubit drive pulses respectively. Part of the solution set is the expectation of the cavity field $\langle\hat{a}\rangle(t)$ and would be enough to fit the time response of the signal in transmission, however in reflection we must also account for the reflected signal from interfaces where there is an impedance mismatch along the lines. We make a simple guess at the form of the total reflection response, where the form is the sum of the Cavity-Bloch response and some reflected constant resonator drive signal $\Gamma\epsilon_m(t)$, where $\epsilon_m(t)$ is the square resonator pulse as before, and Γ is the reflection coefficient and is modelled as a complex constant number. The form of the measured I and Q is thus estimated to be:

$$I \propto \mathrm{Re}[\langle\hat{\mathrm{a}}\rangle + \Gamma\epsilon_{\mathrm{m}}(\mathrm{t})] \tag{C.9}$$

$$Q \propto \mathrm{Im}[\langle\hat{\mathrm{a}}\rangle + \Gamma\epsilon_{\mathrm{m}}(\mathrm{t})] \tag{C.10}$$

The fitting protocol is as follows:

1. Measurements of the time-response of the resonator are made both with the qubit in ground, and with the qubit in the excited state with an initial calibrated $\hat{X}_\pi$-pulse sent to the qubit. The I and Q of each experimental time-response trace are recorded, and the complex data is rotated in the IQ plane so as to put as much information as possible into the Q quadrature, this rotation also aligns the data to the results from the Cavity-Bloch simulations.

2. The data is then manually fitted in the IQ plane to the the model given by Eq. (C.9) and Eq. (C.10), with Γ and the amplitude of $\epsilon_m(t)$ as free parameters that must be consistent between different experiments (only the IQ rotation of the data can be arbitrary between experiments).

3. Simulations of the time-response are made using the fitted parameters, with several different starting qubit population $\langle\hat{\sigma}_z\rangle$. Each simulated Q trace is integrated/time-averaged between a specified start and end time (which are optimised for a large signal-to-noise ratio in experiment). The time-averaged valued form a mapping from integrated signal to qubit state, and may not necessarily be linear.

4. With this mapping, we can convert the measured signal of any time-resolved experiment into the qubit population $\langle\hat{\sigma}_z\rangle$. The time-resolved traces of each point in an experiment are recorded, the IQ data is rotated as before, and the Q traces are integrated in the same measurement window as the previous step. These integration values are then converted to qubit population with the mapping produced by the previous step.

This approach was used to extract $\langle\hat{Z}\rangle$ for all the time resolved experiments in Chapter 5. For the subsequent chapters, we used a simplified protocol whereby the time-averaged I and Q values were plotted in the complex plane and a value of $\langle\hat{Z}\rangle$ was extracted by mapping the point to a linear interpolation between a ground and excited reference point, determined by measuring the qubit with and without an initial $\hat{X}_\pi$-pulse. This process relies on the linearity between the value of I and Q, and the qubit population, which can be confirmed experimentally. For more details on the protocol, see Subsec. 5.2.3 of [65].

Bibliography

[1] T. D. Ladd, F. Jelezko, R. Laflamme, Y. Nakamura, C. Monroe, and J. L. O. Brien, "Quantum computers," *Nature* **464** no. 7285, (2010) 45–53.

[2] M. A. Nielsen and I. L. Chuang, *Quantum Computation and Quantum Information*. Cambridge University Press (CUP), Cambridge, UK, 2000.

[3] R. P. Feynman, "Simulating Physics with Computers," *Technical Report 6* (1982) .

[4] D. Deutsch, "Quantum theory, the Church-Turing principle and the universal quantum computer," in *Royal Society A: Mathematical, Physical, and Engineering Sciences, vol. 400*, pp. 97–117. 1985.

[5] D. Deutsch and R. Jozsa, "Rapid solution of problems by quantum computation," *Proc. R. Soc. Lond. A* **439** no. 553–558, (1992) .

[6] P. W. Shor, "Algorithms for quantum computation: Discrete logarithms and factoring," in *35th Annual Symposium on Foundations of Computer Science*, p. 124. IEEE Computer Society Press, Santa Fe, 1994.

[7] L. K. Grover, "A fast quantum mechanical algorithm for database search," in *28th ACM Symposium on Theory of Computation*, vol. 212. 1996.

[8] P. W. Shor, "Fault-tolerant quantum computation," in *37th Symposium on Foundations of Computing*, pp. 56–65. IEEE Computer Society Press, 1996. `https://arxiv.org/abs/quant-ph/9605011`.

[9] A. Steane, "Multiple-particle interference and quantum error correction," in *Proceedings of the Royal Society of London. Series A: Mathematical, Physical and Engineering Sciences*, pp. 452, 2551–2577. 1996.

[10] R. Laflamme, C. Miquel, J. P. Paz, and W. H. Zurek, "Perfect quantum error correcting code," *Physical Review Letters* **77** (1996) 198–201.

[11] J. A. Jones and M. Mosca, "Implementation of a quantum algorithm on a nuclear magnetic resonance quantum computer," *J. Chem. Phys.* **109(5):164** (1998) .

[12] W. S. Warren, N. Gershenfeld, and I. L. Chuang, "The Usefulness of NMR Quantum Computing," *Science* **277.** no. 5332, (1997) 1688–1690.

[13] C. D. Bruzewicz, J. Chiaverini, R. Mcconnell, and J. M. Sage, "Trapped-Ion Quantum Computing: Progress and Challenges," 2019. `arXiv:arXiv:1904.04178v1`.

[14] J. W. Silverstone, D. Bonneau, J. L. O'Brien, and M. G. Thompson, "Silicon Quantum Photonics Joshua W. Silverstone, Damien Bonneau, Jeremy L. O'Brien, and Mark G. Thompson," *IEEE JOURNAL OF SELECTED TOPICS IN QUANTUM ELECTRONICS* **22** (2016) .

[15] D. Loss and D. P. Divincenzo, "Quantum computation with quantum dots," *Physical Review A* **57** (1998) 120–126.

[16] Jelezko, F and J. Wratchup, "Single defect centres in diamond: A review," *physica status solidi* **203** (2006) 3207–3225.

[17] M. V. G. Dutt, L. Childress, L. Jiang, E. Togan, J. Maze, F. Jelezko, A. S. Zibrov, P. R. Hemmer, and M. D. Lukin, "Quantum register based on individual electronic and nuclear spin qubits in diamond," *Science* **316** (2007) 1312–1316.

[18] H. J. Briegel, T. Calarco, D. Jaksch, J. I. Cirac, and P. Zoller, "Quantum computing with neutral atoms," *Journal of Modern Optics* **47** (2000) 415–451.

[19] F. A. Zwanenburg, A. S. Dzurak, A. Morello, M. Y. Simmons, L. C. Hollenberg, G. Klimeck, S. Rogge, S. N. Coppersmith, and M. A. Eriksson, "Silicon quantum electronics," *Rev. Mod. Phys.* **85** no. 961–1019, (2013) .

[20] J. O'Gorman, N. H. Nickerson, P. Ross, J. J. Morton, and S. C. Benjamin, "silicon-based surface code quantum computer," *NPJ Quantum Information* **2** no. 15019, (2016) .

[21] M. Kjaergaard, M. E. Schwartz, P. Krantz, J. I.-J. Wang, S. Gustavsson, and D. William, "Superconducting Qubits : Current State of Play," 2019. `arXiv:arXiv:1905.13641v1`.

[22] C. J. Ballance, T. P. Harty, N. M. Linke, M. A. Sepiol, and D. M. Lucas, "High-Fidelity Quantum Logic Gates Using Trapped-Ion Hyperfine Qubits," *Physical Review Letters* **117** no. 060504, (2016) .

[23] T. P. Harty, D. T. C. Allcock, C. J. Ballance, L. Guidoni, H. A. Janacek, N. M. Linke, D. N. Stacey, and D. M. Lucas, "High-Fidelity Preparation, Gates, Memory, and Readout of a Trapped-Ion Quantum Bit," *Physical Review Letters* **113** no. 220501, (2014) .

[24] A. H. Myerson, D. J. Szwer, S. C. Webster, D. T. C. Allcock, M. J. Curtis, G. Imreh, J. A. Sherman, D. N. Stacey, A. M. Steane, and D. M. Lucas, "High-Fidelity Readout of Trapped-Ion Qubits," *Physical Review Letters* **100** no. 200502, (2008) .

[25] B. Lekitsch, S. Weidt, A. G. Fowler, S. J. Devitt, and W. K. Hensinger, "Blueprint for a microwave trapped-ion quantum computer," *Science Advances* **3** no. 1601540, (2016) , `arXiv:arXiv:1508.00420v3`.

[26] D. Castelvecchi, "Quantum computers ready to leap out of the lab," *Nature* **541** no. 9, (2017) .

[27] D. Castelvecchi, "Quantum cloud goes commercial," *Nature* **543** no. 159, (2017) .

[28] R. Barends, J. Kelly, A. Megrant, A. Veitia, D. Sank, E. Jeffrey, T. C. White, J. Mutus, A. G. Fowler, B. Campbell, Y. Chen, Z. Chen, B. Chiaro, A. Dunsworth, C. Neill, P. O'Malley, P. Roushan, A. Vainsencher, J. Wenner, A. N. Korotkov, A. N. Cleland, and J. M. Martinis, "Superconducting quantum circuits at the surface code threshold for fault tolerance," *Nature* **508** no. 7497, (2014) 500–503, `arXiv:1402.4848`.

[29] S. Sheldon, E. Magesan, J. M. Chow, and J. M. Gambetta, "Procedure for systematically tuning up cross-talk in the cross-resonance gate," *Physical Review A* **93** no. 060302, (2016) 1–5.

[30] S. S. Hong, A. T. Papageorge, P. Sivarajah, G. Crossman, N. Didier, A. M. Polloreno, E. A. Sete, S. W. Turkowski, M. P. Silva, and B. R. Johnson, "Demonstration of a Parametrically-Activated Entangling Gate Protected from Flux Noise," 2019. `arXiv:arXiv:1901.08035v1`.

[31] N. Ofek, A. Petrenko, R. Heeres, P. Reinhold, Z. Leghtas, B. Vlastakis, Y. Liu, L. Frunzio, S. M. Girvin, L. Jiang, M. Mirrahimi, M. H. Devoret, and R. J. Schoelkopf, "Extending the lifetime of a quantum bit with error correction in superconducting circuits," *Nature* **536** no. 7617, (2016) 441–445.

[32] J. Otterbach, R. Manenti, N. Alidoust, A. Bestwick, M. Block, B. Bloom, S. A. Caldwell, N. Didier, E. S. Fried, S. Hong, P. Karalekas, C. B. Osborn, A. Papageorge, E. C. Peterson, G. Prawiroatmodjo, N. Rubin, C. A. Ryan, D. Scarabelli, M. Scheer, E. A. Sete, P. Sivarajah, R. S. Smith, A. Staley, N. Tezak, W. J. Zeng, A. Hudson, B. R. Johnson, M. Reagor, M. P. Silva, and C. Rigetti, "Unsupervised Machine Learning on a Hybrid Quantum Computer," 2017. `arXiv:arXiv:1712.05771v1`.

[33] A. Kandala, A. Mezzacapo, K. Temme, M. Takita, M. Brink, J. M. Chow, and J. M. Gambetta, "Hardware-efficient variational quantum eigensolver for small molecules and quantum magnets," *Nature* **549** no. 7671, (2017) 242–246.

[34] C. Neill, P. Roushan, K. Kechedzhi, S. Boixo, S. V. Isakov, V. Smelyanskiy, A. Megrant, B. Chiaro, A. Dunsworth, K. Arya, R. Barends, B. Burkett, Y. Chen, Z. Chen, A. Fowler, B. Foxen, M. Giustina, R. Graff, E. Jeffrey, T. Huang, J. Kelly, P. Klimov, E. Lucero, J. Mutus, M. Neeley, C. Quintana, D. Sank, A. Vainsencher, J. Wenner, T. C. White, H. Neven, and J. M. Martinis, "A blueprint for demonstrating quantum supremacy with superconducting qubits," *Science* **360** no. 6385, (2018) 195–199.

[35] J. Kelly, "A Preview of Bristlecone, Google's New Quantum Processor," 2018. `https://ai.googleblog.com/2018/03/a-preview-of-bristlecone-googles-new.html`.

[36] J. Hsu, "Intel's 49-Qubit Chip Shoots for Quantum Supremacy.," 2018. `https://spectrum.ieee.org/tech-talk/computing/hardware/intels-49qubit-chip-aims-for-quantum-supremacy`.

[37] C. Rigetti, "The Rigetti 128-qubit chip and what it means for quantum.," 2018. `https://medium.com/rigetti/the-rigetti-128-qubit-chip-and-what-it-means-for-quantum-df757d1b71ea`.

[38] S. K. Moore, "IBM Edges Closer to Quantum Supremacy with 50-Qubit Processor," 2017. `https://spectrum.ieee.org/tech-talk/computing/hardware/ibm-edges-closer-to-quantum-supremacy-with-50qubit-processor`.

[39] Y. Makhlin, G. Schön, and A. Shnirman, "Quantum-state engineering with Josephson-junction devices," *Rev. Mod. Phys.* **73** (2001) 357–400.

[40] Y. Nakamura, C. D. Chen, and J. S. Tsai, "Spectroscopy of energy-level splitting between two macroscopic quantum states of charge coherently superposed by josephson coupling," *Physical Review Letters* **79** (1997) 2328–2331.

[41] Y. Nakamura, Y. A. Pashkin, and J. S. Tsai, "Coherent control of macroscopic quantum states in a single-cooper-pair box," *Nature* **398** no. 6730, (1999) 86–788.

[42] A. Blais, R. S. Huang, A. Wallraff, S. M. Girvin, and R. J. Scheolkopf, "Cavity quantum electrodynamics for superconducting electrical circuits: An architecture for quantum computation," *Physical Review A - Atomic, Molecular, and Optical Physics* **70** no. 1, (2004) 019901–1, arXiv:0402216 [cond-mat].

[43] A. Wallraff, D. I. Schuster, A. Blais, L. Frunzio, R. S. Huang, J. Majer, S. Kumar, S. M. Girvin, and R. J. Schoelkopf, "Strong coupling of a single photon to a superconducting qubit using circuit quantum electrodynamics," *Nature* **431** no. September, (2004) 94–110, arXiv:0407325 [cond-mat].

[44] S. Haroche and D. Kleppner, "Cavity Quantum Electrodynamics," *Physics Today* **42** (1989) 24–30.

[45] R. J. Thompson, "Observation of normal-mode splitting for an atom in an optical cavity," *Physical Review Letters* **68** no. 8, (1992) 1132–1135.

[46] A. Wallraff, D. I. Schuster, A. Blais, L. Frunzio, J. Majer, M. H. Devoret, S. M. Girvin, and R. J. Schoelkopf, "Approaching unit visibility for control of a superconducting qubit with dispersive readout," *Physical Review Letters* **95** no. 6, (2005) 1–4, arXiv:0502645 [cond-mat].

[47] R. Bianchetti, S. Filipp, M. Baur, J. M. Fink, M. Göppl, P. J. Leek, L. Steffen, A. Blais, and A. Wallraff, "Dynamics of dispersive single-qubit readout in circuit quantum electrodynamics," *Physical Review A - Atomic, Molecular, and Optical Physics* **80** no. 4, (2009) 1–7, arXiv:0907.2549.

[48] R. Versluis, S. Poletto, N. Khammassi, B. Tarasinski, N. Haider, D. J. Michalak, A. Bruno, K. Bertels, and L. Dicarlo, "Scalable Quantum Circuit and Control for a Superconducting Surface Code," *Physical Review Applied* **8** no. 3, (2017) 034021.

[49] B. Foxen, J. Y. Mutus, E. Lucero, R. Graff, A. Megrant, Y. Chen, C. Quintana, B. Burkett, J. Kelly, E. Jeffrey, Y. Yang, A. Yu, K. Arya, R. Barends, Z. Chen, B. Chiaro, A. Dunsworth, A. Fowler, C. Gidney, M. Giustina, T. Huang, P. Klimov, M. Neeley, C. Neill, P. Roushan, D. Sank, A. Vainsencher, J. Wenner,

T. C. White, and J. M. Martinis, "Qubit compatible superconducting interconnects," *Quantum Sci. Technol.* **3** no. 014005, (2018) .

[50] N. T. Bronn, V. P. Adiga, S. B. Olivadese, X. Wu, J. M. Chow, and D. P. Pappas, "High Coherence Plane Breaking Packaging for Superconducting Qubits," *Quantum Sci. Technol.* **3** no. 024007, (2018) , `arXiv:arXiv:1709.02402v2`.

[51] D. Rosenberg, D. Kim, R. Das, D. Yost, S. Gustavsson, D. Hover, P. Krantz, A. Melville, L. Racz, G. Samach, S. J. Weber, F. Yan, J. L. Yoder, A. J. Kerman, and W. D. Oliver, "3D integrated superconducting qubits," *NPJ Quantum Information* **3** no. 42, (2017) .

[52] A. Montanaro, "Quantum algorithms : an overview," *NPJ Quantum Information* **2** no. 15023, (2016) 1–8.

[53] A. W. Cross, L. S. Bishop, S. Sheldon, P. D. Nation, and J. M. Gambetta, "Validating quantum computers using randomized model circuits," 2018. `arXiv:1811.12926v1`.

[54] S. Krinner, S. Storz, P. Kurpiers, P. Magnard, J. Heinsoo, R. Keller, C. Eichler, and A. Wallraff, "Engineering cryogenic setups for 100-qubit scale superconducting circuit systems," 2018. `arXiv:arXiv:1806.07862v1`.

[55] M. Vahidpour, W. O. Brien, J. T. Whyland, J. Angeles, D. Scarabelli, G. Crossman, K. Yadav, Y. Mohan, V. Rawat, R. Renzas, N. Vodrahalli, A. Bestwick, and C. Rigetti, "Superconducting Through-Silicon Vias for Quantum Integrated Circuits," 2017. `arXiv:arXiv:1708.02226v1`.

[56] T. G. Mcconkey, J. H. Béjanin, C. T. Earnest, C. R. H. Mcrae, Z. Pagel, J. R. Rinehart, and M. Mariantoni, "Mitigating leakage errors due to cavity modes in a superconducting quantum computer," *Quantum Sci. Technol.* **3** no. 034004, (2018) .

[57] B. Lienhard, J. Braum, W. Woods, D. Rosenberg, G. Calusine, S. Weber, A. Veps, K. O. Brien, T. P. Orlando, S. Gustavsson, and W. D. Oliver, "Microwave

Packaging for Superconducting Qubits," pp. 1–4. 2019. arXiv:arXiv:1906.05425v1.

[58] A. Dunsworth, R. Barends, Y. Chen, Z. Chen, B. Chiaro, A. Fowler, B. Foxen, E. Jeffrey, J. Kelly, E. Lucero, J. Y. Mutus, M. Neeley, C. Neill, C. Quintana, P. Roushan, D. Sank, A. Vainsencher, T. C. White, H. Neven, J. M. Martinis, A. Megrant, A. Dunsworth, R. Barends, Y. Chen, Z. Chen, B. Chiaro, A. Fowler, and B. Foxen, "A method for building low loss multi-layer wiring for superconducting microwave devices," *Applied Physics Letters* **112** no. 6, (2018) 182601.

[59] J. H. Béjanin, T. G. McConkey, J. R. Rinehart, C. T. Earnest, C. R. McRae, D. Shiri, J. D. Bateman, Y. Rohanizadegan, B. Penava, P. Breul, S. Royak, M. Zapatka, A. G. Fowler, and M. Mariantoni, "Three-Dimensional Wiring for Extensible Quantum Computing: The Quantum Socket," *Physical Review Applied* **6** no. 4, (2016) , arXiv:1606.00063.

[60] W. O. Brien, M. Vahidpour, J. T. Whyland, J. Angeles, D. Scarabelli, G. Crossman, K. Yadav, Y. Mohan, V. Rawat, R. Renzas, N. Vodrahalli, A. Bestwick, and C. Rigetti, "Superconducting Caps for Quantum Integrated Circuits," 2017. arXiv:arXiv:1708.02219v1.

[61] Q. Liu, M. Li, K. Dai, K. Zhang, G. Xue, X. Tan, H. Yu, and Y. Yu, "Extensible 3D architecture for superconducting quantum computing," *Applied Physics Letters* **110** no. 232602, (2017) .

[62] J. Rahamim, T. Behrle, M. J. Peterer, A. Patterson, P. A. Spring, T. Tsunoda, R. Manenti, and G. Tancredi, "Double-sided coaxial circuit QED with out-of-plane wiring," *Applied Physics Letters* **110** no. 22, (2017) 222602.

[63] G. S. Paraoanu, "Microwave-induced coupling of superconducting qubits," *Physical Review B* **74** no. 140504(R), (2006) .

[64] C. Rigetti and M. Devoret, "Fully microwave-tunable universal gates in superconducting qubits with linear couplings and fixed transition frequencies," *Physical Review B* **81** no. 134507, (2010) .

[65] A. Patterson, *Control of Prototype Quantum Processors based on Coaxial Transmon Qubits*. PhD thesis, University of Oxford, 2019.

[66] D. F. Walls, *Quantum optics*. Springer, 2006.

[67] U. Vool and M. H. Devoret, "Introduction to quantum electromagnetic circuits," *International Journal of Circuit Theory and Applications* **45** no. 7, (2017) 897–934.

[68] B. D. Josephson, "Possible new effects in superconductive tunnelling," *Physics Letters* **1** no. 7, (1962) 251–253.

[69] J. Koch, T. M. Yu, J. Gambetta, A. A. Houck, D. I. Schuster, J. Majer, A. Blais, M. H. Devoret, S. M. Girvin, and R. J. Schoelkopf, "Charge-insensitive qubit design derived from the Cooper pair box," *Physical Review A* **76** no. 4, (2007) 1–19, `arXiv:0703002 [cond-mat]`.

[70] M. H. Devoret, "Quantum fluctuations in electrical circuits," in *Quantum Fluctuations: Les Houches Session LXIII*. 1997.

[71] R. F. Voss and R. Webb, "Macroscopic quantum tunneling in 1-um Nb Josephson junctions," *Physical Review Letters* **47** no. 265, (1981) .

[72] M. H. Devoret, J. M. Martinis, and J. Clarke, "Measurements of macroscopic quantum tunnelling out of the zero-voltage state of a current-biased josephson junction," *Physical Review Letters* **55** (1985) 1908–1911.

[73] N. Didier, E. A. Sete, M. P. Silva, and C. Rigetti, "Analytical modeling of parametrically modulated transmon qubits," *Physical Review A* **97** no. 022330, (2018) .

[74] J. Clarke and A. I. Braginski, *The SQUID Handbook: Fundamentals and Technology of SQUIDs and SQUID Systems, I*. Wiley Online Library, 2004.

[75] M. D. Hutchings, J. B. Hertzberg, Y. Liu, N. T. Bronn, G. A. Keefe, M. Brink, J. M. Chow, and B. L. T. Plourde, "Tunable Superconducting Qubits with Flux-Independent Coherence," *Physical Review Applied* **8** no. 044003, (2017) 1–13.

[76] J. Braumüller, M. Sandberg, M. R. Vissers, A. Schneider, S. Schlör, L. Grünhaupt, H. Rotzinger, M. Marthaler, A. Lukashenko, A. Dieter, A. V. Ustinov, M. Weides, and D. P. Pappas, "Concentric transmon qubit featuring fast tunability and an anisotropic magnetic dipole moment," *Applied Physics Letters* **108** no. 3, (2016) , arXiv:1509.08014.

[77] A. Patterson, J. Rahamim, T. Tsunoda, P. A. Spring, S. Jebari, K. Ratter, M. Mergenthaler, G. Tancredi, B. Vlastakis, M. Esposito, and P. J. Leek, "Calibration of the cross-resonance two-qubit gate between directly-coupled transmons," 2019. arXiv:arXiv:1905.05670v1.

[78] L. Allen and J. Eberly, *Optical resonance and two-level atoms*. Dover, 1987.

[79] F. Yan, S. Gustavsson, A. Kamal, J. Birenbaum, A. P. Sears, D. Hover, T. J. Gudmundsen, D. Rosenberg, G. Samach, S. Weber, J. L. Yoder, T. P. Orlando, J. Clarke, A. J. Kerman, and W. D. Oliver, "The flux qubit revisited to enhance coherence and reproducibility," *Nature Communications* **7** (2016) 1–9, arXiv:1508.06299.

[80] Ł. Cywiński, R. M. Lutchyn, C. P. Nave, and S. D. Sarma, "How to enhance dephasing time in superconducting qubits," *Physical Review B* **77** no. 174509, (2008) .

[81] M. J. Biercuk, H. Uys, A. P. Vandevender, N. Shiga, W. M. Itano, and J. J. Bollinger, "Optimized dynamical decoupling in a model quantum memory," *Nature* **458** no. 7241, (2009) 996–1000.

[82] F. Yoshihara, K. Harrabi, A. O. Niskanen, Y. Nakamura, and J. S. Tsai, "Decoherence of flux qubits due to 1/f flux noise," *Physical Review Letters* **97** no. 1670001, (2006) 1–4, arXiv:0606481 [cond-mat].

[83] R. H. Koch, D. P. Divincenzo, and J. Clarke, "Model for 1/f flux noise in SQUIDs and qubits," *Physical Review Letters* **98** no. 26, (2007) 1–4, arXiv:0702025 [cond-mat].

[84] J. Gambetta, A. Blais, D. I. Schuster, A. Wallraff, L. Frunzio, J. Majer, M. H. Devoret, S. M. Girvin, and R. J. Schoelkopf, "Qubit-photon interactions in a cavity: Measurement-induced dephasing and number splitting," *Physical Review A - Atomic, Molecular, and Optical Physics* **74** no. 4, (2006) 1–14, arXiv:0602322 [cond-mat].

[85] D. I. Schuster, A. Wallraff, A. Blais, L. Frunzio, R. S. Huang, J. Majer, S. M. Girvin, and R. J. Schoelkopf, "Ac Stark shift and dephasing of a superconducting qubit strongly coupled to a cavity field," *Physical Review Letters* **94** no. 12, (2005) 1–4, arXiv:0408367 [cond-mat].

[86] D. I. Schuster, A. A. Houck, J. A. Schreier, A. Wallraff, J. M. Gambetta, A. Blais, L. Frunzio, J. Majer, B. Johnson, M. H. Devoret, S. M. Girvin, and R. J. Schoelkopf, "Resolving photon number states in a superconducting circuit," *Nature* **445** no. 7127, (2007) 515–518, arXiv:0608693 [cond-mat].

[87] M. J. Peterer, *Experiments on Multi-Level Superconducting Qubits and Coaxial Circuit QED*. PhD thesis, University of Oxford, 2016.

[88] E. M. Purcell, "Spontaneous emission probabilities at radio frequencies," *Physical Review* **69** no. 681, (1946) .

[89] A. A. Houck, J. A. Schreier, B. R. Johnson, J. M. Chow, J. Koch, J. M. Gambetta, D. I. Schuster, L. Frunzio, M. H. Devoret, S. M. Girvin, and R. J. Schoelkopf, "Controlling the Spontaneous Emission of a Superconducting Transmon Qubit," *Physical Review Letters* **101** no. 080502, (2008) 1–4.

[90] O. Gargiulo, S. Oleschko, M. Zanner, and G. Kirchmair, "Fast flux control of 3D transmon qubits using a magnetic hose," 2018. arXiv:arXiv:1811.10875v1.

[91] B. C. Wadell, *Transmission Line Design Handbook*. 1991.

[92] G. Dolan and J. Dunsmuir, "Very small (20 nm) lithographic wires, dots, rings, and tunnel junctions," *Physica B* **80** no. 87, (1988) .

[93] I. M. Pop, T. Fournier, T. Crozes, F. Lecocq, I. Matei, B. Pannetier, O. Buisson, and W. Guichard, "Fabrication of stable and reproducible sub-micron tunnel junctions," *Journal of Vacuum Science & Technology B* **010607** no. 2012, (2011) , `arXiv:1105.6204`.

[94] C. Wang, C. Axline, Y. Y. Gao, T. Brecht, Y. Chu, L. Frunzio, M. H. Devoret, and R. J. Schoelkopf, "Supplementary Materials for " Surface participation and dielectric loss in superconducting qubits "," *Applied Physics Letters* **107** no. 162601, (2015) 4–9.

[95] V. Ambegaokar and A. Baratoff, "Tunneling between superconductors," *Physical Review Letters* **10:486** no. 95, (1963) .

[96] M. Brink, "Scaling Quantum Processors with Superconducting Qubits," in *Conference Talk at 687th WE-Heraeus Seminar: Scalable Hardware Platforms for Quantum Computing*. Zurich, 2019.

[97] J. M. Fink, *Quantum Nonlinearities in Strong Coupling Circuit QED*. PhD thesis, 2011.

[98] C. M. Quintana, A. Megrant, Z. Chen, A. Dunsworth, B. Chiaro, R. Barends, B. Campbell, Y. Chen, I. Hoi, E. Jeffrey, J. Kelly, J. Y. Mutus, P. J. O'Malley, C. Neill, P. Roushan, D. Sank, A. Vainsencher, J. Wenner, T. White, A. N. Cleland, and J. M. Martinis, "Characterization and reduction of microfabrication-induced decoherence in superconducting quantum circuits," *Applied Physics Letters* **105** no. 062601, (2014) .

[99] J. B. Chang, M. R. Vissers, A. D. Córcoles, M. Sandberg, J. Gao, W. David, J. M. Chow, J. M. Gambetta, M. B. Rothwell, G. A. Keefe, M. Steffen, D. P. Pappas,

J. B. Chang, M. R. Vissers, D. C. Antonio, J. Gao, D. W. Abraham, J. M. Chow, J. M. Gambetta, M. B. Rothwell, G. A. Keefe, M. Steffen, and D. P. Pappas, "Improved superconducting qubit coherence using titanium nitride," *Applied Physics Letters* **103** no. 012602, (2013) .

[100] L. Grünhaupt, U. V. Lüpke, D. Gusenkova, S. T. Skacel, N. Maleeva, S. Schlör, A. Bilmes, H. Rotzinger, A. V. Ustinov, M. Weides, and I. M. Pop, "An argon ion beam milling process for native AlOx layers enabling coherent superconducting contacts," *Applied Physics Letters* **111** no. 072601, (2017) .

[101] A. Kamal, J. L. Yoder, F. Yan, T. J. Gudmundsen, D. Hover, P. Sears, P. Welander, T. P. Orlando, S. Gustavsson, and W. D. Oliver, "Improved superconducting qubit coherence with high-temperature substrate annealing," 2016. `arXiv:arXiv:1606.09262v1`.

[102] C. T. Earnest, T. G. Mcconkey, A. Peters, A. Korinek, H. Yuan, and M. Mariantoni, "Substrate surface engineering for high-quality silicon/aluminum superconducting resonators," 2018. `arXiv:arXiv:1807.08072v1`.

[103] A. Nersisyan, S. Poletto, N. Alidoust, R. Manenti, R. Renzas, C.-v. Bui, K. Vu, T. Whyland, Y. Mohan, E. A. Sete, S. Stanwyck, A. Bestwick, and M. Reagor, "Manufacturing low dissipation superconducting quantum processors," 2019. `arXiv:arXiv:1901.08042v1`.

[104] G. Calusine, A. Melville, W. Woods, R. Das, C. Stull, D. Bolkhovosky, D. Braje, D. Hover, D. K. Kim, X. Miloshi, D. Rosenberg, A. Sevi, J. L. Yoder, E. Dauler, and W. D. Oliver, "Analysis and mitigation of interface losses in trenched superconducting coplanar waveguide resonators," *Applied Physics Letters* **112** no. 062601, (2018) .

[105] C. Wang, C. Axline, Y. Y. Gao, and T. Brecht, "Surface participation and dielectric loss in superconducting qubits," *Applied Physics Letters* **107** no. 162601, (2015) .

[106] T. Brecht, Y. Chu, C. Axline, W. Pfaff, J. Z. Blumoff, K. Chou, L. Krayzman, L. Frunzio, and R. J. Schoelkopf, "Micromachined Integrated Quantum Circuit Containing a Superconducting Qubit," *Physical Review Applied* **7** no. 4, (2017) 1–6, `arXiv:1611.02166`.

[107] L. S. Bishop, E. Ginossar, and S. M. Girvin, "Response of the Strongly Driven Jaynes-Cummings Oscillator," *Physical Review Letters* **105** no. 100505, (2010) .

[108] H. Paik, D. I. Schuster, L. S. Bishop, G. Kirchmair, G. Catelani, A. P. Sears, B. R. Johnson, M. J. Reagor, L. Frunzio, L. I. Glazman, S. M. Girvin, M. H. Devoret, and R. J. Schoelkopf, "Observation of High Coherence in Josephson Junction Qubits Measured in a Three-Dimensional Circuit QED Architecture," *Physical Review Letters* **107** no. 240501, (2011) .

[109] G. Tancredi, G. Ithier, and P. J. Meeson, "Bifurcation , mode coupling and noise in a nonlinear multimode superconducting microwave resonator," *Applied Physics Letters* **103** no. 063504, (2013) 1–6.

[110] T. K. Mavrogordatos, G. Tancredi, M. Elliott, M. J. Peterer, A. Patterson, J. Rahamim, P. J. Leek, E. Ginossar, and M. H. Szyma, "Simultaneous Bistability of a Qubit and Resonator in Circuit Quantum Electrodynamics," *Physical Review Letters* **118** no. 040402, (2017) 1–5.

[111] D. Kajfez and E. J. Hwan, "Q-Factor Measurement with Network Analyzer," *IEEE TRANSACTIONS ON MICROWAVE THEORY AND TECHNIQUES* **MTT-32** no. 7, (1984) .

[112] D. Kajfez, "Q factor measurements, analog and digital," University of Mississippi. 1999.

[113] T. Walter, P. Kurpiers, S. Gasparinetti, P. Magnard, A. Poto, Y. Salathé, M. Pechal, M. Mondal, M. Oppliger, C. Eichler, and A. Wallraff, "Rapid High-Fidelity Single-Shot Dispersive Readout of Superconducting Qubits," *Physical Review Applied* **7** no. 054020, (2017) 1–11.

[114] E. Jeffrey, D. Sank, J. Y. Mutus, T. C. White, J. Kelly, R. Barends, Y. Chen, Z. Chen, B. Chiaro, A. Dunsworth, A. Megrant, P. J. J. O. Malley, C. Neill, P. Roushan, A. Vainsencher, J. Wenner, A. N. Cleland, and J. M. Martinis, "Fast Accurate State Measurement with Superconducting Qubits," *Physical Review Letters* **112** no. 190504, (2014) 1–5.

[115] M. D. Reed, B. R. Johnson, A. A. Houck, L. DiCarlo, J. M. Chow, D. I. Schuster, L. Frunzio, and R. J. Schoelkopf, "Fast reset and suppressing spontaneous emission of a superconducting qubit," *Applied Physics Letters* **96** no. 203110, (2015) .

[116] F. Mallet, F. R. Ong, A. Palacios-laloy, F. Nguyen, P. Bertet, D. Vion, and D. Esteve, "Single-shot qubit readout in circuit quantum electrodynamics," *Nature Physics* **5** no. 11, (2009) 791–795.

[117] J. Braumüller, J. Cramer, S. Schlör, H. Rotzinger, L. Radtke, A. Lukashenko, P. Yang, S. T. Skacel, S. Probst, M. Marthaler, L. Guo, A. V. Ustinov, and M. Weides, "Multiphoton dressing of an anharmonic superconducting many-level quantum circuit," *Physical Review B* **91** no. 054523, (2015) .

[118] T. Behrle, *Simulation and Measurements of Single and Coupled Coaxial Qubits (Masters Thesis)*. 2017.

[119] W. Pfaff, C. J. Axline, L. D. Burkhart, U. Vool, L. Frunzio, L. Jiang, M. H. Devoret, and R. J. Schoelkopf, "Supplementary Material: Controlled release of multiphoton quantum states from a microwave cavity memory," *Nature Physics* **13** (2017) .

[120] J. Heinsoo, C. K. Andersen, A. Remm, S. Krinner, T. Walter, Y. Salathé, S. Gasparinetti, J.-c. Besse, A. Potoˇ, and A. Wallraff, "Rapid High-fidelity Multiplexed Readout of Superconducting Qubits," *Physical Review Applied* **10** no. 034040, (2018) 1–14.

[121] F. Solgun, D. P. Divincenzo, and J. M. Gambetta, "Simple Impedance Response Formulas for the Dispersive Interaction Rates in the Effective Hamiltonians of Low Anharmonicity Superconducting Qubits," 2017. `arXiv:arxiv:1712.08154v1`.

[122] A. D. Córcoles, J. M. Gambetta, J. M. Chow, J. A. Smolin, M. Ware, J. Strand, B. L. T. Plourde, and M. Steffen, "Process verification of two-qubit quantum gates by randomized benchmarking," *Physical Review A* **87** no. 030301, (2013) .

[123] A. D. Córcoles, E. Magesan, S. J. Srinivasan, A. W. Cross, M. Steffen, J. M. Gambetta, A. D. Co, and J. M. Chow, "Demonstration of a quantum error detection code using a square lattice of four superconducting qubits," *Nature Communications* **6** no. 6979, (2015) .

[124] R. C. Bialczak, M. Ansmann, M. Hofheinz, E. Lucero, M. Neeley, A. D. O. Connell, D. Sank, H. Wang, J. Wenner, M. Steffen, A. N. Cleland, and J. M. Martinis, "Quantum process tomography of a universal entangling gate implemented with Josephson phase qubits," *Nature Physics* **6** (2010) 409–413.

[125] J. M. Chow, J. M. Gambetta, L. Tornberg, J. Koch, L. S. Bishop, A. A. Houck, B. R. Johnson, L. Frunzio, S. M. Girvin, and R. J. Schoelkopf, "Randomized benchmarking and process tomography for gate errors in a solid-state qubit," *Physical Review Letters* **102** no. 9, (2009) 1–4, `arXiv:0811.4387`.

[126] E. Magesan, J. M. Gambetta, B. R. Johnson, C. A. Ryan, J. M. Chow, S. T. Merkel, M. P. Silva, G. A. Keefe, M. B. Rothwell, T. A. Ohki, M. B. Ketchen, and M. Steffen, "Efficient Measurement of Quantum Gate Error by Interleaved Randomized Benchmarking," *Physical Review Letters* **109** no. 080505, (2012) 1–5.

[127] K. Geerlings, Z. Leghtas, I. M. Pop, S. Shankar, L. Frunzio, R. J. Schoelkopf, M. Mirrahimi, and M. H. Devoret, "Demonstrating a driven reset protocol for a superconducting qubit," *Physical Review Letters* **110** no. 12, (2013) 1–5, `arXiv:1211.0491`.

[128] X. Y. Jin, A. Kamal, A. P. Sears, T. Gudmundsen, D. Hover, J. Miloshi, R. Slattery, F. Yan, J. Yoder, T. P. Orlando, S. Gustavsson, and W. D. Oliver, "Thermal and Residual Excited-State Population in a 3D Transmon Qubit," *Physical Review Letters* **114** no. 24, (2015) 1–7, `arXiv:1412.2772`.

[129] Z. Wang, S. Shankar, Z. K. Minev, P. Campagne-Ibarcq, A. Narla, and M. H. Devoret, "Cavity Attenuators for Superconducting Qubits," *Physical Review Applied* **11** no. 014031, (2019) .

[130] A. A. Clerk and D. W. Utami, "Using a qubit to measure photon-number statistics of a driven thermal oscillator," *Physical Review A* **75** no. 042302, (2007) 1–12.

[131] J.-H. Yeh, J. LeFebvre, S. Premaratne, F. C. Wellstood, and B. S. Palmer, "Microwave attenuators for use with quantum devices below 100 mK," *J. Appl. Phys.* **121** no. 224501, (2017) .

[132] J. J. Burnett, A. Bengtsson, M. Scigliuzzo, D. Niepce, M. Kudra, P. Delsing, and J. Bylander, "Decoherence benchmarking of superconducting qubits," 2019. `arXiv:arXiv:1901.04417v1`.

[133] S. Schlör, J. Lisenfeld, C. Müller, A. Schneider, D. P. Pappas, A. V. Ustinov, and M. Weides, "Correlating decoherence in transmon qubits: Low frequency noise by single fluctuators," 2019. `arXiv:arXiv:1901.05352v1`.

[134] P. V. Klimov, J. Kelly, Z. Chen, M. Neeley, A. Megrant, B. Burkett, R. Barends, K. Arya, B. Chiaro, Y. Chen, A. Dunsworth, A. Fowler, B. Foxen, C. Gidney, M. Giustina, R. Graff, T. Huang, E. Jeffrey, E. Lucero, J. Y. Mutus, O. Naaman, C. Neill, C. Quintana, P. Roushan, D. Sank, A. Vainsencher, J. Wenner, T. C. White, S. Boixo, R. Babbush, V. N. Smelyanskiy, H. Neven, and J. M. Martinis, "Fluctuations of Energy-Relaxation Times in Superconducting Qubits," *Physical Review Letters* **121** no. 90502, (2018) .

[135] C. Müller, J. H. Cole, and J. Lisenfeld, "Towards understanding two-level-systems in amorphous solids - Insights from quantum circuits," 2018. arXiv:arXiv:1705.01108v2.

[136] M. S. Moeed, C. T. Earnest, J. H. Béjanin, A. S. Sharafeldin, and M. Mariantoni, "Improving the Time Stability of Superconducting Planar Resonators," 2019. https://arxiv.org/abs/1905.00131.

[137] G. Ithier, E. Collin, P. Joyez, P. J. Meeson, D. Vion, D. Esteve, F. Chiarello, A. Shnirman, Y. Makhlin, J. Schriefl, and G. Schön, "Decoherence in a superconducting quantum bit circuit," *Physical Review B* **72** no. 134519, (2005) 1–22.

[138] J. Bylander, S. Gustavsson, F. Yan, F. Yoshihara, K. Harrabi, G. Fitch, D. G. Cory, Y. Nakamura, J. S. Tsai, and W. D. Oliver, "Noise spectroscopy through dynamical decoupling with a superconducting flux qubit," *Nature Physics* **7** no. 7, (2011) 565–570, arXiv:1101.4707.

[139] S. Gustavsson, J. Bylander, F. Yan, P. Forn-Diaz, V. Bolkhovsky, D. Braje, G. Fitch, K. Harrabi, D. Lennon, S. Gustavsson, J. Bylander, F. Yan, Y. Nakamura, T. P. Orlando, and W. D. Oliver, "Driven Dynamics and Rotary Echo of a Qubit Tunably Coupled to a Harmonic Oscillator," *Physical Review Letters* **108** no. 170503, (2012) 1–6.

[140] D. H. Slichter, R. Vijay, S. J. Weber, S. Boutin, M. Boissonneault, J. M. Gambetta, A. Blais, and I. Siddiqi, "Measurement-Induced Qubit State Mixing in Circuit QED from Up-Converted Dephasing Noise," *Physical Review Letters* **109** no. 153601, (2012) 1–5.

[141] F. Yan, S. Gustavsson, J. Bylander, X. Jin, F. Yoshihara, D. G. Cory, Y. Nakamura, T. P. Orlando, and W. D. Oliver, "Rotating-frame relaxation as a noise spectrum analyser of a superconducting qubit undergoing driven evolution,"

Nature Communications **4** no. 2337, (2013) 1–8. http://dx.doi.org/10.1038/ncomms3337.

[142] F. Yoshihara, Y. Nakamura, F. Yan, S. Gustavsson, J. Bylander, W. D. Oliver, and J. S. Tsai, "Flux qubit noise spectroscopy using Rabi oscillations under strong driving conditions," *Physical Review B - Condensed Matter and Materials Physics* **89** no. 020503, (2014) 1–5, arXiv:1402.1247.

[143] A. Shnirman, G. Schön, I. Martin, and Y. Makhlin, "Low- and High-Frequency Noise from Coherent Two-Level Systems," *Physical Review Letters* **94** no. 127002, (2005) 1–4.

[144] A. Phys, S. Sheldon, M. Sandberg, H. Paik, J. M. Gambetta, B. Abdo, J. M. Chow, M. Steffen, S. Sheldon, M. Sandberg, H. Paik, B. Abdo, J. M. Chow, M. Steffen, and J. M. Gambetta, "Characterization of hidden modes in networks of superconducting qubits Characterization of hidden modes in networks of superconducting qubits," *Applied Physics Letters* **111** no. 222601, (2017) .

[145] S. A. Caldwell, N. Didier, C. A. Ryan, E. A. Sete, A. Hudson, P. Karalekas, R. Manenti, M. P. Silva, R. Sinclair, E. Acala, N. Alidoust, J. Angeles, A. Bestwick, M. Block, B. Bloom, A. Bradley, C. Bui, L. Capelluto, R. Chilcott, J. Cordova, G. Crossman, M. Curtis, S. Deshpande, T. E. Bouayadi, D. Girshovich, S. Hong, K. Kuang, M. Lenihan, T. Manning, A. Marchenkov, J. Marshall, R. Maydra, Y. Mohan, W. O. Brien, C. Osborn, J. Otterbach, A. Papageorge, J. Paquette, M. Pelstring, A. Polloreno, G. Prawiroatmodjo, V. Rawat, M. Reagor, R. Renzas, M. Suska, N. Tezak, D. C. Thompson, T. To, M. Vahidpour, N. Vodrahalli, T. Whyland, and K. Yadav, "Parametrically Activated Entangling Gates Using Transmon Qubits," *Physical Review Applied* **10** no. 034050, (2018) 1–8.

[146] Y. Chen, C. Neill, P. Roushan, N. Leung, M. Fang, R. Barends, J. Kelly, B. Campbell, Z. Chen, B. Chiaro, A. Dunsworth, E. Jeffrey, A. Megrant, J. Y.

Mutus, P. J. O'Malley, C. M. Quintana, D. Sank, A. Vainsencher, J. Wenner, T. C. White, M. R. Geller, A. N. Cleland, and J. M. Martinis, "Qubit architecture with high coherence and fast tunable coupling," *Physical Review Letters* **113** no. 22, (2014) 1–5, `arXiv:1402.7367`.

[147] M. A. Rol, F. Battistel, F. K. Malinowski, C. C. Bultink, B. M. Tarasinski, R. Vollmer, N. Haider, N. Muthusubramanian, A. Bruno, B. M. Terhal, and L. Dicarlo, "A fast, low-leakage, high-fidelity two-qubit gate for a programmable superconducting quantum computer," pp. 1–18. 2019. `arXiv:arXiv:1903.02492v1`.

[148] D. C. Mckay, S. Filipp, A. Mezzacapo, E. Magesan, J. M. Chow, and J. M. Gambetta, "Universal Gate for Fixed-Frequency Qubits via a Tunable Bus," *Physical Review Applied* **6** no. 064007, (2016) 1–10.

[149] N. K. Langford, R. Sagastizabal, M. Kounalakis, C. Dickel, A. Bruno, F. Luthi, D. J. Thoen, A. Endo, and L. Dicarlo, "Supplmentary Material: Experimentally simulating the dynamics of quantum light and matter at deep-strong coupling," *Nature* **8** no. 1715, (2017) 1–18.

[150] S. E. D. Graaf, A. A. Adamyan, T. Lindström, D. Erts, S. E. Kubatkin, A. Y. Tzalenchuk, and A. V. Danilov, "Direct Identification of Dilute Surface Spins on Al 2 O 3 : Origin of Flux Noise in Quantum Circuits," *Physical Review Letters* **118** no. 057703, (2017) 1–5.

[151] P. Kumar, S. Sendelbach, M. A. Beck, J. W. Freeland, Z. Wang, H. Wang, C. C. Yu, R. Q. Wu, D. P. Pappas, and R. Mcdermott, "Origin and Reduction of 1 = f Magnetic Flux Noise in Superconducting Devices," *Physical Review Applied* **6** no. 041001, (2016) 1–5.

[152] S. E. D. Graaf, L. Faoro, J. J. Burnett, A. A. Adamyan, A. Y. Tzalenchuk, S. E. Kubatkin, T. Lindström, and A. V. Danilov, "Suppression of low-frequency charge

noise in superconducting resonators by surface spin desorption," *Nature Communications* **9** no. 1143, (2018) 3–8.

[153] J. Luneau, *Introducing flux tunability to coaxmon architecture (Masters Thesis).* 2018.

[154] S. Gustavsson, J. Bylander, F. Yan, W. D. Oliver, F. Yoshihara, and Y. Nakamura, "Noise correlations in a flux qubit with tunable tunnel coupling," *Physical Review B - Condensed Matter and Materials Physics* **84** no. 014525, (2011) , `arXiv:1104.5212`.

[155] M. D. Reed, *Entanglement and Quantum Error Correction with Superconducting Qubits.* PhD thesis, Yale University, 2013.

[156] C. Neill, P. Roushan, K. Kechedzhi, S. Boixo, S. V. Isakov, V. Smelyanskiy, B. Chiaro, A. Dunsworth, K. Arya, R. Barends, B. Burkett, Y. Chen, Z. Chen, A. Fowler, B. Foxen, M. Giustina, R. Graff, E. Jeffrey, T. Huang, J. Kelly, P. Klimov, J. Mutus, M. Neeley, C. Quintana, D. Sank, A. Vainsencher, J. Wenner, H. Neven, and J. M. Martinis, "Supplementary Materials for A blueprint for demonstrating quantum supremacy with superconducting qubits," *Science* **360** no. 195, (2018) .

[157] M. Kounalakis, C. Dickel, A. Bruno, N. K. Langford, and G. A. Steele, "Supplementary Material: Tuneable hopping and nonlinear cross-Kerr interactions in a high-coherence superconducting circuit," *NPJ Quantum Information* **4** no. 38, (2018) 1–11.

[158] M. Mirhosseini, E. Kim, X. Zhang, A. Sipahigil, P. B. Dieterle, A. J. Keller, A. Asenjo-garcia, D. E. Chang, and O. Painter, "Waveguide-mediated interaction of artificial atoms in the strong coupling regime," pp. 1–19. 2018. `arXiv:arXiv:1809.09752v1`.

[159] R. Ma, B. Saxberg, C. Owens, N. Leung, Y. Lu, J. Simon, and D. I. Schuster, "Supplementary Material: A dissipatively stabilized Mott insulator of photons," *Nature* **566** (2019) 0–18.

[160] Y. Salathé, *Toolbox for quantum computing and digital quantum simulation with superconducting qubits*. PhD thesis, ETH Zurich, 2018.

[161] J. Braumüller, M. Marthaler, A. Schneider, A. Stehli, H. Rotzinger, M. Weides, and A. V. Ustinov, "Supplementary Material: Analog quantum simulation of the Rabi model in the ultra-strong coupling regime," *Nature Communications* **8** no. 779, (2017) 1–12.

[162] D. C. Mckay, C. J. Wood, S. Sheldon, J. M. Chow, and J. M. Gambetta, "Efficient Z gates for quantum computing," *Physical Review A* **96** no. 022330, (2017) 1–8.

[163] I. Yang, *Flux Bias Control in a Coaxial Superconducting Qubit Architecture (Masters Thesis)*. 2019.

[164] P. A. Spring, S. Sosnina, T. Tsunoda, B. Vlastakis, and P. J. Leek, "Modelling of TM Modes in Periodically-Shorted Cavities for Circuit QED," 2019. `arXiv:1909.02104`. `http://arxiv.org/abs/1909.02104`.

[165] P. Brooks, A. Kitaev, J. Preskill, P. Brooks, A. Kitaev, and J. Preskill, "Protected gates for superconducting qubits," *Physical Review A* **87** no. 052306, (2013) 1–26.

[166] L. B. Nguyen, Y.-h. Lin, A. Somoroff, N. Grabon, and V. E. Manucharyan, "The high-coherence fluxonium qubit," pp. 1–12. 2018. `arXiv:arXiv:1810.11006v1`.

[167] W. C. Smith, A. Kou, X. Xiao, U. Vool, and M. H. Devoret, "Superconducting circuit protected by two-Cooper-pair tunneling," 2019. `arXiv:arXiv:1905.01206v1`.

[168] M. Roth, N. Moll, G. Salis, M. Ganzhorn, D. J. Egger, S. Filipp, and S. Schmidt, "Adiabatic quantum simulations with driven superconducting qubits," *Physical Review A* **99** no. 022323, (2019) 1–11.